Spectroscopic Studies of Interstellar Molecules

Mark Clifford Whelan

Ph.D. Chemistry

University of Sussex

June 2017

Abstract

Astrochemistry is a wide ranging and varied field of study. Recent discoveries have highlighted the diversity of chemistry in the interstellar medium (ISM) and shown why it is worthy of significant attention. Although chemical evolution of the ISM occurs in the gas and solid phases, this work addresses solely solid phase processes using temperature programmed desorption (TPD) and reflection absorption infrared spectroscopy (RAIRS).

Of particular interest is the formation and behaviour of pre-biotic molecules, such as the isomers of $C_2O_2H_6$ (methyl formate, acetic acid and glycolaldehyde), which have a significant role in the formation of amino acids. Formic acid is related to the three $C_2O_2H_6$ isomers and it is believed to play a role in their formation. However, studies of the behaviour of formic acid on astronomically relevant surfaces are limited. In this work, structural changes within formic acid are probed and the interaction with water, the most abundant solid phase species in interstellar ices, is examined. Both species were found to affect each other's structural evolution in a non-trivial manner. The desorption of formic acid from water was shown to be complex and furthermore, the formic acid desorption routes were found to be highly dependent on the relative amount of formic acid present.

Not only is water the most abundant species in the solid phase, it partakes in many of the processes that are responsible for the chemical complexity of the ISM. The majority of water in space is proposed to have an amorphous porous structure, called amorphous solid water (ASW), that is able to accommodate guest molecules. Structural changes within ASW trap guest molecules above their natural sublimation temperatures, increasing the opportunities available for chemical processing. Whilst the ASW to crystalline ice phase change is well documented, the initial compaction of ASW is subject to considerable debate. Differing techniques and systems yield an array of temperatures over which compaction occurs. This work compares different probe molecules and techniques when examining the compaction process. It was found, using TPD, that whilst there were some variances in the trapping of different probes, they yielded comparable compaction temperature ranges. These findings were corroborated by investigations using RAIRS. The present work makes it clear that the compaction of ASW requires substantial additional work and that comparisons between different studies that involve ASW must be carried out carefully.

Acknowledgements

Before I thank the people who have helped me get to this point, I would like to acknowledge the EPSRC and the University of Sussex School of Life Sciences for financing my PhD.

My first thanks go to my supervisor, Professor Wendy A. Brown. I would like to thank her for giving me the opportunity after my MSci project to continue in her research group as a PhD student. Her supervision and guidance throughout this PhD has been invaluable. Over the past years she has always been someone who I can rely on for help and advice, whether the matter at hand is related to my PhD or not, and I am truly grateful for this.

I would like to thank the people that I have worked with over the years and who have provided me with invaluable support and friendship: Dr Daren Burke, Naitik Panjwani, David Whitewood, Sean Ayling, Dr Tara Salter and James Stubbing. I would like to offer special thanks to Dr Fabrizio Puletti, who I worked closely with during my time at UCL. He taught me a lot of what I know now and has become a good friend. I have particularly fond memories of many of the conferences that we attended together, the Friday singalongs and pero…perro…pero…perro.

Thanks must also be given to the numerous friends who have supported me throughout my PhD. First and foremost, I would like to say thank you to Daniel Culpan. Not only has Daniel read my thesis but he has been the best friend I could ask for. He has listened to me moan and picked me up during tough times, and I cannot express how grateful to him I am. Special thanks should also go to Dr Joe Manzi for not only reading some of my thesis, but being an incredible and lifelong friend. I would also like to say thanks to Tom Moore, who made sure that when I arrived at Sussex I was welcomed into the PhD group here at Sussex. Over the last few years he has become a friend that I can always rely on. I also want to say thanks to Hayley Rand and Gavin Roffe, both of whom are great friends that have always been there when I've needed them. I unfortunately do not have the space to individually thank all of the people that helped me here but I am grateful to them all.

Finally, I would like to say thank you to my family, Mum, Dad, Nicola, Del and Chris. You have supported me through everything I have ever done and always believed that I can achieve anything that I want to, for that, I am eternally grateful.

List of Abbreviations

ASW	Amorphous solid water
cASW	Compact amorphous solid water
CI	Crystalline ice
FTIR	Fourier transform infrared
HDA	High-density amorphous ice
HOPG	Highly oriented pyrolytic graphite
IP	Ion pump
LDA	Low-density amorphous ice
LEED	Low energy electron diffraction
L_m	Langmuir
LO	Longitudinal optical
MCT	Mercury cadmium telluride
OFHC	Oxygen-free high conductivity
pASW	Porous amorphous solid water
QMS	Quadrupole mass spectrometer
RAIRS	Reflection absorption infrared spectroscopy
TO	Transverse optical
TOF-SIMS	Time-of-flight secondary ion mass spectrometry
TPD	Temperature programmed desorption
TSP	Titanium sublimation pump
UHV	Ultra-high vacuum
vHDA	Very-high-density amorphous ice

Contents

List of Figures

List of Tables

1 Introduction

The space between the stars, the interstellar medium (ISM), is generally viewed as an area of emptiness and deadness, but this could not be further from the truth. The ISM is known to contain many gaseous atoms and molecules, as well as solids in the form of dust grains and ices. The field of study examining the formation, behaviour and roles of these gases and solids, known as astrochemistry, has developed into a wide-ranging and international area of research.

The work presented here uses surface science techniques to examine two astronomically relevant molecules: formic acid and water. It aims to answer the ultimate question of how do ices that contain these molecules evolve and change with increasing temperatures? Furthermore, by answering this question, this work aims to improve our understanding of the interaction between the gas phase and solid phase chemistry of the interstellar medium.

1.1 The Interstellar Medium

1.1.1 History

The origins of the ISM as a subject of human interest can be traced back several centuries to the late 18th century and the court of King George III. William Herschel, whose discovery of Uranus led to him being made the King's private astronomer[1], observed areas of space where there seemed to be a total lack of stars and called them 'holes in the sky'.[2,3] He believed that these holes in the sky were regions where there were no stars, voids in space. It is now known that these regions are in fact clouds of dust and gas that are able to block the light of stars behind them. These clouds exist in the space between stars, the ISM, and are the birthplace of new stars and planets.[4,5]

An example of one these holes in the sky, or clouds, can be seen in Figure 1.1, which shows the nearby molecular cloud Barnard 68 in the visible and near-infrared regions. It can be seen that the molecular cloud appears black in the visible and near-infrared regions due to the dust and gas blocking the light from the stars behind the cloud. Initially, those holes in the sky were merely an annoyance to astronomers, but eventually their true identity as clouds of dust and gas was discovered and they subsequently became an area of interest in their own right.

With the advent of telescopes that detect in the infrared, the true nature of the 'holes in the sky' could be demonstrated. The right hand side of Figure 1.1 shows the Barnard 68 cloud in the visible (coloured blue), near-infrared (green) and, crucially, the infrared (red) regions. The cloud of dust is obscuring the visible light, but by using infrared detectors it is possible to see through the cloud and observe the numerous stars behind it.[6]

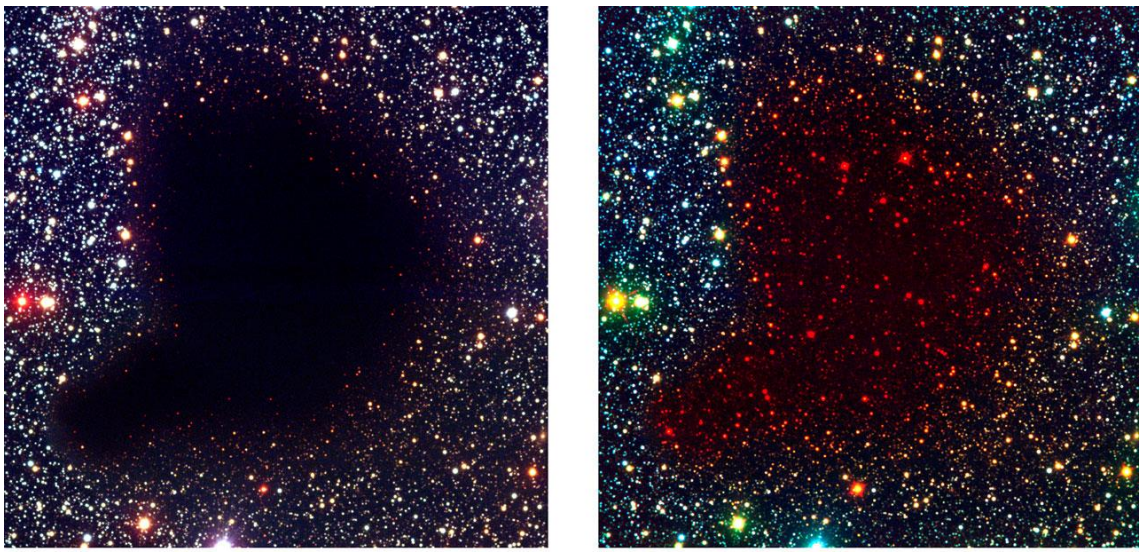

Figure 1.1 – Molecular cloud Barnard 68. The image on the left shows the cloud in the visible and near-infrared regions. The image on the right is the same image but includes, in red, the infrared region. Image taken from https://www.eso.org/public/images/eso0102c/ (accessed on 26/03/2016).

1.1.2 Inhomogeneous Model of the ISM

The dust and gas mentioned previously, known as interstellar matter, accounts for just 10-15% of the mass of our galaxy, the Milky Way.[7] The chemical make-up of the ISM is dominated by hydrogen, making up (by number) 90.8% of the total. This is followed by helium, representing 9.1% of the total, with the remainder made up of heavier elements such as carbon, nitrogen, oxygen, silicon and iron.[8–10] In regards to the physical make-up, gases account for 99-99.5%, by mass, of interstellar matter, with the remainder (0.5-1%) found as solids (dust).[7,11] The dispersion and character of the interstellar matter is far from homogeneous, with the generally accepted theory being that there exists three overarching phases in the ISM, categorised by gas temperature and density.[12,13]

The most extreme of the phases is the hot ionised medium (HIM), sometimes referred to as coronal gas.[14] Within the HIM, temperatures can reach up to 10^6 K with densities as low as 10^{-4} atoms cm^{-3}, with the phase occupying 50-70% of the ISM volume but only a

fraction of its mass.[7,11,12] It is generally accepted that the origin of the HIM is largely from supernova explosions, with a contribution from the powerful stellar winds produced by stars prior to supernova.[7,14] One step down the ladder of extremity is the warm ionised medium (WIM) and the warm neutral medium (WNM). These typically have temperatures up to 10^4 K and densities of 0.1-0.5 atoms cm^{-3}, with their reported contributions to the overall volume varying significantly, but making up the majority of the volume after the HIM.[7,11] The least extreme phase has temperatures below 100 K and is subdivided into molecular/dense clouds and the cold neutral medium (CNM), also called diffuse clouds. Together they constitute <1% of the ISM volume but account for ~50% of the mass.[11] Clouds with characteristics between those of diffuse and molecular clouds have been called translucent clouds by some in the literature.[11,15]

The CNM, or diffuse clouds, have a density ranging from 50-100 cm^{-3} and temperatures of 50-100 K.[6,7,11,16] The quoted density is the number density, rather than the atomic density, because although the majority of the CNM is atomic, there is a small contribution from diatomic and polyatomic species.[6] These clouds can collapse under their own gravity to form denser molecular clouds.[5] An example of a molecular cloud can be seen in Figure 1.2, which shows the Taurus molecular cloud. Within these clouds the density is much higher, ranging from 10^2-10^6 cm^{-3}, and the temperature is much colder: 10-20 K.[5,7,11] Dense clouds can be of the order of 100 light years (~9.5×10^{17} m) in diameter and have masses of up to a million times the mass of our Sun.[17] Although diffuse and molecular/dense clouds account for less than 1% of the ISM volume together, the diffuse clouds are the major constituent.[11] Within dense clouds, molecular species are dominant, and most of the hydrogen present is molecular (H_2), compared with diffuse clouds where most hydrogen is atomic (H).[6] Due to the low temperature and higher density within molecular/dense clouds, it is also possible for gases to accrete onto dust grains, forming icy mantles around the grains. These icy mantles are key to the chemical evolution of the ISM and will be discussed in more detail in subsequent sections. If massive enough, over the so called Jeans mass, molecular/dense clouds may begin to condense and collapse under their own gravity, forming a new star - a protostar - at the centre.[17,18] The Jeans mass is typically of the order of thousands or tens of thousands of the mass of our Sun and depends on the density and temperature of a cloud.[17]

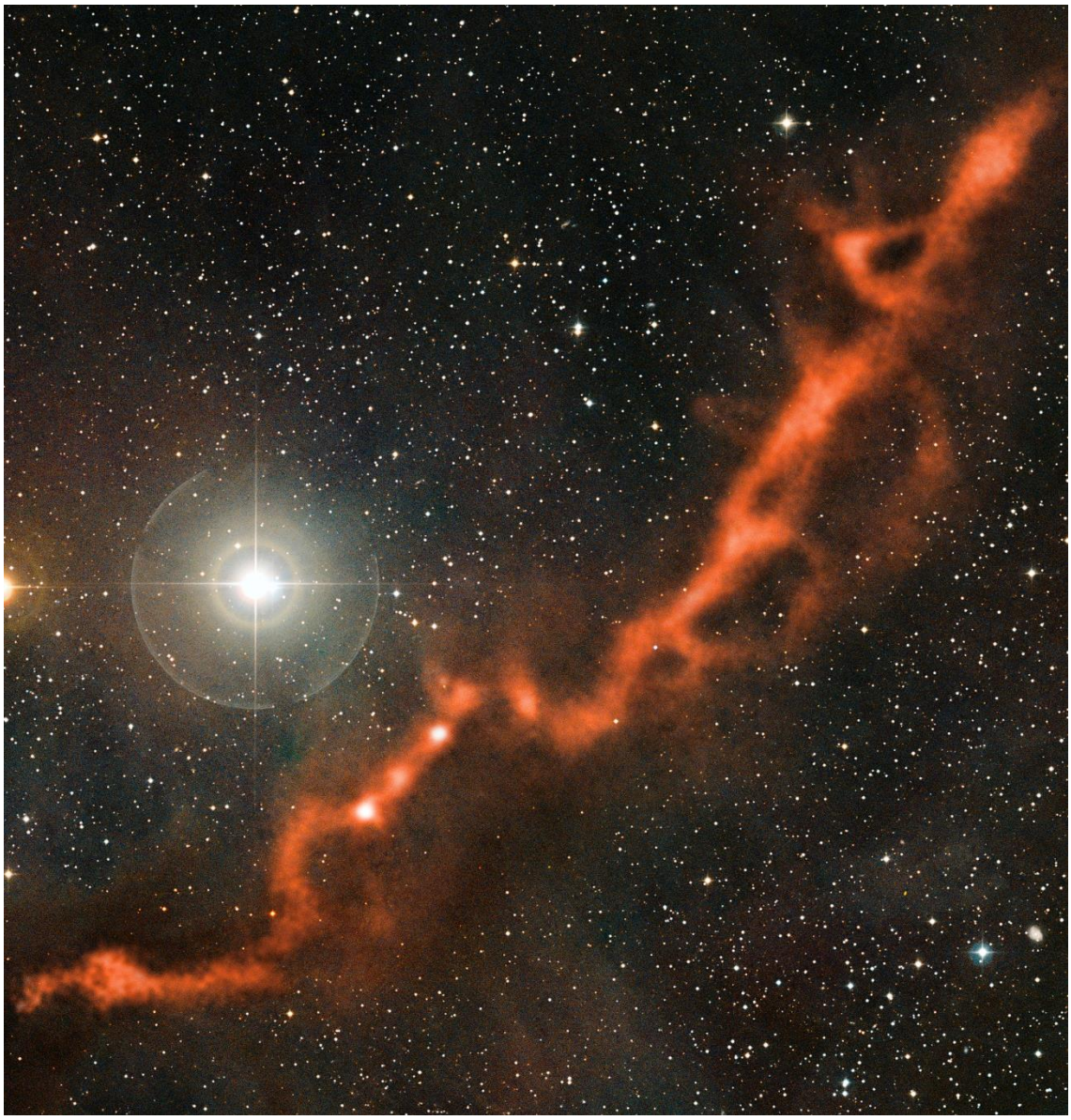

Figure 1.2 – Image of the Taurus molecular cloud. Image credit: taken from https://www.eso.org/public/images/eso1209a/ (accessed on 28/03/2016).

Within the ribbon of dust in Figure 1.2, shown in orange, a number of protostars and young stars can be seen, with additional stars poised to be formed from dense regions of the ribbon. A protostar will begin to warm the region around it, creating what is called a hot core. The heat provided by the hot core drives chemistry on the dust grain surfaces in icy mantles and can lead to the sublimation of the species adsorbed on the surfaces of grains and in the icy mantles. These processes can be grouped together under the term thermal processing and will be discussed further in later sections. Once in the gas phase, these desorbed species can undergo further chemistry, and these processes ultimately lead to the rich chemical make-up of hot cores that is observed.

The remnants of the dust cloud can form a rotating, or planetary, accretion disk that surrounds the protostar, which can then give rise to a planetary system. During the formation of the planetary system the dust aggregates into ever larger bodies, some of which can be knocked out of the planet-forming region into orbit around the star and become a comet.[5] Dust grains can be re-injected into the ISM by processes such as stellar winds from stars or by supernovae events that occur during the death of a star.[5,6,19]

1.2 Dust Grains

The exact nature of dust composition is still not fully known, but it is believed that they are largely siliceous (~95% of which is known to be amorphous[20,21]) and carbonaceous.[2,3] There are various sources of information concerning dust grains, such as interstellar extinction, infrared spectra and elemental depletion.

Interstellar extinction refers to the absorption and scattering of electromagnetic radiation by gas and dust, and is usually plotted against wavelength.[22] The average interstellar extinction curve in the visible and UV is shown in Figure 1.3 and is one of the sources of dust grain information. The extinction curve is generally unremarkable, save for a 'bump' at 2175 Å (4.6 μm^{-1}), rising from low to high wavelengths.[20]

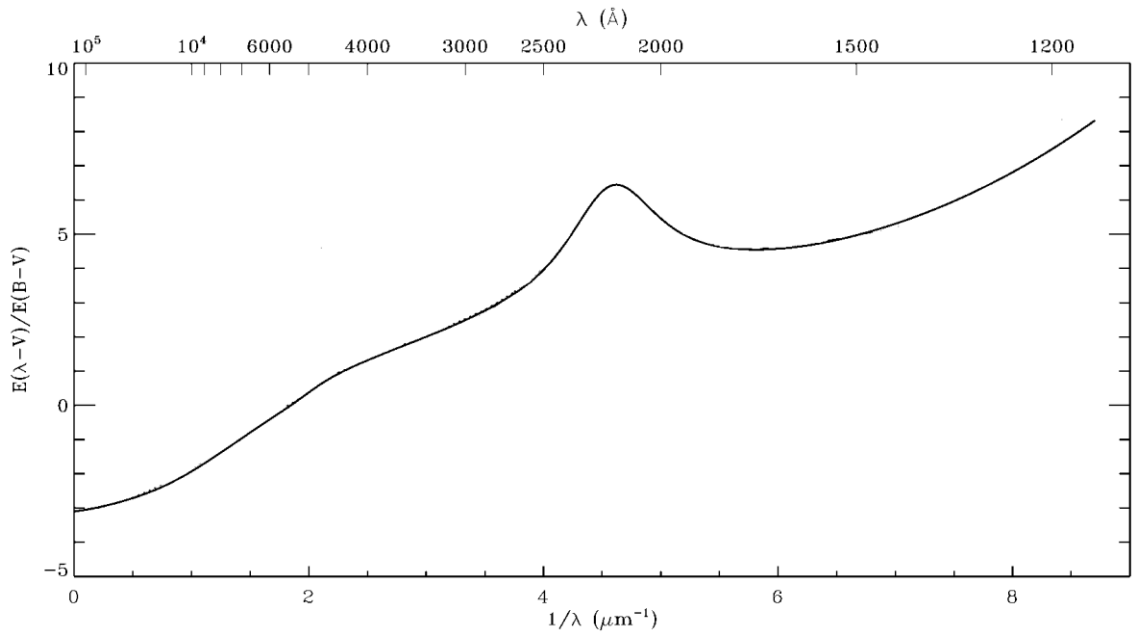

Figure 1.3 – Interstellar extinction as a function of wavelength, adapted from reference [23].

The size of grains and an indication of composition can be estimated by modelling the extinction curve. Using fits to the curve, the general consensus is that interstellar dust

grains are between a few nanometres and just under a micron in size.[2,3,7,19] The 'bump' at 2175 Å is reported to be caused by small carbonaceous particles, possibly polyaromatic hydrocarbons (PAHs), while the low wavenumber increase is a consequence of the presence of PAHs and small silicate particles.[2,7,19] Detected starlight is often a few percent linearly polarised, suggesting that at least some dust grains are not spherical and are partially aligned with the interstellar magnetic field.[2]

Further evidence of the presence of silicate dust grains can be obtained from spectra recorded using the European Space Agency (ESA) Infrared Space Observatory (ISO). Figure 1.4 shows an example of an ISO spectrum and it can be seen that the silicate absorption band (Si-O stretch) at ~10 μm is one of the most dominant features. The other species labelled relate to species adsorbed on the grains as icy mantles.

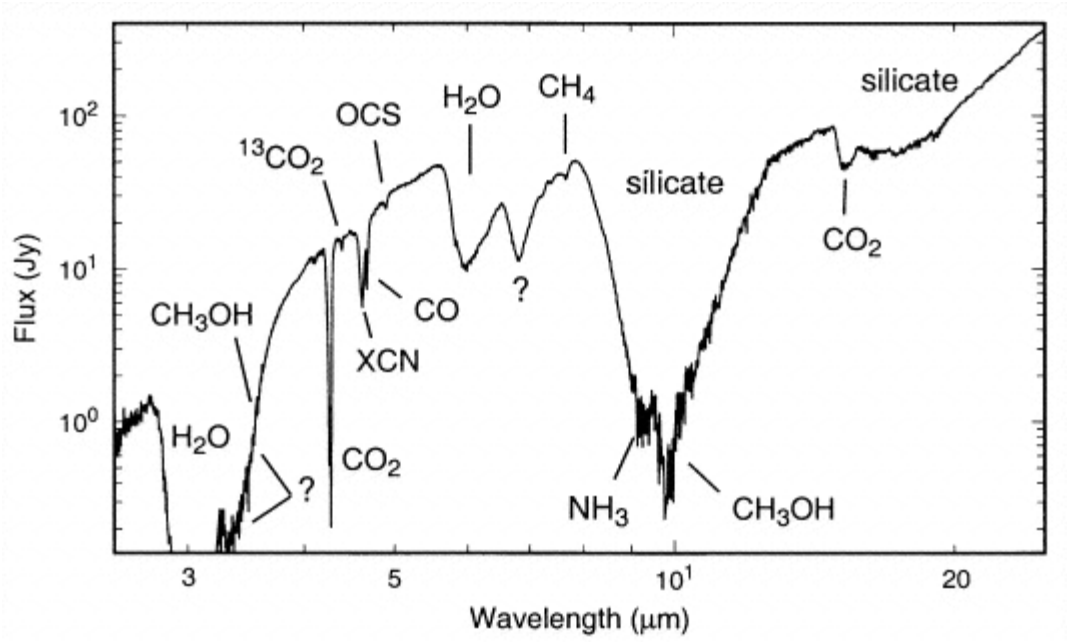

Figure 1.4 – Infrared spectrum of the young star W33A taken using the ESA ISO satellite. Taken from reference 24.

Additional information regarding the composition of dust grain can be obtained from the elemental depletion. Put simply, this shows that whatever is missing from the gas must be in the solid. This is done by calculating the elemental depletions from an assumed standard stellar composition (the relative elemental abundances present).[2] Table 1.1 shows a list of elemental depletions for the line of sight towards the bright star ζ Ophiuchi. From these calculations it has been found that there are significant depletions not only in

carbon, oxygen and silicon (as predicted from modelling the extinction curve) but also magnesium, chromium, iron, titanium and calcium.[2,25] It should be noted that whilst carbon seems to be largely in the gas phase, due to its anticipated abundance there is in fact more carbon locked up in dust grains than any of the other elements listed in Table 1.1 except oxygen.

Table 1.1 – List of the average elemental stellar abundances (relative to hydrogen) and the calculated fraction of these elements that remain in the gas phase in the line of sight towards the star ζ Ophiuchi. Table adapted from reference 25.

Element	Stellar Abundance (Relative to Hydrogen)	Fraction Remaining in Gas Phase
C	2.1×10^{-4}	0.63
O	4.6×10^{-4}	0.72
Mg	2.5×10^{-5}	0.24
Si	1.9×10^{-5}	0.09
Cr	3.2×10^{-7}	0.06
Fe	2.7×10^{-5}	~0
Ti	6.5×10^{-8}	0.08
Ca	1.6×10^{-6}	~0

Using the elemental depletions, it has been proposed that siliceous grains are based on olivine ($Mg_{2x}Fe_{2-2x}(SiO_4)$) and pyroxene ($Mg_xFe_{1-2x}(SiO_3)$) structures.[20] One theory is that silicate-based dust grains are composed of an iron-rich core, surrounded by a magnesium-rich mantle.[26] Using the elemental abundances detected towards ζ Ophiuchi, it was reported that whilst there cannot be any firm conclusions, siliceous grains based on olivine structures can be considered a reasonable approximation.[20,27] With regards to the carbonaceous material, it is proposed that a range of structures could be present, in addition to PAHs, such as amorphous carbon, graphite and diamond.[7,20]

1.3 Chemistry and Icy Mantles on the Grain Surfaces

If the dust grain surface is cold enough and if the cloud is sufficiently dense, then icy mantles can form around the grain.[28] Within these ices there exists a range of molecular species, some of which are highlighted in the infrared spectrum shown in Figure 1.4. The most abundant species in icy mantles are water, methanol, CO, CO_2 and NH_3, with water generally the most dominant species,[28] followed by CO. The detected abundances within icy mantles do not reflect the gas phase composition due to a number of factors, such as differences in chemical reactivity between the phases.[28] In addition to acting as substrates for accretion of icy mantles and thus forming chemical reservoirs, dust grains themselves have a number of important roles in the chemical evolution of the ISM. One such role is acting as catalysts, lowering energy barriers for reactions.[29] A second role is providing a sink for newly formed species to dump excess energy.[30] The final role is that grains provide a meeting site for species that would normally have a very low probability of meeting in the gas phase. These facts show that dust grains do not just harbour molecular species, but that they can also be key to their formation. In fact, it is known that for many species the detected abundances cannot be produced or maintained by gas phase reactions alone and that grains must play a part.[22]

One very important chemical process in the ISM that is dependent on dust grains fulfilling the roles highlighted above is the formation of molecular hydrogen. When only gas phase routes to H_2 production were examined a number of problems arose. Firstly, when H_2 forms from two H atoms, it can be in a highly excited vibrational state, above the dissociation limit, and without a third body it will simple break apart as soon as it forms. Secondly, a route involving electrons is not important due to the insufficient amount of electrons available.[31] It was eventually theorised that the dust grains were key to forming molecular hydrogen in the detected abundances.[31–33] Not only does the dust grain provide a sink for the nascent energy present after formation, but it can improve the statistical likelihood of two hydrogen atoms encountering one another after they both have collided and stuck onto the grain.[31] The mechanism by which two hydrogen atoms collide varies and is dependent on factors such as the grain surface identity and cloud density.[31]

It is known that chemical formation on grain surfaces must also be considered for other species in addition to H_2 because gas phase routes are often not efficient enough to produce the abundances detected. This problem is further compounded when destructive

processes are factored in. In addition to atomic/molecular collision routes, chemistry on grain surfaces can be driven thermally or by ultraviolet radiation,[34–36] X-ray or cosmic ray bombardment[37] from nearby stars, or from within the centre of the cloud where a new star may be forming.

Thermal processing of icy mantles, driven by young stellar objects called hot cores, can result in atomic/molecular diffusion, structural changes and ultimately, desorption of species into the gas phase. Desorption of icy mantles allows the constituent species to be available to partake in further chemical evolution in the gas phase. Desorption of icy mantles does not occur at the same time for all species, rather each species has distinct desorption temperatures that are governed by factors such as surface identity, heating rate and, often, the thermal evolution of the highly abundant water.[38–43]

Grain surface chemistry, followed by desorption and release of new species into the gas phase, combine to result in a rich and varied chemistry, particularly in hot cores.[44] This rich chemistry is evident from the 194 molecules that have so far been detected in the ISM (see Table 1.2). It is interesting to note that all of the species detected that have 6 or more atoms, regarded as complex by astrochemists,[45–49] are organic molecules, i.e. carbon-based.

An area that has gained much attention from astrochemists is the star-forming region Sgr B2. Close to the galactic centre, Sgr B2 is a large cloud, termed a giant molecular cloud, spanning 45 parsecs (~1.4×10^{15} km) and with a mass of approximately six million times that of our Sun.[50–52] It was found that within the region there were two hot compact "clumps", Sgr B2 (M) and Sgr B2 (N). Observations showed that Sgr B2 (N) had a much richer chemical make-up, with some species having up to five times the abundance in Sgr B2 (N) compared to Sgr B2 (M).[47,48,50,53–55] Within Sgr B2 (N) some of the complex organic molecules detected include formaldehyde (H_2CO),[47] methanol (CH_3OH),[47] formic acid (HCOOH),[56,57] methyl formate ($HCOOCH_3$),[58] acetone ($(CH_3)_2CO$),[59] ethylene glycol ($(CH_2OH)_2$),[60] acetic acid (CH_3COOH)[61] and glycolaldehyde ($HOCH_2COH$).[53,62–64] A number of these species (methyl formate, acetic acid and glycolaldehyde) have been identified as having the possibility, due to structural similarities, of producing pre-biotic molecules, such as glycine (NH_2CH_2COOH), within warm regions like Sgr B2 (N).[45,47,65,66] By having the potential to form pre-biotic species, these species are highly important to the field of astrobiology.

Table 1.2 – Detected molecules in the ISM as of February 2016. "?" Denotes assignments that have reasonable chances of being correct. "(?)" Denotes assignments where (partial) overlap of detection lines cannot be ruled out. Adapted from http://www.astro.uni-koeln.de/cdms/molecules (accessed 14/03/2016). Highlighted in bold red and purple are the two species that are focused on in this thesis.

2 Atoms	3 Atoms	4 Atoms	5 Atoms	6 Atoms	7 Atoms	8 Atoms
H_2	C_3	c-C_3H	C_5	C_5H	C_6H	CH_3C_3N
AlF	C_2H	l-C_3H	C_4H	l-H_2C_4	CH_2CHCN	$HC(O)OCH_3$
AlCl	C_2O	C_3N	C_4Si	C_2H_4	CH_3C_2H	CH_3COOH
C_2	C_2S	C_3O	l-C_3H_2	CH_3CN	HC_5N	C_7H
CH	CH_2	C_3S	c-C_3H_2	CH_3NC	CH_3CHO	C_6H_2
CH^+	HCN	C_2H_2	H_2CCN	CH_3OH	CH_3NH_2	CH_2OHCHO
CN	HCO	NH_3	CH_4	CH_3SH	c-C_2H_4O	l-HC_6H
CO	HCO^+	HCCN	HC_3N	HC_3NH^+	H_2CCHOH	CH_2CHCHO (?)
CO^+	HCS^+	$HCNH^+$	HC_2NC	HC_2CHO	C_6H^-	CH_2CCHCN
CP	HOC^+	HNCO	**HCOOH**	NH_2CHO	CH_3NCO	H_2NCH_2CN
SiC	**H_2O**	HNCS	H_2CNH	C_5N		CH_3CHNH
HCl	H_2S	$HOCO^+$	H_2C_2O	l-HC_4H		
KCl	HNC	H_2CO	H_2NCN	l-HC_4N		
NH	HNO	H_2CN	HNC_3	c-H_2C_3O		
NO	MgCN	H_2CS	SiH_4	H_2CCNH (?)		
NS	MgNC	H_3O^+	H_2COH^+	C_5N^-		
NaCl	N_2H^+	c-SiC_3	C_4H^-	HNCHCN		
OH	N_2O	CH_3	HC(O)CN			
PN	NaCN	C_3N^-	HNCNH			
SO	OCS	PH_3	CH_3O			
SO^+	SO_2	HCNO	NH_4^+			
SiN	c-SiC2	HOCN	H_2NCO^+ (?)			
SiO	CO_2	HSCN	$NCCNH^+$			
SiS	NH_2	H_2O_2				
CS	$H3^+$	C_3H^+				
HF	SiCN	HMgNC				
HD	AlNC	HCCO				
FeO ?	SiNC					
O2	HCP					
CF^+	CCP					
SiH ?	AlOH	**9 Atoms**	**10 Atoms**	**11 Atoms**	**12 Atoms**	**>12 Atoms**
PO	H_2O^+	CH_3C_4H	CH_3C_5N	HC_9N	c-C_6H_6	$HC_{11}N$
AlO	H_2Cl^+	CH_3CH_2CN	$(CH_3)_2CO$	CH_3C_6H	n-C_3H_7CN	C_{60}
OH^+	KCN	$(CH_3)_2O$	$(CH_2OH)_2$	C_2H_5OCHO	i-C_3H_7CN	C_{70}
CN^-	FeCN	CH_3CH_2OH	CH_3CH_2CHO	$CH_3OC(O)CH_3$	$C_2H_5OCH_3$?	C_{60}+
SH^+	HO_2	HC_7N				
SH	TiO_2	C_8H				
HCl^+	C_2N	$CH_3C(O)NH_2$				
TiO	Si_2C	C_8H^-				
ArH^+		C_3H_6				
NO^+ ?		CH_3CH_2SH (?)				

Highlighted in red in Table 1.2 is formic acid, the simplest carboxylic acid and first organic acid detected in the ISM.[56,57] It has been detected in numerous interstellar environments, in both the gas[45,67–73] and solid phase,[73,74] where it accounts for 1-5% of icy mantles on dust grains.[75] Formic acid is believed to take part in the formation of many of the pre-biotic molecules and their precursors discussed above.[45,65] It is also thought to have a role in the formation of other complex ISM molecules, such as dimethyl ether (CH_3OCH_3).[76]

Over recent years, many of the pre-biotic molecules have garnered significant attention regarding their production, behaviour on grains and in icy mantles, desorption and reaction pathways,[54,62,77–81] whilst formic acid has received comparably less attention. This is despite the fact that in some hot cores, formic acid has been reported to be more abundant than those species that gain considerable attention, namely formaldehyde, methanol, methyl formate and dimethyl ether.[82–87]

Owing to the levels of detection of formic acid, its involvement in chemical reactions both in icy mantles and in the gas phase and the possibility of it interchanging between the solid and gaseous phases, knowledge of how formic acid desorbs from dust grains is key to fully understanding the nature of formic acid in the ISM.[82] Since the majority of dust grain icy mantles are water, an appreciation of the influence of water on the desorption of formic acid is required in order to properly understand interstellar desorption processes on grain surfaces. Formic acid and water can interact via van der Waals interactions, as well as by hydrogen bonds.[88] The presence of hydrogen bonding between the two species is likely to influence, and most likely complicate, the desorption of formic acid. Further to this, the temperature range over which formic acid desorbs has been shown to overlap with the temperature range that water undergoes a phase transition and then desorbs.[38,89] This has significant ramifications for the desorption of formic acid as it means that it has the time to potentially become trapped within the initially porous water ice.[90] The possibility of hydrogen bonding and the potential of formic acid trapping within water also make the formic acid-water system far from trivial.

1.4 Water in the ISM

Water is by far the most abundant species in most interstellar ices, constituting up to 70% of the icy mantle. This continues to make this relatively small and simple molecule an important topic of research, even though it was detected nearly 50 years ago in 1969.[91]

The solid phase abundances of water in dust grain icy mantles cannot be accounted for solely by gas phase production and accretion, and as such both gas phase and grain surface production routes must be considered.[15]

Gas phase formation routes for water are centred on cold ion-molecule or high temperature neutral-neutral reactions. The former starts with H_2^+ (formed on grain surfaces, then ionised in the gas phase by cosmic rays) and proceeds to H_3O^+, which can then slowly undergo dissociative recombination with electrons to form gaseous water.[15,92-94] This water can be destroyed by either reaction with numerous gaseous ions or by photodissociation.[15] High temperature neutral-neutral reactions occur when areas are warmed by, for example, events such as shocks.[95] The main grain surface routes to water start with surface-bound O, O_2 or O_3 and proceed largely by sequential atomic hydrogenation.[96] In addition to these routes, it has been proposed that the reaction of surface-bound OH and H_2 will proceed via quantum tunnelling, even considering its large activation barrier.[97] The dominant route on the grain surface is dependent on local conditions.[97–101] The key conclusion is that there appears to be surface routes to water formation in a wide range of ISM environments and that, as with molecular hydrogen, grain surface processes are crucial to producing the observed abundances.

It is generally thought that the majority of water in ISM ices adopts an amorphous structure, amorphous solid water (ASW),[102–104] with a limited amount adopting a crystalline structure, crystalline ice (CI).[15,105,106] Evidence of the phase of water in the ISM is obtained by comparing infrared spectra acquired using observations from the likes of the ESA ISO with those from the laboratory.[15] The OH stretching band in infrared spectra is broad for ASW whereas for CI is a sharp central peak with defined shoulders either side. ASW can be regarded, particularly when compared with CI, as a highly porous and rough structure, almost sponge-like.[90] Upon heating, ASW undergoes an irreversible phase transition to the more ordered CI.[38,107]

ASW can accommodate guest molecules within its structure and potentially trap them above their natural sublimation points. By retaining species above their natural sublimation points, ASW can act as reservoir for a whole host of molecules, keeping them in much closer proximity to each other than they would otherwise be in the gas phase. In turn, this gives species the time and space to encounter one another and subsequently react. Some of the chemical evolution can be driven via processing by external forces,

such as UV or cosmic ray bombardment. These molecules can then be released during either the high temperature phase change of ASW to CI or during the eventual desorption of CI.[38,41,42,108] It is believed that a mechanism for trapping molecules in water is the thermally induced compaction observed in ASW.[38,41] This process results in porous ASW (pASW) transforming into compact ASW (cASW). During compaction, it is proposed that species in the porous cavities of pASW become trapped as the pores are closed off to the vacuum.

There have been suggestions in the literature that pASW is not present and water in the ISM is dominated by cASW.[15,109] However, absence of pASW in the ISM is refuted by others in the literature, and therefore the compaction process could still be responsible for trapping other species within ASW.[15,110–112] Ices in the ISM are subjected to events such as stellar shocks, these are associated with supernova remnants expanding into the ISM and the outflows of young stars,[15] and it has been proposed that such occurrences may have compacted ices that were initially porous.[112–114] It would therefore seem that the presence of pASW in the ISM is probable, therefore validating the necessity of its study.

In addition to the questions regarding the properties of water posed by astronomers and astrochemists, physical chemists are also still trying to understand the properties of this relatively simple and terrestrially abundant molecule.[115] One particular area of research in the physical chemistry arena is the phases adopted by water, with the literature reporting 16 crystalline phases and 2 sets of amorphous phases of solid water, which can be further divided into subsets.[115–117] It is clear that the study of water is a wide-ranging, varied and interesting field of research, with contributions from astronomers, chemists and physicists alike.

1.5 Experimental Astrochemistry

Experimental studies are used in combination with the work of astronomers to provide information on the chemical and physical processes occurring on interstellar grain surfaces. The vast majority of experimental studies utilise cryogenics and vacuum systems in order to mimic the conditions found in the ISM as closely as possible. Typically, high-vacuum (HV) and ultra-high vacuum (UHV) chambers are used, which can reach pressures of ~10^{-7}-10^{-8} mbar and <10^{-10} mbar, respectively.

Reflecting the variety of dust grain compositions in the ISM, a range of materials are used as substrates in laboratory experiments. Some of the materials chosen reflect the carbonaceous and silicaceous nature of grains, such as amorphous silica,[118] olivine,[119] graphene[120] and graphite.[121–124] In addition to grain analogues, other substrates have been used that typically promote physisorption, such as thin layers of polycrystalline gold,[38,89] gold coated copper,[125] KBr[126,127] and CsI.[75]

The surface science techniques employed vary depending on the nature of the study and experimental set-up. Examples of the techniques used are electron diffraction,[90,128,129] temperature programmed desorption (TPD),[38,120,124] reflection absorption infrared spectroscopy (RAIRS),[120] transmission infrared spectroscopy[126] and laser interference coupled with infrared spectroscopy.[111] The work presented here utilises two of these techniques, TPD and RAIRS. TPD can be used to study desorption of pure and multicomponent ices and how the presence of one species affects desorption of another.[38] Using TPD spectra, kinetic parameters of desorption can be obtained that can then be used to model desorption under different conditions.[44] In addition to this, TPD can also be used to study phase changes and physical processes, such as compaction, within ices.[120] RAIRS can be used to examine variations in the bonding within molecules that may be caused by structural changes or by interactions with other species.[41,44] RAIRS can also be used to obtain information about the orientation of species with respect to the surface normal (discussed in Chapter 2). Both TPD and RAIRS can be coupled with a probe molecule in order to examine changes within an ice of interest where it is not possible to directly examine the ice.[40,130–133]

In addition to the techniques and their uses detailed above, there are other areas of experimental astrochemistry that, whilst not directly relevant to the work presented here, should be mentioned. One such area is the examination of the effect of irradiation or energetic particle bombardment on the morphology and composition of ices. These studies aim to mimic processing of interstellar grains and ices by UV radiation from, for example, young stars and by bombardment of cosmic rays.[134,135]

Laboratory astrochemistry is just one component of the wider field. When coupled with observations and computational studies, experimental studies can yield a vast amount of information on the processes that occur within the ISM.

1.6 Overview

This thesis has two key sections, both of which utilise RAIRS and TPD: investigations into formic acid (chapters 3 and 4) and investigations into the compaction of ASW (chapters 5 and 6). All the work presented here was carried out using a model carbonaceous interstellar dust grain surface, highly oriented pyrolytic graphite (HOPG), held at ~20 K under UHV. A more detailed discussion of the experimental set-up and of the techniques used is given in Chapter 2.

Chapter 3 deals with formic acid desorption from HOPG. Investigations into formic acid desorption from astronomically relevant surfaces are quite limited, particularly from carbonaceous surfaces, with the majority of studies focusing on metal surfaces that promote chemisorption.[136–138] Those studies that do examine formic acid desorption do so in a minor capacity. Whilst it is likely that formic acid will not exist on dust grains alone, an understanding of the interactions between two formic acid molecules and between formic acid and the substrate lays the foundation for studying more complex systems, such as the interactions between formic acid and water.

Chapter 4 looks at the more astronomically relevant system of formic acid in the presence of water. Here the nature of formic acid desorption from, initially, highly porous ASW is examined with the aim of improving the way in which formic acid desorption from interstellar icy mantles is modelled. As both formic acid and water can hydrogen bond with themselves and with each other, the effect of hydrogen bonding on the structural evolution of each species is examined. Chapters 3 and 4 together aim to further our understanding of the behaviour of formic acid, a simple and relatively abundant species, in ices on interstellar dust grains.

Chapters 5 and 6 examine the compaction of pASW to cASW. Whilst the transition from ASW to CI has been, and still is, extensively studied and hence is fairly well understood, there is debate surrounding the compaction of ASW. Much of this debate is centred on the temperature region over which it occurs, with differing techniques and probes providing sometimes conflicting conclusions. Therefore, the work presented in the second part of this thesis compares different probes and different techniques (TPD and RAIRS) using the same experimental set-up. Chapter 5 examines how the ability of water to trap a probe molecule (CO_2 and CS_2) changes as compaction proceeds using TPD. Chapter 6

also uses a probe (CO) to track the compaction of water but utilises RAIRS, rather than TPD, to do so.

If the compaction of ASW is responsible for trapping of other species in ISM icy mantles, then an understanding of the temperature range over which it occurs is vital. With many smaller and weakly bound species desorbing at very low temperatures, the range over which they can be trapped may be limited and so the compaction process of pASW to cASW must be understood accurately to allow astronomers to properly understand the processes within/on interstellar ices.

The results of this thesis will enable astrochemical simulations to model the processes that occur in the interstellar medium more accurately. The first half of the thesis will provide specific information regarding the desorption of water-formic acid systems. The second half of the thesis will shed light on the contentious issue of ASW compaction by answering some of the questions that surround this process.

2 Experimental Set-Up and Techniques

2.1 Experimental Set-Up

The experimental set-up used in this work is designed to mimic the conditions observed in the ISM, as much as technically possible. This means that both ultra-high vacuum (UHV) and very low surface temperatures are needed. In order to achieve this, a multi-pump system is used in conjunction with a closed-cycle helium refrigerator, both of which will be discussed in detail in this section. Additionally, the sample must be able to be heated to several hundred Kelvin to ensure that the sample surface is clean and in order to study the effects of warming on ices. Heating is achieved using a resistive heating circuit that will also be discussed in this chapter.

2.1.1 UHV Chamber

The UHV chamber (Figure 2.1) is a multi-level stainless steel vessel that has a translatable (x, y and z directions) and rotatable cold finger at its centre, at the end of which is the sample mount. UHV, with a base pressure of ~1×10^{-10} mbar, is achieved by use of a multi-pump system (a schematic of which is shown in Figure 2.2) in conjunction with baking the chamber.

Initially, rough vacuum (~10^{-2}-10^{-3} mbar) is reached using a rotary pump (Œrlikon Leybold, Trivac D8B). Subsequently, high vacuum (~10^{-7}-10^{-8} mbar) is attained with a turbomolecular pump (Leybold, Turbovac 151), backed by the aforementioned rotary pump. The backing pressure of the turbomolecular pump is monitored via a Pirani gauge (Edwards, APG-100-XM) and reaches ~7×10^{-4} mbar. To reach true high vacuum, an ion pump (IP) (Physical Electronics, Captorr Ion Pump) and a titanium sublimation pump (TSP) (Physical Electronics, Boostivac TSP) are used, with the TSP mounted within the ion pump. The TSP works by depositing a layer of clean titanium which then goes on to readily react with reactive gases (for example H_2 and CO_2) that are difficult to remove via the rotary, turbomolecular and ion pumps. It is set to monitor the pressure every 2-3 hours when experiments are not being conducted and if it reads above 1×10^{-10} mbar it fires for 30 seconds

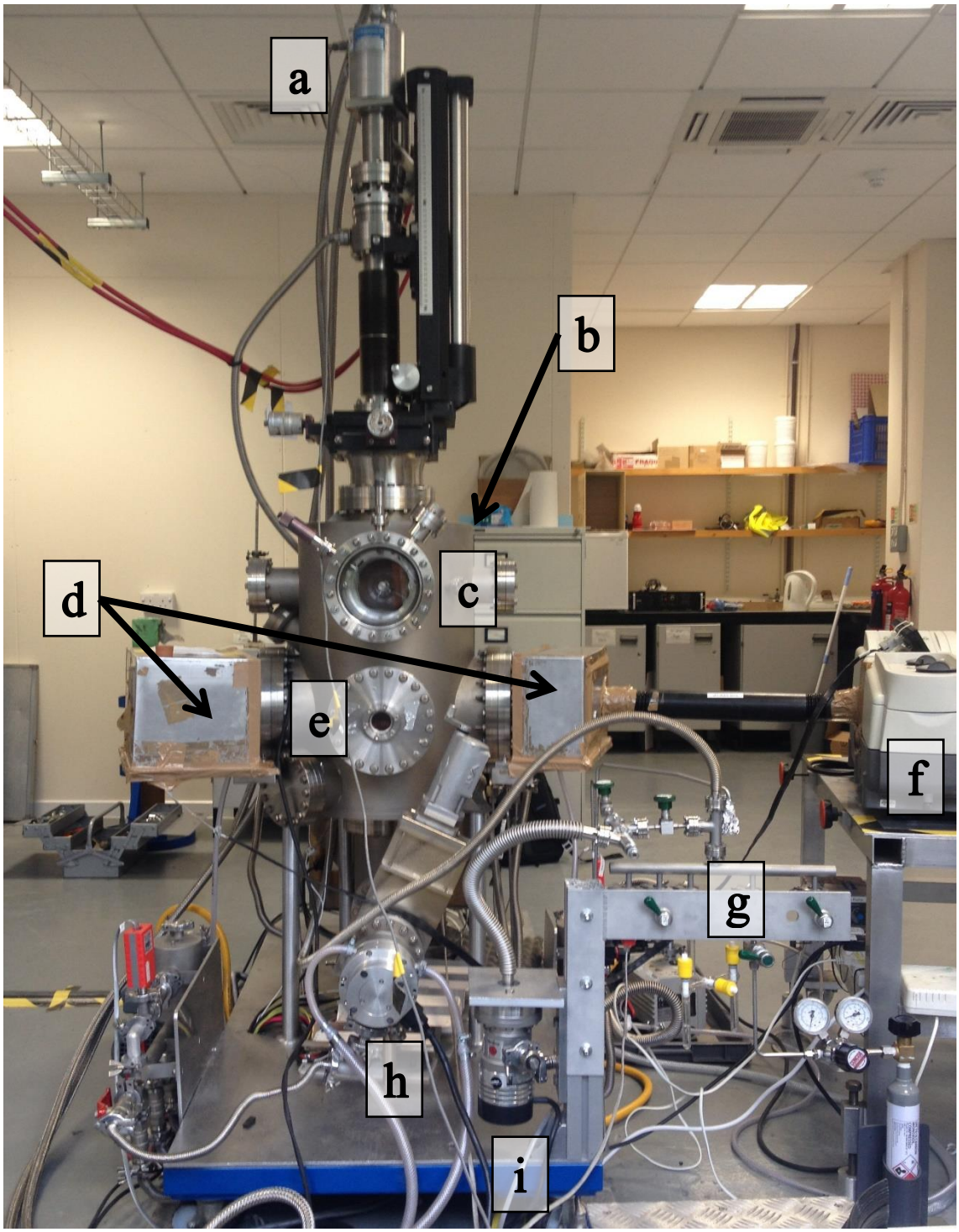

Figure 2.1 – Photograph of the UHV chamber used throughout this thesis. Key features shown are (a) the closed cycle helium refrigerator, (b) the UHV chamber, (c) low-energy electron diffraction optics (not used), (d) boxes housing the infrared detector and optics, (e) an ultraviolet window (not used), (f) the infrared spectrometer, (g) the dosing manifold, (h) the main turbomolecular pump and (i) the gas line turbomolecular pump. Out of view are the ion pump and titanium sublimation pump (opposite h), the mass spectrometer (opposite e) and the ion gauge (opposite c). Further details of the individual components are given in this section.

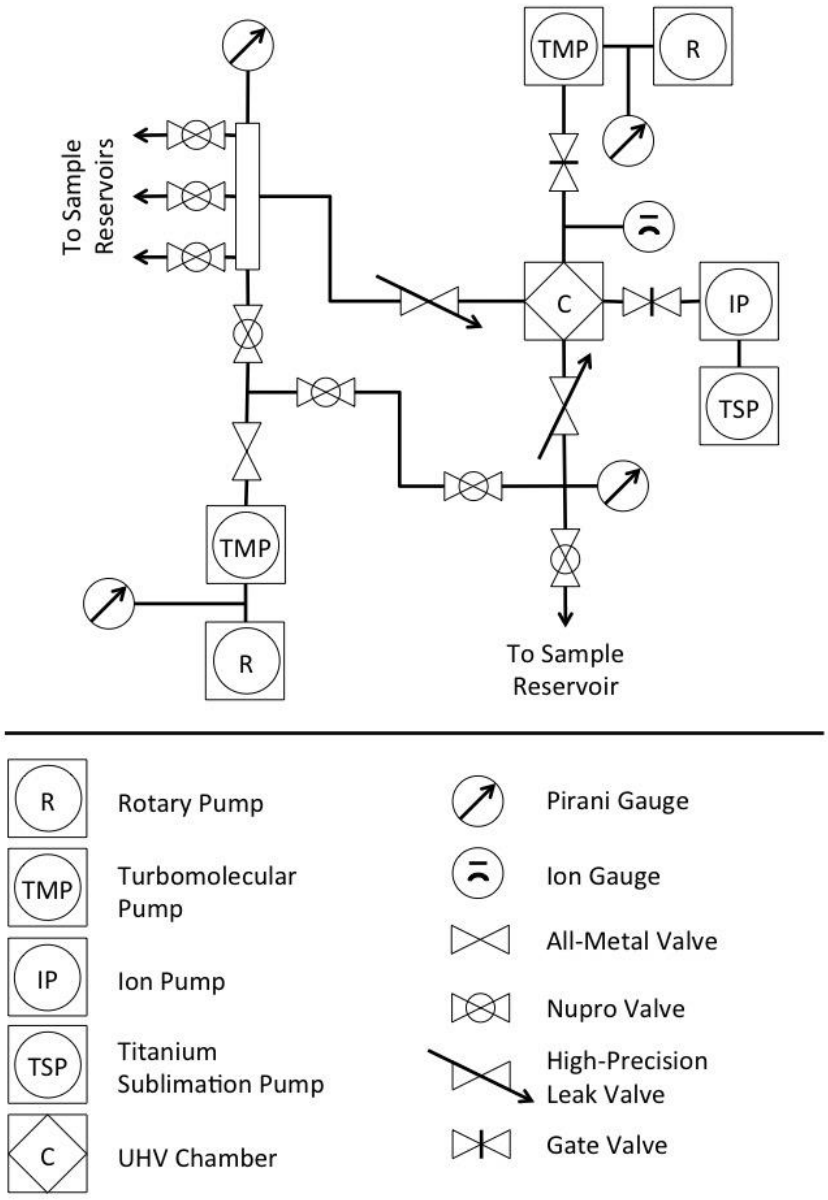

Figure 2.2 – Schematic of the UHV chamber and dosing manifold pumping system.

In order to achieve UHV the chamber must be baked to at least 375 K for no less than 24 hours in order to remove gases adsorbed on the internal surfaces of the chamber, cold finger and pump surfaces. During baking, the chamber is pumped only by the rotary and turbomolecular pumps in order to allow the ion pump surfaces to be regenerated. Baking the chamber is not only required when bringing the chamber down from atmospheric pressure but is also needed after a substantial run of experiments. Such extended periods of operation can result in the chamber essentially 'choking', which manifests itself as long pump down times and can only be remedied with a bake.

At the base of the chamber, opposite one another, are two gate valves. Attached to one gate valve is the IP/TSP and the other gate valve connects to the turbomolecular pump and its backing line (see Figure 2.2). This set-up is used for a number of reasons. Firstly, it allows the sequential pumping down of the chamber from atmosphere to high vacuum, thus minimising the workload on the pumps. Secondly, it allows the IP to be isolated from the chamber if there is a suspected fault that may lead to an undesirable increase in the chamber pressure. And finally, if there is work needing to be done on the chamber, then it can be vented whilst leaving the IP under vacuum, which is preferable for ensuring its longevity.

The analytical, or experimental, part of the chamber can be divided into two levels: an upper and a lower level. The upper level houses the ion gauge (ITL Ltd.), used as the main chamber pressure monitor, a viewing port, the optics for low energy electron diffraction (LEED) (not used in this thesis) and a number of unused, blanked, ports. The lower level contains the ports used in all experimental aspects of the work presented here, and their relative positions are depicted in Figure 2.3. Infrared light is admitted and recovered from the chamber via two differentially pumped KBr windows, whose orientation relative to the sample and each other is optimised for reflection absorption infrared spectroscopy (RAIRS), which will be discussed in more detail in a subsequent section of this chapter. A quadrupole mass spectrometer (QMS) (Hiden Analytical, HAL 201 PIC) is mounted on the lower level, opposite the ultraviolet window (see Figure 2.1). The QMS is used to carry out residual gas analysis (RGA) and to facilitate temperature programmed desorption (TPD) experiments, which will be discussed further on. Two all metal high precision leak valves (VG Scienta, LVM Series) are mounted at 45° either side of the QMS to precisely admit adsorbates to the chamber. Each leak valve has a stainless-steel pipe attached to direct adsorbates towards the centre of the chamber. The leak valves connect to sample reservoirs and the vacuum line as depicted in Figure 2.2, together they comprise the dosing line. One leak valve is connected to a single reservoir whilst the other connects to a manifold that accommodates up to four chemicals of interest. Liquids are attached via glass dosing vessels (sealed with Young's taps or Nupro valves) and gases are admitted directly from their cylinders or lecture bottles using regulators. The dosing line is pumped by a small turbomolecular pump (Œrlikon Leybold, Turbovac 50), backed by a rotary pump (Leybold, Trivac D5E) and can reach ~8×10^{-4} mbar. The dosing line was re-designed, during this work, to allow the isolation of each leak valve and its

reservoir from one another and from the vacuum line. By being able to isolate each valve it is possible to simultaneously dose two different chemicals whilst also minimising contamination of the dosing line. Pressure measurement of the dosing line is via two Pirani gauges (Edwards, APG-100-XM/XLC), one in each of the two isolatable reservoir sections (see Figure 2.2). The backing pressure of the small turbomolecular pump is also monitored via a Pirani gauge.

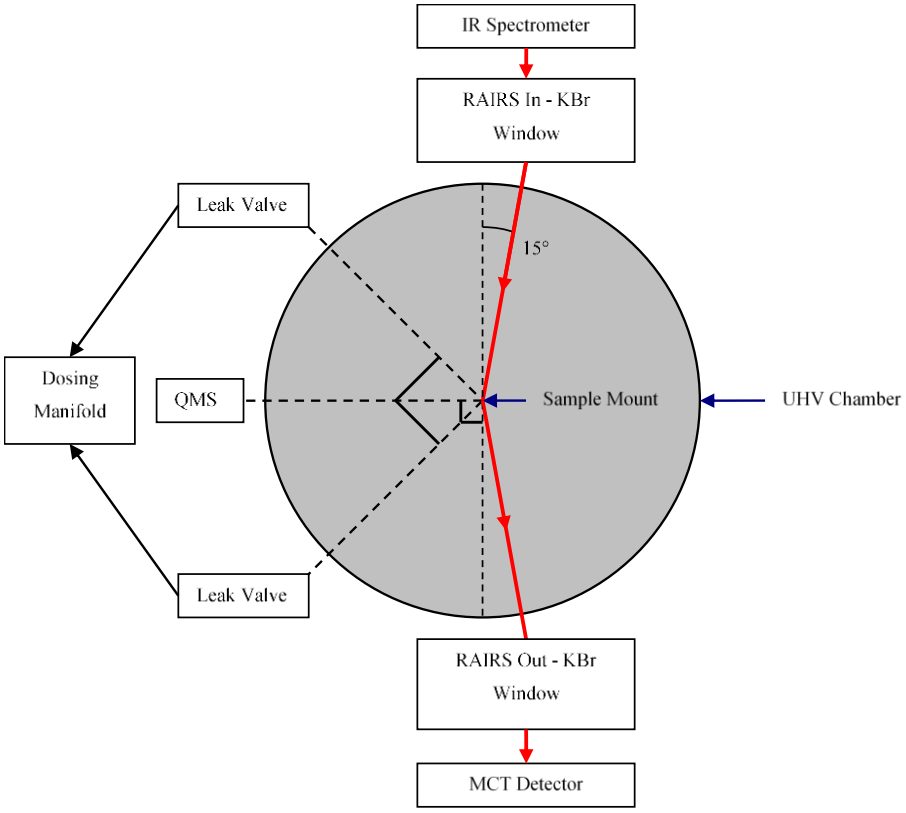

Figure 2.3 – Schematic of the lower level of the UHV chamber. Dashed lines indicate the positions and angles of experimental ports with respect to one another. Red arrows indicate the infrared beam path. Not depicted are a number of viewing ports.

2.1.2 Cold Finger and Cooling

As mentioned previously, the sample mount is attached to the end of a cold finger that is mounted on a manipulator. The manipulator gives the cold finger precise movement in the x, y and z directions, as well as allowing it to rotate. The cold finger is made of oxygen-free high conductivity (OFHC) copper, allowing the sample mount to be cooled efficiently. Cooling is achieved using a closed cycle helium refrigerator (SHI-APD Cryogenics Inc., HC-2D-1) positioned at the top of the cold finger, see Figure 2.1, label

a. It takes approximately 10 hours to cool the sample from room temperature to ~20 K. The sample temperature is monitored by an N-type, Nicrosil-Nisil (Ni-Cr-Si and Ni-Si alloys), thermocouple. The thermocouple exits the chamber via a feedthrough that connects to a control unit (Eurotherm Ltd., ε2408). Since this feedthrough is at room temperature the thermocouple must be heat sinked in order to prevent the ambient temperature of the room passing down to the sample. Heat sinking is achieved by tightly winding the thermocouple wire round the cold finger as it passes down to the sample. Once the wire has reached the sample mount it has cooled sufficiently so it does not hinder the cooling of the sample.

Surrounding the entire cold finger, bar a 180° slit around the sample, is a gold coated radiation shield. This aids in cooling by reducing the warming effects of blackbody radiation from the internal walls of the chamber. The aforementioned slit in the shield is just enough to allow the sample to be visible to the mass spectrometer and infrared radiation.

2.1.3 Sample Mount and Sample

The sample mount was designed by Dr Daren Burke (former post-doctorate) to allow the sample to be cooled and heated as efficiently as possible, whilst minimising the amount of heat passed from the sample to the rest of the cold finger during experiments. Minimising heat transfer during experiments is important for two primary reasons. Firstly, to avoid damaging the closed cycle helium refrigerator and secondly, to prevent the appearance of artefact desorption features that are a consequence of desorption from surfaces other than the sample. Additionally, the resistive heating circuit was designed to be electrically isolated from the rest of the sample mount in order to prevent it from short-circuiting through the mount and cold finger. The design can be seen in Figure 2.4 and a discussion of the key elements is given below.

As with the cold finger, the sample mount is made from OFHC copper to allow for efficient cooling of the sample. The sample mount is attached to the end of the cold finger, with a pair of silver foil sheets between them. The silver foil is used to improve the thermal conductivity of the join, aiding the cooling of the sample mount and sample. As can be seen in Figure 2.4, directly below the join with the cold finger, there are a number of blocks, spacers and wires. These make up the junction of the heating wires (Kapton coated, Ag plated Cu) with the heating filaments (W/Re). The heating wires, leading to

the top of the cold finger, are stripped at the end and inserted into two OFHC copper blocks. These blocks are electrically insulated from one another by a ceramic spacer and from the sample mount by a sapphire spacer, thus preventing a short circuit. Sapphire is used, as opposed to another ceramic spacer, because of the variation in its thermal conductivity with temperature. At low temperatures its thermal conductivity is high (at 20 K the thermal conductivity is ~11,000 W m^{-1} K^{-1})[139], whilst at higher temperatures it is low (at 100 K the thermal conductivity is ~350 W m^{-1} K^{-1}).[139] The sapphire thus allows the OFHC copper blocks and the filaments to be cooled efficiently. Conversely, during heating the sapphire minimises the amount of heat transferred from the heating circuit into the sample mount and cold finger. Tungsten rods, with a hole bored into their centres, are inserted into the bottom of each OFHC copper block. Into each of these blocks a W/Re (75% W, 25% Re) filament is inserted, held in place by silver solder. The filaments then lead to the sample, as seen in Figure 2.4.

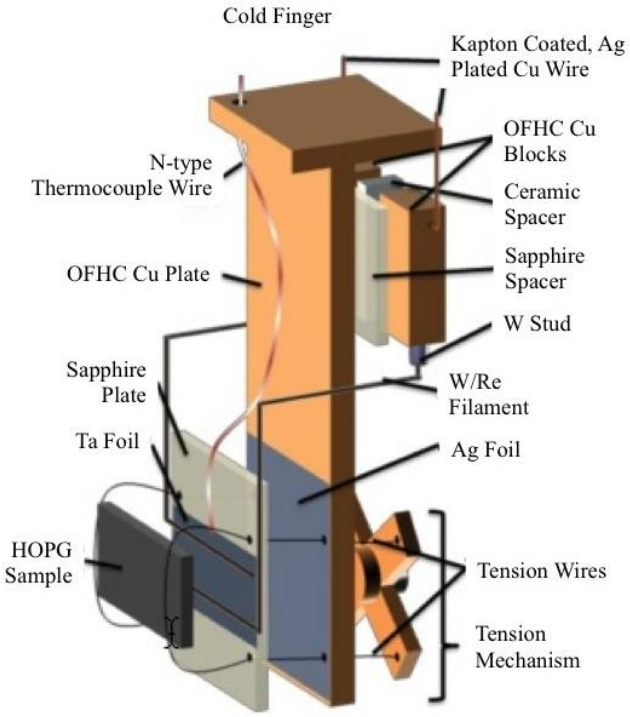

Figure 2.4 – Schematic of the sample mount. Taken from reference [140]. HOPG refers to highly oriented pyrolytic graphite.

A 20 × 10 × 2 mm piece of HOPG (Goodfellow Ltd.) is used for the sample. HOPG is composed of sheets of graphene held together by weak intermolecular forces (Figure 2.5) and has a highly ordered crystal structure. The surface can be considered to be very smooth, flat and pure. HOPG was chosen primarily as it is considered to be a suitable

interstellar dust grain analogue, simulating the carbonaceous component of interstellar dust grains.[44,141] It also has experimentally advantageous qualities. Firstly, HOPG is very stable to thermal shocking, making it ideal for use as a surface in TPD experiments, where the surface temperature can vary by several hundred Kelvin in a matter of minutes. The thermal stability of HOPG also means that it should have a very long lifetime, minimising both time and financial costs. Secondly, HOPG is chemically stable and relatively inert. Thirdly, due to the well-ordered surface HOPG is also easily modelled by computational methods, such as density functional theory, providing a complimentary route to understanding experimental data.[142–145]

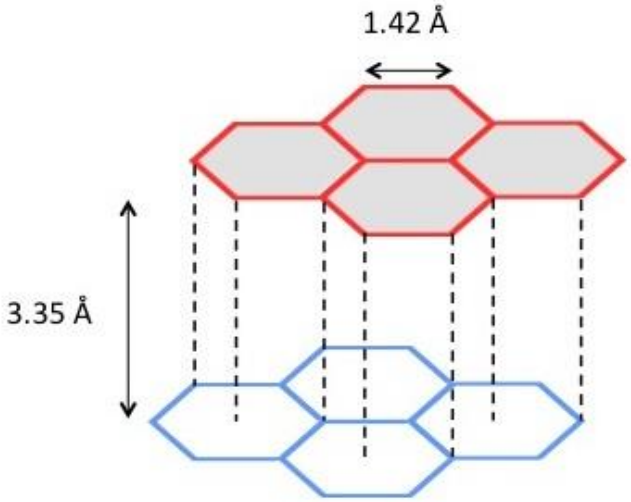

Figure 2.5 – Diagram showing the first and second graphene layers of HOPG. Arrows indicate the C-C bond length and the interplanar distance (to scale).[146] Dashed lines are to illustrate the stacking nature of the layers.

The HOPG is attached to the sample mount with a number of layers between them, as can be seen in Figure 2.4. Each of these layers is chosen for a specific reason and are as follows, from bottom to top:

1. Four sheets of silver foil – as mentioned in reference to the cold finger and sample mount joint, silver foil is used to improve thermal conductivity between the upper layers and the mount.

2. Sapphire plate – as discussed before, sapphire is used to electrically insulate the upper layers from the mount, and thus cold finger. It also allows efficient cooling of the sample whilst minimising the heat passed from the heating circuit into the mount and cold finger. The sapphire here is blackened using the amorphous

carbon produced from a burning candle. This prevents the sapphire reflecting any of the IR light from its surface and interfering with RAIRS experiments.

3. Tantalum foil (20 × 10 × 2 mm) – primarily used to complete the heating circuit and provide a location for the thermocouple to be attached. The thermocouple wire is spot welded to the top of the foil to allow the sample temperature to be monitored. Tantalum is used as it has a high melting point, thus preventing the creation of metallic vapour that could have otherwise been deposited on the sample and sample mount.

4. Heating filaments (W/Re alloy) – these lead from the OFHC copper blocks behind the sample mount onto the Ta foil. In order to prevent a short circuit, it is ensured that these filaments do not come into contact with the sample mount.

5. HOPG (20 × 10 × 2 mm) – used for the previously discussed reasons. The HOPG sample has two straight grooves cut on its back, with a slight notch in the centre of the top edge. These grooves align with the heating filaments and the thermocouple spot-weld respectively. The grooves/notch are used to ensure that there is maximum contact between the HOPG and the Ta foil, thus ensuring the best possible thermal conduction.

The sample (and lower layers) are held on to the mount by a tension mechanism, used to spread the force across the sample as evenly and tightly as possible, thus improving thermal conductivity and allowing the sample to be cooled to ~20 K. It works by using two tension wires that loop over the sample and pass through the sapphire, silver foil and mount. These two wires pass through four holes in a OFHC copper cross and are secured by four screws, see Figure 2.4. This cross sits atop an OFHC copper cap that is in direct contact with the sapphire plate, but which is electrically isolated from the mount via a ceramic ring. At the centre of the cross is a screw that, when tightened, pushes the cross away from the sapphire, thus pulling the wires and sample tighter against the mount.

2.2 Experimental Techniques

2.2.1 General Experimental Methods

To obtain accurate and clear TPD and RAIR spectra, it is imperative that the HOPG surface is as clean as possible before it is exposed to adsorbates. A clean surface is

necessary to ensure that experiments begin without contamination of the surface by background gases and/or adsorbates. Cleaning occurs, firstly, before the sample is mounted whilst at atmospheric pressure and then secondly, whilst under vacuum. Prior to the sample being mounted and put under vacuum the "Scotch Tape method"[147–149] is used to produce a fresh surface. Since HOPG consists of repeating layers of weakly bound stacked graphene a clean surface can be obtained by simply peeling off the top layer with a piece of sticky tape. When under vacuum, the sample is cleaned by a technique called flashing. This involves using the resistive heating circuit to rapidly heat the sample until all adsorbates have desorbed. After a bake, whilst at room temperature, the sample is heated to 500 K for ~3 minutes (or until the pressure in the chamber is decreasing significantly, thus indicating that desorption from the surface has ceased) two or three times. This is to ensure that the sample is as clean as possible prior to cooling. Once the sample has reached ~ 20 K further flashing is required since residual gases in the chamber will freeze out onto the surface. However, since the sample is now at ~ 20 K it is flashed to only 200-220 K. This is to limit the strain put on the sapphire and the heating filaments that they would otherwise experience if it were flashed from 20 to 500 K.

The sample is held at 220 K for 3 minutes after each TPD experiment to ensure total desorption, it is then flashed before the next experiment. 220 K is chosen as this is sufficient to desorb any of the species used during experiments under UHV. To confirm the surface is clean, blank TPD spectra are taken which, if the surface is clean, will show no desorption peaks over the range of the temperature ramp.

Before an adsorbate is admitted to the chamber it too must be cleaned. In the case of gaseous molecules this involves obtaining the highest purity source reasonably possible. However, for liquids it is not so simple because even when purchased at high purity levels, absorption of gases will almost certainly occur. Once attached to the dosing manifold and placed under rough vacuum, the surface of the liquid is pumped to remove the most volatile of the absorbed gases, after which the liquid will be subjected to multiple freeze-pump-thaw cycles. These involve freezing the liquid with liquid nitrogen, pumping on the resulting ice and then thawing the ice whilst still pumping. Once thawed the liquid is isolated from the vacuum and the process repeated until there is no evolution of bubbles during the thaw stage (this usually takes 3-5 cycles). To prevent contamination of one

adsorbate by another the gas line and manifold are flushed at least two times prior to filling with a new species.

Once the adsorbates have been cleaned and the sample prepared, growth of ices proceeds. Dosing is via two high precision all metal leak valves and is calculated using Langmuir, where 1 Langmuir (L_m) = 1×10^{-6} mbar × 1 second. The ion gauge is used (uncorrected) to monitor the dose pressure, whilst the QMS is simultaneously used to record the presence of the adsorbate and any possible impurities. The area under a dosing curve is proportional to the dose, or exposure, and can be used to ensure consistent dosing. An example of a dosing curve can be seen in Figure 2.6, where the areas under individual dosing curves are plotted against their expected dose.

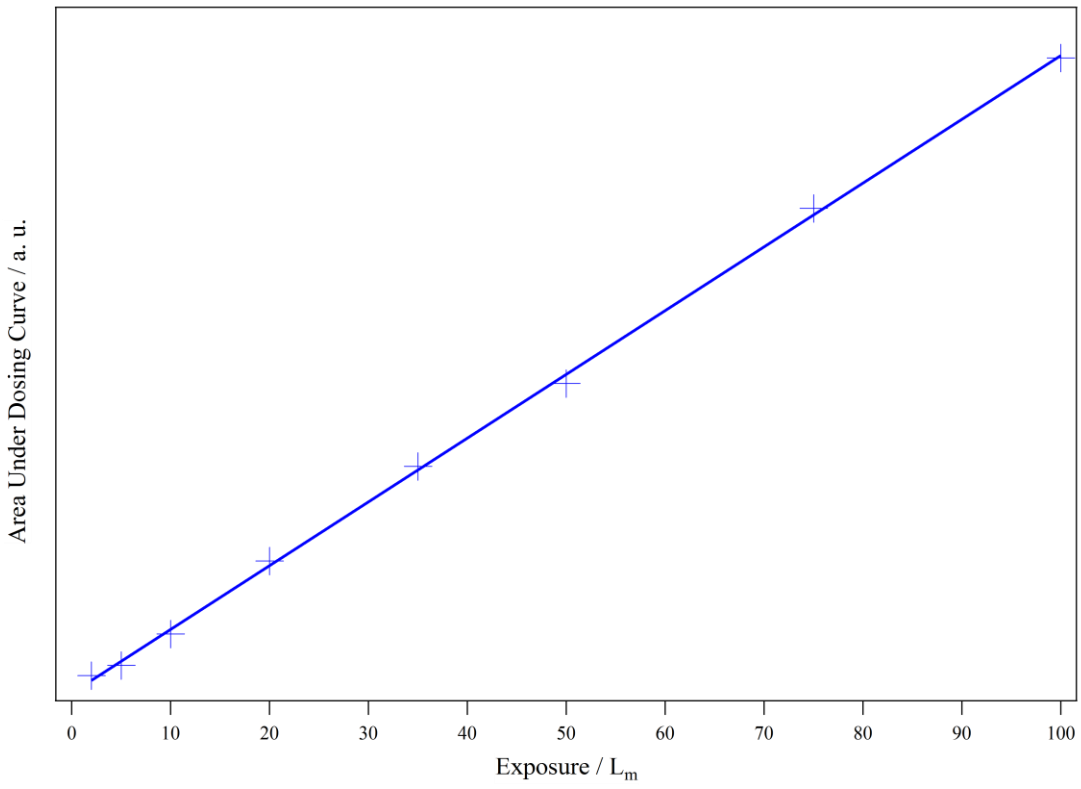

Figure 2.6 – Example of a dosing curve for formic acid deposited on HOPG at ~20 K. The area under each dosing curve is plotted against the expected dose.

Mixtures are prepared by using both of the all metal high precision leak valves. The rate of adsorbate admittance for the major component is controlled via the ion gauge, whilst the QMS is used for the minor component. In order to control dosing via the QMS a dosing curve for the species in question must first be obtained so that the required signal level can be calculated.

2.2.2 Temperature Programmed Desorption

TPD is a relatively simple mass spectrometry based technique that is destructive in nature. That is, once an experiment is finished, it is not possible to conduct further studies since the adsorbate of interest will have desorbed. Although the experimental procedure is fairly simple, it is nonetheless a powerful tool.

2.2.2.1 TPD Experimental Method

The first step in a TPD experiment is to grow the ice of interest and then position the sample so that it points directly at the entrance of the mass spectrometer. The position of the sample in relation to the QMS acts to minimise the detection of desorption from surfaces other than the sample. A linear heating rate of 0.50 ± 0.01 K s^{-1} (in the work presented here) is then applied to the sample by the resistive heating circuit previously discussed, an example of which is given in Figure 2.7. The heating is controlled by iTools (Eurotherm Ltd.) software and produced by a power supply (Thurlby Thandar Instruments Ltd., Xantrex, XFR 40-70). Desorption of pre-set masses are then monitored with respect to time. Once the temperature ramp is completed, the mass spectrometer signal intensity is plotted against temperature to give a TPD spectrum.

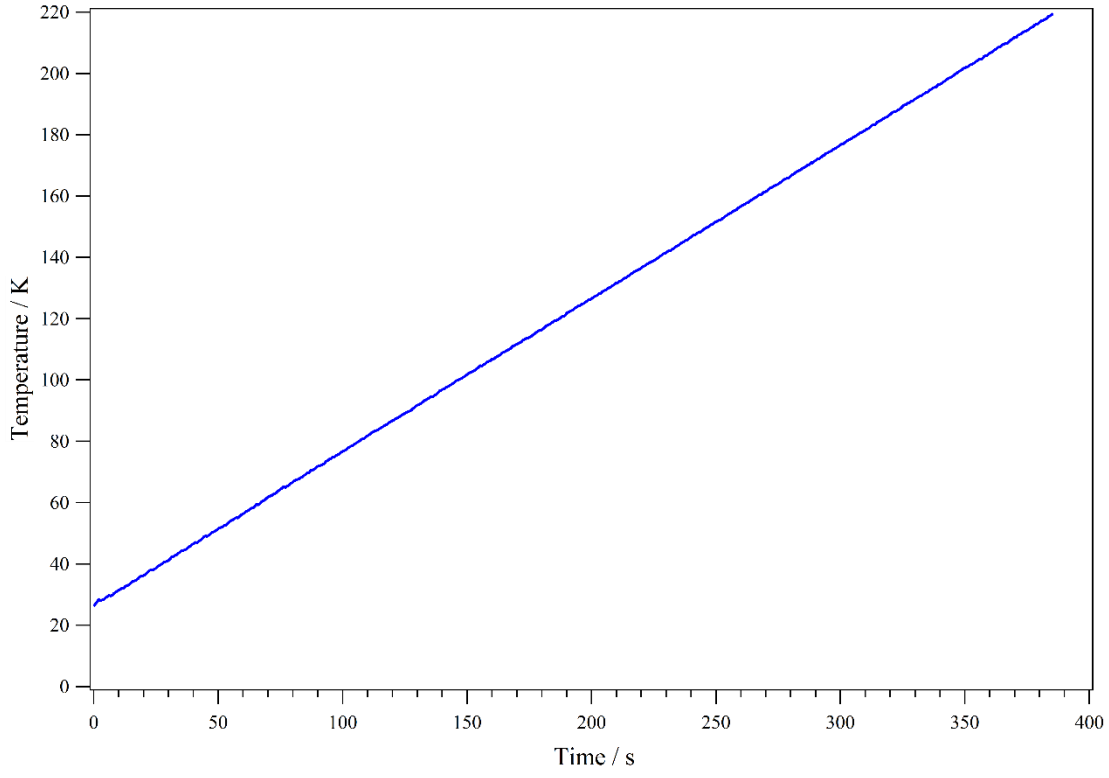

Figure 2.7 – Plot of the linear heating ramp used in TPD experiments.

2.2.2.2 Analysis of TPD

TPD is used to obtain, amongst other things, the kinetic parameters of desorption: the energy of desorption (activation energy for desorption), E_{des}, order of desorption, n and the pre-exponential factor, υ_n. These parameters are linked to the rate of desorption, r_{des}, by the Polanyi-Wigner equation (Equation 2.1),[150] where θ is the coverage, t is the time, R is the gas constant and T is the temperature.

$$r_{des} = -\frac{d\theta}{dt} = \nu_n \theta^n \, exp\left(\frac{-E_{des}}{RT}\right) \qquad \textbf{2.1}$$

The energy of desorption is a measure of the strength of the interactions between the adsorbate and the surface and the adsorbate with other molecules on the surface. The higher the energy the stronger the interaction and the more energy required to desorb. The order of desorption is a reference to the extent to which the adsorbate concentration affects the rate of desorption. Zero order kinetics (n = 0) implies that desorption is independent of coverage. This is true for very thick layers where the coverage is essentially infinitely large. First order kinetics (n = 1) are observed for simple molecular and atomic desorption and second order (n = 2) for recombinative desorption. Fractional desorption orders can be obtained in a number of different systems, for example where clusters form on the surface or where there is significant hydrogen bonding present.[141,151] The pre-exponential factor can be considered as an attempt frequency for the adsorbate to desorb.

There are a number of methods to obtain the kinetic parameters of desorption from the Polanyi-Wigner equation (Equation 2.1), a detailed discussion of which is given by King.[150] All of the methods rely on various manipulations of the Polanyi-Wigner equation and are based on differing assumptions or experimental techniques. Leading edge analysis is used in this thesis and although it is not explicitly discussed by King,[150] it can be considered to be a variant on line shape analysis.[152] Leading edge analysis assumes that the pre-exponential factor and the energy of desorption do not vary with the coverage, these assumptions were validated by Bolina *et al.*.[123] This is an acceptable assumption for the work described in this thesis since the adsorbates studied in this work are likely to be physisorbed on HOPG.[123]

The mass spectrometer signal, at any given temperature, is directly proportional to the rate of desorption[141] and thus Equation 2.1 can be rewritten as Equation 2.2. As the mass

spectrometer signal, *I(T)*, is proportional to the rate of desorption it follows that the area under the TPD curve is proportional to the coverage, allowing θ to be substituted with the relative coverage, θ_{rel}.[123]

$$I(T) \propto \nu_n \theta_{rel}^n \, exp\left(\frac{-E_{des}}{RT}\right) \qquad 2.2$$

Taking the natural logarithm of Equation 2.2 yields Equation 2.3.

$$ln[I(T)] \propto ln(\nu_n) + nln(\theta_{rel}) - \frac{E_{des}}{RT} \qquad 2.3$$

By plotting *ln[I(T)]* against $ln(\theta_{rel})$, for a given fixed temperature and range of coverages, the order of desorption can thus be calculated as the gradient of the resulting straight line. The relative coverages are taken as the areas on the high-temperature side of the fixed temperature, as depicted by the dashed line and shaded area in Figure 2.8 for the 50 L_m spectrum.

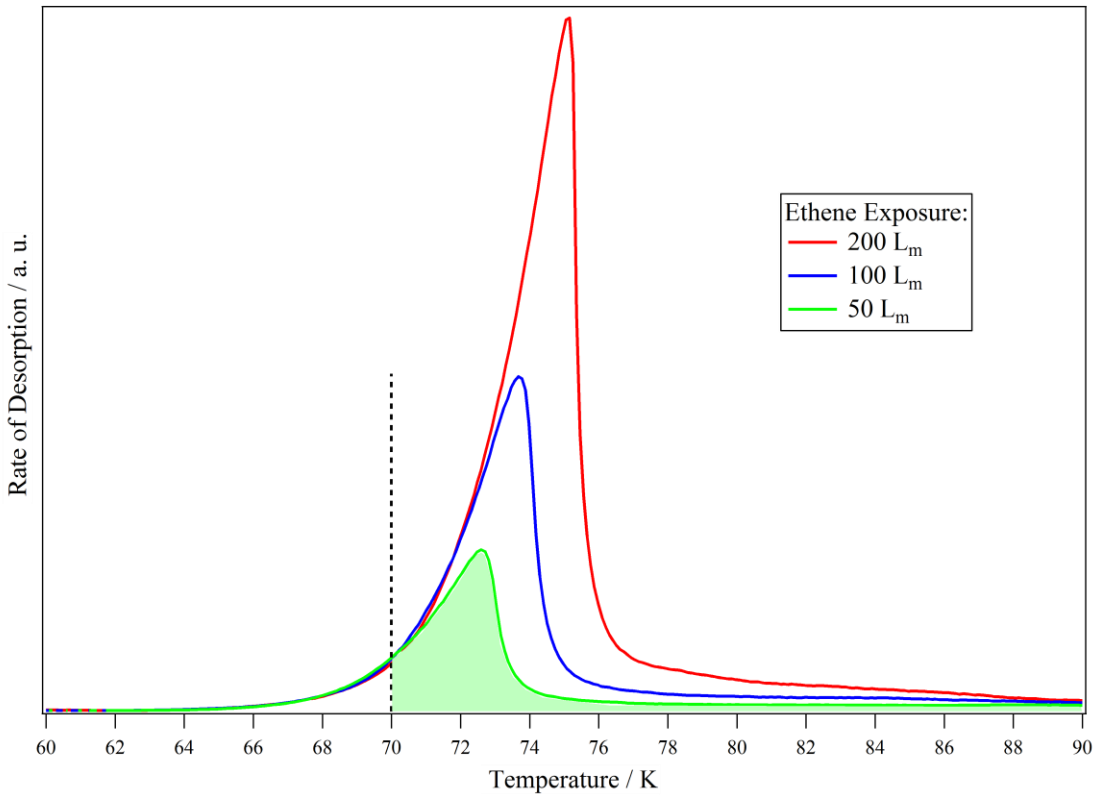

Figure 2.8 – Example of a family of TPD spectra (ethene on HOPG). The shaded area represents the area used to calculate the relative coverage of 50 L_m of ethene at 70 K.

With a value for the order of desorption, Equation 2.3 can be transformed into Equation 2.4, which takes the form $y = mx + c$. This allows the energy of desorption to be obtained from the gradient of a plot of $ln[I(T)]\text{-}nln(\theta_{rel})$ versus $1/T$.

$$ln[I(T)] - nln(\theta_{rel}) \propto ln(\upsilon_n) - \frac{E_{des}}{RT} \quad 2.4$$

Calculation of the pre-exponential factor requires the absolute, as opposed to relative, coverage. Since this is not directly measurable using the set-up used in this work, the coverage, N_m (molecules), is calculated using the rate of impingement, Z (molecules m^{-2} s^{-1}), time, t (s), and sample area, A (m^2). Equation 2.5 defines N_m as a function of the aforementioned variables and shows the full calculation used, where p is the pressure, m is the mass of a molecule, k_B is the Boltzmann constant and T_g is the gas temperature (set to 300 K). Equation 2.5 does not include a sticking probability factor since this is assumed to be 1, a valid assumption for surfaces at ~20 K.

$$N_m = ZAt = \frac{pAt}{\sqrt{2\pi m k_B T_g}} \quad 2.5$$

Once the absolute coverage is known it can be used to scale the relative coverage, giving the absolute coverage. Further manipulation of the Polanyi-Wigner equation, in combination with the absolute coverage, yields the pre-exponential factor (Equation 2.6).

$$\upsilon_n = \frac{I(T)}{\theta^n exp\left(\frac{-E_{des}}{RT}\right)} \quad 2.6$$

By obtaining the kinetic parameters of desorption a molecule can subsequently be incorporated into multi-species desorption models. Astrochemical models utilise these parameters to simulate desorption on astronomically relevant timescales[122,153,154].

In addition to abstracting the kinetic parameters of desorption, TPD can be used to investigate phase changes, trapping of one species by another, chemical evolution, adsorbate/surface interactions and ice growth mechanisms. In the case of phase changes, for example, any such change will usually result in a change of vapour pressure that can be manifested in the TPD spectrum as a shoulder or new peak. Both formic acid and water, the key molecules of interest in this thesis, display the shoulder in TPD spectra as they undergo phase changes to crystalline structures. Further information regarding structural changes in the ices can be obtained by using varying rates of heating. For the

example of a phase change from an amorphous state to a crystalline state, if a fast heating rate is used the ice will likely desorb prior to crystallisation, whereas a slow rate would result in the ice fully crystallising prior to desorption. The result would be two different peak temperatures. However, if an intermediate heating rate was used, a dual feature desorption signal should be observed. The low temperature feature would be considered to be desorption of the amorphous ice, that then ceases due to depletion caused by desorption and the crystallisation process. The second, higher temperature, feature would thus be desorption of the crystalline species since it would have a lower vapour pressure than the amorphous ice.

2.2.3 Reflection Absorption Infrared Spectroscopy

RAIRS, like TPD, is a relatively simple method that can yield a great deal of information about an adsorbate system. It is a non-destructive technique that, like typical infrared experiments, yields information regarding the bonding within adsorbate molecules, as well as bonding between the adsorbate and substrate. For single component or simple multi-component ices, RAIRS can be used to indisputably identify a species. However, with more complex systems it is likely that overlapping of bands will occur. In these instances, by using key, strong and sensitive features, such as carbonyl stretching modes in adsorbates, RAIRS can still be used to identify species within reasonable doubt. In addition to identifying species present, RAIRS can be used to track phase changes since spectral features are often influenced by the structural arrangement in which they exist. A simple and well-studied example of this is water ice. Amorphous water exhibits a broad and formless peak, whereas, crystalline water has a sharp central peak and two clearly defined shoulders due to its well-ordered structure (Figure 2.9).

RAIRS is based on analysing the difference between an incident and reflected beam of infrared radiation that has passed through an adsorbate. The difference is a consequence of vibrational modes absorbing some of the infrared radiation, which itself results from the coupling of the radiation's electric field with the electric dipole moment of the adsorbate vibration. Like typical infrared spectroscopy, for a signal to be seen in a RAIR spectrum the dipole moment of the vibrational mode must change during the vibration. However, since this is reflection spectroscopy, a further rule must be obeyed for a signal to be visible, the metal surface selection rule. Although HOPG is not a metal, it is considered to be semi-metallic. This is because in terms of reflectance, it behaves much

like a metal, having an intermediate reflectivity between a metal and a dielectric substance, and as such the metal surface selection rule applies.[155,156]

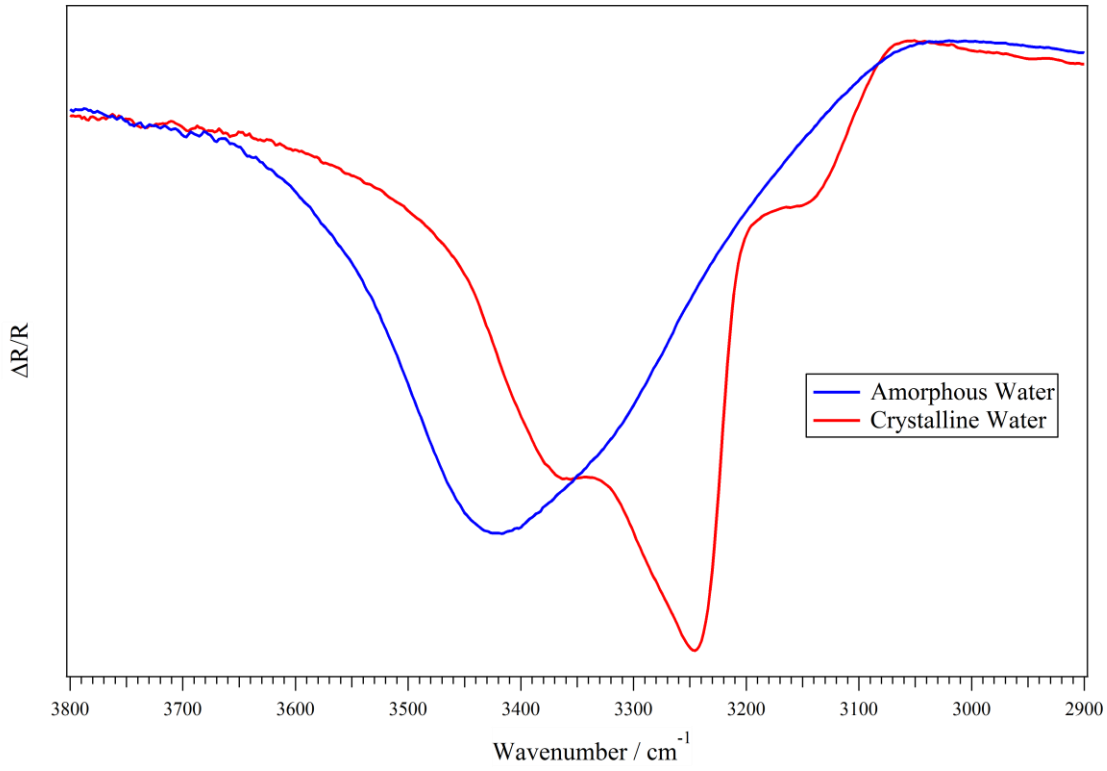

Figure 2.9 – RAIR spectra of equal amounts of amorphous and crystalline water, showing only the O-H stretching band.

The metal surface selection rule can be explained by considering the composition of the incident and reflected radiation.[157,158] The incident beam's (I) electrical field vector can be split into two components, one in the plane of incidence (E_p) and one parallel to the surface (E_s), see Figure 2.10. A single component can be obtained by using polarised light: p-polarised for the parallel component and s-polarised for the perpendicular component. The resulting reflected beam (R) can equally be split into two components with respect to the plane of incidence (E_p' and E_s'). Assuming 100% reflectance, E_s undergoes a 180° phase change at a metal surface and thus fully cancels itself out. Contrastingly, for large angles of incidence (large θ), called grazing angles, E_p is enhanced. In practice, θ is usually set to ~85° because for metals typically used in RAIRS, such as gold and nickel, this is the average optimum angle that gives maximum enhancement of E_p.[158,159] However, for HOPG, owing to its semi-metallic nature, enhancement is maximised for a θ of ~73°.[155,156] In addition to enhancement of E_p, using grazing angles results in a large path length through the ice. Since it is the coupling of the

electric field vector to the vibration's dipole moment that results in a RAIRS signal, only vibrations whose change in dipole moment has a component perpendicular to the surface will be present in a RAIR spectrum. Following from this, the metal surface selection rule thus states that only vibrations causing dipole moment changes with a component perpendicular to the surface will be visible in a RAIR spectrum.

Although the metal surface selection rule may at first glance appear to hinder the investigative power of RAIRS it can actually be utilised to reveal information regarding the orientation of adsorbates with respect to the surface.[160] For example, the growth of a spectral feature may not be due to the increasing presence of a particular vibration but may in fact be caused by an orientation change that causes the vibration's dipole change to have an increasingly perpendicular nature, with respect to the surface.

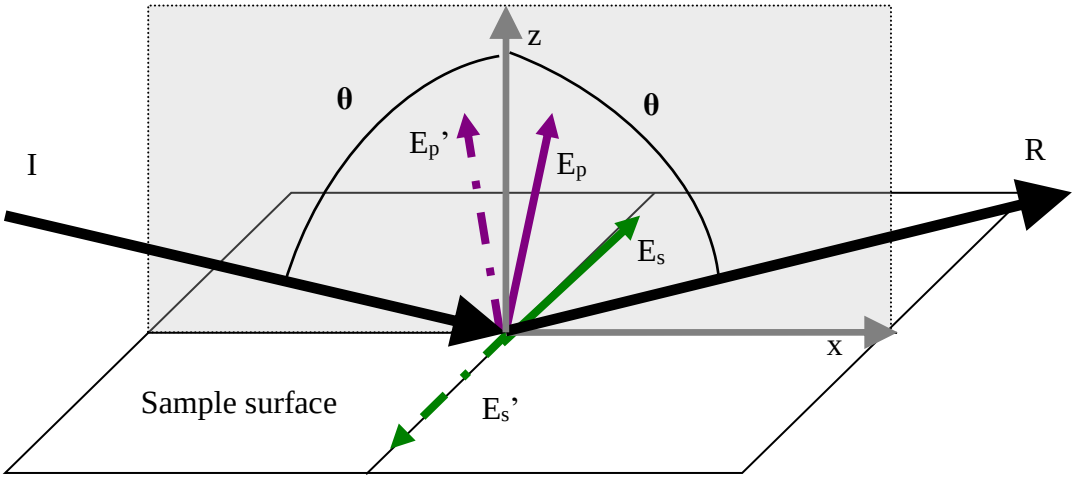

Figure 2.10 – Diagram showing the different components of the electrical field vector for the incidence and reflected light from a surface. See main text for definitions of labels.

A schematic of the RAIRS set-up is detailed in Figure 2.11. The infrared radiation originates from a Fourier transform infrared (FTIR) spectrometer (Thermo Scientific, Nicolet 600 FT-IR) and passes into a sealed box (marked * Figure 2.11). It is reflected off a pair of mirrors that focus the beam through the KBr window and onto the HOPG surface. In order to achieve the maximum possible reflectance from the HOPG surface an angle of incidence of ~75° is used. The reflected beam passes out of the chamber and into another sealed box (marked # Figure 2.11), where it is reflected and focused by a second pair of mirrors into a liquid nitrogen cooled mercury cadmium telluride (MCT) detector. The detector and spectrometer are linked to a computer running OMNIC (Thermo Scientific), which is able to control the spectrometer and also process the resulting

spectra. The sealed boxes (marked * and # in Figure 2.11) and the spectrometer are not under vacuum and so are purged of water and carbon dioxide, these being the two most abundant and strongly infrared absorbing molecules in air. The purge system ensures that the abundance of carbon dioxide and water in the spectrometer and optics boxes are constant, thereby allowing their signals to be removed when a spectrum is referenced to the background. Carbon dioxide and water are purged by using a compressed air system with a refrigeration air drier (water dew point = 3 °C) (MTA, Dry Energy Hybrid) and a regenerative desiccant drier (Dominic Hunter, Nitrox CO2RP280). The regenerative desiccant drier removes carbon dioxide and water using activated alumina.

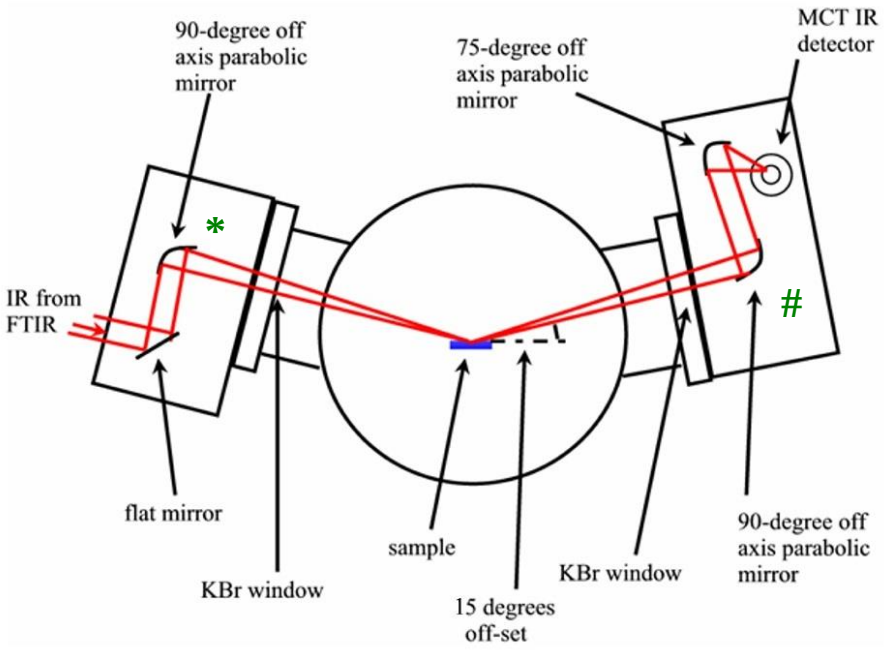

Figure 2.11 – Schematic of the RAIRS set-up used. Taken from reference [161].

The general method of obtaining RAIR spectra involves three key steps. First, recording a background spectrum of the bare surface. Then, preparing the sample ice and finally, recording the sample RAIR spectrum. Reported RAIR spectra are obtained using the relation expressed in Equation 2.7, where *R* refers to the sample and R_0 to the background.

$$R_{reported} = \frac{\Delta R}{R_0} = \frac{R - R_0}{R_0} \qquad 2.7$$

The division by the background accounts for the inhomogeneity in the intensity of the infrared source with respect to the frequency. By accounting for the inhomogeneity, band strengths in an individual spectrum can be directly compared. A RAIR spectrum is

produced from the co-addition of 256 individual scans taken with a resolution of 4 cm^{-1}. The high number of co-added spectra results in a high signal-to-noise ratio (from ~20 to ~300), thus improving the quality of spectra. The co-addition of 256 scans is chosen as a compromise between better signal-to-noise ratio and experimental time.

As was alluded to previously, RAIRS is often used to study phase changes within ices, or more generally, to study the way in which an ice evolves with increasing temperature. For example, in Chapters 3 and 4 RAIRS is used to examine the crystallisation of formic acid into polymeric chains by tracing the splitting and shifting of key spectral features. To follow the structural evolution of interest a range of annealing experiments are conducted. Ices are subjected to repeated annealing cycles with spectra being taken between each cycle. The annealing temperature is reached by heating at a rate of 0.5 K s^{-1} and then holding the elevated temperature for 3 minutes. In Chapters 3 and 4, the annealing occurs up to 160 K. Once the heating has finished and the sample has begun to cool, the RAIR spectrum is taken. This process is repeated with ever increasing temperatures until desorption.

3 Pure Formic Acid Adsorption on HOPG

3.1 Introduction

Formic acid is the simplest carboxylic acid. It has two hydrogen bonding groups (O-H and C=O) and has a pK_a of ≈ 3.7,[162] making it moderately acidic. All of these factors make it an interesting molecule for study. Surface science studies of formic acid are wide ranging and include applications in fields such as fuel cells,[163] catalysis,[164] photochemistry[165] and atmospheric chemistry.[89,166] Key to the decision to study formic acid in this work is that it has been detected in numerous environments throughout the interstellar medium (ISM)[45,56,65,67–75,167,168] and is believed to actively partake in its chemical evolution.[45,65,76] Whilst it is unlikely that there will be pure formic acid ices in the ISM, an understanding of the interactions between formic acid molecules in the absence of other species is needed before the interactions between formic acid and other astronomically relevant species can be properly understood. Therefore, this chapter deals with the nature of the formic acid-formic acid interaction, whilst Chapter 4 will deal with more astronomically relevant formic acid-water interactions.

Zuckerman *et al.*[56] first detected formic acid in the direction of Sagittarius B2 using an Earth-based telescope, making it the first organic acid to be detected. Eventually it was detected in a variety of environments, in both the gas and solid phase. Gas phase detections were made in star-forming regions,[67] hot cores,[45,68] hot corinos,[69] the galactic centre cloud[70,75] and cold dark clouds.[71,72] Solid phase detections were made for icy mantles in high and low mass star forming regions,[73,74] as well as on the comet Hale-Bopp.[167,168] Formic acid is more abundant in the solid phase than it is in the gas phase[167], by up to a factor of 10^4 in some places.[65,67,75] Calculated solid phase abundances vary from location to location, but generally formic acid accounts for 1-5% of an icy mantle, with respect to water.[75]

Formation of formic acid in the gas phase has been proposed to occur by two routes: $HCO^+ + H_2O$ or $O_2^+ + CH_4$. Both routes are then followed by electron recombination.[167,169] However, these two pathways cannot account for the observed abundances, particularly around protostars where they are both inefficient routes.[167] The inability of gas phase routes to reproduce the observed abundances, as well as detection of solid formic acid in icy mantles, means that surface formation pathways must be

considered. Proposed surface routes are based upon energetic processing of ices containing water and CO. This energetic processing is produced by galactic cosmic rays, which consist of ~98% protons and have the ability to penetrate an icy mantle. These galactic cosmic rays are known to be a key player in the chemical evolution of the ISM.[65]

Hudson and Moore simulated galactic cosmic ray bombardment by irradiating water and carbon monoxide mixtures with protons.[134] They detected, amongst other things, methanol, methane and formic acid. Bennett *et al.* noted that proton bombardment of ices would result in the ionisation of molecules on the surface and thus generate high-energy electrons.[65] In order to simulate interstellar ices being penetrated by galactic cosmic rays Bennett *et al.* bombarded mixtures of water and CO with high-energy electrons. Electron bombardment of water results in dissociation of water into H + OH, either of which can go on to react with CO to form HCO or HOCO, respectively (see below). These can then go on to react readily with the remaining product of water dissociation to form formic acid.[65]

$$CO + H \rightarrow HCO \quad \text{…followed by…} \quad HCO + OH \rightarrow HCOOH$$

$$CO + OH \rightarrow HOCO \quad \text{…followed by…} \quad HOCO + H \rightarrow HCOOH$$

In addition to the water and CO formation pathways it has also been proposed that formic acid can be produced from low-energy electron irradiation of methanol. Boamah *et al.* irradiated methanol ices with electrons of different energies in an attempt to synthesise prebiotic molecules relevant to the ISM.[170] Boamah *et al.* reached their conclusions by comparing the different cracking fragments in temperature programmed desorption (TPD) experiments and clear evidence of formic acid production could not be found. UV photolysis of methanol and methanol/CO mixtures was shown by Oberg *et al.* to produce formic acid.[135] Bennett *et al.*[65] also reported that the formic acid production route proposed by Garrod and Herbst,[82] that required HO• and HCO• (produced by reaction of gaseous H with O and CO, respectively) to diffuse across the surface and react, would be unlikely due to radical immobility at 10 or 20 K. The generally accepted view in the literature is that formic acid production in the ISM requires energetic processing of some description, likely to be by either UV irradiation or by galactic cosmic rays.

The astronomical interest of formic acid extends beyond its wide spread existence, since it is also believed to partake in the formation of other complex organic species. Formic

acid shares structural similarities with the three isomers of $C_2O_2H_4$ (acetic acid, methyl formate and glycolaldehyde) and with glycine, the simplest amino acid. It has therefore been proposed that it could play a part in the formation of these biologically important molecules in space,[45,65,76] thus having important ramifications in the field of astrobiology.

Due to its ability to form multiple hydrogen bonds, formic acid can form one of four distinct phases,[137,171–174] as shown in Figure 3.1: monomers, dimers, β-crystalline/polymer and α-crystalline/polymer.

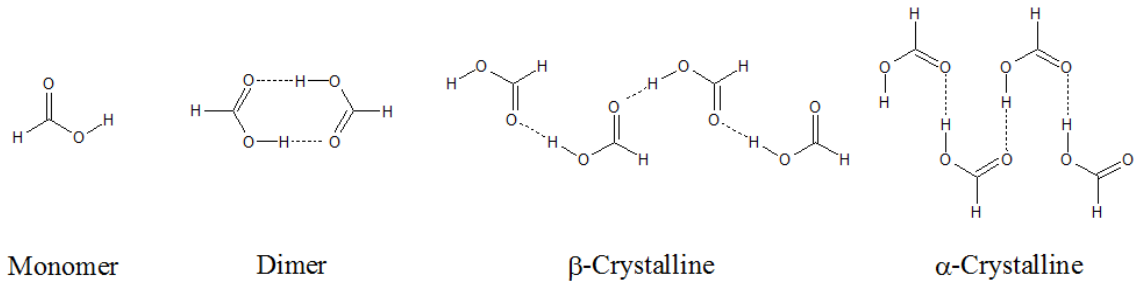

Figure 3.1 – The four structures of formic acid: monomeric dimeric, β-crystalline and α-crystalline.

The α-crystalline structure is the most stable owing to its compact, long-range hydrogen bonded structure. In the gas phase formic acid exists predominantly as a dimer[126,171] since this is ~59-76 kJ mol^{-1} more stable than the monomer.[163,175] The enhanced stability originates from the cyclic structure of the dimer. This is formed by two short hydrogen bonds and results in an 8-membered ring (shown in the second image from the left in Figure 3.1). Providing the surface is cold enough and does not promote chemisorption, formic acid will remain as dimers when it adsorbs, with the temperature below which formic acid remains as dimers depends upon the substrate.[126] Upon heating, the dimeric units unlock and rearrange, ultimately adopting the α-crystalline structure.[89,126]

There are a significant number of surface science studies examining formic acid adsorbed on a wide variety of substrates. The following are a selection of the substrates used in the literature: Cu(110)[136], Pd_{1ML}/Mo(110)[176], Pd(111)[177], Pd(100)[178], TiO_2(110)[179], Pt(111)[163,180], Pt(110)[181], W[182,183], Ru(001)[184], Rh(111)[185], Ni(111)[186], Ag(111)[174], Au(111)[187], polycrystalline gold[38,89], CsI[75] and KBr[126]. None of the substrates listed above are applicable to astrochemistry and several (Cu(110), Pd_{1ML}/Mo(110), Pd(111), Pd(100), Pt(110), Pt(111), W, Ru(001), TiO_2(110) and Rh(111)) promote chemisorption of formic acid. In the ISM dust grain surfaces are carbonaceous and silicaceous in nature and

therefore, likely to promote physisorption – rather than chemisorption – hence the use of highly oriented pyrolytic graphite (HOPG) in the work presented here.

When formic acid is adsorbed onto the substrates that promote chemisorption it will, depending on the substrate temperature, either immediately decompose to form a surface bound formate or will do so upon sufficient heating. These formate species then proceed to react and desorb by several different pathways. If sufficiently thick layers are deposited, then multilayer desorption of formic acid is observed over a wide range of temperatures (150-210 K). These systems may not be directly comparable with physisorbed systems but multilayers of formic acid on a layer of formate bound to the substrate should desorb in a comparable manner to multilayers of formic acid physisorbed directly to the substrate and are therefore still considered.

Studies involving the use of Au(111), Ag(111), polycrystalline gold, KBr and CsI substrates do not report chemisorption of formic acid, nor the associated decomposition. Considering the identity of these substrates, physisorbed systems are to be anticipated. However, it is reported that pre-oxidised Ag or Au will be reactive to formic acid adsorption, again this is wholly expected[174].

As part of a comprehensive study of astronomically relevant molecules, which informed work by Viti *et al.*[154], Collings *et al.*[38] observed a two-feature TPD profile for multilayers of formic acid desorbing from polycrystalline gold (peaks at ~135 and ~150 K). The two-feature profile suggested to Collings *et al.* that during the temperature increase, formic acid underwent a phase change at ~140 K, however, they did not address the identity of the phases.

Also using a polycrystalline gold substrate, Hellebust *et al.* investigated formic acid in cirrus cloud mimics.[89] Although the substrate temperature was 100 K, much higher than surface temperatures in the ISM and those used by Collings *et al.*[38], the findings are still of use to the work presented here. Hellebust *et al.* found that adsorption at 100 K resulted in an amorphous ice comprised of dimeric units and that after sufficient annealing, between 160 and 180 K, the ice crystallises to form the α-crystalline structure (shown in Figure 3.1). These conclusions were reached by analysis of reflection absorption infrared (RAIR) spectra. TPD experiments of formic acid deposited on the polycrystalline gold substrate at 100 K showed a two-feature desorption profile, similar to that observed by

Collings *et al.*.[38] However, the temperatures reported by Hellebust *et al.*[89] were ~40 K higher than those reported by Collings *et al.*.[38] The reason for this discrepancy is unknown and was not addressed by Hellebust *et al.*.[89]

Using transmission infrared spectroscopy and a CsI substrate, Bisschop *et al.*, studied the spectral evolution of formic acid in various systems (including pure ices) with increasing temperature.[75] It was found that above 135 K formic acid crystallises and that this process was irreversible. As the substrates used by Bisschop *et al.* (CsI)[75] and Collings *et al.* (polycrystalline gold)[38] promote physisorption, the large discrepancy in crystallisation temperatures reported is unusual, a possible cause may be that the two studies used different heating methods from one another.

Both Bisschop *et al.*[75] and Hellebust *et al.*[89] made substantial reference to a study by Cyriac and Pradeep[126] that probed the infrared spectral evolution of formic acid as it crystallises. They reported that crystallisation in their system initiated at 98 K and was complete by 135 K, in agreement with the study by Bisschop *et al.*.[75] It would appear that even on substrates that promote physisorption, the phase change of formic acid and the accompanying spectral evolution requires further investigation.

Detailed studies of formic acid adsorption and desorption from a carbonaceous substrate, such as HOPG, under astronomically relevant conditions are lacking in the literature. Therefore, a range of TPD experiments of formic acid adsorbed on HOPG were conducted to understand the nature of formic acid desorption and to calculate the desorption kinetics.

Further to this, there appears to be significant discrepancies in the literature regarding the temperature profile of the phase change in formic acid. A largely pure formic acid ice that can undergo significant crystallisation is unlikely in the ISM. However, understanding the crystallisation process in pure formic acid ices is the first step to fully appreciating the effect of a second species, such as water, on this process. Therefore, RAIRS annealing experiments were conducted to pinpoint the onset of crystallisation and to subsequently track the progress of this phase change.

3.2 Experimental

The formic acid was obtained from Sigma Aldrich with a purity of ≥ 98% and was subjected to multiple freeze-pump-thaw cycles to remove any absorbed gases. Ices were grown *in situ* by backfilling the chamber, with doses measured in Langmuir (1 L_m = 1 × 10^{-6} mbar s). Prior to dosing, the surface of the liquid was pumped on for at least a minute to further ensure purity.

TPD experiments were conducted using a heating rate of 0.50 ± 0.01 K s^{-1}. The mass spectrometer monitored formic acid desorption by scanning for masses 46 (parent ion, $HCOOH^+$) and 29 (main cracking fragment, HCO^+) simultaneously. Although both mass 29 and 46 were recorded, only mass 29 was used for the discussions below because, as can be seen in Figure 3.2, both exhibit the same desorption profile, differing only in intensity. Furthermore, mass 29 is the most intense fragment and so has the best signal-to-noise ratio. All exposures of formic acid on HOPG exhibit identical profiles for the two masses. This indicates that formic acid desorbs as an intact molecule and that the observed fragmentation occurs in the quadrupole mass spectrometer (QMS).

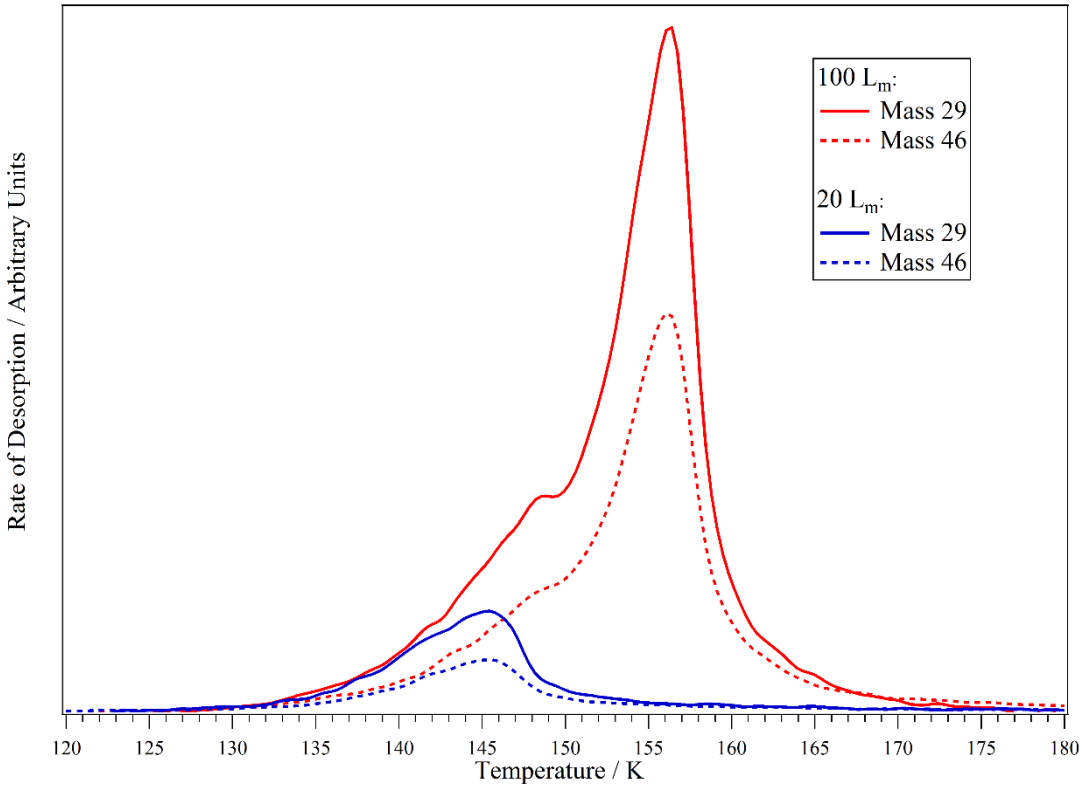

Figure 3.2 – Mass 29 and mass 46 TPD spectra for 20 and 100 L_m of formic acid deposited on HOPG at ~20 K.

RAIR spectra were obtained using a resolution of 4 cm^{-1} with the co-addition of 256 scans. Annealing experiments were conducted by raising the temperature at a rate of 0.5 K s^{-1} and then holding the desired temperature for 3 minutes. The sample was then allowed to cool and the spectrum recorded.

3.3 TPD Studies of Formic Acid Adsorbed on HOPG

A range of formic acid exposures were used to prepare pure ices of differing thicknesses on HOPG at ~20 K. The TPD spectra (mass 29) of these ices can be seen in Figures 3.3 and 3.4. Division of the spectra is for clarity, with the 20 L_m spectrum being shown in both plots to allow comparison of scales.

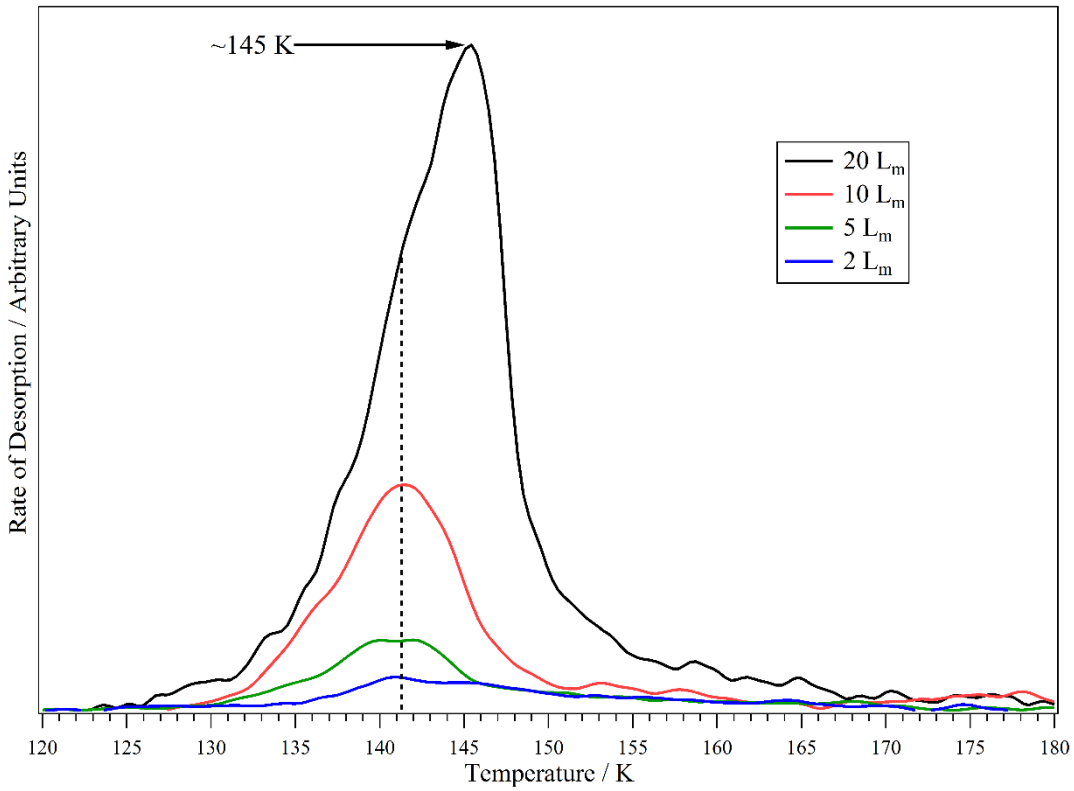

Figure 3.3 – TPD spectra of 2-20 L_m of formic acid (mass 29), adsorbed onto HOPG at ~20 K.

As can be seen in Figure 3.3, the smallest exposure of 2 L_m has a single desorption feature at ~141 K. Exposures of 5 and 10 L_m also produce a single desorption feature that, whilst larger and clearer than the 2 L_m spectrum, remains centred at ~141 K. Owing to the increased intensity it is also possible to observe that the 5 and 10 L_m peaks are approximately symmetric. Upon increasing the exposure to 20 L_m, a significant change in the desorption profile is observed. The peak temperature shifts to ~145 K and the profile is no longer symmetrical.

The 35 L_m spectrum in Figure 3.4 shows a further evolution in the peak shape with the appearance of an additional feature on the low temperature side of the main peak, which itself has shifted to ~150 K. Increasing the exposure up to 100 L_m results in the low temperature feature becoming more defined and the main peak shifting up to ~156 K. It is also clear that the leading edges, both before the low temperature feature and after, are largely shared. The profile of the peak is also now highly asymmetric.

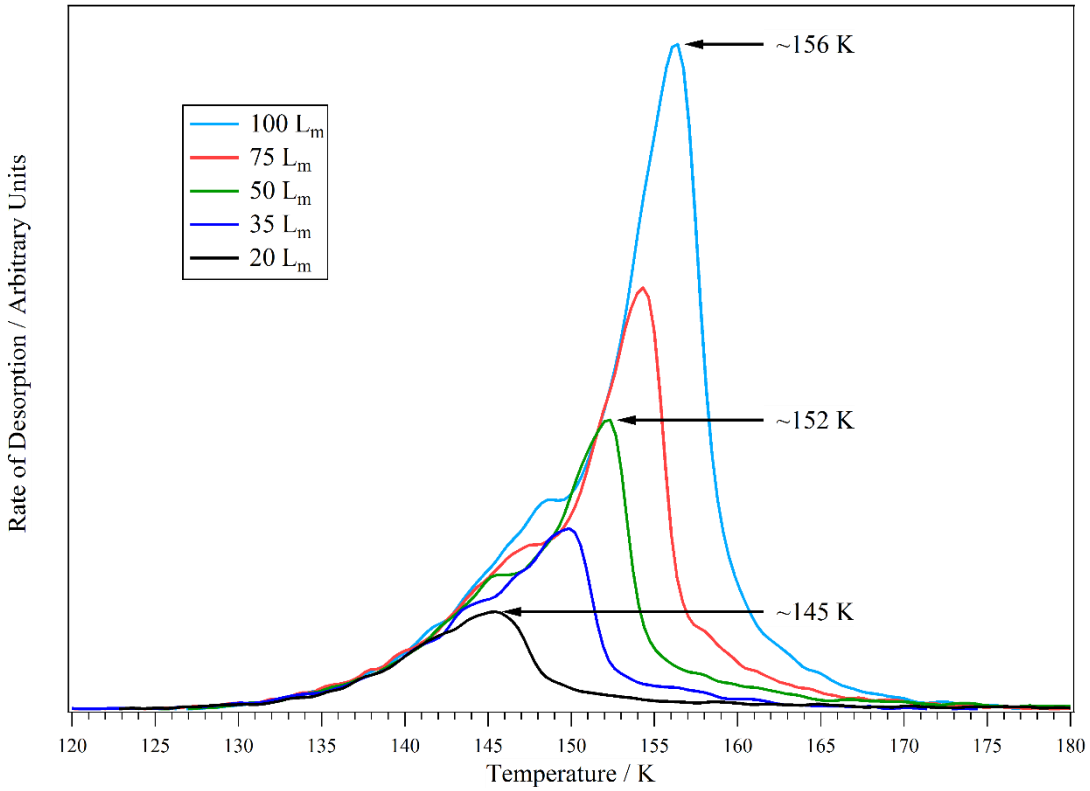

Figure 3.4 – TPD spectra of 20-100 L_m of formic acid (mass 29), adsorbed onto HOPG at ~20 K.

By evaluating the way in which the TPD peak profiles vary with coverage it is possible to estimate the order of desorption. The 2-10 L_m spectra are all centred at ~141 K and have a symmetrical profile; a peak temperature independent of coverage and a symmetrical profile are indicative of first order desorption. The peak temperatures of 20-100 L_m spectra increase with coverage (from ~145 to ~156 K), furthermore, the spectra share leading edges and have asymmetric peak profiles; peak properties such as these suggest zero order desorption. First order desorption is usually seen for monolayer and sub-monolayer desorption whilst zero order is common for multilayer desorption. The absolute order of desorption will be confirmed later following quantitative analysis of the TPD spectra.

The low temperature feature – that appears as a shoulder – observed in the TPD spectra for higher coverages (Figure 3.4) grows in intensity and shifts to higher temperatures (from ~144 to 149 K) with increased coverage. The appearance of a shoulder at higher coverages, and the aforementioned behaviour of such a feature, is also witnessed in water TPD spectra and is assigned to the amorphous to crystalline water phase transition.[188,189] Therefore, the low temperature shoulder observed in Figure 3.4 is attributed to a crystallisation process within the formic acid multilayer ice. Collings *et al.* also observed a low temperature shoulder for formic acid deposited on polycrystalline gold and attributed it to a phase change similar to that observed for water.[38] The shoulder appears due to a decrease in the vapour pressure that would be expected after an amorphous to crystalline phase change. Crystallisation of formic acid can be probed using RAIRS and will be discussed in Section 3.4.

As mentioned in Chapter 2, the integrated area under a TPD curve is proportional to the amount of adsorbate on the surface. This relationship is illustrated in Figure 3.5 where the integrated areas under the TPD spectra in Figures 3.3 and 3.4 are plotted against the relevant exposures. The linear relationship between formic acid exposure and integrated area under the TPD spectra indicates that the sticking probability is constant across all coverages studied.

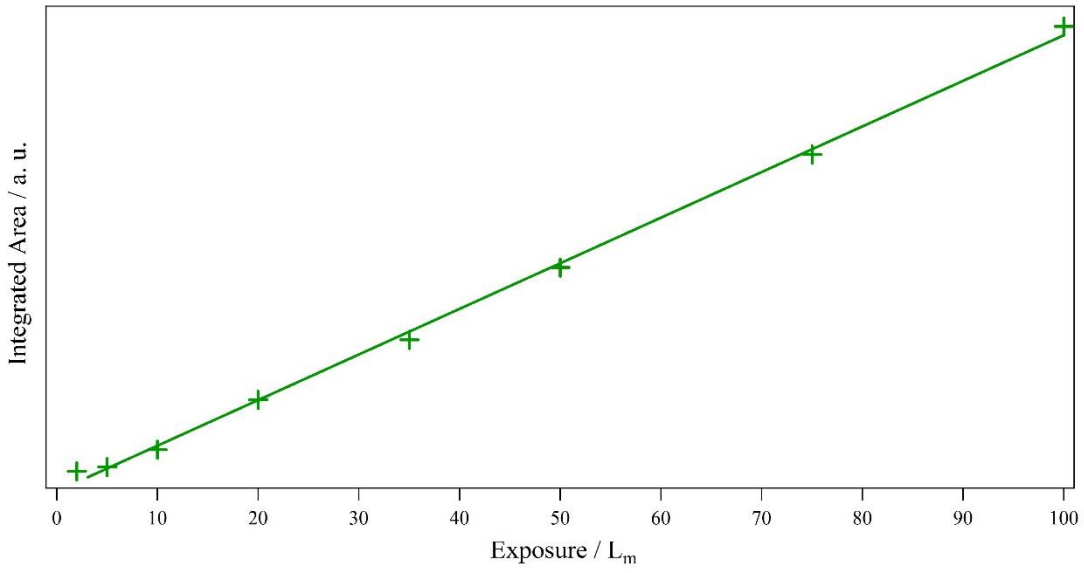

Figure 3.5 – Integrated area under TPD curves for a range of formic acid exposures. Data points correspond to the spectra shown in Figures 3.3 and 3.4. The line is to guide the eye and was produced by a linear fit to the data points.

3.3.1 Quantitative Analysis of TPD Data

Leading edge analysis of a stack of TPD spectra can yield the key desorption kinetic parameters: order of desorption, energy of desorption and pre-exponential factor. Desorption kinetics are used to model desorption temperatures under astronomically relevant heating rates, which are many orders of magnitude lower than used in typical laboratory set-ups.[39,154] These desorption temperatures are then used by astronomers to model desorption processes in astronomically relevant ice systems.

3.3.1.1 Monolayer Order of Desorption

Orders of desorption are obtained from the gradient of a plot of ln(I(T)) versus ln(θ_{rel}) at a given temperature for a range of exposures. A range of 133-140 K was used for the TPD spectra shown in Figure 3.3, as for all coverages shown this range lies on the leading edge. Visual inspection of the TPD spectra in Figure 3.3 allows for preliminary assignment of orders of desorption. As such, 2-10 L_m are used to calculate the order for monolayer desorption and higher coverages will be used for the multilayer calculations, which will be discussed later. Figure 3.6 shows one of the order plots, used to calculate the monolayer desorption order at 138 K. No errors are shown in Figure 3.6 because the error in θ_{rel} is a function of the error in I(T) and T, both of which can be considered insignificant in comparison to the error resultant from the scatter in the points.

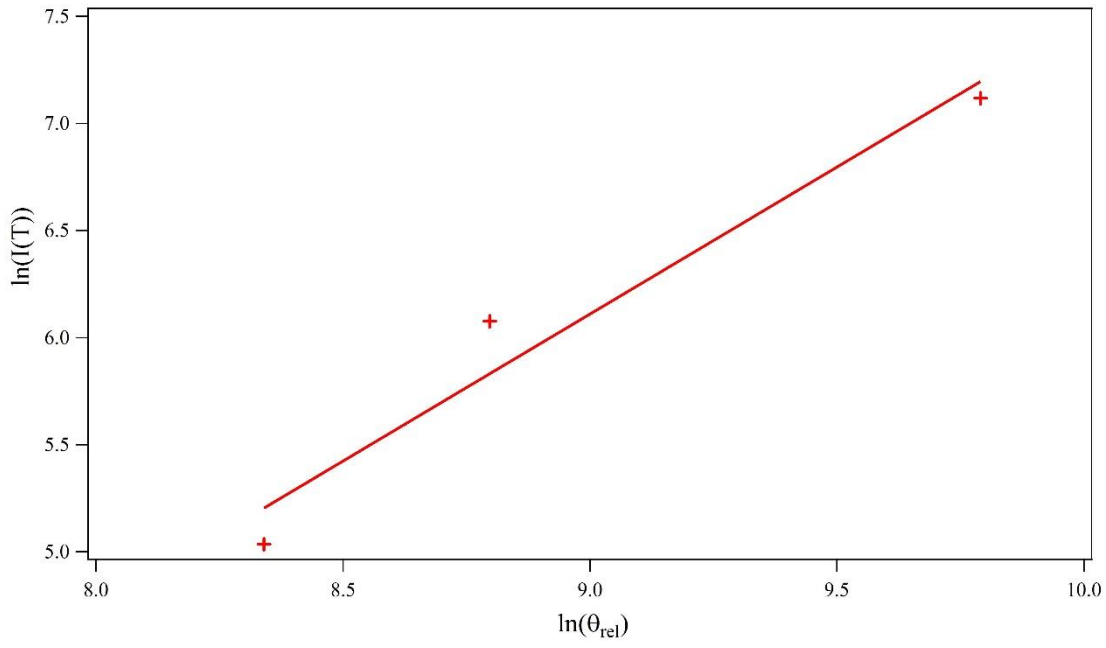

Figure 3.6 – Plot of ln(I(T)) against ln(θ_{rel}) for formic acid at a temperature of 138 K. The line shown is the linear fit whose gradient corresponds to the order of desorption for monolayer desorption.

Table 3.1 lists the orders of desorption calculated at each temperature for 2-10 L_m of formic acid deposited on HOPG. Consequently, the average monolayer desorption order was calculated as 1.37 ± 0.05. The error quoted corresponds to twice the standard error of the mean. Using twice the standard error of the mean gives a greater confidence interval for the calculated values.

Table 3.1 – Orders calculated for monolayer desorption of 2-10 L_m of formic acid deposited on HOPG.

Temperature / K	Order of Desorption
133.0	1.21
133.5	1.20
134.0	1.29
134.5	1.41
135.0	1.48
135.5	1.52
136.0	1.47
136.5	1.40
137.0	1.40
137.5	1.45
138.0	1.37
138.5	1.33
139.0	1.35
139.5	1.33
140.0	1.36

The calculated value for the monolayer order is considerably higher than the expected value of 1. Fractional orders have previously been obtained for molecules such as methanol[123,190] and are attributed to hydrogen bonding between the adsorbates. This is consistent with formic acid being able to form multiple hydrogen bonds via its O-H and C=O groups. Since there is no indication of a phase change in TPD spectra, it is proposed that formic acid monolayer desorption occurs from an amorphous ice. Furthermore, RAIRS experiments (discussed later) indicate that this amorphous formic acid ice consists of dimeric units. However, the nature of the formic acid species (monomer or dimer) that actually desorbs from the surface is unknown because it is not possible to detect dimers, during dosing or desorption, by the QMS. The inability to detect dimers with the QMS is most likely due to the dimer breaking apart as it enters the spectrometer.

3.3.1.2 Monolayer Energy of Desorption

Once the order of desorption is known it is possible to calculate the energy of desorption. A plot of $\ln(I(T))-n\ln(\theta_{rel})$ against 1/T has a gradient of $-E_{des}/R$ and thus by a simple manipulation of this gradient, the energy of desorption can be obtained. Figure 3.7 shows the plot of $\ln(I(T))-n\ln(\theta_{rel})$ against 1/T corresponding to the TPD spectrum that was recorded for 5 L_m of formic acid deposited onto HOPG. The error bars for $\ln(I(T))-n\ln(\theta_{rel})$ were calculated using $\delta n \times \ln(\theta_{rel})$. This method takes account of the maximum and minimum values of n and their effect on the calculation of $\ln(I(T))-n\ln(\theta_{rel})$.

Table 3.2 lists the desorption energies calculated for the 2, 5 and 10 L_m TPD spectra. Using n = 1.37, the average monolayer desorption energy for formic acid on HOPG was found to be 48.9 ± 5.1 kJ mol^{-1}. The errors listed in Table 3.2 correspond to one standard deviation. However, the error quoted with the average is calculated by propagating twice the individual standard deviations. Propagating twice the standard deviation offers a greater confidence interval for the calculated energy of desorption. At 10%, the stated error is appropriate and allows significant confidence in the calculated monolayer energy. The value calculated here is likely to correspond to the energy of desorption for an amorphous formic acid monolayer as there is no clear change in the rate of desorption that would normally accompany crystallisation (due to the subsequent decrease in vapour pressure), as seen in the multilayer spectra in Figure 3.4.

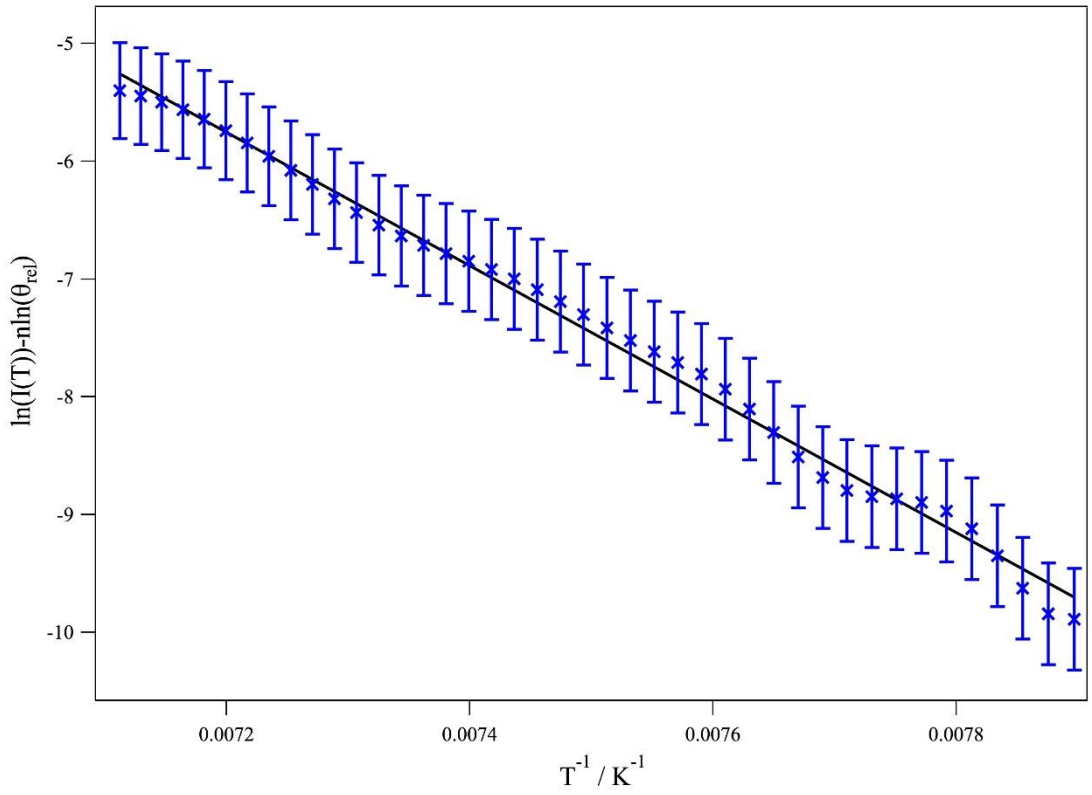

Figure 3.7 – Plot of ln(I(T))-nln(θ_{rel}) against 1/T (using n = 1.37) from the TPD spectrum corresponding to 5 L_m of formic acid on HOPG. The linear fit is used to calculate the gradient.

Table 3.2 – Calculated energies of desorption for monolayer formic acid on HOPG.

Formic Acid Exposure / L_m	Energy of Desorption / kJ mol^{-1}
2	48.3 ± 4.8
5	47.1 ± 2.4
10	51.2 ± 5.4

Desorption kinetics of formic acid on HOPG have not previously been published and as such, the values reported here cannot be directly compared. However, a comparison between formic acid and other hydrogen bonding molecules can be made.

Studies of methanol desorption from HOPG by Brown and Bolina[122,123] reported that monolayer desorption occurred at ~144 K with an energy of 47.9 kJ mol^{-1}. More recently, Smith *et al.*[191] calculated the desorption energies of the first three layers of methanol on a graphene coated Pt(111) substrate as 45.4, 44.4 and 43.6 kJ mol^{-1} (1^{st}, 2^{nd} and 3^{rd},

respectively). In addition to methanol, Smith *et al.* also reported the desorption energies of the first, second and third layers of ethanol as 52.0, 50.6 and 48.6 kJ mol^{-1}, respectively. The studies by Brown and Bolina[122,123] and by Smith *et al.*[191] indicate that the value calculated in this work for monolayer desorption of formic acid from HOPG is reasonable.

3.3.1.3 Monolayer Pre-Exponential

In order to calculate the pre-exponential factors, the absolute coverage of the adsorbate is required, as opposed to the relative coverage. Calculation of the absolute coverage and the subsequent rearrangement of the Polanyi-Wigner equation to obtain the pre-exponential is detailed in Chapter 2. Pre-exponential factors have the units $(\text{molecules m}^{-2})^{1-n}\,s^{-1}$, where n is the order of desorption.

Table 3.3 lists the pre-exponential factors calculated for monolayer desorption of formic acid from HOPG, using n = 1.37 and E_{des} = 48.9 kJ mol^{-1}. The error interval is obtained by varying the energy and order of desorption within their errors, with the maximum variation in the pre-exponential taken as its error. The average pre-exponential factor for monolayer desorption is $4.7 \times 10^{11\pm2.3}\,(\text{molecules m}^{-2})^{-0.37}\,s^{-1}$, with the error in the average obtained by propagating through the individual errors listed in Table 3.3. The value calculated is very close to the value of $10^{12\text{-}13}\ s^{-1}$ expected for perfect first order desorption,[104,152] with the discrepancy possibly resulting from the fractional desorption order calculated here.

Table 3.3 – Calculated pre-exponential factors for monolayer formic acid adsorbed on HOPG.

Formic Acid Exposure / L_m	Pre-Exponential Factor / $(\text{molecules m}^{-2})^{1-n}\,s^{-1}$
2	$3.8 \times 10^{11\pm2.7}$
5	$6.3 \times 10^{11\pm2.8}$
10	$4.1 \times 10^{11\pm2.8}$

The calculated pre-exponential factor for monolayer desorption of formic acid from HOPG is in agreement with those calculated for other physisorbed molecules such as methanol[123,192], H_2S[193], and NH_3[192], thus further indicating its validity.

3.3.1.4 Multilayer Order of Desorption

In order to calculate the order for multilayer desorption, the 20-100 L_m spectra were analysed over the same temperature range used for the order of monolayer desorption. Figure 3.8 is a plot of ln(I(T)) against $\ln(\theta_{rel})$ at a fixed temperature of 138 K. For comparison with the data points used to calculate the multilayer order of desorption, Figure 3.8 also includes the data points used to calculate the monolayer order of desorption, shown in Figure 3.6. Table 3.4 lists the calculated order for each temperature. The average order for multilayer desorption is 0.10 ± 0.03, with the error calculated in the same manner as for the monolayer order of desorption.

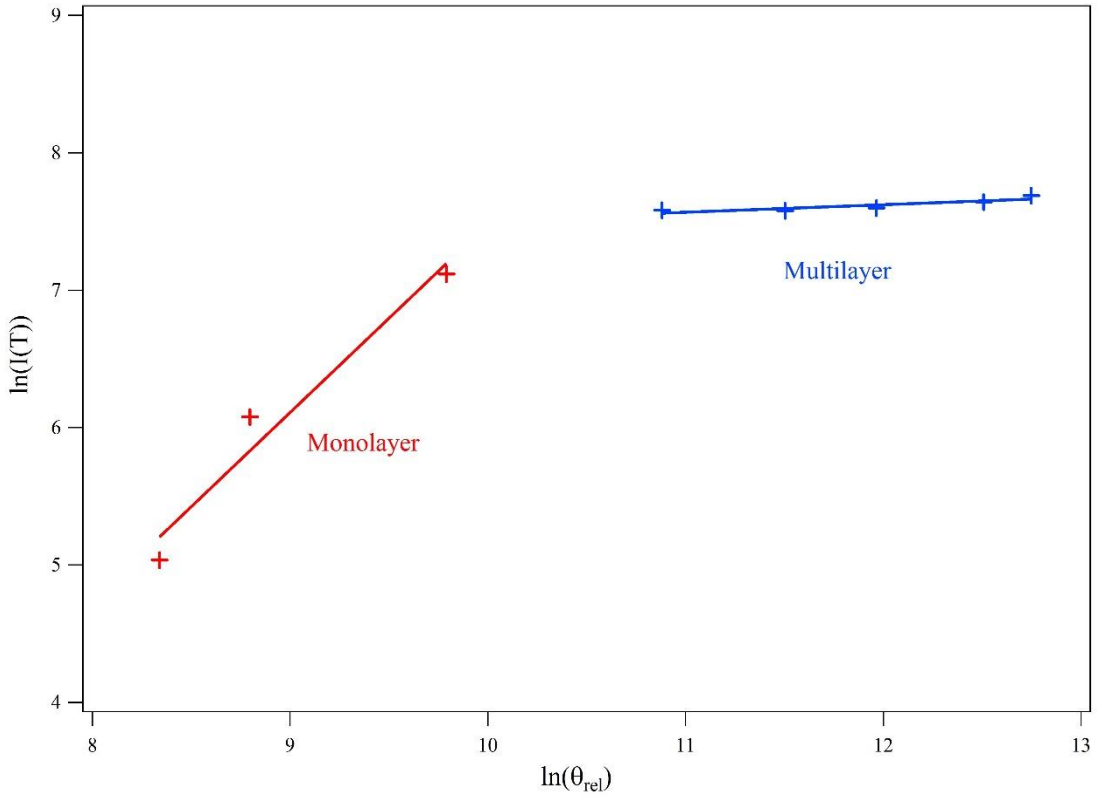

Figure 3.8 – Plot of ln(I(T)) against $\ln(\theta_{rel})$ at a fixed temperature of 138 K. The lines shown are the linear fits whose gradients correspond to the order of desorption for monolayer (red) and multilayer (blue) desorption.

The calculated value for the multilayer order of desorption is quite close to the expected value of n = 0. As mentioned previously, fractional orders are attributed to hydrogen bonding between the adsorbates. By comparing the effect of including 20 L_m in the order calculations it was possible to vindicate its inclusion in the multilayer calculations. When removed from the multilayer calculations there was minimal change in the order (the average change was ~0.06), however, upon inclusion of 20 L_m in the monolayer

calculations the order changed by a significant amount (the average change was ~0.37). This indicates that 20 L_m does indeed illustrate multilayer desorption characteristics, and not monolayer.

Table 3.4 – Orders calculated for multilayer desorption of 20-100 L_m of formic acid adsorbed on HOPG.

Temperature / K	Order of Desorption
133.0	0.03
133.5	0.06
134.0	0.15
134.5	0.15
135.0	0.19
135.5	0.13
136.0	0.17
136.5	0.11
137.0	0.06
137.5	0.04
138.0	0.05
138.5	0.05
139.0	0.07
139.5	0.02
140.0	0.03

3.3.1.5 Multilayer Energy of Desorption

The multilayer energy of desorption was calculated from the 20-100 L_m TPD spectra in Figure 3.4. The range used for each spectrum does not pass the shoulder and so the calculated value corresponds to desorption of pre-crystalline formic acid. Figure 3.9

shows the plot of ln(I(T))-nln(θ_{rel}) against 1/T corresponding to the TPD spectrum that was recorded for 50 L_m of formic acid deposited onto HOPG. The error bars were calculated in the same way as those shown in Figure 3.7. The average energy of desorption for multilayer formic acid on HOPG, using n = 0.10, is 37.1 ± 1.4 kJ mol^{-1}. The error quoted with the average is twice each individual error propagated through. Propagating through two times each standard deviation, rather than one, offers a greater confidence interval. The error quoted with the multilayer value is noticeably smaller than that quoted with the monolayer value since the multilayer energy is obtained using a larger number of data points.

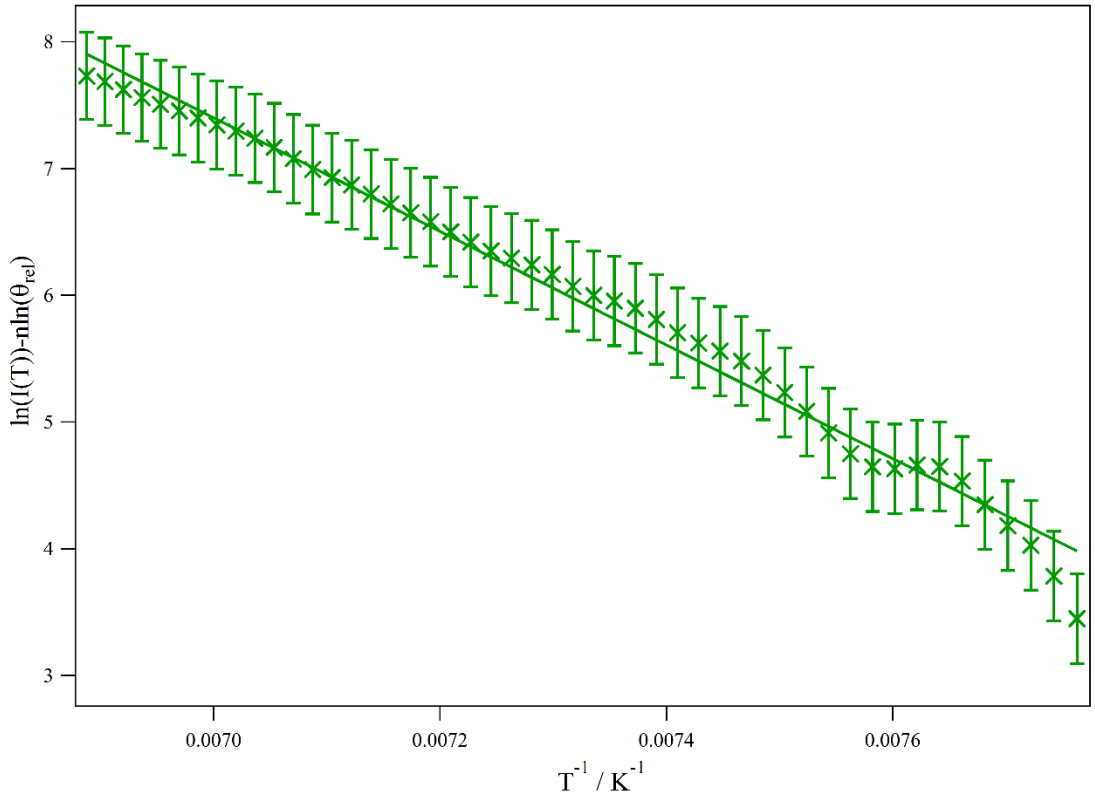

Figure 3.9 – Plot of ln(I(T))-nln(θ_{rel}) against 1/T (using n = 0.10) from the TPD spectrum corresponding to 50 L_m of formic acid on HOPG. The linear fit is used to calculate the gradient.

Considering that multilayer formic acid desorbs at higher temperatures than monolayer formic acid, a multilayer energy of desorption of 37.1 ± 1.4 kJ mol^{-1} is much lower than expected. Furthermore, by comparison with other species that have similar structures and desorption ranges, it would seem that 37.1 kJ mol^{-1} is too low.[104,121–123,141,191,193] As such, it would appear that leading edge analysis of formic acid multilayer desorption from HOPG has failed. This may be due to the ice initially being amorphous and composed of dimers and then the subsequent phase change to a crystalline ice. Consequently, no pre-

exponential can be derived using this method and an alternative method must be employed to obtain desorption kinetics.

3.3.1.6 Modelling the TPD Spectra

An alternative method to obtain desorption kinetics is using simulations from a stochastic integration package (Chemical Kinetics Simulator (CKS) Version 1.0, IBM) to fit the experimental data.[104,153,194] The basic premise of the model is that TPD spectra are a function of two processes, each with its own rate: desorption of the ice into the gas phase (Equation 3.1) and the pumping away of the gas (Equation 3.2). It is detection by the mass spectrometer of adsorbates that have desorbed into the gas phase (N_{gas}), as a function of temperature, that gives rise to a TPD spectrum.

$$N_{ice} \rightarrow N_{gas} \qquad 3.1$$

$$N_{gas} \rightarrow N_{pumped} \qquad 3.2$$

The rate of desorption (Equation 3.1) is given by the Polanyi-Wigner equation and the pumping rate (Equation 3.2) was previously estimated for the UHV chamber used in this work.[122] Initial surface coverages were calculated using the values obtained from the rate of impingement calculations used in obtaining the pre-exponential factors. The fits were evaluated by visually comparing the simulated data with the experimental spectra. Initially, the method was tested with monolayer desorption values to ensure its validity.

Figure 3.10 shows a comparison between the experimental and simulated desorption of 10 L_m of formic acid from HOPG. The simulated spectrum was calculated using the following kinetic values: E_{des} = 49.5 kJ mol^{-1}, n = 1.35, ν_n = 7.6 × 10^{10} (molecules m^{-2})$^{-0.35}$ s^{-1}, $\theta_{initial}$ = 2.24 × 10^{19} molecules m^{-2} and a pumping rate of 0.25 s^{-1}. A good fit is clearly achieved and all kinetic values used fall well within the error intervals calculated in the previous section using the experimental data. This indicates that the kinetic values obtained for monolayer desorption are sensible and that the pumping rate used is appropriate. The simulated data appears to deviate from the empirical data above 150 K. This is likely due to a combination of two factors: pumping of desorbed formic acid lingering in the chamber and desorption of formic acid from surfaces other than the sample. Both effects are observed for other species studied using the experimental set-up used here.

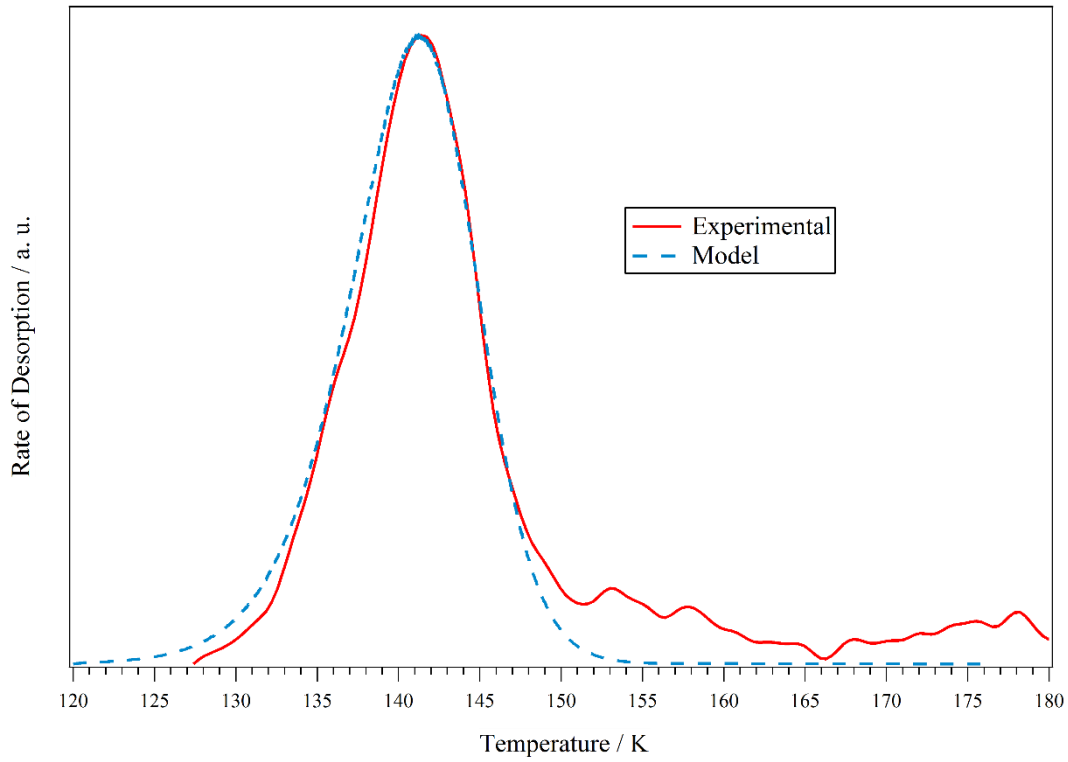

Figure 3.10 – Comparison of the experimental and simulated spectra corresponding to desorption of 10 L_m of formic acid from HOPG.

Although the TPD profile for multilayer desorption is clearly more complex than the profile for monolayer desorption, multilayer desorption was simulated using the two-step process used above. The purpose of this was to demonstrate that it was possible to obtain leading edges and peak temperatures, comparable to those observed experimentally, using kinetics that were in agreement with those calculated for monolayer formic acid and multilayers of other species. To accurately model the phase change observed in multilayer TPD spectra, a number of additional steps would be required: desorption of pre-crystalline formic acid, conversion from amorphous to crystalline formic acid, and desorption of crystallised formic acid. The conversion step would require two currently unknown parameters, the activation energy and rate of crystallisation. These cannot be measured in the experimental set-up used here, nor have they been calculated elsewhere. Whilst the progress of the phase change is discussed in the following sections of this chapter, these experiments utilise step-wise annealing cycles, rather than linear heating ramps, and hence are not beneficial to modelling the conversion process in TPD experiments.

It was possible to fit the major peak in the 100 L_m multilayer spectrum using the following kinetic parameters: E_{des} = 50.5 kJ mol^{-1}, n = 0.10 and $\nu_n = 2.4 \times 10^{34}$ (molecules m^{-2})$^{0.9}$ s^{-1}, with a pumping rate of 0.25 s^{-1} and an initial surface coverage of 2.24×10^{20} molecules m^{-2}. The simulated 100 L_m TPD spectrum is shown in Figure 3.11 alongside the experimentally obtained 100 L_m spectrum. It can be seen that for the major peak, both the leading edge and peak temperature fit well. The pre-exponential used in the model is higher than the values reported for methanol, H_2S and water, however, it does agree well with values reported for multilayer desorption of ethanol[191,195] and acetic acid.[193]

The higher formic acid exposures shown in Figure 3.4, which have overlapping shared leading edges, were modelled in the same way as the 100 L_m TPD spectrum discussed above. The kinetic parameters used to simulate each spectrum are listed in Table 3.5. These were then averaged and used as an estimate of the multilayer desorption kinetics. Therefore, the estimated multilayer desorption kinetics for formic acid adsorbed on HOPG are: E_{des} = 50.8 ± 0.3 kJ mol^{-1}, n = 0.10 ± 0.1, ν_n = (3.0 ± 0.6) $\times 10^{34}$ (molecules m^{-2})$^{0.9}$ s^{-1}. All of the simulations used a pumping rate of 0.25 s^{-1} and an initial surface coverage scaled from that used in the 100 L_m simulation.

Both the energy of desorption and the pre-exponential factor compare well with values obtained for multilayer desorption of other hydrogen bonding molecules like ethanol[191,195] and acetic acid.[121,193] The values for multilayer desorption obtained using CKS and those for monolayer desorption calculated above now correlate well with the behaviour observed in experimental TPD spectra.

Table 3.5 – Kinetic parameters used to model the 50, 75 and 100 L_m spectra shown in Figure 3.4.

Formic Acid Dose / L_m	Energy of Desorption / kJ mol^{-1}	Order of Desorption	Pre-Exponential Factor / (molecules m^{-2})$^{1-n}$ s^{-1}
100	50.5	0.10	2.4×10^{34}
75	50.9	0.10	3.6×10^{34}
50	50.9	0.11	3.2×10^{34}
Average	50.8 ± 0.3	0.10 ± 0.1	$(3.0 \pm 0.6) \times 10^{34}$

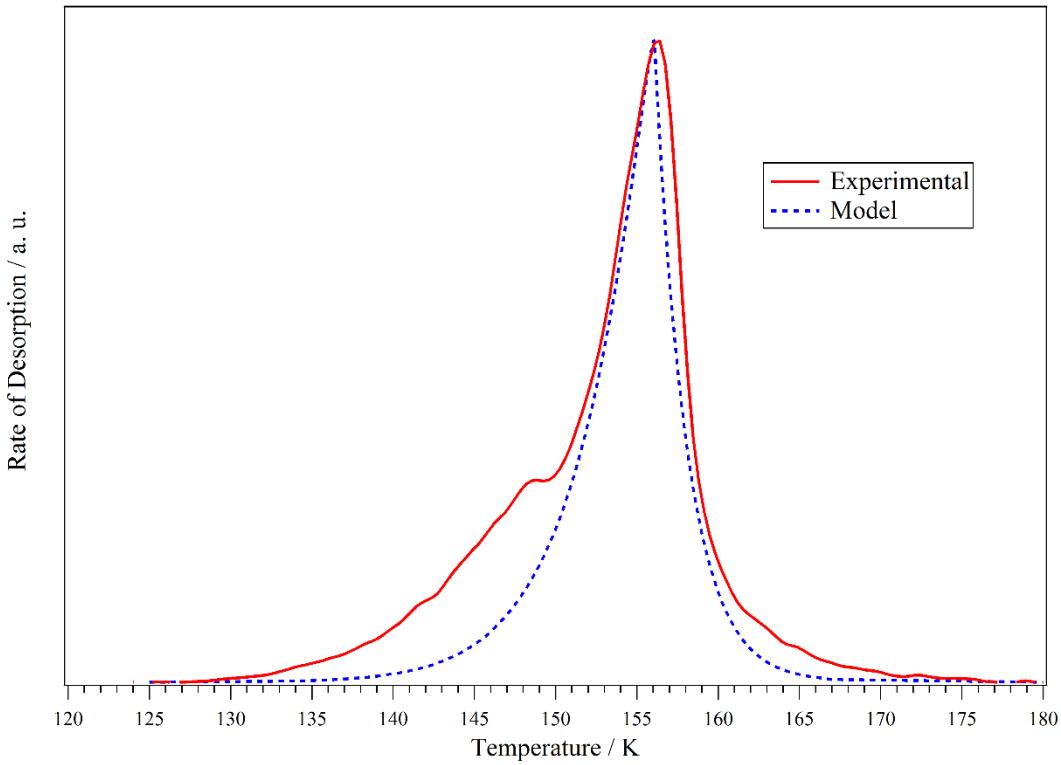

Figure 3.11 – Comparison of the experimental and simulated spectra corresponding to desorption of 100 L_m of formic acid from HOPG.

3.4 RAIRS of Formic Acid Adsorbed on HOPG

Infrared studies were also conducted for formic acid deposited on HOPG at ~20 K. The evolution of the ice with increasing temperature was studied to confirm the presence of a phase change that was apparent spectra as a low temperature shoulder in multilayer TPD. Further to confirming the presence of a phase change, by understanding the spectral evolution of pure ices with temperature it allows the interaction of formic acid and water (Chapter 4) to be better understood.

Figure 3.12 shows the RAIR spectrum recorded for 100 L_m of formic acid deposited onto HOPG at 26 K. Table 3.6 lists the key peaks and their assignment, by comparison with the literature, for ease of reference.

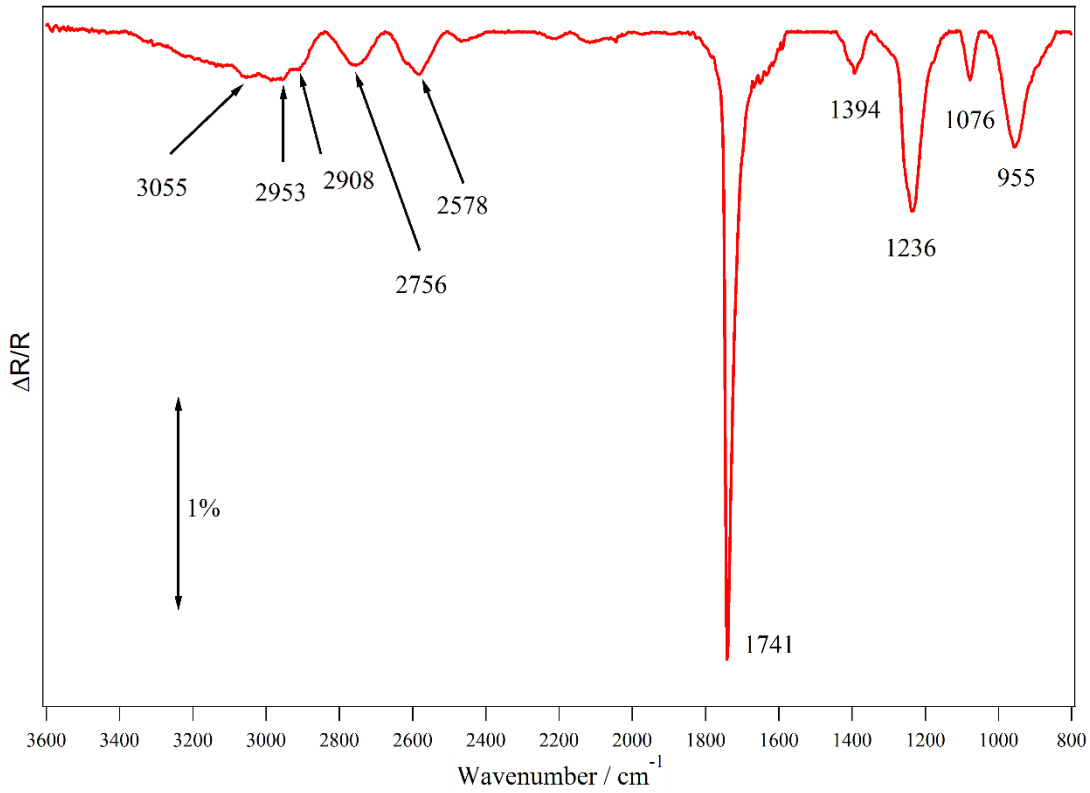

Figure 3.12 – RAIR spectrum of 100 L_m of formic acid deposited on HOPG at 26 K.

Upon inspection of Figure 3.12, the most striking feature is a strong and sharp absorption at 1741 cm^{-1}, corresponding to the C=O stretch (νC=O). There is a clear shoulder evident on the low wavenumber side of the C=O stretch at ~1625 cm^{-1}. The noise on this shoulder results from absorption by water vapour that is present in the infrared optics boxes outside the chamber, a consequence of an imperfect purge. Between the carbonyl stretch (νC=O) at 1741 cm^{-1} and 800 cm^{-1} there are four key features assigned: the C-H deformation (δC-H) at 1394 cm^{-1}, the C-O stretch (νC-O) at 1236 cm^{-1}, the C-H out-of-plane bend (πC-H) at 1076 cm^{-1} and the O-H out-of-plane bend (πO-H) at 955 cm^{-1}.

In the high wavenumber region of the spectrum there are four key assignments: two O-H stretches (νO-H) at 2578 and 2756 cm^{-1}, a combination band (νC=O + νC-O) at 2953 cm^{-1} and a C-H stretch (νC-H) at 3055 cm^{-1}. The peak at 2908 cm^{-1} is clear but is unable to be assigned using the literature or by combination of other bands evident in Figure 3.12. The fairly broad peak profiles and their assignments suggest that a non-crystalline ice structure consisting of dimeric units is present at 26 K.

Table 3.6 – Assignment of vibrational frequencies of 100 L_m of formic acid on HOPG at 26 K. For comparison, literature values for vapour phase monomers[171], vapour phase dimers[171] and dimers on polycrystalline gold[89] are included.

This Work (cm^{-1})	Vapour Phase		Dimers on Gold at 100 K (cm^{-1})[89]	Mode	Mode Description
	Monomers (cm^{-1})[171]	Dimers (cm^{-1})[171]			
3055	2943	2957	3050	νC-H	C-H Stretch
2953	-	-	2950	νC=O + νC-O	C=O + C-O Stretches Combination
2908	-	-	-	-	-
2756	-	-	2748	νO-H	O-H Stretch
2578	-	-	2577	νO-H	O-H Stretch
1741	1770	1754	1735	νC=O	C=O Stretch
1394	1387	1365	1390	δC-H	C-H Deformation/ C-H Bend (In-Plane)
-	1229	1450	-	-	O-H Deformation
1236	1105	1218	1228	νC-O	C-O Stretch
1076	1033	1050	1082	πC-H	C-H Bend (Out-of-Plane)
955	636	917	972	πO-H	O-H Bend (Out-of-Plane)

Vapour phase values for formic acid reported by Millikan *et al.*[171] are included in Table 3.6 as they are frequently referred to in studies of formic acid ices. Whilst the values reported by Millikan *et al.* do not correlate fully with the reported values for formic acid

on HOPG, the peaks listed from Figure 3.12 are in closer agreement with vapour phase dimers than with vapour phase monomers. Owing to the constraints that are applied to molecular vibrations in a solid, there would not be expected to be total agreement between vapour phase and solid phase values. There is, however, considerable agreement between the values reported here and those reported for formic acid dimers adsorbed on polycrystalline gold by Hellebust *et al.*.[89] This alongside the previously discussed TPD results suggests that formic acid deposited on HOPG at 26 K forms an amorphous ice consisting of dimer units. This conclusion is confirmed by Gantenberg *et al.*[175] who, by comparison of DFT calculations with Ar matrix experiments, stated that the presence of a complex band structure between 2500 and 3100 cm^{-1} and a low wavenumber shoulder on the υC=O feature, as seen in Figure 3.12, indicated the presence of formic acid dimers as opposed to monomers.

RAIR spectra collected after annealing 100 L_m of formic acid to a range of temperatures are shown in Figures 3.13 (2200-800 cm^{-1} region) and 3.14 (3600-2400 cm^{-1} region). The 160 K spectrum is included to show that by this temperature, the ice has fully desorbed. Desorption between 150 and 160 K, as indicated in Figures 3.13 and 3.14, is consistent with the 100 L_m TPD spectrum shown in Figure 3.4. The broad feature between 3200 and 3300 cm^{-1} (Figure 3.14) is attributed to water freezing out on the detector window. This is confirmed by it remaining after annealing the surface to 220 K, a high enough temperature for both water and formic acid to desorb from HOPG. In general, upon heating, the RAIR spectra show a number of changes, most notably splitting and shifting of a number of spectral features. Spectral splits differ from shifts by the appearance of new features from the original, whereas shifting does not alter the number of features. The most obvious changes are in the 800-2200 cm^{-1} region (as shown in Figure 3.13). Between 26 and 130 K the πO-H band (955 cm^{-1}) sharpens and is blue shifted to 986 cm^{-1}, whilst the υC-O band (1236 cm^{-1}) profile shape alters somewhat. The πC-H (1076 cm^{-1}) is also blue shifted by 8 cm^{-1} to 1084 cm^{-1}. Over this temperature range there do not appear to be any substantial changes between 2400 and 3600 cm^{-1} (Figure 3.14).

At 133 K, there are multiple distinct changes in peak shapes and positions in the 800-2200 cm^{-1} region (Figure 3.13), indicating significant structural changes. The πO-H and πC-H peaks sharpen but do not appear to shift further. The υC-O band and the δC-H band do not shift, but both split into sharp doublets. The 1741 cm^{-1} carbonyl stretch (νC=O)

decreases in intensity as the low wavenumber shoulder begins to develop into a distinct peak. In addition to decreasing in intensity, the νC=O band red shifts by ~4 cm^{-1}.

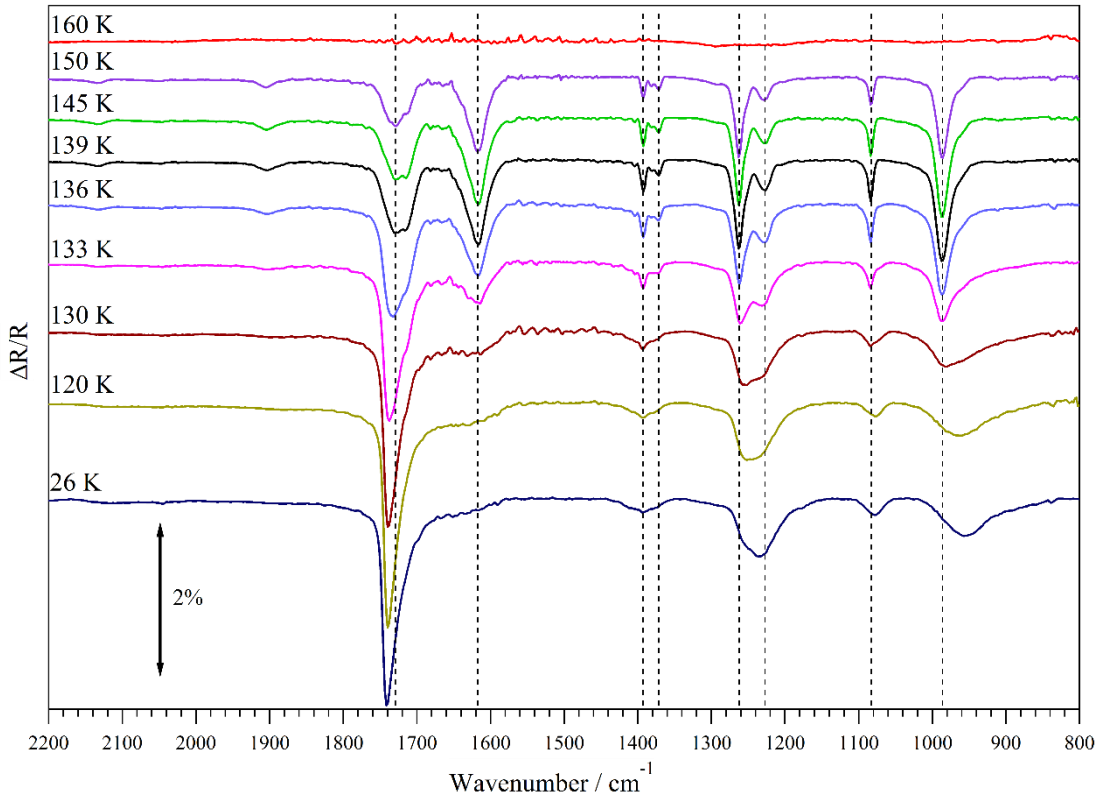

Figure 3.13 – 2200-800 cm^{-1} region of RAIR spectra collected after annealing 100 L_m of formic acid dosed on HOPG at 26 K to the indicated temperatures. Dashed lines are to guide the eye.

After annealing to 133 K, the most prominent changes in the 2400 and 3600 cm^{-1} region (Figure 3.14) are the sharpening of the features between 2850 and 3100 cm^{-1}, and the growth of a low wavenumber shoulder, at 2546 cm^{-1}, on the νO-H (2578 cm^{-1}) peak. There is also a slight growth in the intensity of the νO-H peak.

From 136 to 150 K there appears to be minimal changes in the spectra below 1400 cm^{-1}, other than the appearance of a small central shoulder in the δC-H feature (1394 cm^{-1}). This is in contrast to the υC=O feature (~1731 cm^{-1}) that exhibits further red shifting, an apparent passing of intensity from the high to the low wavenumber feature at 1616 cm^{-1} and the appearance of a shoulder at 1714 cm^{-1}. The key differences between the 136-150 K spectra and the 133 K spectrum in the high wavenumber region (Figure 3.14) are the continued sharpening of the 2850-3100 cm^{-1} features, the flattening of the νO-H features between 2700 and 2800 cm^{-1} and the growth of the shoulder (2546 cm^{-1}) on the νO-H peak (2578 cm^{-1}), which ultimately dominates the feature by 139 K. The spectral

evolution shown in Figure 3.13 is also observed, at the same temperatures, when 50 L_m of formic acid is deposited on HOPG at ~22 K. This suggests that, over this range of coverage, there is no dependence of the process responsible for the spectral evolution on the quantity of formic acid present.

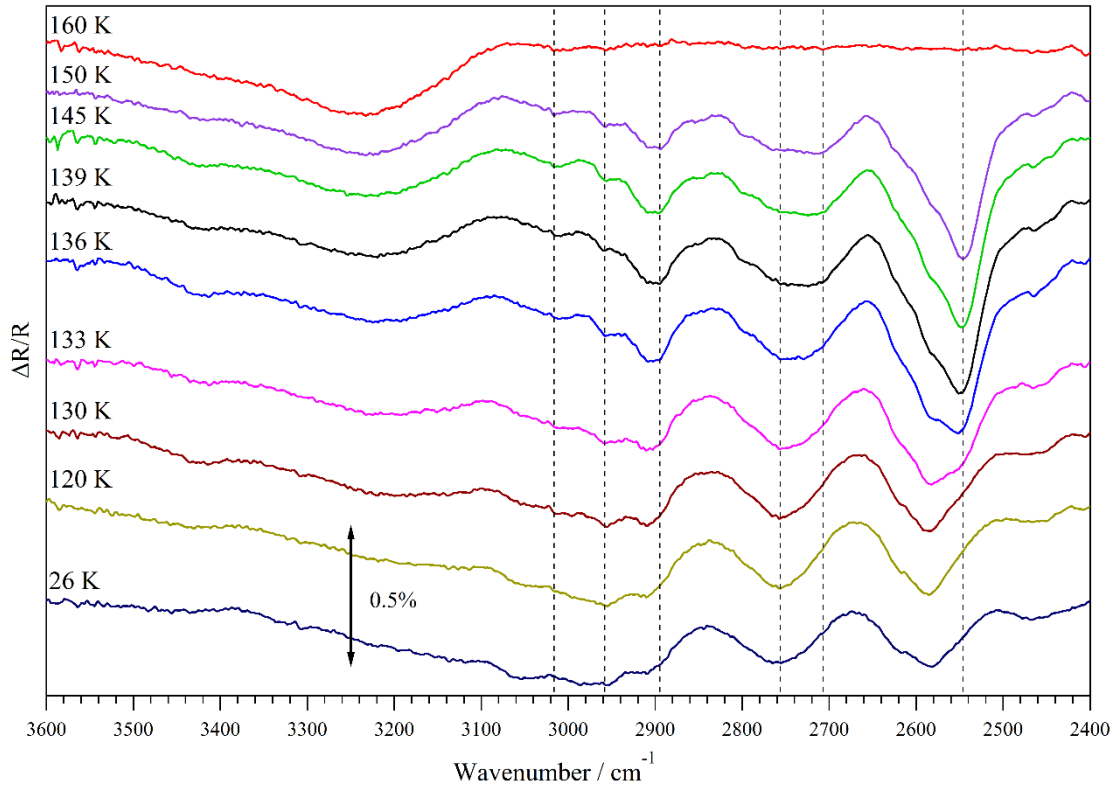

Figure 3.14 – 3600-2400 cm^{-1} region of RAIR spectra collected after annealing 100 L_m of formic acid dosed on HOPG at 26 K to the indicated temperatures. Dashed lines are to guide the eye.

The evolution of the peaks at 133 K, and the minimal changes thereafter, support the premise that at 133 K the ice has undergone a major structural change. This is consistent with the TPD experiments described earlier. However, it should be noted that direct comparison of temperatures between RAIRS and TPD is not possible owing to the differing methods of heating (annealing and cooling versus constant linear heating ramp). As discussed in the introduction, two distinct crystalline structures of formic acid exist: α-crystalline and β-crystalline (Figure 3.1). Both are polymeric chains linked by hydrogen bonds. Table 3.7 lists the peak positions of the key features observed in the 150 K spectrum (shown in Figures 3.12 and 3.13) and compares them to literature values for the α- and β-structures. It can be seen that where assignments are possible, they are largely consistent with the α-structure. As such, it is concluded that above 133 K formic acid adopts the α-crystalline structure.

Table 3.7 – Table listing the key features observed for 100 L_m of formic acid deposited on HOPG at 26 K and subsequently annealed to 150 K. For comparison, literature values for α- and β-crystalline formic acid are included.

This Work	α-crystalline Peak Values (cm^{-1})[171,174]	β-crystalline Peak Values (cm^{-1})[173]	Mode	Mode Description
2958	2958	2960	νC-H	C-H Stretch
2895	2892	2900	νO-H	O-H Stretch
2756	-	-	-	-
2707	2712	2700	νO-H	O-H Stretch
2582	-	-	-	-
2546	2532	2540	νO-H	O-H Stretch
1730	1720	-	νC=O	C=O Stretch
1714	1703	-		
1616	1609	1620		
1392	1391	-	δC-H	C-H Deformation
1381	1381	1378		
1371	1370	1371		
1263	1255	1248	νC-O	C-O Stretch
1227	1224	1210		
1084	1083	1078	πC-H	C-H Bend (Out-of-Plane)
986	974	947	πO-H	O-H Bend (Out-of-Plane)

Since it has been established that at higher temperatures the formic acid ice adopts the α-crystalline structure, the origin of the spectral splitting can be explained. By considering the chain unit cell, the fundamental modes can be split into in-phase and out-of-phase motions with regards to adjacent monomer units. Figures 3.15and 3.16 depict the extreme

structures that can be considered as the limits toward which the vibration tends. Since hydrogen can only form a single bond, the unit O–H^{-}–O in Figure 3.16 should be considered as the result of the resonance between –O^{-} H–O– and –O–H O^{-}–. It was deduced that for in-plane motions, both the in- and out-of-phase components are IR active, whilst for out-of-plane motions, only one component will be IR active.[75,171,196] This is entirely consistent with the results presented here, as the only features in the 800-2000 cm^{-1} region to not show splitting are the πC-H (1076 cm^{-1}) and πO-H (955 cm^{-1}), both of which are out-of-plane bends. Furthermore, by considering the extreme structures of the vibrations that occur for in-phase and out-of-phase motions, it was found that the in-phase motions occur at lower frequencies than the out-of-phase motions.[75,171,196]

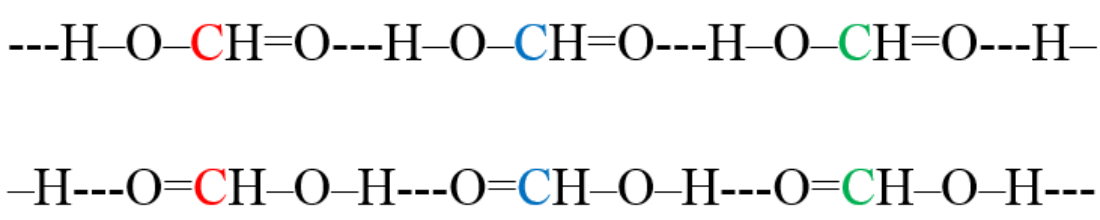

Figure 3.15 – Extreme structures showing the limit of C=O vibrations that are in-phase.

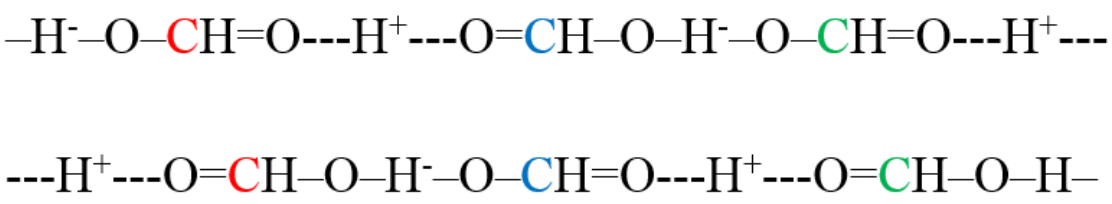

Figure 3.16 – Extreme structures showing the limit of C=O vibrations that are out-of-phase.

In the discussion above, the splitting of the νC=O and the δC-H was attributed to the energetically distinct in-phase and out-of-phase motions of adjacent monomers, however, in Table 3.7 three components have been listed (1730, 1714 and 1616 cm^{-1}, and 1392, 1281 and 1371 $^{-1}$) and assigned for these two modes. The origin of the clear shoulder on the carbonyl stretch is uncertain. It is unlikely that it is due to dimeric species remaining because by 139 K, the spectral evolution of the other key features below 2000 cm^{-1} has stopped and therefore it would appear that the phase change to the α-crystalline structure has been completed.

There is some discussion in the literature as to the nature of the peaks around 1380 cm^{-1}. In the work presented here, above 133 K the feature centred at 1380 cm^{-1} is composed of the three overlapping peaks. To display this clearly and reinforce the assignment of three

components, the overall feature was fit with three Gaussian curves. The resulting profile is compared with the 145 K experimental spectrum from Figure 3.17.

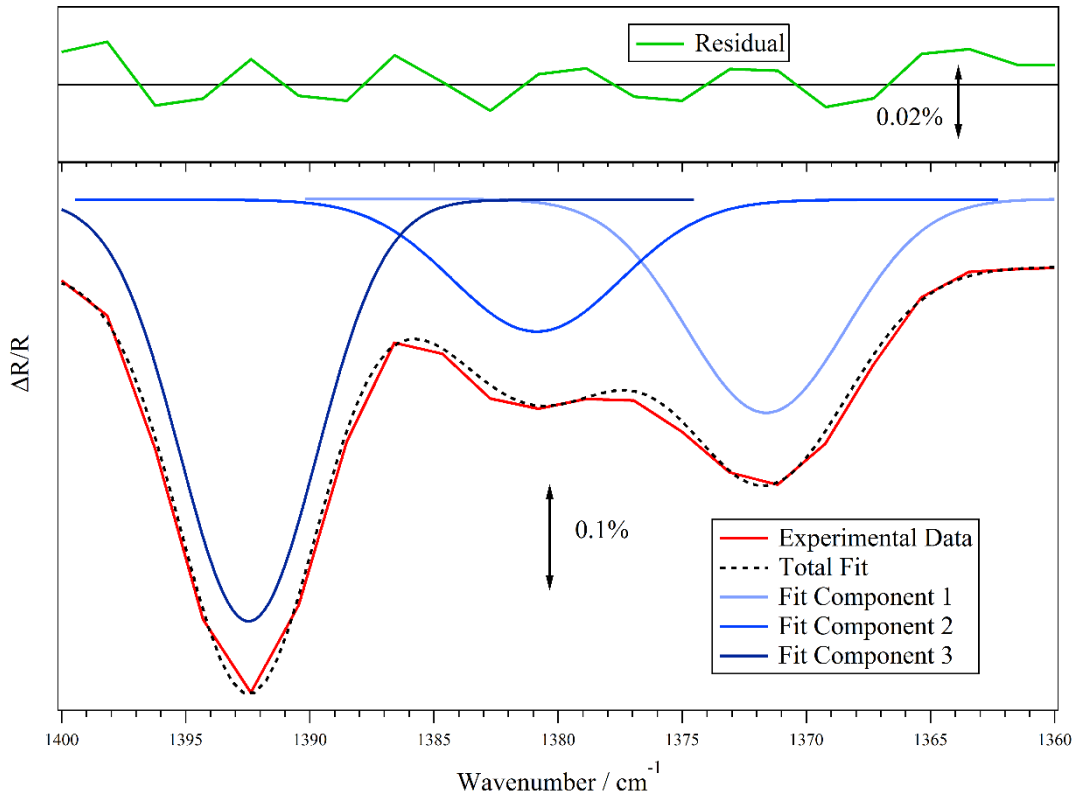

Figure 3.17 – Lower panel: Comparison of the 1360-1400 cm^{-1} region (corresponding to the C-H deformation mode, δC-H) of the experimental spectrum collected after annealing 100 L_m of formic acid to 145 K (red) and a fit (dashed) produced from three Gaussian curves (blue traces). Upper panel: Residual of the fit shown in the lower panel. The horizontal line is the zero-line.

From Figure 3.17, it is clear that the δC-H feature is comprised of three separate peaks. Millikan and Pitzer[171] identified two medium strength peaks (1391 and 1370 cm^{-1}) and a weaker central peak (1381 cm^{-1}) in crystalline ice and attributed them not to in-phase or out-of-phase motions between adjacent units, but instead to three-dimensional crystal splitting. Hellebust *et al.*[89] also observed a weak central peak in the δC-H feature and, in agreement with Millikan and Pitzer, assigned it to three-dimensional crystal splitting. In contrast to these studies, Raval and Munro[196] do not observe the central feature and Cyriac *et al.*[126] and Watanabe *et al.*[137] do not address the peaks around 1380 cm^{-1} in their discussions. Watanabe *et al.* do, however, address in-phase and out-of-phase splitting of the νC=O and νC-O modes only. Considering the literature, and the consistent appearance of the central peak in the work presented here, the splitting of the δC-H into a triplet, rather than a doublet, is attributed to three-dimensional crystal splitting. However, it

should be noted that the observed splitting in the C=O and C-O stretches is, in line with the literature, still attributed to the in-phase and out-of-phase motions of adjacent units. Linking the splitting observed in the νC=O and νC-O with the coupling of adjacent unit vibrations within a chain is consistent with these groups forming the backbone of the polymer chains that comprise α-crystalline formic acid.

In addition to visual inspection of RAIR spectra, it is possible to obtain further insight into the evolution of the ice by using difference spectra. Spectra are subtracted from an initial spectrum to locate subtle changes in the spectra as a function of some variable, in this case temperature. Each of the annealing spectra were subtracted from the 26 K spectrum and the results of the first five temperatures are shown in Figure 3.18. If a peak has grown in the RAIR spectrum, the corresponding difference spectrum will show a positive peak in the same position. A negative feature in the difference spectrum represents decreasing peak intensity.

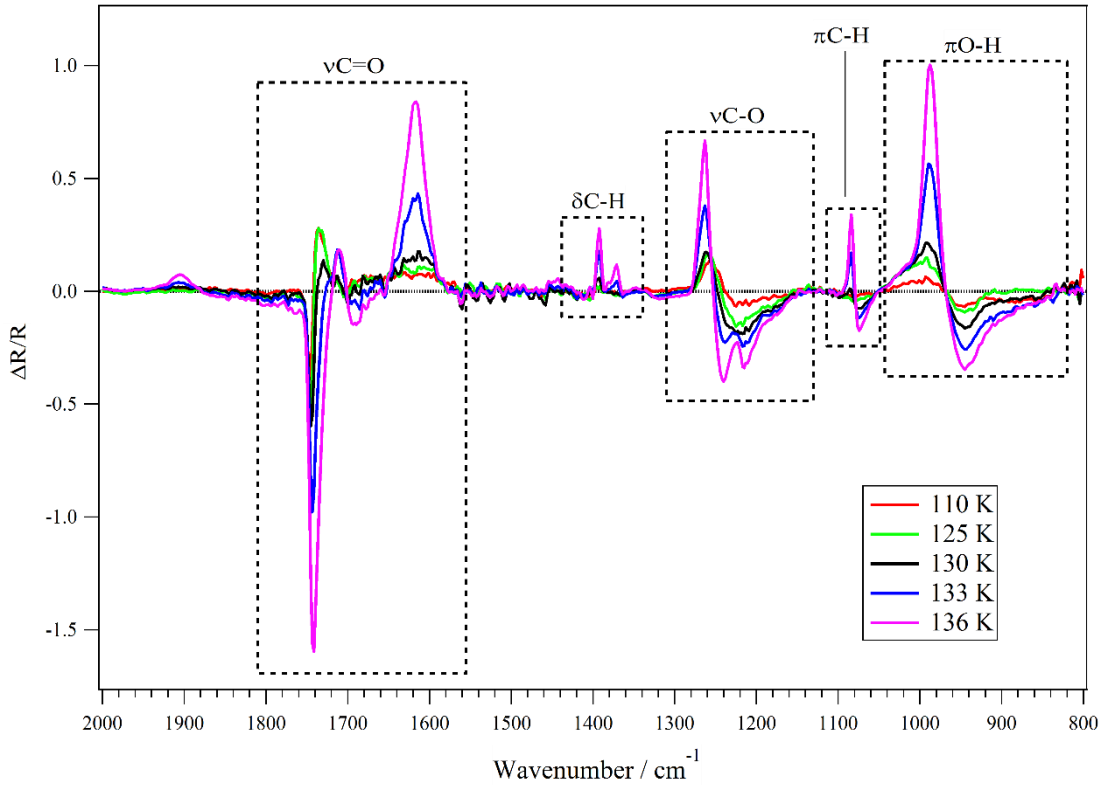

Figure 3.18 – Difference spectra of the indicated annealing spectra subtracted from the 26 K spectrum of 100 L_m formic acid deposited on HOPG at 26 K.

It can be seen from Figure 3.18 that at 110 K there are clear changes in several of the RAIRS features. For example, the negative peak at ~943 cm^{-1} and the adjacent positive

peak at ~987 cm^{-1} indicate that the πO-H band has already begun to shift by this temperature. This is also seen in the νC=O band at 1741 cm^{-1} and the νC-O band at ~1243 cm^{-1}. Furthermore, the in-phase carbonyl stretch has also already begun to grow at 110 K. Between 110 and 130 K these changes become more evident whilst the δC-H and πC-H bands also show evolution. Splitting of the δC-H and νC-O bands becomes obvious at 133 K and the in-phase carbonyl stretch feature grows significantly. The 2400-3600 cm^{-1} region (not shown) also shows that even at 110 K, the νO-H modes are already growing in intensity. By examining the difference spectra, it can be concluded that whilst α-crystalline formic acid becomes dominant at 133 K, the ice is already mobile at temperatures as low as 110 K.

Analysis of the difference spectra corresponding to 139 and 145 K (not shown) indicate that most spectral changes have ceased by 139 K. This suggests that the structural evolution of the ice has largely finished. Between 145 and 150 K some of the new or shifted peaks begin to decrease in intensity, signalling desorption of the crystalline formic acid; this agrees with the TPD experiments discussed earlier.

Since the splitting of the νC-O and νC=O modes into two distinct components is a clear indication of crystallisation, the integrated area of each component in the two modes was calculated as a function of temperature. The top half of Figure 3.19 illustrates how the integrated area of the in-phase and out-of-phase components varies with annealing temperature. At first glance the behaviour of the components appears to be very similar, except for the fact that initially, the out-of-phase component is dominant in the νC=O mode, whereas it is the in-phase motion that is dominant in the νC-O mode. However, both show that below 130 K there are subtle changes to the areas of each of the components, in agreement with the difference spectra. Between 130 and 139 K there are rapid changes in the size of the components in both modes, but interestingly, in the υC-O mode the change is so extreme that the out-of-phase motion becomes dominant over the in-phase. This reverse of dominance is also seen in the νC=O mode but to a much lesser extent. There then appears to be a slow decrease of both components in both modes above 140 K, consistent with the difference spectra. Finally, between 150 and 160 K total desorption occurs. The lower half of Figure 3.19 shows how the area of each component relative to the total area of the mode depends on the annealing temperature. It is clear that in both modes, the dominant component constitutes ~95% of the overall mode at 110 K.

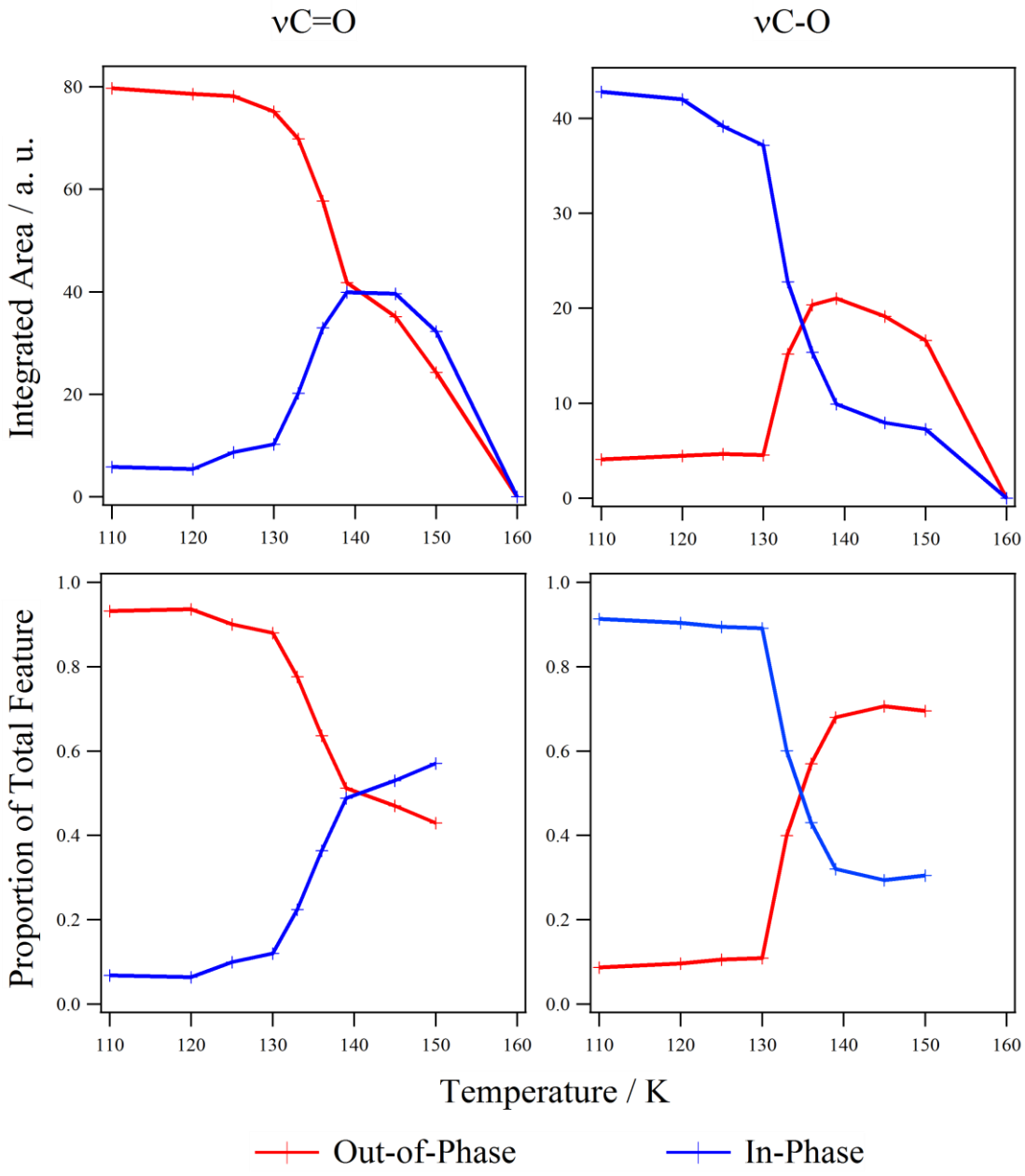

Figure 3.19 – Figure showing the changes in the C=O and C-O stretches as a function of annealing temperature. The left-hand side corresponds to the C=O stretch mode (centred around 1700 cm^{-1}) and the right-hand side corresponds to the C-O stretch mode (centred around 1200 cm^{-1}). Upper graphs show the integrated area of the out-of-phase (red) and in-phase (blue) components of each mode. The lower graphs show the relative contribution of each component to the overall feature.

Between 139 and 150 K the relative amount of each component in the νC-O mode remains fairly constant, suggesting that the decreases seen in the upper graphs is indeed due to the desorption of the ice and not any further structural change. The similarity in the general trend of behaviour between the two modes indicates that both are a result of the same process, crystallisation of the ice. However, it is not fully understood why the dominant

component in the υC=O mode is opposite to that in the υC-O mode. In addition to demonstrating that the structural changes have largely ceased above 139 K, the lower panels show that analysis using just the absolute areas can be misleading.

Analysis of RAIRS experimental data indicates that when formic acid is deposited on HOPG at 26 K it forms an amorphous ice consisting of dimeric units. Upon heating, formic acid undergoes structural changes that ultimately lead to the ice adopting the α-crystalline structure. Although 133 K marks the temperature at which a significant proportion of the ice is crystalline, difference spectra and analysis of band splitting suggests that the ice is mobile at temperatures as low as 110 K. A crystallisation temperature of ~133 K is within the broad range of ~100-180 K reported in the literature[75,89,126,137,181] and only 2 K less than the reported value of 135 K by Bisschop *et al.*.[75] Cyriac and Pradeep[126] stated that at 98 K, a large percentage of the ice was crystalline but not until 135 K was it fully crystalline. If the heating mechanism had been the same as in the work presented here it is possible that there would be better agreement because formic acid on HOPG, CsI or KBr is likely to be physisorbed and thus surface effects should be minimal. Hellebust *et al.*[89] partly attributed their high crystallisation temperatures of 160-180 K to the thickness of the ice; however, when 50 L_m of formic acid was deposited on HOPG at 22 K (not shown) splitting due to crystallisation becomes evident at 133 K, just as in the 100 L_m spectra shown in Figure 3.13. It is unclear if the transition from dimers to the α-crystalline form is direct or via the β-crystalline form, but by tracing the πO-H (out-of-plane bending) mode it appears that β-crystalline formic acid is not formed. Between 139 and 145 K it appears that the phase change is complete and slow desorption of the crystalline ice commences. At temperatures above 150 K desorption is rapid and by 160 K total desorption has occurred, in agreement with TPD.

3.5 Summary

TPD investigations of formic acid adsorbed on HOPG at ~20 K indicate that at low coverages (-10 L_m) monolayers form and at exposures of 20 L_m and above multilayers form. The high exposure TPD spectra show the evolution of a low-temperature shoulder attributed to an amorphous to crystalline phase change. As formic acid is admitted to the chamber as dimers and then physisorbs on the HOPG surface, it is expected that the amorphous phase consists of dimeric units.

The kinetics of desorption for monolayer formic acid on HOPG were calculated using leading edge analysis. The values calculated were n = 1.37 ± 0.05, E_{des} = 48.9 ± 5.1 kJ mol^{-1} and $\nu_n = 4.7 \times 10^{11\pm2.3}$ (molecules $m^{-2})^{-0.37}$ s^{-1}. These values are reasonable when compared to values for other physisorbed molecules in the literature. However, leading edge analysis appeared to break down when dealing with multilayer desorption, possibly due to the ice initially being amorphous and composed of dimers and then the subsequent phase change to a crystalline ice. Simulation of TPD spectra using a stochastic integration package showed that, using physically appropriate values, the major desorption feature could be fitted. The average kinetic parameters used were: E_{des} = 50.8 ± 0.3 kJ mol^{-1}, n = 0.10 ± 0.1, $\nu_n = (3.0 \pm 0.6) \times 10^{34}$ (molecules $m^{-2})^{0.9}$ s^{-1}. Whilst it is highly unlikely that formic acid will exist in pure ices in the ISM, the calculated kinetics presented here are a starting point to accurately model the desorption of formic acid from astronomically relevant substrates.

Using RAIRS it was possible to confirm that at base temperature (26 K) formic acid ice is amorphous and consists of dimers. Upon heating to ~133 K, it undergoes a phase change to the α-crystalline structure, which is completed between 139 and 145 K. It was not possible to conclusively deduce whether the change was direct, or whether it proceeded via the β-crystalline structure. However, by tracing the πO-H (out-of-plane bending) it appears that the β-crystalline structure is not formed. The temperature range obtained for the phase transition to the α-crystalline structure agrees with the literature.

4 Interactions Between Formic Acid and Water

4.1 Introduction

Formic acid has been detected in the interstellar medium (ISM)[22] and is believed to play an active role in a number of different reaction pathways that ultimately lead to the formation of complex organic species.[45,65,75,76,127] It is proposed that formic acid is formed by one of two key routes. The first route involves energetic processing of water and carbon monoxide.[65] The second route involves CO and the OH radical, with one of the competing products being water.[197] In light of the proposed routes to formic acid production and the fact that water is the most abundant species in interstellar ices,[99,154] it is likely that formic acid will exist in an aqueous environment in the ISM.[75,198] Therefore, an understanding of the interaction between formic acid and water is needed to fully appreciate the chemistry of interstellar ices.

Formic acid can hydrogen bond via two different groups, the O-H group and the C=O group.[163,165] Having two possible bonding sites on formic acid allows for a variety of geometries when it interacts with water. For example, it can use both sites to bind to a single water molecule, in a pincer like manner, or it can bind to two different water molecules. Because of the multiple possible geometries (see Figure 4.1), the exact nature of the formic acid-water interaction is not trivial and is of interest to fields such as atmospheric chemistry[89,165,182,199,200] and fuel cells[163,187], in addition to the astrochemical interest detailed here. The geometries shown in Figure 4.1 correspond to energy minima on the potential energy surface for 1:1 and 1:2 complexes calculated by George and Sander.[201]

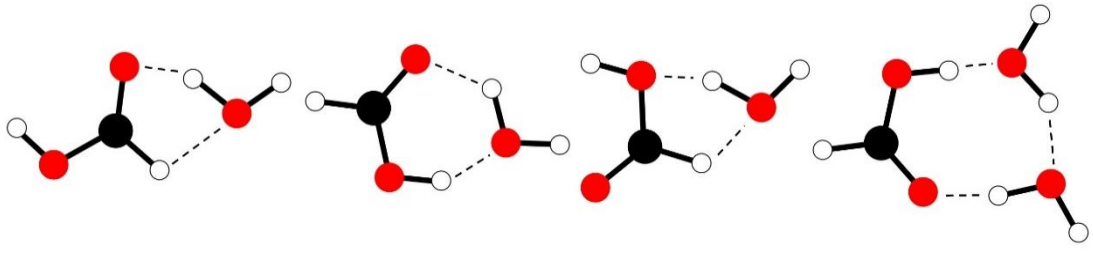

Figure 4.1 – The possible formic acid-water hydrogen bonding geometries. Solid red circles are oxygen, white circles are hydrogen and black circles are carbon.

In Chapter 3, formic acid was shown to undergo an irreversible phase change from an amorphous ice consisting of dimers to a crystalline phase consisting of polymeric chains.

Desorption of formic acid from HOPG commenced between 130 and 135 K, with a peak temperature of 141 K. A desorption peak temperature of ≥141 K places formic acid desorption well within the temperature region of the amorphous solid water (ASW) to crystalline ice (CI) phase change (which occurs between ~140 and ~150 K), as well as the desorption of water pre- and post-phase change. This further adds to the importance of understanding the interaction between the two species.

Previous investigations into the interaction between formic acid and water focused on the mobility of formic acid on or in a water ice, and whether formic acid is deprotonated to form the formate ion ($HCOO^-$). The influence of formic acid on the crystallisation of water, and vice versa, also featured in several the key investigations.[38,75,126,182,183,186,202,203] A variety of experimental and computational methods have been used to study the formic acid-water interaction, for example, time of flight secondary ion mass spectrometry (TOF-SIMS).[202,203] Whilst not always directly comparable to the techniques used in this work – temperature programmed desorption (TPD) and reflection absorption infrared spectroscopy (RAIRS) – these studies are still very useful to the present work.

TOF-SIMS was used by Souda to investigate the way in which formic acid behaves when adsorbed on a layer of D_2O at 15 K.[202,203] It was reported that above 50 K the adsorbed formic acid becomes mobile and forms a double hydrogen bond to the surface. The mobility of the formic acid continued until 150 K, whereby the acid layer became fully hydrated. Souda reached this conclusion by observing a decrease in the yield of $H^+(HCOOH)_n$ ions and an increase in the HD_2O^+ ions, which they attributed to formic acid molecules hydrogen bonding to the D_2O molecules. In the later publication by Souda,[203] it was reported that formic acid on the surface remains there because it is difficult for the water to incorporate the hydrophobic C-H group of formic acid into the bulk water ice. Subsequently, the acid acts as a surfactant, reducing the surface tension of the D_2O layer and quenching the bulk morphological change that would occur above 165 K in D_2O. This ultimately leads to formation of droplets of liquid-like water. Souda reports that there is no evidence for the irreversible ASW to CI phase transition and that when polar adsorbates are absent, D_2O becomes mobile above 140 K, before forming the droplets of liquid-like water above 145 K.[203]

In later work by Souda, particular attention was paid to the large scale structure of a formic acid layer.[186] Prior to examining the D_2O-formic acid interaction, Souda discussed

the behaviour of formic acid on the Ni(111) surface in the absence of water. It was shown that when formic acid was deposited at 15 K it adopted a porous structure, but that annealing to 100 K resulted in a loss of the porosity. Having characterised formic acid adsorbed on Ni(111), Souda then examined the interaction between the acid and D_2O. With sufficient heating (>150 K) D_2O could penetrate into a layer of non-porous formic acid. Souda concluded from this that by 150 K, the D_2O had sufficient energy to disrupt the formic acid hydrogen bonds and embed itself within the acid layer. This suggests that the formic acid-D_2O bond is energetically more favourable than that between two formic acid molecules. Whilst ices with formic acid dominant over water are unlikely in the ISM, the findings of Souda still provide a valuable insight into the interaction between formic acid and water and their mobility in relation to one another.

In addition to discussing the formic acid-water interaction, Souda[203] remarks that, contrary to much of the literature,[75,126,182,183] the splitting observed in formic acid infrared spectra (see Chapter 3) is not a property of crystallisation. They state that the splitting is a consequence of molecular rotations causing hydrogen bonds to reorganise.

Collings *et al.* used TPD to survey the desorption of a range of astronomically relevant molecules, including formic acid, from a polycrystalline gold substrate, an ASW layer and a water mixture.[38] TPD of pure formic acid showed a two-feature desorption profile and Collings *et al.* attributed this to a phase change in the formic acid.[38] Formic acid deposited on ASW showed a single formic acid desorption feature at ~152 K, with the water desorbing at ~160 K. One formic acid desorption feature was also observed for the mixture, however, it peaked higher than in the layered system, just above the water peak. This suggested to Collings *et al.* that the formic acid-water bond was stronger than either the formic acid-formic acid bond, or the water-water bond.[38] A key component of this work was the assignment of the surveyed species to desorption categories.[38] Formic acid was assigned as H_2O-like and thus its desorption could be modelled as a single desorption feature coincident with water, scaled for abundance with respect to water. Viti *et al.* subsequently used the categories of desorption to model interstellar (IS) ice evolution on astronomically relevant timescales.[154]

Following Collings *et al.* assignment of a phase change in formic acid during TPD,[38] Cyriac and Pradeep examined the surface dependence of the phase change using transmittance infrared spectroscopy.[126] It was found that the nature of the surface greatly

affected the crystallisation of formic acid. When directly deposited on KBr at 18 K, crystallisation commenced at 98 K and was complete by 135 K. On an ASW layer, crystallisation was rapid and early, starting and finishing between 37 and 41 K. This early onset was attributed to the greater mobility of formic acid on an amorphous water surface. When formic acid was deposited on CI, the crystallisation onset and pace is similar to when it is deposited on KBr, commencing at 83 K and being complete by 125 K. Furthermore, it was also shown that regardless of the surface, the initial infrared spectrum of formic acid was the same and that its phase change was irreversible.[126]

Further infrared transmission studies by Bisschop *et al.* reported that formic acid and water mixtures only show the characteristic splitting of the key formic acid spectral features as the water crystallises at 150 K.[75] Since the authors reported that formic acid spectral features in pure ices show splitting at 135 K, they concluded that when formic acid is in a water matrix the onset of crystallisation is delayed.

Using a multi-technique approach, consisting of TPD, metastable impact electron spectroscopy (MIES) and ultraviolet photoemission spectroscopy (UPS), Bahr *et al.*[183] and Borodin *et al.*[182] studied formic acid adsorption on water. The system examined consisted of 1 monolayer of formic acid deposited on 5 bilayers of water, which had been pre-adsorbed on tungsten at 80 K. It was observed that up to 120 K the top layer consisted of only formic acid and that above 120 K, partial solvation of the upper water layers occurred. TPD showed that water and formic acid desorption commences at ~140 K. The main cracking fragment, mass 29 (HCO^+), showed a clear feature at 152 K, whilst no such feature was observed for the parent ion, mass 46 ($HCOOH^+$). Based on cluster calculations in collaboration with Allouche,[204] the cause of the differing mass signals was attributed to the desorption of formic acid-water complexes. Relatively little of the formic acid desorbs in these complexes and the majority remains in the upper layers as the water desorbs through it. From this, the authors concluded that formic acid had not crystallised into chains, as otherwise the water would not be able to desorb through it. As the water desorbs (TPD peak at 163 K) the formic acid falls down towards the tungsten substrate and chemisorbs. Chemisorption of formic acid results in a desorption event above 180 K. Kazempoor and Pirug also report the formation of formic acid-water complexes by use of infrared studies on Au(111).[187] Furthermore, Bahr *et al.*[183] and Allouche[204] suggested that even though complexation occurs, ionisation of formic acid does not occur.

Water-formic acid complexes have also been reported by George and Sander.[201] They reached their conclusions by comparison of *ab initio* calculations and matrix isolation infrared spectroscopy. Formation of complexes resulted in the shifting of infrared features, with the magnitude and direction depending upon the mode. The most stable complex geometry was found to be formic acid hydrogen bonding to the water by both its O-H and C=O groups, with a stabilisation energy of 43 kJ mol^{-1}.[201]

Allouche used DFT calculations to study the strengths of interaction between clusters and isolated molecules of formic acid and water.[204] The strength of the formic acid-water hydrogen bond strength was calculated to be 37 kJ mol^{-1}, whilst the formic acid-formic acid hydrogen bond was calculated to be 30 kJ mol^{-1}. These calculations confirmed the findings of Collings *et al.*,[38] in that the formic acid-water interaction is stronger than the formic acid-formic acid interaction.

Formic acid-water interactions are also of interest to atmospheric chemistry and one particular area of study is cirrus clouds that reside in the upper atmosphere.[89] Hellebust *et al.* studied the formic acid-water interaction as part of an investigation into the effects of organic acids and ammonia on upper atmosphere chemistry.[89] Ices were prepared on a polycrystalline gold substrate and examined using RAIRS and TPD.[89] They reported that when formic acid was deposited on a layer of water at 100 K, some of the formic acid infrared spectral features (the OH stretch, the OCO deformation and the OH bend) shifted by 4-10 cm^{-1}.[89] However, the carbonyl stretch was only redshifted by a very small amount. Co-deposited mixtures of formic acid and water exhibited crystallisation of formic acid between 170 and 180 K, whereas crystallisation in pure formic acid was observed between 160 and 180 K. RAIRS of mixtures also indicated that partial ionisation of the acid occurs – not observed for layers. Using TPD experiments of formic acid and water mixtures, they determined that formic acid-water complexes desorb between 170 and 175 K. Molecular formic acid aggregates and water (uncoordinated) desorb at 190 K. They concluded that ionisation can only occur in the bulk, requiring free O-H bonds in the water, Thus, in the presence of CI, formic acid ionisation does not occur.[89] Park and Woon also concluded that when formic acid is embedded within a sufficient amount of water, it can deprotonate to form the formate anion stabilised by H_3O^+.[205]

Considering the data discussed in this section, the present work aims to further the understanding of the nature of the formic acid-water interaction and the way in which the

two species coexist in ices. TPD and RAIRS have been used to examine the manner in which formic acid can penetrate and reside within a water ice. Subsequently, these techniques have been used to study the progression of structural changes that result from heating.

4.2 Experimental

To ensure it was free from absorbed contaminants, the water used in the work presented here was distilled, deionised and subjected to multiple freeze-pump-thaw cycles. Formic acid was handled as previously described in Chapter 3.

Ices were grown *in situ* by backfilling the chamber, with doses measured in Langmuir (1 $L_m = 1 \times 10^{-6}$ mbar s). Layered ices were prepared by depositing the first species and then allowing the chamber pressure to return to approximately base pressure, after which the second species was deposited. The preparation of mixtures was performed as described in Chapter 2. Prior to filling the dosing lines, the surface of each liquid was briefly pumped on to further ensure purity.

TPD experiments were conducted with a heating rate of 0.5 K s^{-1}. Mass 18 was monitored for water, whilst simultaneously monitoring masses 29 (main fragment, HCO^+) and 46 (parent ion, $HCOOH^+$) for formic acid. RAIR spectra were obtained with a resolution of 4 cm^{-1} and by the co-addition of 256 scans. When annealing ices, the temperature of interest was reached by heating at a rate of 0.50 ± 0.01 K s^{-1} and then holding the substrate at that temperature for 3 minutes. The RAIR spectrum was then obtained after allowing the substrate to cool to near base temperature.

Crystalline water was prepared by holding the sample surface at 140 K during deposition. Crystallinity was confirmed using RAIRS.[141] It was observed that the sticking probability whilst dosing at 140 K was reduced. Therefore, by using the integrated TPD area, it was calculated that an exposure of ~160 L_m was needed to obtain an ice approximately the same thickness as when 100 L_m of water was deposited at ~24 K. This equated to the sticking probability being 38% lower.

4.3 Results and Discussion

4.3.1 Formic Acid Deposited on 100 L_m of ASW

Layers of formic acid deposited on top water were studied to understand the way in which the species interact. These systems also allow for the investigation of trapping and diffusion of formic acid within the water ice, an appreciation of which is needed to understand how formic acid desorbs from water rich ices, which are prevalent in the ISM.

Before assigning the desorption features seen when formic acid is deposited on water, the differences between the formic acid mass signals should be addressed. Figure 4.2 shows a comparison between the mass 29 (main cracking fragment) and mass 46 (parent ion) signals recorded during TPD of 10 and 50 L_m of formic acid adsorbed on 100 L_m of water, with both species deposited with a substrate temperature of 24 K. The mass 46 signals are consistently lower, as expected, and there are no features present on one mass trace that are not present in the other. There is a very slight difference in the 10 L_m spectra between 140 and 150 K but they are likely due to the trace being close to the base line.

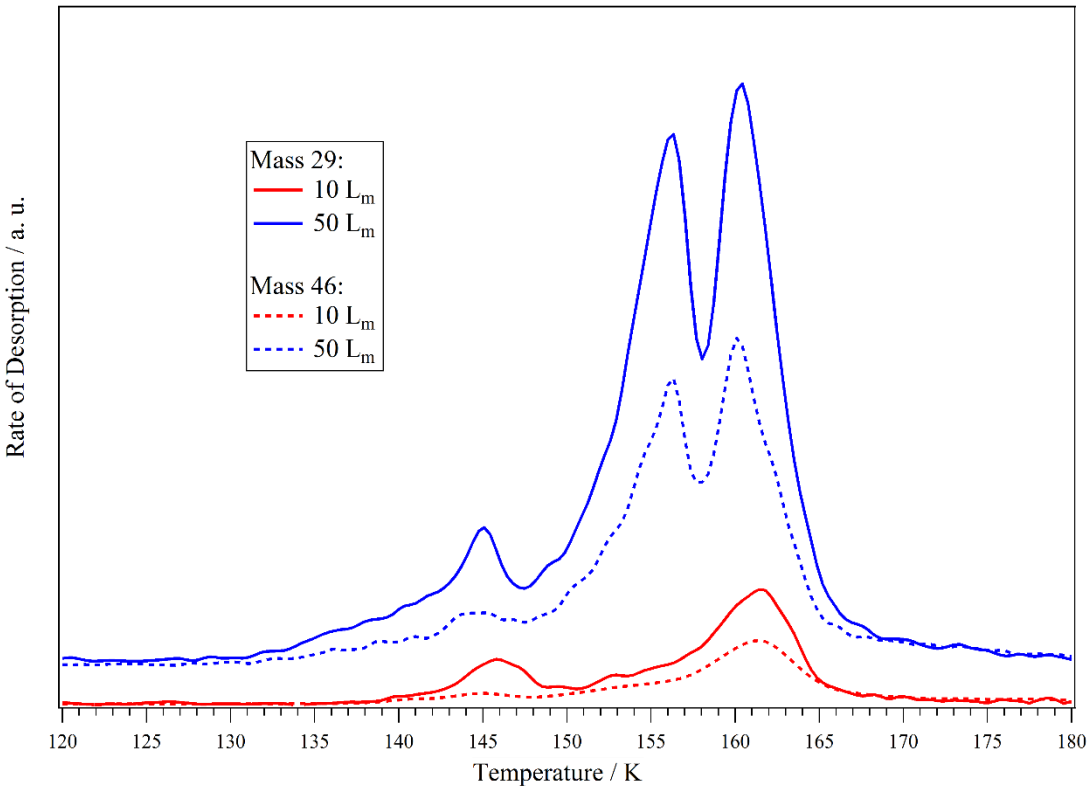

Figure 4.2 – Comparison between the mass 46 and mass 29 traces for 10 and 50 L_m of formic acid on 100 L_m of water. Both species were adsorbed at 24 K.

Bahr *et al.*[183] and Borodin *et al.*[182] observed distinct differences between the mass 29 and mass 46 TPD signals. Mass 29 showed clear desorption features during water desorption whilst mass 46 did not. They attributed this difference to desorption of formic acid and water complexes, rather than formic acid monomers, because when in complexes with water, formic acid would fragment differently in the mass spectrometer. This is contrary to the observations discussed above where the mass 46 traces show the same features as the mass 29, albeit with a lower intensity. This suggests that complexation is not observed in the present work. The discrepancy between the work presented here and Bahr *et al.*[183] and Borodin *et al.*[182] is not clear but may be because in their studies the layered systems were, comparably, very thin and so the nature of the binding in their ice may be affected by formic acid chemisorbed to the tungsten substrate. Whilst all the features in the mass 29 traces are present in the mass 46 traces, the ratio between the mass signals is not constant. The average ratio between the mass 29 and mass 46 traces is calculated to be 1.9, with a standard deviation of 0.63, or 34%. The average ratio between the masses in Chapter 3 was calculated to be 1.8, with a standard deviation of 0.07, or 4%. The large difference in the standard deviations highlights how the ratio is more stable in the pure spectra than when water is present. This indicates that whilst there is no evidence of complexation, there is evidently a strong interaction between formic acid and water that is affecting the fragmentation pattern, causing it to be far from constant.

Figure 4.3A depicts the TPD spectra (mass 29) recorded after adsorbing differing amounts of formic acid on top of 100 L_m of water. 100 L_m of water was chosen because it is known from previous experiments using the experimental set-up used here, that this amount covers the substrate and forms multilayers.[141] Multilayers are needed in order to allow the interaction of formic acid with water to be studied free from substrate effects. Deposition of both formic acid and water in Figure 4.3A occurred with the substrate at ~24 K. Water adsorbed at ~24 K adopts an amorphous porous structure called ASW.[42,129,141] Figure 4.3B shows, for comparison with panel A, the mass 29 spectra corresponding to pure formic acid exposures of 20 and 50 L_m on HOPG. By comparing the TPD spectra of formic acid when it is deposited on ASW and when it is deposited on HOPG, it is clear that water is having a substantial influence on the desorption of formic acid.

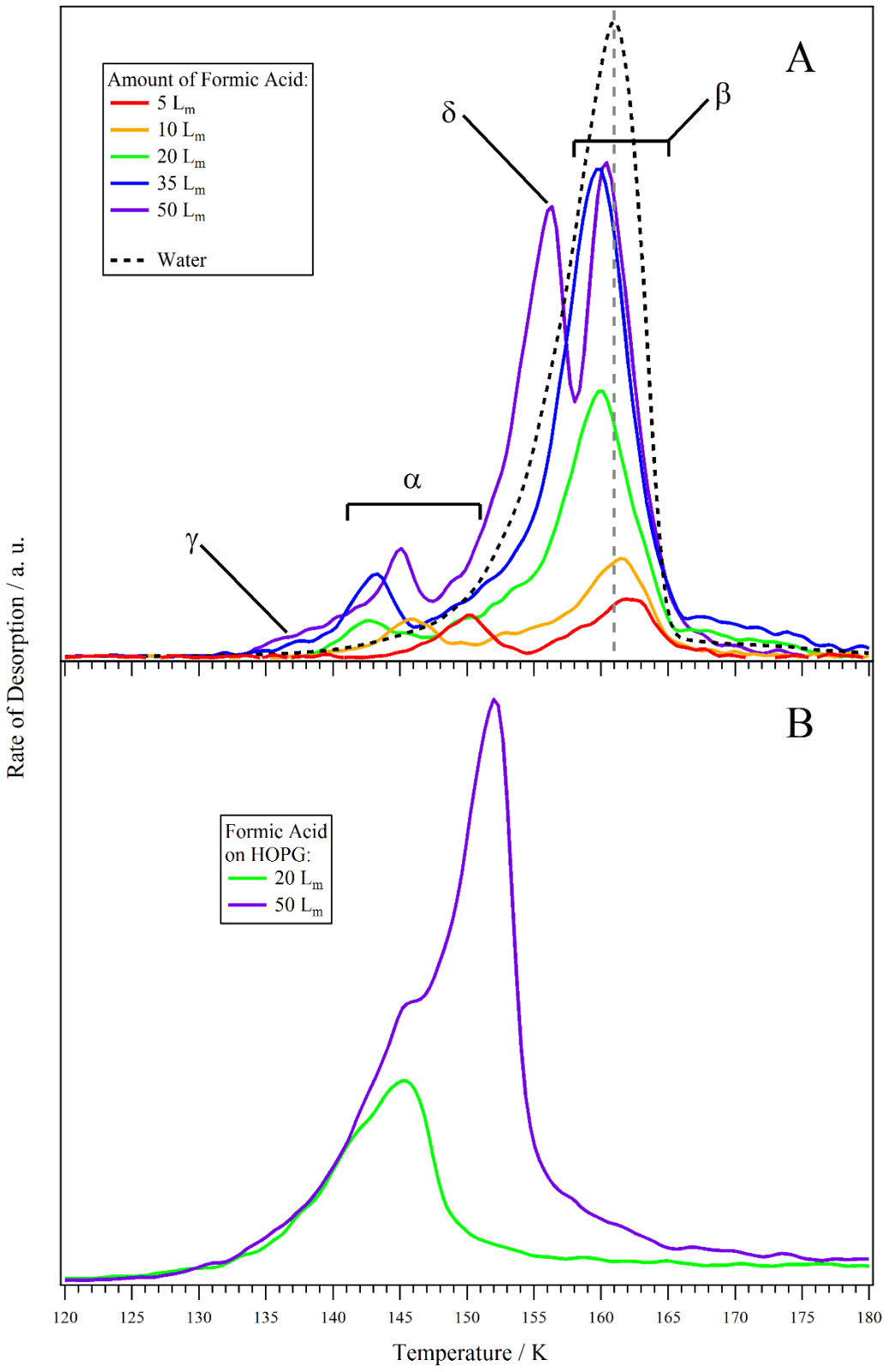

Figure 4.3 – Mass 29 TPD spectra for formic acid deposited at 24 K on A) 100 L_m of water and B) HOPG. The dashed trace is the water spectrum corresponding to the 10 L_m exposure of formic acid and is shown for comparison. The dashed vertical grey line indicates the peak water desorption temperature of 161 K.

Assignment of the formic acid desorption features seen in the TPD spectra shown in Figure 4.3 is not trivial. The complexity of the desorption profiles is a consequence of the closeness in the desorption temperatures of formic acid and water, and also the fact that both species can form multiple hydrogen bonds. It is also evident that the behaviour of formic acid is related to the amount present, relative to water.

When a 100 L_m layer of ASW is exposed to 5 L_m of formic acid, the resulting mass 29 TPD spectrum shows two distinct features, as seen in Figure 4.3 A. The high temperature feature, labelled β, has a broad leading edge and peaks at ~162 K, slightly higher than the water peak temperature. The low temperature feature, labelled α, is well defined and peaks at 150 K. Upon increasing the exposure to 10 L_m and then 20 L_m, peak β increases in intensity and shifts to the low temperature side of the water desorption peak. Peak α maintains the same intensity but shifts down in temperature to 143 K. Further increasing the exposure to 35 L_m results in continued growth of peak β, but its position does not shift any further. Peak α and has increased in intensity and temperature. Furthermore, peak α now has a broader leading edge, labelled γ, which extends to ~133 K. With a 50 L_m formic acid exposure peak β appears to maintain its position and shows only a slight increase in intensity. Peak α continues to grow and increase in temperature, with the leading edge (feature γ) becoming very broad but still beginning at ~133 K. The most prominent change between the 35 and 50 L_m spectra is the appearance of a defined peak at 156 K in the 50 L_m spectrum, labelled δ.

Before discussing the assignment of the formic acid desorption features, the nature of water desorption during TPD experiments should briefly be addressed. When water is deposited at 24 K on HOPG it will adopt an amorphous structure, ASW.[44,122,141,206] During TPD, depletion of ASW can occur by desorption or by it undergoing a phase change to CI. Providing an appropriate heating rate is used, the point at which all of the ASW has desorbed or been converted to CI can be observed as a bump on the leading edge of the water TPD spectrum.[141,191,207] This bump is a consequence of CI having a lower vapour pressure than ASW, and consequently, a slightly higher desorption temperature.

During the crystallisation process, pathways can form throughout the water ice that lead to the surface.[40] If other molecules have become trapped in the water, then these pathways can offer a route to desorption.[42,44,188,208] If the molecules in question have been trapped above their natural sublimation temperatures, then the appearance of a pathway to the

vacuum will result in desorption that is abrupt and rapid. Owing to the explosive nature of this desorption mechanism it is termed volcano desorption.[42] Volcano desorption has been observed for a range of astronomically relevant molecules, such as OCS and CO_2.[38,188]

All the water TPD profiles associated with the differing formic acid exposures have a defined peak at 161 K like the example shown in Figure 4.3. This peak corresponds to the desorption of CI. However, the temperature and shape of the ASW to CI shoulder varies as the formic acid exposure is changed. Figure 4.4 focuses on the ASW to CI shoulders, with the remainder of the spectra omitted for clarity. The water spectrum associated with a 5 L_m formic acid exposure has a slight shoulder at 150 K. Upon increasing the formic acid exposure to 20 L_m, this shoulder moves down to 143 K and becomes slightly more defined. Increasing the formic acid exposure up to 50 L_m sees the temperature decline reverse, with the shoulder moving up to 145 K and becoming well defined.

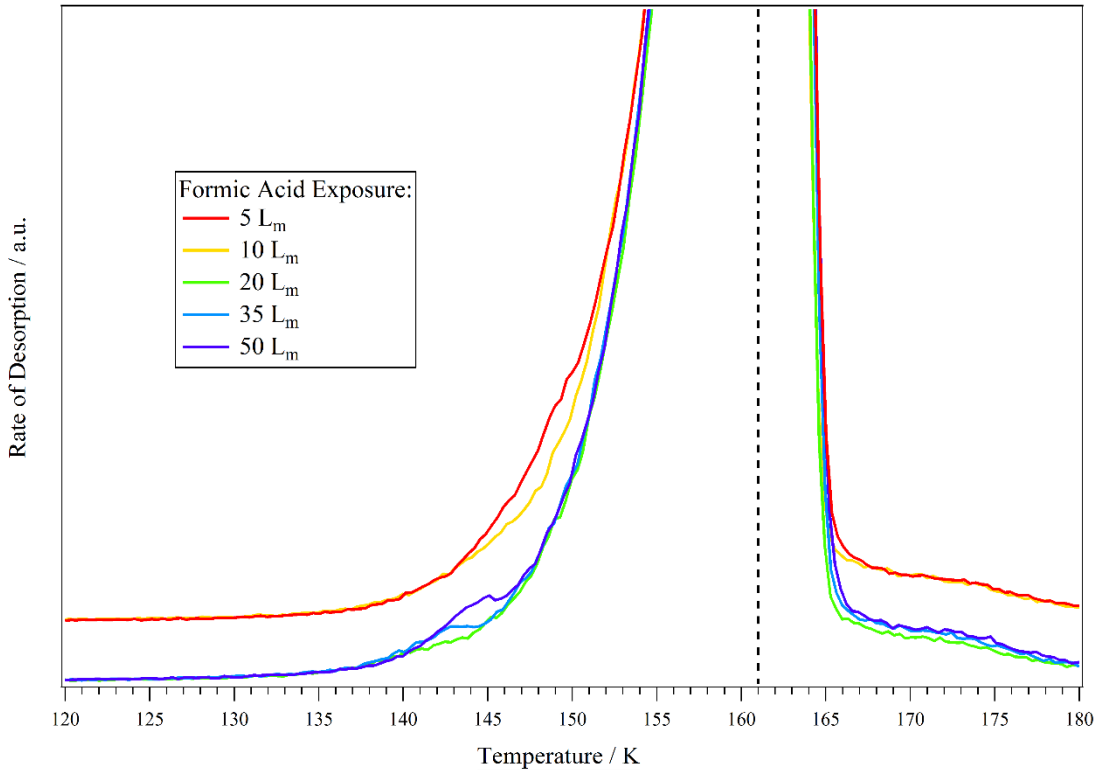

Figure 4.4 – Water TPD spectra from experiments of formic acid deposited on 100 L_m of water. The whole spectra are not shown so that the variation in the low temperature shoulder can be observed. The dashed line indicates the main water desorption feature at 161 K. The 5 and 10 L_m spectra are offset for clarity.

Each of low temperature formic acid features (peaks α) occurs coincident with the water crystallisation shoulder, suggesting that peak α is linked to the water phase change. This implies that formic acid is being released via a mechanism akin to volcano desorption, this process being reliant upon formic acid becoming trapped within the water layer. Therefore, the movement of peak α is due to the shifting water phase change discussed above. Trapping of formic acid within the water layer could occur by diffusion or thermally induced mixing. Diffusion or thermally induced mixing of formic acid and water is plausible considering the ability of formic acid to hydrogen bond and the pre-desorption mobility observed in pure formic acid ices. Although the profile observed for formic acid is not the typically sharp peak often seen for volcano desorption,[42,108] since it is clearly linked to the water phase change, peak α is assigned as volcano desorption.

In addition to the volcano desorption feature discussed above, peak β is also common to all the formic acid spectra in Figure 4.3A. Since peak β is approximately coincident with the desorption of CI it is assigned as co-desorption of formic acid with CI. Co-desorption usually occurs when an adsorbate is trapped within a water ice and is unable to desorb through the water ice or during the ASW to CI phase change, thus only being able to desorb as the water around it does so. Co-desorption may also occur when there is a particularly strong interaction between an adsorbate and water. In the case of formic acid, it is expected that it can both trap in water and form strong hydrogen bonds with water. Therefore, it is proposed that when formic acid becomes trapped in water there will be two distinct formic acid environments: formic acid directly bound to water and formic acid surrounded by other formic acid molecules. This suggests that the formic acid co-desorption feature (peak β) will evolve as the formic acid exposure is varied, which is exactly what is observed in Figure 4.3A. For the lowest formic acid exposures (5 and 10 L_m), peak β occurs at a higher temperature than the CI peak (1 and 1.5 K, respectively), which is centred at 161 K. For formic acid exposures of ≥20 L_m, peak β shifts to the low temperature side of the CI peak.

Peak β (formic acid co-desorption), for the lowest formic acid exposures (5 and 10 L_m), occurring at a higher temperature than water suggests that the bond between formic acid and water is stronger than the bond between two water molecules. This is because the desorption of formic acid and water molecules bound to each other will only peak after the majority of the water desorbs. This is in agreement with the observations of Collings

et al.[38] and the DFT cluster calculations of Allouche.[204] Therefore, this indicates that for the lowest exposures of formic acid, the dominant formic acid environment is formic acid directly bound to water. Whilst for formic acid exposures ≥20 L_m, the dominant environment is formic acid surrounded by formic acid. Mixtures of formic acid and water, where water is the dominant species, also demonstrate the same trend as the layered systems, whereby increasing the relative amount of formic acid results in the co-desorption feature shifting from the high side of the water peak to the low side. This is because as the relative amount of formic acid increases, it is more likely that formic acid will be deposited alongside other formic acid molecules, rather than water.

In order to better understand the behaviour of formic acid in the presence of water, as well as confirming the assignments of peaks α and β, additional formic acid-water systems were examined, one such system was formic acid on CI. CI is non-porous and so diffusion of formic acid into CI is not expected to be possible. This means that there is no trapping mechanism and as such, volcano desorption cannot occur. Furthermore, co-desorption should be limited or non-existent. However, there may still be interactions between the CI surface and formic acid. Figure 4.5 shows 50 L_m of formic acid deposited on CI, also included for comparison is the same amount of formic acid on ASW, the water spectra have been omitted for clarity.

There are two key features in the formic acid on CI spectrum, shown in Figure 4.5: a shoulder at ~145 K and a large peak at ~157 K, which is approximately coincident with peak δ in the formic acid on ASW spectrum. The onset of the shoulder's desorption is approximately the same as feature γ in the formic acid on ASW spectrum. Therefore, it would appear that the features in the formic acid on CI spectrum are linked with peak δ and feature γ. It is clear from Figure 4.5 that are no features comparable with peaks α or β in the formic acid on CI spectrum. Since it is expected that CI will not trap formic acid, the absence of peaks α and β confirms the assignments of peaks α and β to volcano desorption and co-desorption, respectively. Conversely, formic acid-water mixtures only show features akin to peaks α or β. Mixtures are by definition an intimate dispersion of formic acid within a water ice and therefore it is anticipated that volcano desorption and co-desorption should occur.

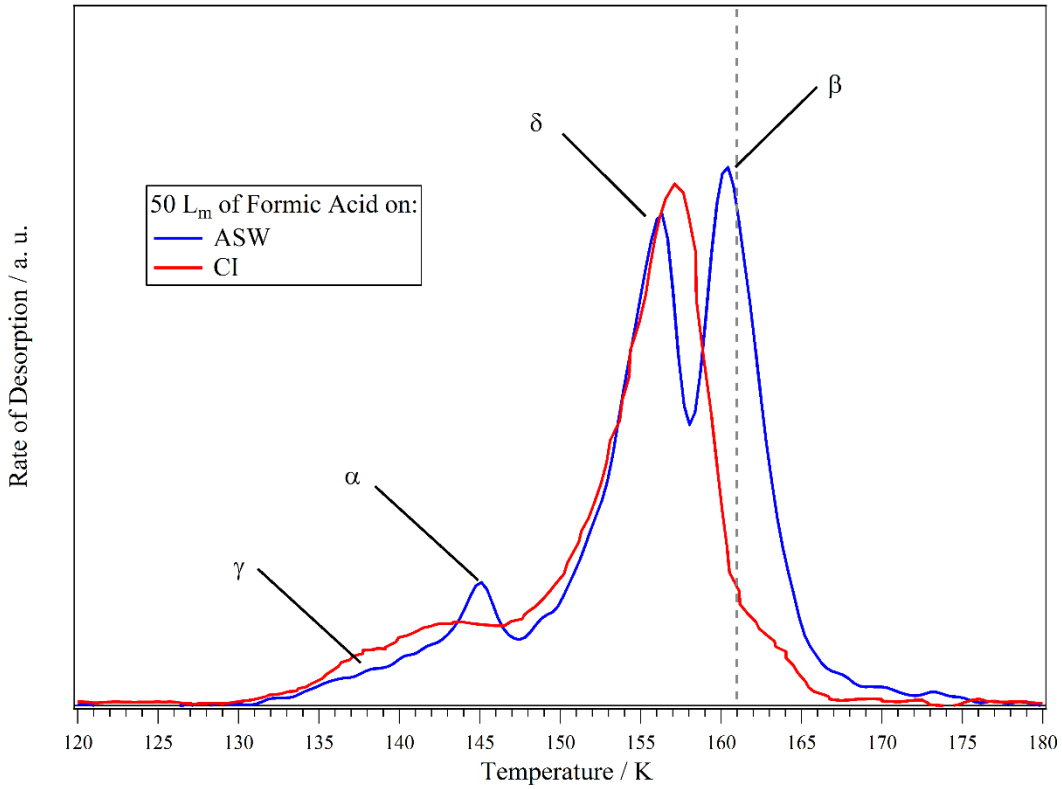

Figure 4.5 – Mass 29 trace for 50 L_m of formic acid deposited on 100 L_m of amorphous water (blue trace) and crystalline water (red trace). The water spectra have been omitted for clarity. The dashed line indicates the main water desorption peak at 161 K.

For formic acid exposures of 35 and 50 L_m on ASW, there is a broad leading edge (feature γ) on the volcano peak (peak α) that extends to ~133 K, see Figure 4.3A. The onset of desorption shifts with the volcano peak for the lower formic acid exposures (5-20 L_m), whereas for both the 35 and 50 L_m exposures, the onset of desorption is at ~133 K. This is despite the volcano peak continuing to shift. This suggests that feature γ in the 35 and 50 L_m spectra corresponds to desorption from an environment not present for the lower exposures. An onset of desorption at ~133 K is close to that observed for pure formic acid deposited on HOPG (Figure 4.3B), and for formic acid on CI (Figure 4.5). Considering the proximity of these desorption onset temperatures, and the inability of CI to trap formic acid, it seems that feature γ in the 35 and 50 L_m spectra of Figure 4.3A corresponds to formic acid desorbing from a layer consisting solely of formic acid on top of the water. The feature γ leading edges in the 35 and 50 L_m spectra are not quite shared so it is uncertain whether this is multilayer, or monolayer desorption.

The change in the co-desorption peak (peak β) intensity between 35 and 50 L_m is minimal compared to that between 20 and 35 L_m, suggesting that the co-desorption feature is

saturating. Additionally, the lack of significant variation in the temperature of the co-desorption peak between 35 and 50 L_m in Figure 4.3A further suggests saturation of this peak. If only the upper layers of water are accessible to formic acid, as proposed by Bahr *et al.*[183] and Borodin *et al.*[182], then it is expected that these upper layers would saturate at some point. Saturation of the internal spaces within the water ice would result in formic acid remaining on the surface of the water. This conclusion also supports the above assignment of feature γ to desorption of formic acid from a layer consisting solely of formic acid on the surface of the water.

Peak δ, at 156 K, in the 50 L_m spectrum in Figure 4.3A can be assigned by considering the assignments of the other features. After sufficient exposures, the outer layers and internal spaces of the water ice saturate with formic acid. Once saturation occurs, further increasing the formic acid exposure will result in formic acid remaining on top of the water ice. After a 50 L_m exposure of formic acid, not only has the water ice saturated, but there is enough formic acid on the surface that some of it can crystallise and hence not desorb until a higher temperature, giving rise to peak δ. Chapter 3 showed that upon sufficient heating, formic acid will crystallise. TPD spectra showed a shoulder that was a result of crystalline formic acid having a lower vapour pressure than amorphous formic acid. Comparing the 50 L_m traces in panels A and B of Figure 4.3, a desorption temperature of 156 K is higher than would be expected for crystalline formic acid if water were not present (50 L_m of formic acid on HOPG has a peak temperature of 152 K). It is therefore proposed that whilst the formic acid has crystallised, it is a delayed process in comparison to formic acid on HOPG. In the 50 L_m trace of Figure 4.3A water desorption is well underway when the onset of peak δ is observed. This suggests that the layer of formic acid, whilst crystalline, does not form a continuous barrier over the whole ice that prevents the desorption of water. This contrary to the conclusions of Bahr *et al.*[183] who stated that formic acid on top of water could not crystallise as it would prevent the desorption of the underlying waster, which they observed. RAIRS data, discussed later, supports the assignments made here.

The observation of a peak nearly coincident with peak δ when formic acid is deposited on CI (Figure 4.5) appears to confirm the assignment of peak δ to the desorption of crystalline formic acid. This is because, as discussed above, it is expected that – due to the CI structure being non-porous – formic acid will remain on the surface of CI. The

peak at ~157 K in the formic acid on CI spectrum being nearly coincident with peak δ also implies that even though the water surface is crystalline, it still influences the behaviour of formic acid.

It was not possible to calculate desorption kinetics for formic acid deposited on ASW. This is primarily due to the complex nature of the desorption profiles observed in Figure 4.3A and the presence of co-desorption. However, the evolution of the observed formic acid desorption features as exposure is varied indicates that the interaction between formic acid and water is stronger than that between two formic acid molecules. This agrees with the conclusions of Collings *et al.*[38] and Allouche.[204] It is the strong interaction between water and formic acid that is key to the trapping and retention of formic acid above its natural sublimation point.

Directly comparable studies of formic acid and water in the literature are limited, however, structurally related species such as acetic acid and methanol can be used for comparison. Burke *et al.* showed that, for exposures of 1 to 50 L_m, acetic acid desorbs from HOPG between 152 and 166 K.[121] Burke *et al.* also showed that the desorption profile of acetic acid on ASW is complex and has three key desorption events.[209] The lowest temperature peak (148 K) observed was assigned as acetic acid desorption from the ASW pores, this was based on its absence in acetic acid on CI spectra. A central feature (at ~160 K) that peaked just after the main water peak was attributed to monolayer acetic acid, in direct contact with the water, co-desorbing with water. Crucially, Burke *et al.* observed a high temperature peak that occurred after the water desorption peak which was attributed to desorption of crystalline acetic acid.[121] It would therefore appear that the formation of crystalline acetic acid did not impede desorption of water from the surface. If water can desorb through acetic acid that is crystallising, then it is plausible that it could do so through a layer of formic acid crystallising. This thus appears to confirm the assignment of peak δ and the peak at ~157 K in the formic acid on CI spectrum in Figure 4.5. Methanol was also shown to undergo thermally induced mixing when deposited on an ASW layer,[44,210] giving rise to both volcano and co-desorption. The observation of thermally induced mixing of methanol and water reinforces the conclusion that formic acid is able to diffuse into the water layer beneath it.

4.3.2 Formic Acid Deposited on 50 L_m of ASW

To confirm that the evolution of the formic acid desorption peaks (in particular, peaks β and δ, and feature γ) seen in Figure 4.3A is due to saturation of the water layer, formic acid was deposited on top of a 50 L_m water ice (deposited at ~24 K). The TPD spectra obtained after 5, 10 and 20 L_m of formic acid were deposited onto 50 L_m of water are shown in Figure 4.6.

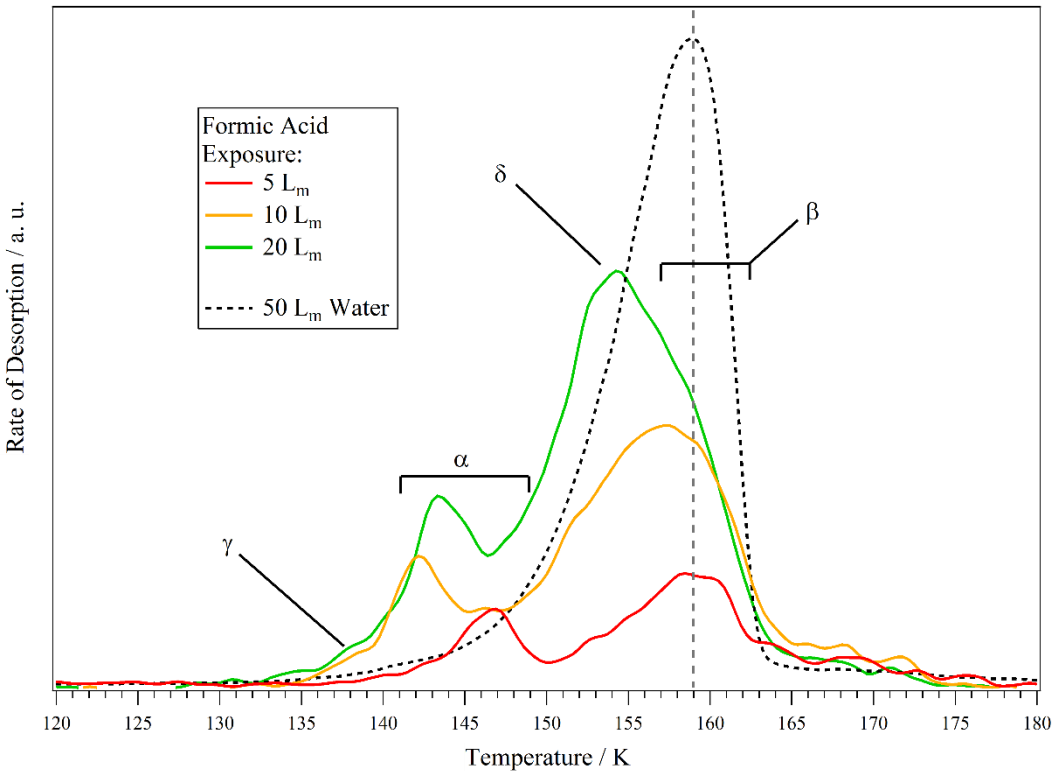

Figure 4.6 – Formic acid TPD spectra obtained after depositing 5, 10 and 20 L_m of formic acid onto 50 L_m of water. All adsorbates were deposited at ~24 K.

The water TPD spectra corresponding to the formic acid spectra shown in Figure 4.6 are shown in Figures 4.7 and 4.8 . The dashed lines in Figure 4.7 indicate the temperature of peak α in the corresponding formic acid spectrum shown in Figure 4.6. Figure 4.8 shows that the water TPD spectra are comparable, other than the ASW to CI phase change shoulder. The slight differences in peak height arise from dosing error and constitute a minor variance in the overall peak size. The inset of Figure 4.8 shows that the 50 and 100 L_m spectra of water correspond to multilayer desorption of water, indicated by a shared leading edge and increasing peak temperature with coverage.

As with the lower exposures of formic acid deposited on 100 L_m of water, a 5 L_m exposure of formic acid on 50 L_m of water shows two distinct desorption features, peaks α and β. Peak α (146-147 K) is volcano desorption, a consequence of the ASW to CI phase change. Peak β (159 K) is almost exactly coincident with the water desorption peak and arises due to co-desorption of formic acid with water. The temperature of the co-desorption feature (peak β) in the 100 L_m water systems is shifted from the high temperature side of the water peak to the low temperature side after a 10 L_m exposure of formic acid. The observation that a 5 L_m exposure of formic acid on 50 L_m of water results in a formic acid co-desorption feature coincident with the water peak confirms the assertion that the temperature shift is a result of increasing saturation of the water. This is because 5 L_m of formic acid on 50 L_m of water is a relatively thicker layer than 5 L_m of formic acid on 100 L_m of water. Therefore, saturation of a 50 L_m water ice, and the associated temperature changes, takes less formic acid than a 100 L_m water ice, as expected.

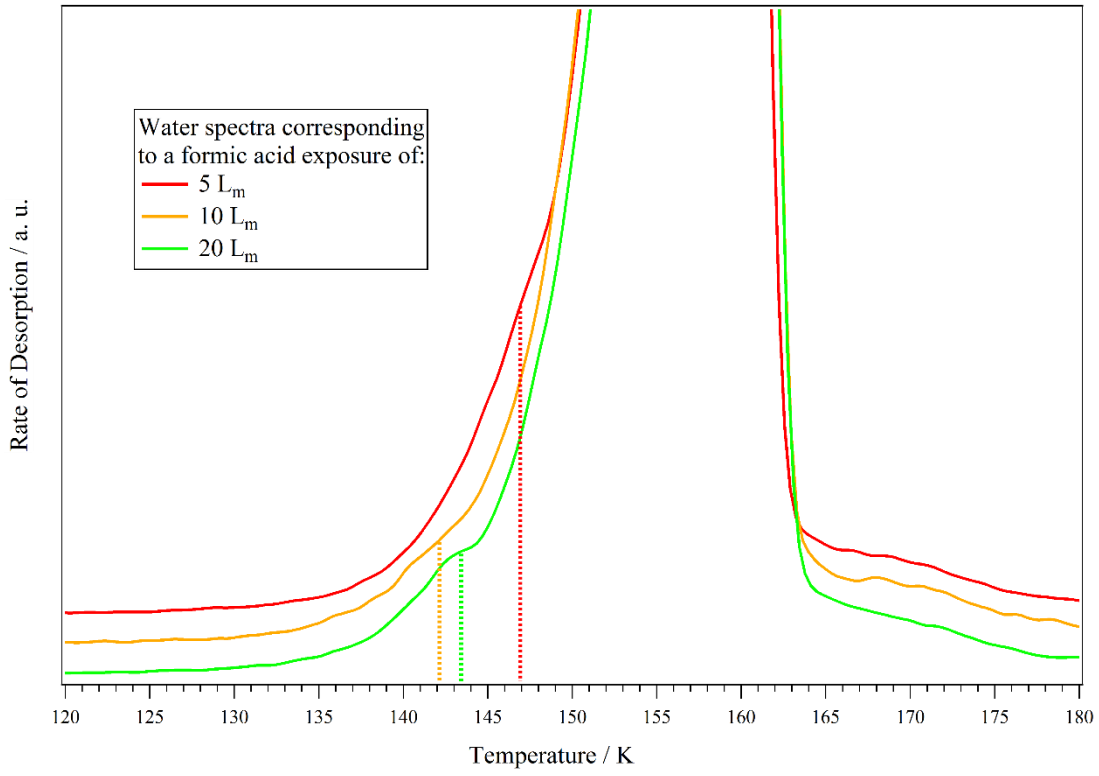

Figure 4.7 – Water TPD spectra obtained after depositing 5, 10 and 20 L_m of formic acid onto 50 L_m of water. All adsorbates were deposited at ~24 K. The dashed lines indicate the temperature of peak α in the corresponding formic acid spectrum shown in Figure 4.6.

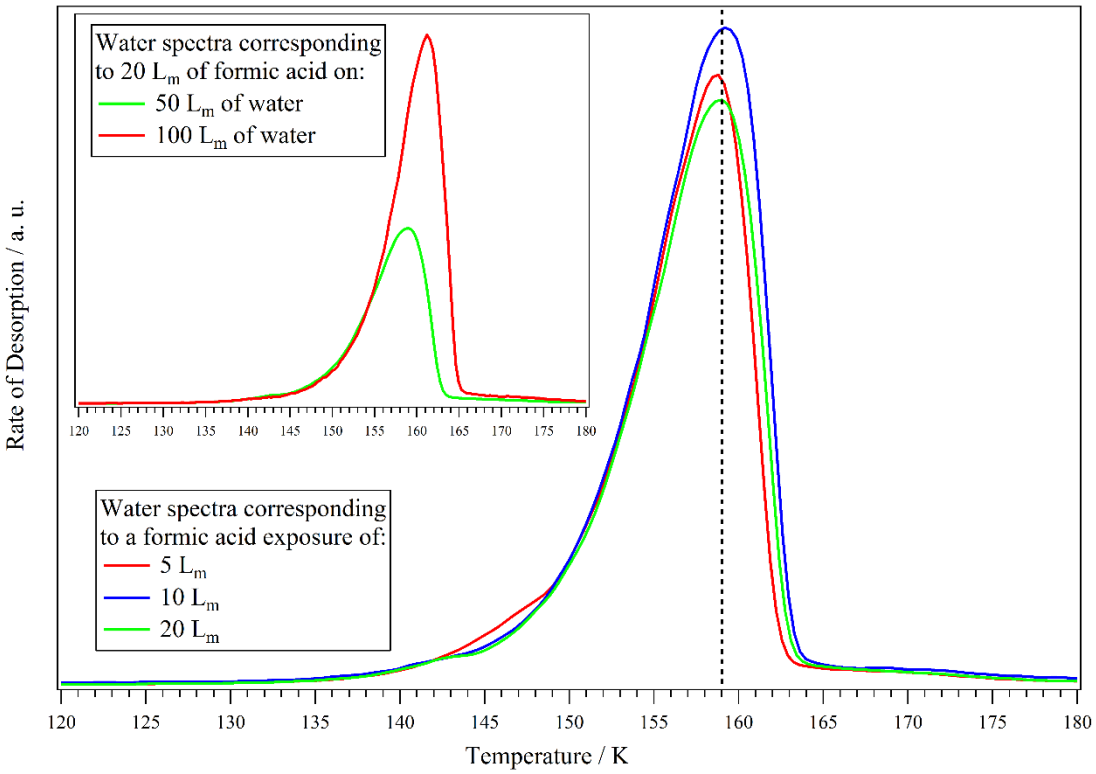

Figure 4.8 – Full water TPD spectra obtained after depositing 5, 10 and 20 L_m of formic acid onto 50 L_m of water. Inset: Water TPD for 50 and 100 L_m of water with 20 L_m of formic acid adsorbed on top. All adsorbates were deposited at ~24 K.

Increasing the formic acid exposure to 10 L_m results in some key changes compared to the 5 L_m spectrum. Peak α (volcano desorption) shifts from ~147 to 142 K, in line with the shift in the ASW to CI shoulders on the associated water spectra (Figure 4.7). In addition to this, peak α in the 10 L_m spectrum is higher than in the 5 L_m spectrum, and it has a leading edge (feature γ) that extends to just below 135 K. These changes are comparable with those observed between 5 or 10 L_m, and 35 L_m of formic acid on 100 L_m of water (Figure 4.3A). Thus, it appears that the water (50 L_m) layer is approaching saturation, and that some of the formic acid remains on the water surface in a layer consisting solely of formic acid. In addition to the changes discussed above, increasing the formic acid exposure from 5 to 10 L_m results in peak β broadening and shifting from 159 K to ~158 K, see Figure 4.6. Peak β is now clearly on the low temperature side of the main water peak. This, by consideration of the observations in the previous section, reinforces the conclusion that 10 L_m of formic acid is saturating 50 L_m of water.

20 L_m of formic acid on 50 L_m of water shows considerable differences to the 5 and 10 L_m of formic acid on 50 L_m of water (Figure 4.6), and the 20 L_m of formic acid on 100 L_m of water spectra. Figure 4.9 shows a comparison of the 20 L_m spectra from different systems.

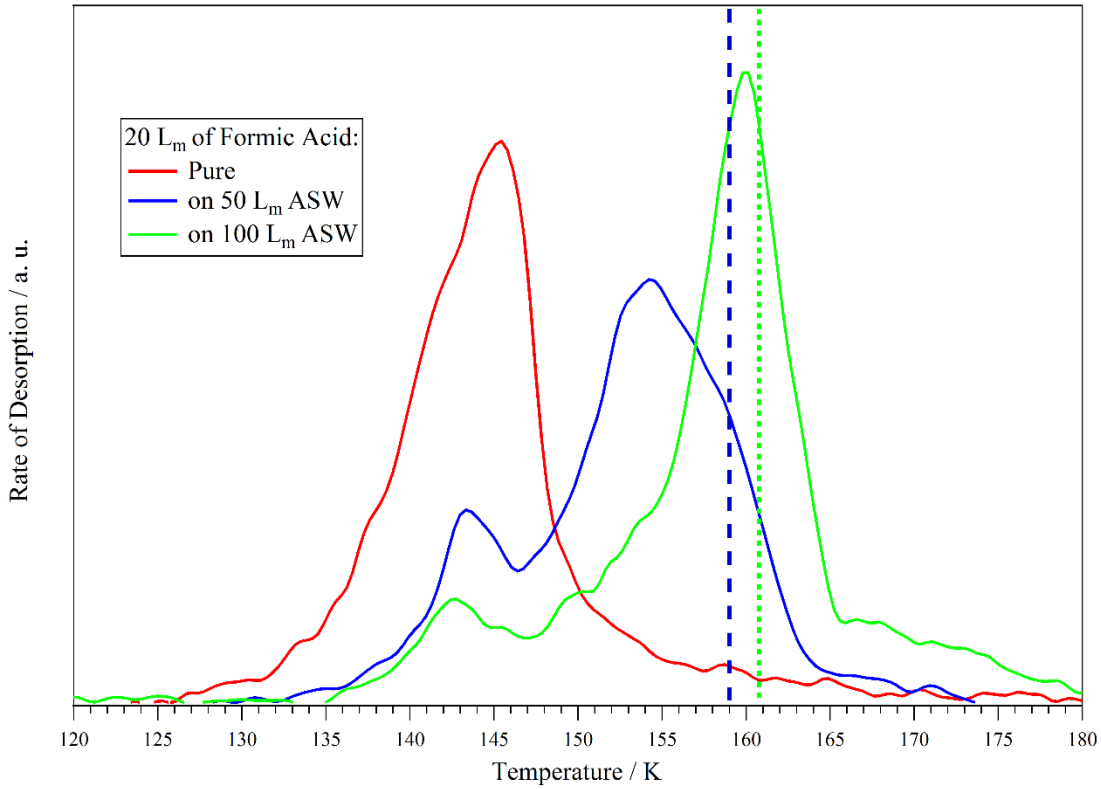

Figure 4.9 – TPD spectra obtained after depositing 20 L_m of formic acid on HOPG (red), 50 L_m of ASW (blue) and 100 L_m ASW (green). The substrate was at ~24 K during all deposition. The blue and green dashed lines show the 50 and 100 L_m water desorption temperatures, respectively.

The onset of the leading edge (feature γ) on the volcano desorption peak (peak α) for 20 L_m of formic acid on 50 L_m of water extends to ~133 K. This is the same temperature as observed for 35 and 50 L_m formic acid on 100 L_m of water and is close to the onset of desorption for pure formic acid adsorbed on HOPG. This confirms the assignment of the leading edge on the volcano peak to desorption of formic acid from the surface of water, which can only occur after saturation of the water. Peak α (volcano desorption) in the 20 L_m spectrum occurs 1 K higher than in the 10 L_m spectrum, in line with the ASW to CI phase change shoulders in the corresponding water TPD spectra (Figure 4.7). The reversal in the temperature decrease of peak α was observed in Figure 4.3A after saturation had occurred. The dominating feature in the 20 L_m of formic acid on 50 L_m of water spectrum (Figures 4.6 and 4.9) is comprised of two individual features at ~154 K and ~158 K. The appearance of feature γ in the 20 L_m of formic acid on 50 L_m of water spectrum, and the relative positions of peak α in each of the spectra in Figure 4.6, indicates saturation of the water. Therefore, the two features at ~154 K and ~158 K can be assigned to desorption of crystalline formic acid on the water surface (feature δ) and to desorption of formic acid from within the water (co-desorption, peak β), respectively. As with the 100 L_m water

systems, upon saturation of the water layer, formic acid will remain on the surface of the water. Then, if there is a sufficient amount of formic acid on the surface, it will be able to crystallise before it desorbs. In Figure 4.3A, the crystalline formic acid feature (peak δ) is a distinct peak, whereas in Figure 4.6 it overlaps with the co-desorption peak (peak β). The reason for this disparity may be due to the decreased water desorption temperature, which is expected for a thinner multilayer. This brings the formic acid co-desorption peak down in temperature and causes it to overlap with peak δ.

Comparing the behaviour of the three systems after a 20 L_m exposure of formic acid (Figure 4.9) confirms that the evolution of the TPD spectra with increasing coverage is a consequence of the ability of water to accommodate formic acid within its structure. The leading edge of the volcano peak in the 50 L_m ASW spectrum of Figure 4.9 extends further than the same feature in the 100 L_m ASW spectrum because 20 L_m of formic acid is a relatively larger exposure on 50 L_m than it is on 100 L_m. Therefore, the extent of saturation will be greater for the 50 L_m water ice. The co-desorption component of the main feature in the 50 L_m ASW spectrum is considerably smaller than the co-desorption feature in the 100 L_m ASW, exactly as to be expected since with a smaller water layer the space available to formic acid will be reduced. Therefore, the relationship between the co-desorption features in the 20 L_m of formic acid on 50 and 100 L_m of water further substantiates the conclusion that this feature is a consequence of formic acid moving within the water ice and then residing there. This is due to diffusion or thermally induced mixing. The coverage dependence of the co-desorption feature, which has been shown to be present for 50 and 100 L_m water ices, suggests that whilst the formic acid-water hydrogen bond is stronger than either species with itself,[38,204] the increasing proximity between adsorbed formic acid molecules weakens the interaction.

4.3.3 RAIRS Formic Acid on Water

The interaction between formic acid and water can be probed further using RAIRS. Figure 4.10 shows the 800-2000 cm^{-1} region for RAIR spectra collected after exposing a 100 L_m water ice to 50 L_m of formic acid at 21 K and then annealing the ice to the indicated temperatures. The small sharp peaks between ~1450 and ~1700 cm^{-1} correspond to absorption by atmospheric water and are a consequence of an imperfect purge within the infrared spectrometer and the optics boxes. The feature at ~950 cm^{-1} in the formic acid on HOPG spectrum corresponds to the O-H out-of-plane bend.

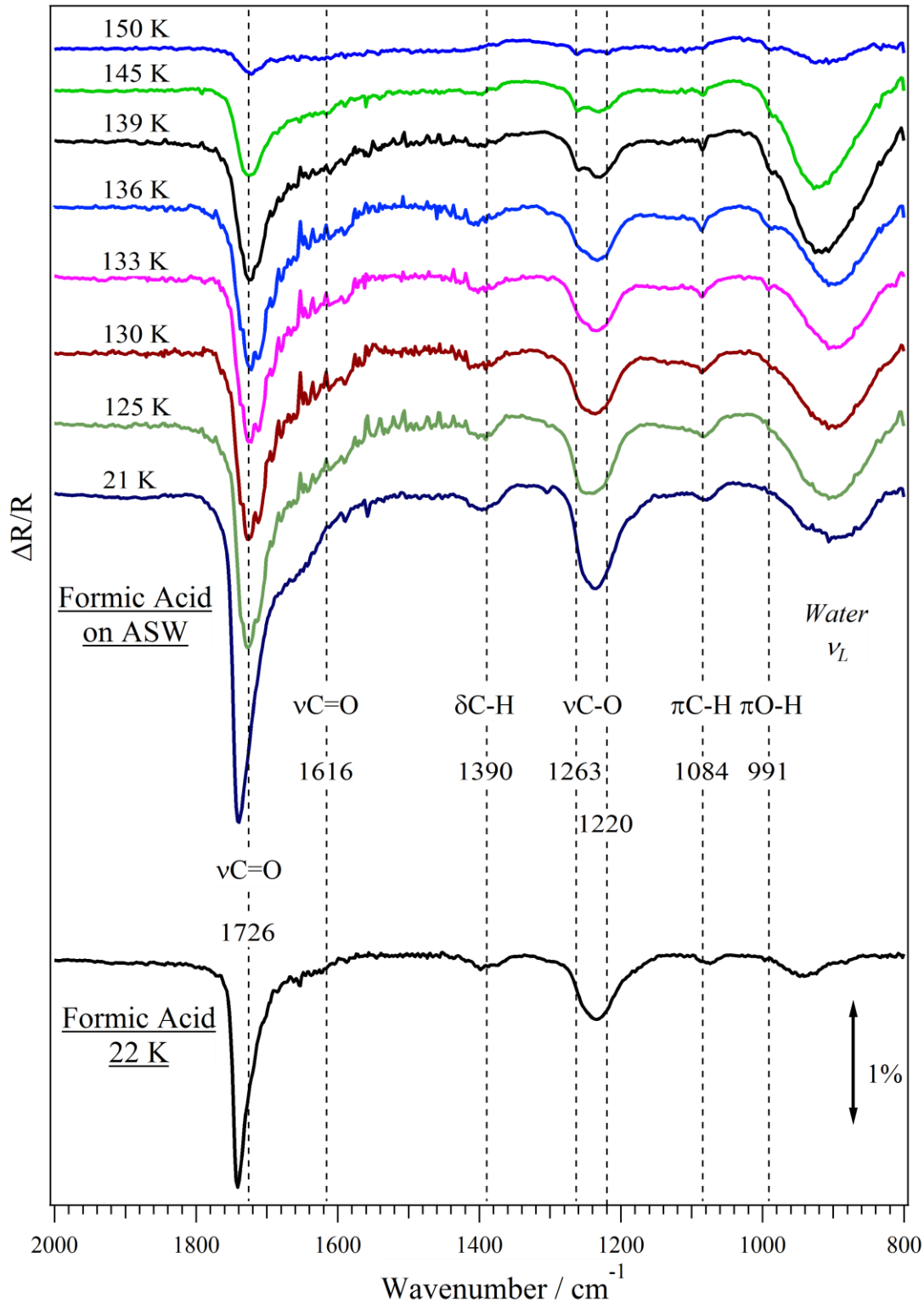

Figure 4.10 – The 800-2000 cm^{-1} region of the RAIR spectra of 50 L_m of formic acid deposited on 100 L_m of water and then annealed to the indicated temperatures. The bottom trace was obtained after depositing 50 L_m of pure formic acid on HOPG at 21 K and is included for comparison with the other spectra. All deposition occurred at ~21 K.

Comparing the 21 K spectrum for 50 L_m of formic acid on 100 L_m of water (dark blue trace in Figure 4.10) with the 22 K spectrum obtained after depositing 50 L_m of pure formic acid on HOPG (bottom black trace in Figure 4.10) showed no apparent differences in peak positions. Since the peak positions were the same in the 50 and 100 L_m of pure formic on HOPG spectra (Chapter 3), the assignments made in the previous chapter for 100 L_m of pure formic acid on HOPG apply to the features seen in Figure 4.10. The strong absorption between 1600 and 1800 cm^{-1} (peak at 1741 cm^{-1}) corresponds to the carbonyl stretch (νC=O) and the slightly weaker, but still significant, absorption at 1236 cm^{-1} is the C-O stretch (νC-O). There are also two weak features, the C-H deformation (δC-H) at 1396 cm^{-1} and the C-H out-of-plane bend (πC-H) at 1080 cm^{-1}. In addition to the formic acid features, the frustrated libration mode of water was observed at around 900 cm^{-1} (ν_L).[44,211] This large broad feature appears to overlap with the O-H deformation peak for formic acid, which was observed at ~950 cm^{-1} in the pure spectrum. As all other major peaks are still observable for the layered ice, it is likely that the O-H deformation mode of formic acid is not observable due to the strong absorption in the same region by water. This agrees with the observations of Cyriac and Pradeep, who saw no differences in peak positions at 21 K when comparing formic acid on KBr and ASW.[126]

Upon heating the layered ice of formic acid on top of water a number of changes occur (Figure 4.10). Annealing to temperatures below 125 K does not produce spectral evolution. However, annealing to 125 K results in a decrease and redshift in the main carbonyl stretch (νC=O) feature from 1741 to 1726 cm^{-1}. This indicates that the structure of formic acid on the ASW has changed. The same feature shifts ~3 cm^{-1} for a pure ice at the same temperature. A shift of 15 cm^{-1} indicates that the carbonyl group is involved in a particularly strong interaction, most likely with water. The C-H deformation at ~1390 cm^{-1} (δC-H) appears to lose a small amount of intensity, but does not seem to shift. The C-O stretch (νC-O) centred at ~1230 cm^{-1} flattens but remains centred at around ~1230 cm^{-1}. The C-H out-of-plane bend (πC-H) at ~1075 cm^{-1} sharpens very slightly and also blueshifts by ~6 cm^{-1}. There is no apparent evolution of the O-H out-of-plane bend (πO-H) from the frustrated libration mode of the water. Although the O-H out-of-plane bend in pure formic acid ices has shifted significantly by this temperature it is likely that the water libration mode (ν_L) is still obscuring the peak.

The changes in the spectra described above are comparable with those observed for formic acid deposited on HOPG, and suggests that at 125 K the formic acid is mobile but not necessarily undergoing any significant large-scale structural changes. This is in line with Cyriac and Pradeep's assertion that formic acid is highly mobile on the ASW surface.[126] However, Cyriac and Pradeep suggest that an outcome of high mobility is the rapid crystallisation of formic acid. This is not observed in the TPD or RAIRS presented here, nor is it observed from layered systems of methanol or acetic acid discussed previously.[44,209]

Heating to 130 and 133 K results in a number of spectral changes. There is a subtle decrease in the carbonyl stretch (νC=O) peak at 1726 cm^{-1}, but it does not change position. The shoulder at 1616 cm^{-1} on the main carbonyl stretch peak is possibly starting to evolve into a peak. Conversely, in the pure formic acid on HOPG spectra, at 133 K the shoulder was already a clear peak that had begun to grow in intensity (whilst the main νC=O peak at ~1730 cm^{-1} decreased in intensity). The C-H deformation (1396 cm^{-1}) becomes significantly less intense and thus less defined. The C-O stretch (1236 cm^{-1}) loses some intensity but begins to show shoulders at ~1220 and ~1260 cm^{-1}, which are precursors of splitting. These shoulders, and the subsequent splitting in the C-O stretch feature, result from formic acid beginning to form chains. By forming chains, the in-phase and out-of-phase C-O stretching modes between adjacent formic acid units become energetically distinct.[75,171,196] In contrast to the layered system, in the pure ice system there is the distinct beginnings of splitting in both the C-H deformation and the C-O stretch by 133 K (Chapter 3). Figure 4.11 shows the C-O stretch feature from the formic acid on HOPG and formic acid on ASW spectra side-by-side for comparison. It is clear from Figure 4.11 that the evolution of this band is drastically different in the two systems. By 133 K the C-H out-of-plane bend (πC-H) blueshifts by a further 4 cm^{-1} to ~1084 cm^{-1} and is considerably sharper, this is comparable with the behaviour seen for a pure ice. A small peak at ~990 cm^{-1} on the high wavenumber tail of the water libration mode is evident at 133 K, this corresponds to the O-H out-of-plane bend (πO-H). The beginnings of splitting evident in the C-O stretch and the appearance of the O-H out-of-plane bend suggests that the formic acid may be starting to rearrange into polymeric chains. However, by comparison with the pure formic acid spectra (Figure 4.11) it seems that by 133 K crystallisation is not as advanced, as evident by the lack of definition in the peak profile.

The losses in intensity are likely to be due to partial desorption of formic acid, linked to feature γ observed in the TPD spectra in Figure 4.3A that initiates at ~133 K.

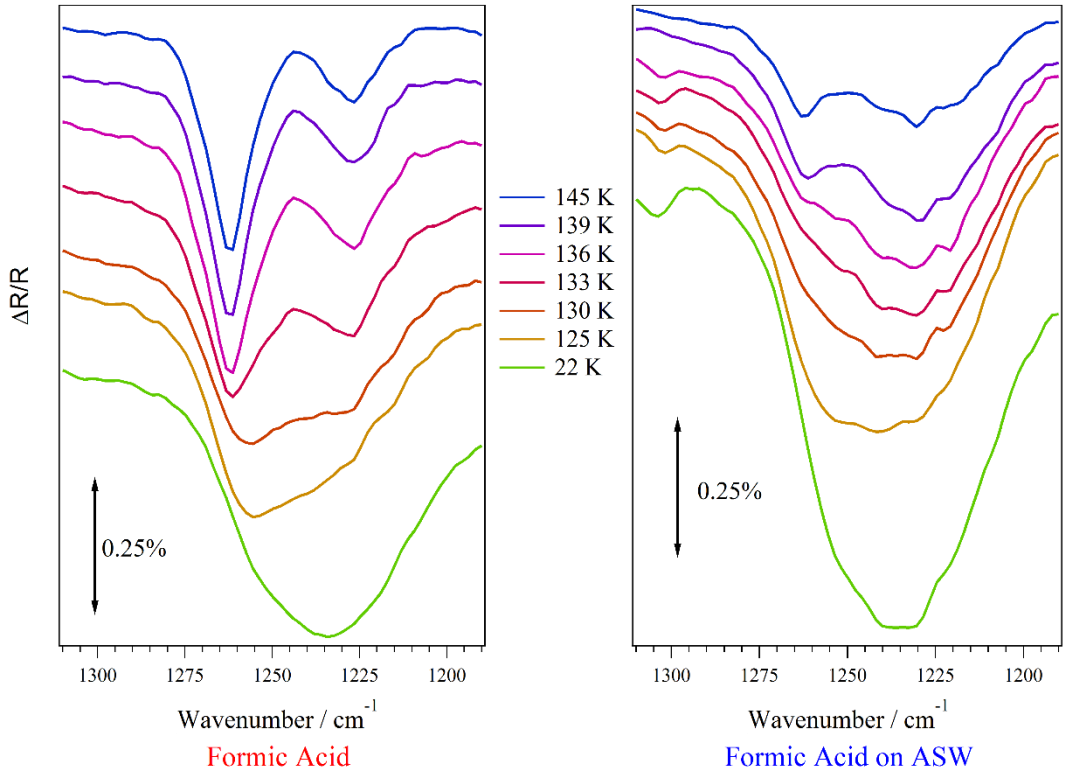

Figure 4.11 – 1150-1350 cm^{-1} region (containing the formic acid C-O stretching mode) of RAIR spectra of 50 L$_m$ of formic acid on HOPG (left panel) and 100 L$_m$ of ASW (right panel), annealed to the indicated temperatures. All deposition occurred at ~22 K.

Upon annealing to 136 K, and then to 139 K, there is significant evolution in the spectra in Figure 4.10 (highlighted by Figure 4.11). The C=O stretch (νC=O, 1720 cm^{-1}) has decreased in intensity and the low wavenumber shoulder is more distinct. The distinction between the low and high wavenumber components of the C=O stretch are, as with the C-O stretch (νC-O, centred at ~1240 cm^{-1}), due to formic acid beginning to crystallise. As the formic acid polymeric chains begin to form, the in-phase and out-of-phase C=O stretches between adjacent formic acid units become energetically distinct.[75,171,196] The C-H deformation (δC-H, ~1390 cm^{-1}) is virtually unobservable by 139 K. The C-O stretch has clearly begun to split, whilst the C-H out-of-plane bend (πC-H, ~1090 cm^{-1}) shows no further evolution. The C-O stretch starting to split, and the sharpness in the C-H out-of-plane bend, indicate that crystallisation has occurred to a small extent by 139 K. The water frustrated libration mode (ν_L, ~900 cm^{-1}) sharpens and blueshifts. Consequently, the peak corresponding to the O-H out-of-plane bend now overlaps with the water

frustration mode and appears as a clear shoulder on the water feature at 990 cm^{-1}. The intensity losses observed after annealing to 136 and 139 K indicate further partial desorption of formic acid. The formic acid desorbing is amorphous formic acid on the surface of the water. This corresponds to feature γ in in the 50 L_m of formic acid on 100 L_m of water TPD spectrum in Figure 4.3A. Splitting and sharpening of some of the infrared features, taken as an indication of formic acid crystallisation, may be enhanced by the desorption of amorphous formic acid. As the amorphous formic acid desorbs, the crystalline spectral features will be more discernible.

After annealing to 136 and 139 K, the water frustrated libration mode (ν_L) shifts from ~900 to ~920 cm^{-1} and its full width half maximum (FWHM) decreases by ~2 cm^{-1}. This suggests that water has become mobile and begun the phase change from ASW to CI. Therefore, some of the formic acid desorption seen in Figure 4.10, and discussed above, may be volcano desorption. Volcano desorption was observed at 145 K in the 50 L_m of formic acid on 100 L of water TPD spectrum in Figure 4.3A (peak α).

By 145 K there is no spectral evolution, other than intensity losses, observable in Figure 4.10. This suggests that structural changes of formic acid have stopped and that the only process occurring is desorption. For example, Figure 4.11 shows that whilst the profile of the C-O stretch feature is largely unchanged between 139 and 145 K, the intensity has decreased. Heating to 150 K results in significant intensity losses across all features. Further heating to 160 K results in total desorption of formic acid and water.

The significant desorption evident in Figure 4.10 at 145 K is assigned to the desorption of all the formic acid that remained on the water surface. This corresponds to the peak at 156 K in the TPD spectrum (peak δ, Figure 4.3A). As a result of this desorption, the only formic acid remaining is that which is trapped within the water ice. This assignment is based on the observation that there is only minor water desorption by 145 K and so any formic acid trapped in the water will remain so. This trapped formic acid will then desorb via co-desorption once the water begins to desorb, this is evident in TPD experiments as peak β in Figure 4.3A. If formic acid has saturated the water, as suggested by the TPD experiments, then there will be pockets of formic acid molecules embedded in the water ice. Some of the formic acid in these pockets may be able to start forming chains, which could give rise to the RAIRS signal that remains at 145 K. Chapter 3 and Figure 4.11 shows that if water were absent, formic acid would be fully crystalline by 145 K, however,

the formic acid remaining embedded in the water ice only appears to be partially crystalline. This could be because the pockets of formic acid might be being constrained by the surrounding water and thus may not have sufficient freedom of movement to fully crystallise. The simultaneous formic acid and water losses at 150 K further confirm assignment of co-desorption in TPD experiments (peak β in Figure 4.3). Total desorption of water and formic acid at 160 K is in agreement with TPD, whereby desorption of both species is complete at approximately the same time.

To further examine the differences between formic acid on HOPG and formic acid on water, the difference spectra can be studied. Difference spectra are produced by subtracting the spectrum taken at base temperature from each of the annealing spectra. This allows growths or loses in features to observed as positive or negative peaks respectively. Figure 4.12 shows a comparison between the 1150-1350 cm^{-1} region (containing the formic acid C-O stretch) of the difference spectra for formic acid on HOPG and formic acid on ASW.

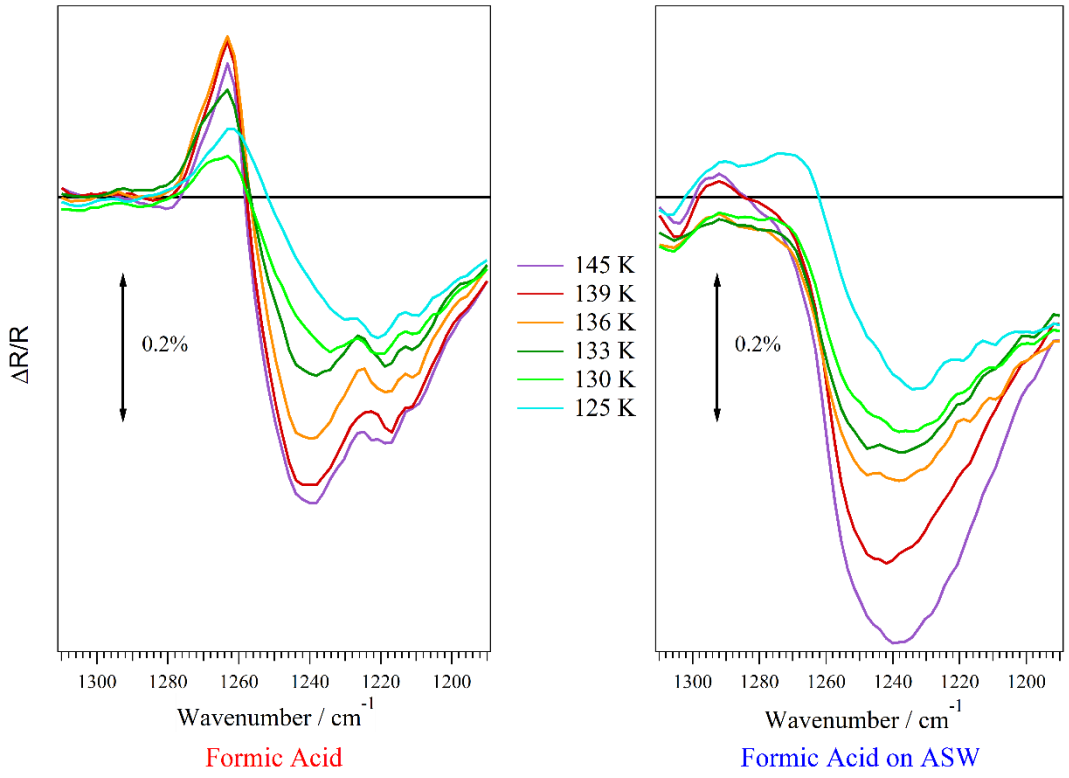

Figure 4.12 – Difference spectra of the 1150-1350 cm^{-1} region (containing the formic acid C-O stretch) for the indicated annealing spectra subtracted from the base temperature spectrum of 50 L_m of formic acid deposited on HOPG or 50 L_m of formic acid deposited on 100 L_m of ASW. The solid horizontal lines are the zero-lines. Positive peaks indicate a growth and negative peaks a reduction.

The lack of any significant degree of crystallisation is clear from the formic acid on ASW difference spectra (Figure 4.12), where the positive peak relating to the growth of the sharp peak at 1261 cm^{-1} is absent. This does not mean that there is no crystallisation, rather it means that, unlike in the pure formic acid spectrum, the peak at 1261 cm^{-1} does not develop sufficiently so that it becomes the dominant feature.

Figure 4.13 shows the 2500-3050 cm^{-1} region of the RAIR spectra shown in Figure 4.10. With regards to the formic acid features at 21 K, there are distinct peaks at 2590 and 2758 cm^{-1} that correspond to O-H stretches (νO-H). There is a broad feature between 2892 and 2966 cm^{-1} that encompasses the combination mode (νC=O + νC-O) assigned in the pure spectrum. The C-H stretch identified in the pure spectrum at 2958 cm^{-1} cannot be observed in the layered system since the intense and broad water O-H stretching mode, which peaks at 3425 cm^{-1}, dwarfs it. As observed in Figure 4.10 (which showed the 800-2000 cm^{-1} region) there are minimal differences between the base temperature spectrum for formic acid adsorbed on HOPG and the spectrum for formic acid adsorbed on ASW, indicative of formic acid remaining as a pure layer on top of the water.

Upon heating, there are limited changes in the formic acid features between 2500 and 3050 cm^{-1}, shown in Figure 4.13. However, even for the pure ice this region does not change as much as the 800-2000 cm^{-1} region (Figure 4.10). By 130 K, the 2590 cm^{-1} O-H stretch redshifts by 8 cm^{-1}, whilst the 2758 cm^{-1} O-H stretch redshifts by 17 cm^{-1}. The broad feature between 2902 and 2966 cm^{-1} narrows and develops two slight peaks at 2899 and 2929 cm^{-1}. Between 133 and 139 K there is only slight losses in intensity. There are minimal changes until 145 K, where there is a significant intensity loss. Between 150 and 160 K full desorption occurs. The evolution of the features shown in Figure 4.13 follow the general trend seen for pure formic acid, however, at no point do they reach the same extent of change. For example, between base temperature and 145 K, the low wavenumber O-H stretch redshifts 14 cm^{-1} in Figure 4.13 – compared to ~40 cm^{-1} in pure formic acid ices. Therefore, the evolution of the formic acid features shown in Figure 4.13 is consistent with the conclusions discussed earlier in reference to Figure 4.10. Whilst there appears to be some degree of crystallisation, the extent of it does not reach that seen for pure formic acid on HOPG at any point before the formic acid desorbs.

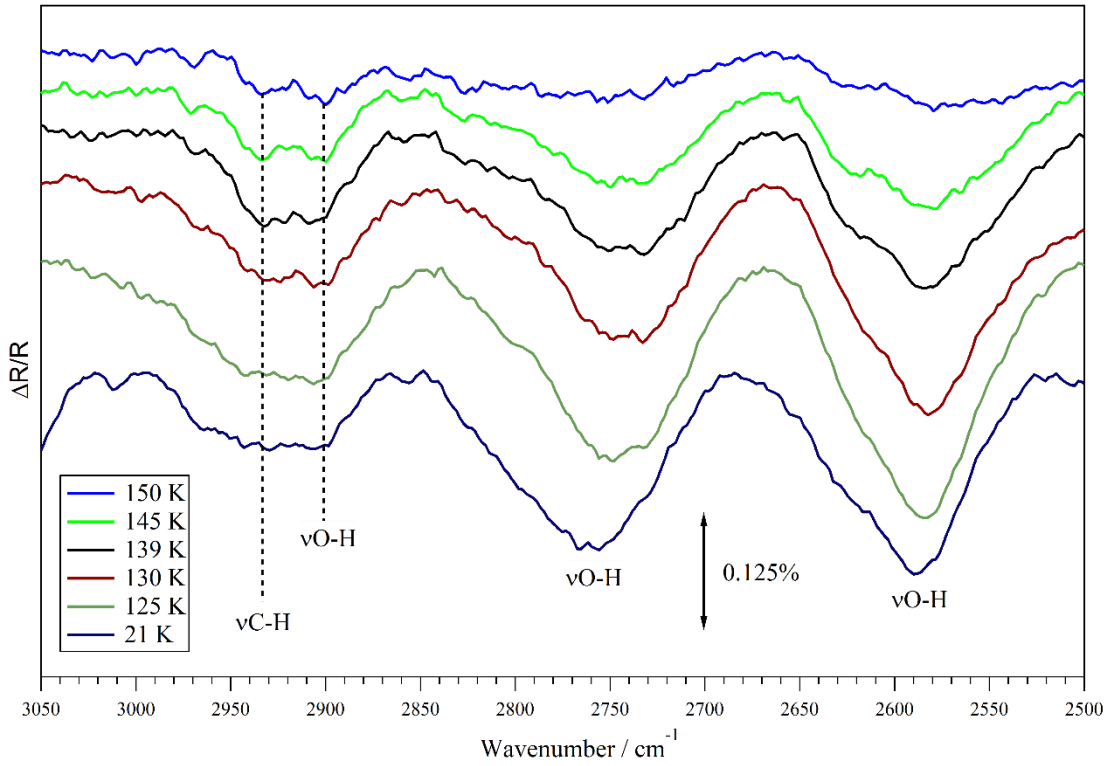

Figure 4.13 – The 2400-3050 cm^{-1} region of the RAIR spectra of 50 L_m of formic acid deposited on 100 L_m water ice and then annealed to the indicated temperatures. Deposition occurred at 21 K.

The 4000-3050 cm^{-1} region containing the water O-H stretching mode, of the RAIR spectra for 50 L_m of formic acid on 100 L_m of water is shown in a later part of this chapter. This section will examine the water O-H stretching mode from different ice systems.

4.3.4 Water and Formic Acid Mixtures

To study the formic acid and water interaction in more detail, water dominated mixtures were prepared and examined using TPD and RAIRS. Figure 4.14 depicts the TPD spectra obtained after simultaneously dosing different amounts of formic acid and water. The TPD spectra shown in Figure 4.14 correspond to ices with a total exposure of ~110 L_m, with formic acid constituting either 7 or 11% of the total, and water the remainder.

Figure 4.14 shows that in each mixture, formic acid displays two distinct features: volcano desorption during the ASW to CI phase transition (peak α) and co-desorption with crystalline water (peak β). Peak α is ~5 K lower in the 11% mixture than in the 7% mixture, in line with the ASW to CI phase change shoulder in the water TPD spectra. It is expected that the ASW to CI phase change in the 11% ice will occur at a slightly lower temperature than the 7% ice due to the smaller amount of water present. However, it is also likely that, as observed for layered systems, the amount of formic acid present will

affect the ASW to CI phase change. The ASW to CI phase change is examined in more detail in a later section of this chapter.

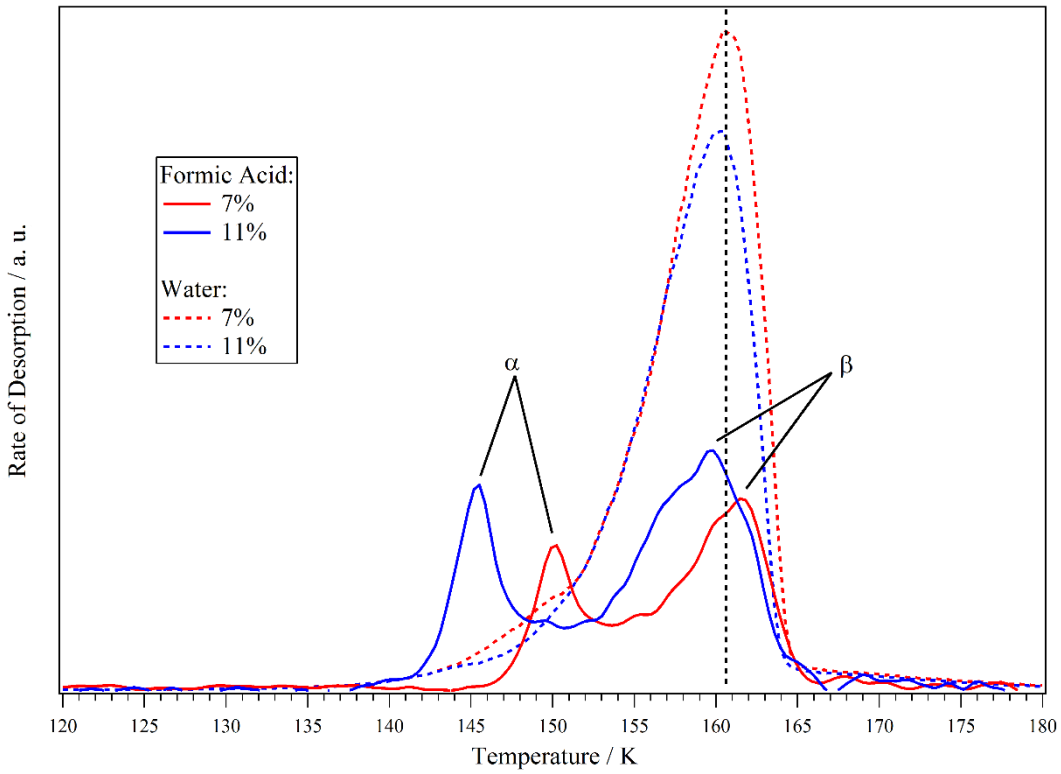

Figure 4.14 – TPD spectra of formic acid and water simultaneously deposited at ~24 K. Red traces - 7% formic acid/water mixture. Blue traces - 11% formic acid/water mixture. Solid lines - mass 29 (formic acid) signal. Dashed lines - mass 18 (water) signal.

The formic acid co-desorption peak (peak β) occurs after the water peak temperature in the 7% mixture, whereas in the 11% mixture, peak β is nearly coincident with the water peak. As observed for layered ices, when the relative amount of formic acid increases, the co-desorption shifts from the high side of the water peak to the low side. This indicates that, as the relative amount of formic acid in the ice increases, interactions between different formic acid molecules within the water increases. Therefore, the ice becomes less like a pure water ice dotted with formic acid, and pockets of formic acid may exist.

The volcano desorption peaks in Figure 4.14 (peak α) are much sharper than those observed in layered ices (Figures 4.3A and 4.6). Figure 4.15 shows a comparison of the TPD spectra from the different ice systems. The cause of the sharpness is that in mixtures, formic acid is intimately mixed from the beginning, and so there should be less variation in the environments that it resides in. Therefore, desorption occurs over a narrower range.

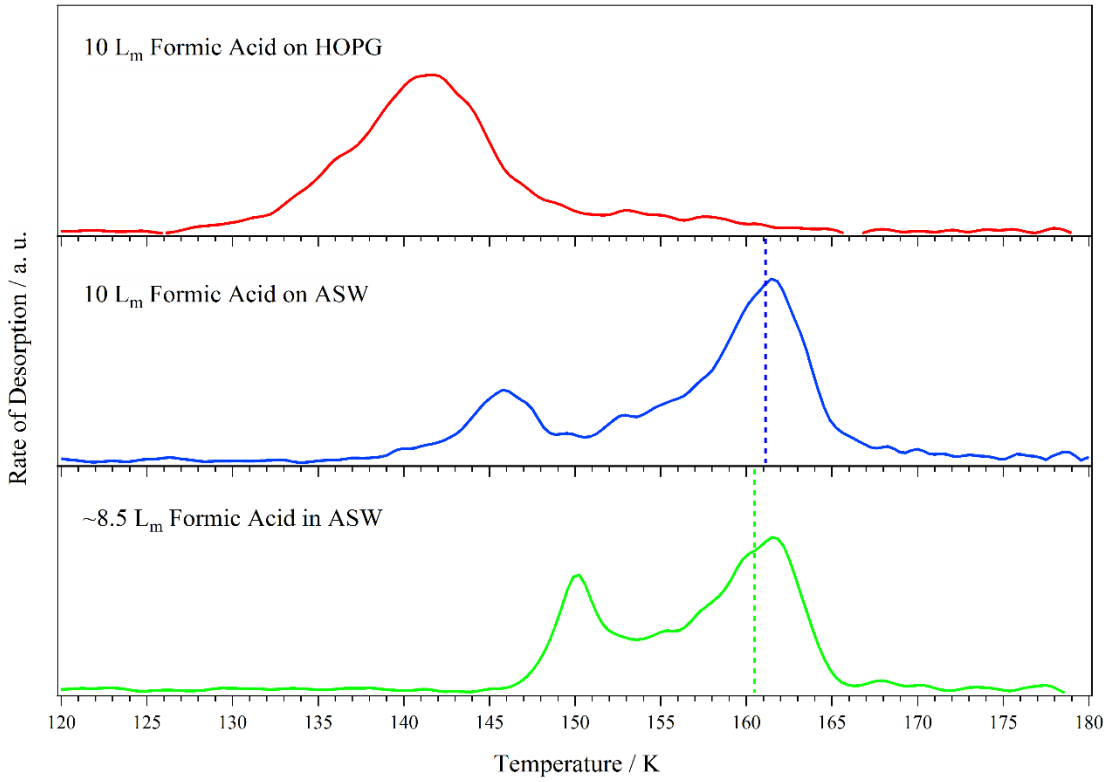

Figure 4.15 – TPD spectra recorded after depositing 10 L_m of formic acid at ~24 K on HOPG (top) and on 100 L_m of water (middle), and ~8.5 L_m formic acid simultaneously with water (bottom). The dashed lines correspond to the peak positions of the corresponding water spectra.

It was proposed earlier in this chapter that the co-desorption feature peaking on the high side of the water peak was due to the strength of the formic acid-water hydrogen bond. If this were the case, then the co-desorption feature of mixtures that contain relatively small amounts of formic acid should peak further above the water peak than the equivalent layer. It can be seen by comparing the different systems in Figure 4.15 that this is exactly what occurs, with the temperature gap between the water peak and the formic acid co-desorption peak is smaller in the layered ice than in the mixture.

A mixture of formic acid and water (20 and 80 L_m, respectively, dosed simultaneously) was examined using RAIRS in order to see if there were any spectral changes comparable with pure and layered systems. The base temperature and a low annealing temperature spectra are shown in Figure 4.16, they are shown alongside spectra from layered and pure ices for comparison. Whilst the layered and pure spectra shown in Figure 4.16 are resulting from larger exposures of formic acid, the amount of formic acid in the mixture was chosen to ensure that formic acid was the minor constituent of a water dominated ice, whilst also ensuring that the features were observable.

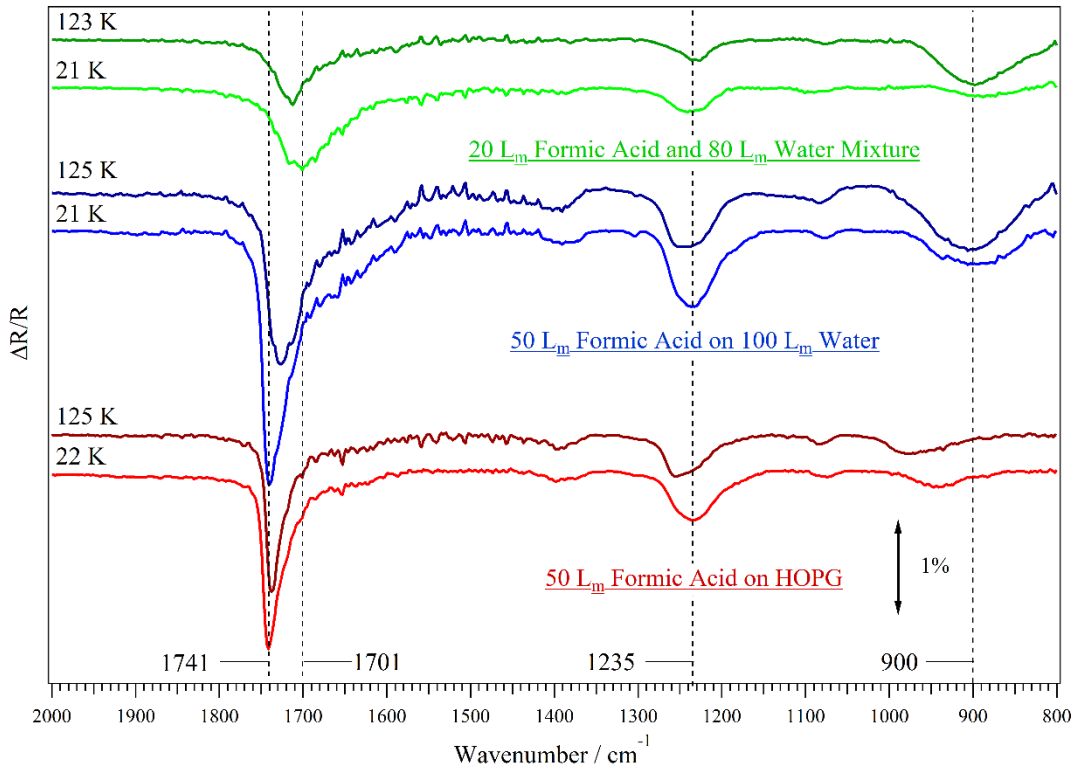

Figure 4.16 – RAIR spectra collected after depositing formic acid in different environments at base temperature (21/22 K) and then annealing to 123 or 125 K. Red traces – 50 L_m of formic acid deposited on HOPG at 22 K. Blue traces – 50 L_m of formic acid deposited on 100 L_m of ASW, both deposited at 21 K. Green traces – 20 L_m of formic acid simultaneously deposited with 80 L_m of water at 21 K.

Figure 4.16 shows that the main features observable in the mixed ice spectra are the formic acid C=O (1701 cm^{-1}) and C-O (1234 cm^{-1}) stretches (νC=O and νC-O, respectively), with the water frustrated libration mode (ν_L) just below 900 cm^{-1}. For the mixed ice, the C-O stretch is centred at approximately the same position as in the layered and pure systems. However, the C=O stretch is ~40 cm^{-1} lower in the mixture. This is to be expected because at 21 K the layered system will consist of two isolated layers of water and formic acid, owing to the immobility of formic acid at 21 K. Whereas, at 21 K, the mixture will already consist of formic acid dispersed throughout the water ice and since the C=O group is heavily involved in hydrogen bonding, a spectral shift is to be expected.

There were no observable changes in the formic acid infrared features for any of the ice systems when annealing to temperatures <123 K. Upon annealing the pure ice to 125 K, the only change in the spectrum is the splitting in the C-O stretching mode (νC-O). Contrastingly, annealing the layered system to the 125 K results in a loss of definition in the C-O stretch and the C=O stretch (νC=O) band red shifts by ~14 cm^{-1} to 1726 cm^{-1}.

Annealing the mixed ice to 123 K results in a blue shift of the C=O stretch from 1701 to 1713 cm^{-1} and the C-O stretch appears to become less symmetric and also red shifts slightly. The C=O stretching mode of the layered system shifting towards the position of the same feature in the mixed ice 123 K spectrum is consistent with thermally induced mixing of formic acid and water. The difference in the position of the C=O stretch modes between the layered and mixed ices is likely to be due to the extent of mixing - partial compared to total, respectively. Further annealing of the mixed ice results in no significant spectral evolution of the formic acid features. This is in contrast to the behaviour observed in pure and layered ices, which show continued spectral evolution. The subtle shifts observed after annealing the mixture to 123 K are likely due to the deposited dimers of formic acid breaking apart and forming stronger hydrogen bonds with the water around them. Above 123 K, there are no changes observed in the peak profiles for the formic acid-water mixture until desorption occurs between 150 and 160 K.

The absence of a low wavenumber shoulder on the C=O stretch and the absence of splitting in the C-O stretch (shown in Figure 4.17) indicate that at no point in the mixed ice does the formic acid crystallise. Figure 4.11 shows that above 136 K there is a degree of splitting evident in the layered ice spectra. This is totally absent in Figure 4.17, thus confirming that crystallisation of formic acid in a formic acid-water mixture does not occur. This is because in a water-dominant ice, the majority of formic acid will be bound to water and since the water-formic acid interaction is stronger than the formic acid-formic acid interaction, it is not energetically favourable to break the formic acid-water bond in order to form chains of formic acid.

As discussed earlier, the amount of formic acid in the mixed ice was less than in the pure and layered ices. The amounts of formic acid and water chosen for the mixed ice was done to ensure that formic acid was the minor constituent, whilst remaining observable in the RAIR spectra. Therefore, whilst the differences between the spectra in Figure 4.16 are concluded to be due to the extent of mixing in the ice systems, coverage effects cannot be conclusively ruled out. However, since there is no spectral evolution in the mixed ice spectra above 123 K (Figure 4.17), it is proposed that the preferred environment of formic acid is embedded within the water ice, rather than in contact with other formic acid molecules.

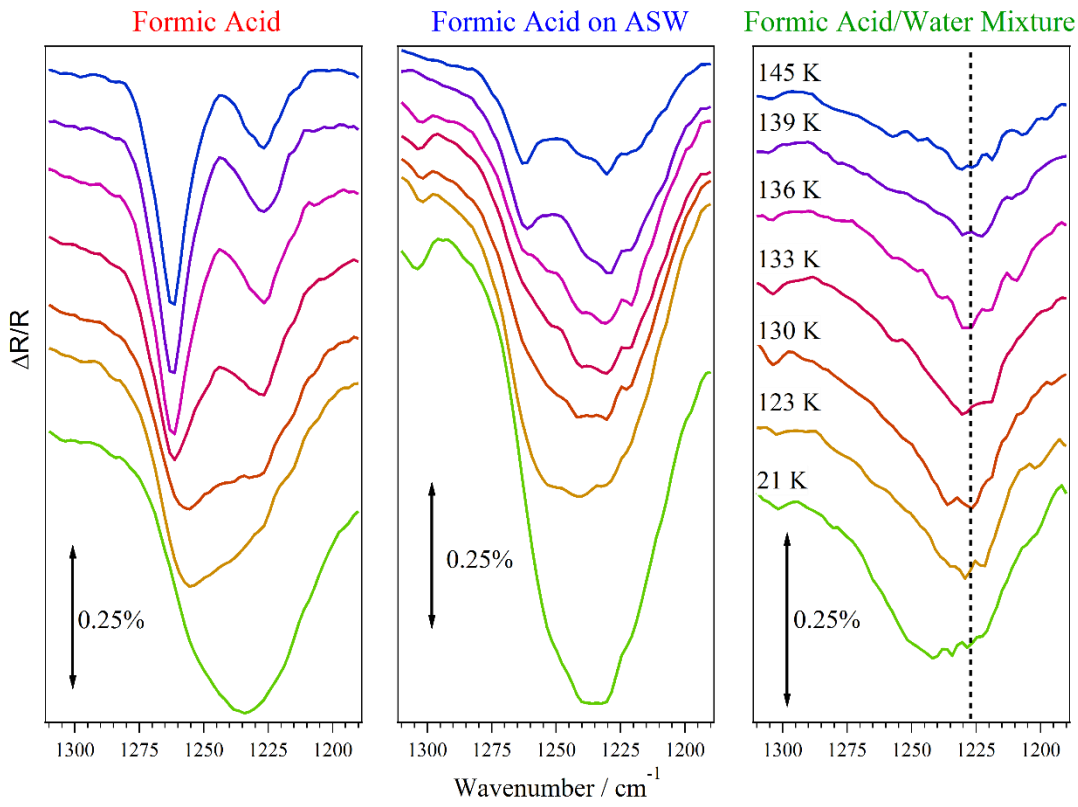

Figure 4.17 – 1310-1190 cm^{-1} region (containing the C-O stretching mode) of RAIR spectra collected after annealing different formic acid containing systems to the indicated temperature. The systems are, from left to right: 50 L_m of formic acid adsorbed on HOPG at 22 K, 50 L_m of formic acid adsorbed on 100 L_m of ASW at 21 K and 20 L_m of formic acid co-deposited with 80 L_m of water at 21 K.

4.3.5 The Effect of Formic Acid on the Structural Evolution and Subsequent Desorption of Water

It was shown earlier that the temperature of the ASW to CI shoulder, and thus formic acid volcano peak, was dependent on the amount of formic acid present. Increasing the formic acid exposure from 5 to 20 L_m results in the ASW to CI shoulder shifting from 150 to 143 K and in doing so, becoming clearer. Further increasing the exposure to 50 L_m sees the shoulder move up to 145 K and become more defined. It is clear from the shifting ASW to CI shoulder and shifting formic acid volcano peaks, that when formic acid is adsorbed on top of water it has a direct effect on the crystallisation of water. Furthermore, this effect of formic acid on the water crystallisation process is dependent on the amount of formic acid. It appears that for relatively thin formic acid films, ASW crystallisation occurs at a lower temperature than when formic acid is absent. However, formic acid exposures that are near or above the point of saturating the water ice (above 20 L_m), result in this effect being reduced.

Using RAIRS, the progression of the ASW to CI phase change can be observed by monitoring the water O-H stretching mode (~3600-3000 cm^{-1}) since it is highly dependent on the structure of the ice. The water O-H stretching mode for the layered system discussed earlier (50 L_m of formic acid on 100 L_m of water) is shown in Figure 4.18.

Below 125 K there are minimal changes in the profile of the water O-H stretching mode. However, upon heating to 125 K, the ice is mobile and has lost some of its amorphous character. This is indicated by the main peak shifting to 3402 cm^{-1} and developing two shoulders at ~3320 and ~3160 cm^{-1}. Between 125 and 133 K there are no observable changes. Annealing to 136 K sees a subtle shoulder appear at ~3280 cm^{-1}, suggesting that the ASW to CI phase change has begun. At 139 K, crystallisation has clearly commenced, evident from the redshift and splitting of the 3402 cm^{-1} feature. Annealing to 145 K shows some additional crystallisation, but it also shows a reduction in intensity, suggesting that a small amount of desorption has occurred. By 150 K the water feature has significantly changed to be comprised of a central peak at 3244 cm^{-1} that has two shoulders at ~3160 and ~3175 cm^{-1}. The spectral profile of water in the 150 K spectrum indicates that the water is fully crystalline, but that it has undergone significant desorption.

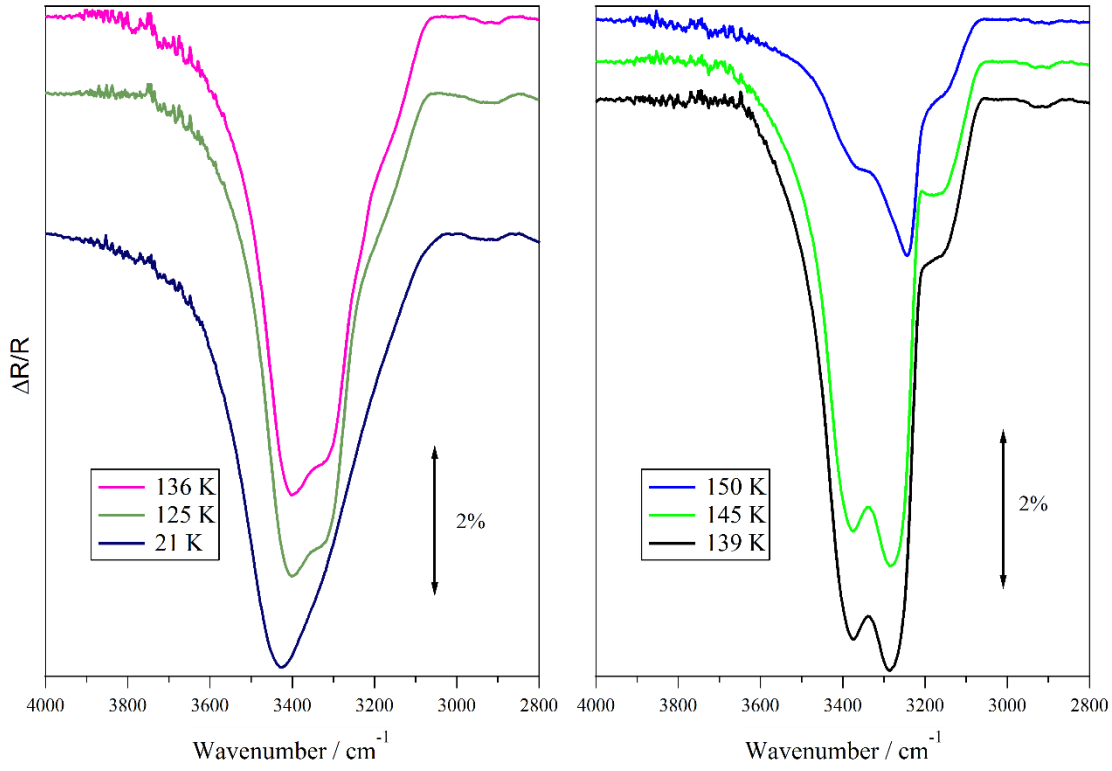

Figure 4.18 – The 3050-4000 cm^{-1} region of the RAIR spectra recorded after a 50 L_m of formic acid on 100 L_m water ice was annealed to the indicated temperatures. Both species were deposited at 21 K.

To examine the effect of formic acid on the crystallisation of water, the RAIR spectra of formic acid containing ices are compared with those of pure water ices – the 100 L_m of pure water is shown in Figure 4.19. The pure water ice is mobile at 120 K, evident by the two shoulders on the low wavenumber side of the main peak. The difference between the 140 K and the 145 K spectra indicates that the ice has fully crystallised. Annealing to 150 K leads to partial desorption of the ice, annealing to 160 K results in total desorption.

Splitting indicative of the commencement of crystallisation is observed at 139 K for the layered ice of 50 L_m of formic acid on 100 L_m of water (Figure 4.18), however, no such splitting is observed at 140 K for the pure water ice (Figure 4.19). This indicates that crystallisation of water starts at a lower temperature in the layered ice than in the pure ice. Full crystallisation of a pure water ice occurs by 145 K whereas for the layered system the ice is still largely amorphous at this temperature. The layered ice only shows full crystallisation by 150 K, at which point a significant amount has already desorbed. Therefore, whilst the onset of water crystallisation is at a lower temperature when 50 L_m of formic acid is present on top of 100 L_m of water, the evolution with increasing temperature is reduced.

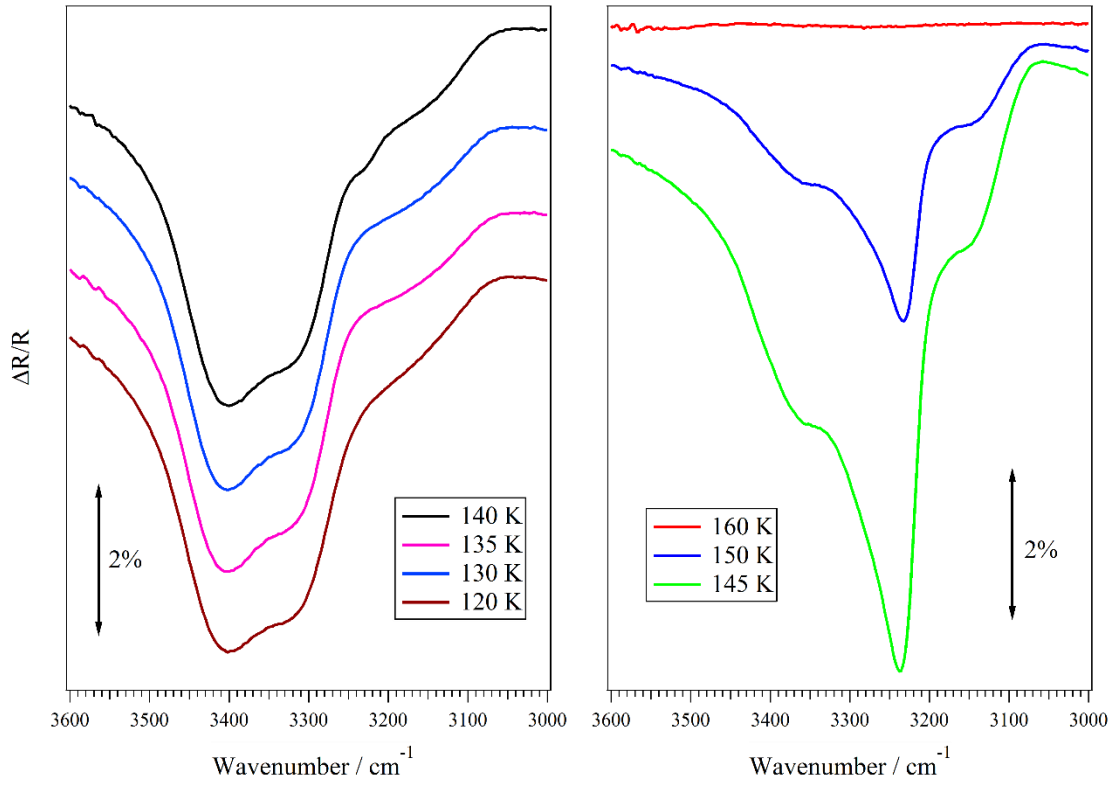

Figure 4.19 – RAIR spectra obtained after annealing 100 L_m of pure water to the indicated temperatures. The ice was deposited on HOPG at ~24 K.

Comparing the 150 K and the 160 K spectra of the pure and layered systems (Figures 4.18 and 4.19) indicates that desorption of the CI is unaffected by the presence of formic acid on top of the water. This is also evident by the water peak temperature observed in TPD spectra of layered ices whereby regardless of the shifting ASW to CI shoulder, the main desorption peak corresponding to CI desorption remains centred at 161 K.

Figure 4.20 shows the 3000-3700 cm^{-1} region (containing the water O-H stretching mode) of RAIR spectra collected after annealing a co-deposited mixture of 20 L_m of formic acid and 80 L_m of water. The traces corresponding to annealing temperatures up to 133 K in Figure 4.20 show the same profile as the spectra obtained after annealing a pure water ice up to 135 K (Figure 4.19) and those obtained after annealing a layered ice up to 133 K (Figure 4.18). At 136 K, as with the layered ice, the co-deposited ice develops a small shoulder at ~3250 cm^{-1}, suggesting that the ASW to CI phase change has just begun. This shoulder is not observed in the pure water ice until 140 K. Further annealing of the co-deposited ice to 139 K results in a high degree of crystallisation, as evident by the large central peak with two distinct shoulders either side of it. This is in contrast to both pure water ices and layered ices where this level of crystallisation is not evident until 145 K and 150 K, respectively. Burke and Brown also observed an early onset of ASW to CI when methanol was co-deposited with the water[188]. Methanol is the corresponding alcohol to formic acid and can hydrogen bond with water and thus it is entirely reasonable that it too would affect water in a similar manner to formic acid.

Upon annealing the co-deposited ice to 145 K, it is possible that the water has crystallised more and the intensity has dropped slightly. The drop in intensity suggests that desorption may have just begun at 145 K in the co-deposited ice. Annealing to 150 K results in almost all of the ice desorbing. Total desorption of the ice is observed after annealing it to 160 K. A small amount of water desorption was also observed for the layered ice after annealing it to 145 K. However, annealing the layered ice to 150 K did not result in as greater intensity loss as observed for the co-deposited ice. It is not clear why there is such a difference in the progression of desorption for the layered and mixed ices, because TPD experiments showed that the desorption of water was comparable for the two ice systems. However, it may be due to the mixed ice having a relatively smaller amount of water than the layered ice. Or it could be due to smaller cluster sizes resulting in a reduced melting point.

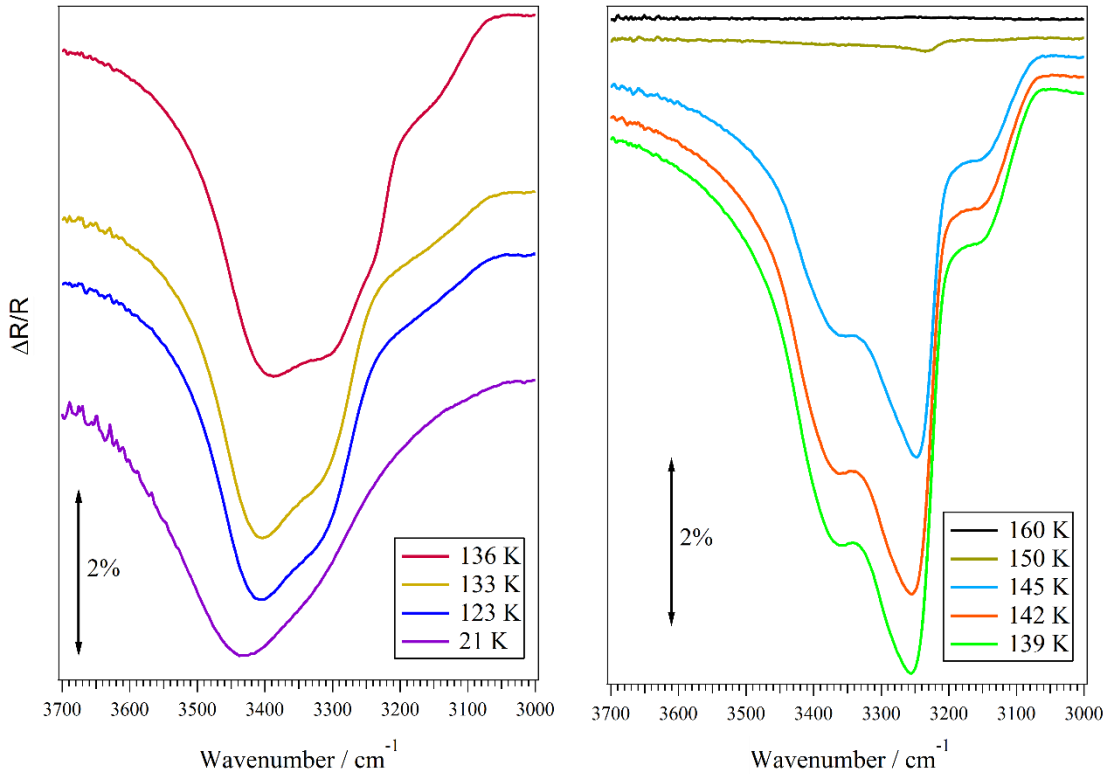

Figure 4.20 – RAIR spectra obtained after annealing a co-deposited mixture of 20 L_m of formic acid and of 80 L_m of water to the indicated temperatures. The ice was deposited on HOPG at ~21 K.

Comparing pure water ice with layered and co-deposited formic acid-water ices it seems that the presence of formic acid causes an early onset of water crystallisation. However, the progress of the phase change is then affected by the nature of formic acid dispersion within the ice. Further investigations, possibly using computational methods, would be needed in order to probe this effect further but one possibility is that formic acid acts as a nucleation point for water crystallisation to start. The difference between layers and mixtures is proposed to be due to the nature of formic acid dispersion throughout the ice. In a mixture, formic acid will be present throughout the ice and provide nucleation points at numerous positions within it. However, in a layered ice, formic acid is present in pores and limited to the upper layers and so the nucleation points will likely be limited to the upper layers of water. This would mean that the effect of formic acid on the onset of crystallisation is lessened in layers compared to mixtures.

4.4 Summary

The interactions between formic acid and water have been shown to be complex. Formic acid can strongly bind to water, and in doing so, can remain within a water ice until most of the water has desorbed. This is the case for both layered and mixed ices systems,

meaning that the accommodation of formic acid within water ices above its natural sublimation point should be accounted for in ISM chemical models. The amount of formic acid that can be accommodated is dependent on the amount of water present. If the water ice becomes saturated with formic acid, the formic acid forms pure layers on top. These layers of formic acid desorb at approximately the same temperature as formic acid on HOPG. However, when there are sufficient amounts of formic acid on the surface, formic acid can crystallise. This crystalline formic acid then undergoes desorption at a higher temperature than when formic acid is deposited on HOPG. The desorption processes of formic acid-water systems are summarised in the cartoons shown in Figure 4.21.

An alternative interpretation of the data presented here is that there is direct desorption of formic acid from the HOPG substrate. When water is deposited onto HOPG the initial stages of ice growth is via the formation of 2D and then 3D islands.[141,212] If the exposure of water is sufficiently low, there will be islands of ASW with bare patches of HOPG. Therefore, the adsorption of formic acid would occur onto ASW and onto HOPG. Formic acid desorbing directly from the HOPG could give rise to feature γ and peak δ if there was enough formic acid such that the relative amount adsorbed on the HOPG was significant.

The alternative interpretation of the data presented here has been dismissed for several reasons. The first reason for dismissal of the alternative explanation comes from analysis of water TPD experiments. It has been shown on the experimental set-up used here that water exposures of greater than 6 L_m result in no bare patches on the HOPG and that the observation of the ASW to CI phase change indicates significantly thick multilayers.[141] Water multilayers in this work are confirmed by analysis of the TPD spectra shown in Figure 4.8 where it is clear that both 50 and 100 L_m of water demonstrate multilayer desorption. The second reason for dismissal comes from analysis of the formic acid TPD spectra. The onset and peak temperatures for feature γ and peak δ should be closer to the temperatures seen in Chapter 3 if they were resulting from formic acid directly desorbing from HOPG. Furthermore, if there were bare patches of HOPG it would be probable that the desorption of crystalline formic acid would be observed prior to saturation of the water layer. The clear link between these events is indicative of a solid water layer with no bare patches of HOPG.

Formic acid shows multiple desorption features for both layered and mixed ice systems, summarised in Figure 4.21. Collings *et al.*[38] and Viti *et al.*[154] suggested that formic acid desorption can be modelled as a single process at the same temperature as water, this clearly needs revision. All the layered systems studied here show a desorption pathway linked to the ASW to CI phase change (see the 145 K cartoon in Figure 4.21), as well as co-desorption with water (see the 160 K cartoon in Figure 4.21). Thicker layers of formic acid also exhibited desorption from the surface of the water. However, whilst modelling formic acid as an intermediate molecule by Collings *et al.*[38] and Viti *et al.*[154] would better describe its desorption mechanism in astronomically relevant ices, it would not account for the effect of formic acid on the crystallisation process of water. The model used does not allow for the other species influencing the desorption or structural changes of water. Further to this, reclassification would not account for the variation in the co-desorption temperature that is dependent on the relative abundance of formic acid with respect to water. As was mentioned above, further studies are needed to fully understand the ASW to CI phase change dependence on the presence of hydrogen bonding capable molecules. Formic acid is found in numerous regions of the ISM (as discussed in Chapter 3) and so accurately modelling its desorption in the presence of water (the most abundant species in interstellar dust grain icy mantles) is key to properly understanding the evolution of interstellar ices. Furthermore, models that are reliant on the kinetics of water that do not allow for variations in the processes of water may be too simple.

Whilst it is clear from work presented here that there are several formic acid-water environments, there was no evidence for the desorption of complexes or for ionisation of formic acid. Therefore, any proposed reaction pathways that require the formate ion must account for its production via routes other than thermally induced reactions with water.

In addition to its ability to be accommodated in water ices, formic acid was shown to have a direct effect on the crystallisation of water. It appears that the presence of formic acid on water causes an early onset of the ASW to CI phase change. The temperature that the phase change is observed at is dependent on the relative amount of formic acid present. Mixtures of formic acid and water also show that the water phase change is dependent on the relative amount of formic acid. As with methanol-water mixtures,[188] formic acid co-deposited with water results in an early onset of the ASW to CI phase change. This has an important implication in the ISM, where the onset of the water phase change, and

the resultant volcano desorption of volatile species (such as CH_4, H_2S, CO_2 and SO_2[38,154]), is a significant route for these species into the gas phase. Future work could include how the water phase change is affected when small quantities of hydrogen bonding species (such as formic acid, methanol and acetic acid) are present together in a water ice. Computational studies might be used to study the process and dynamics of crystallisation when there is a nucleation point capable of forming multiple hydrogen bonds, such as formic acid, present within the water.

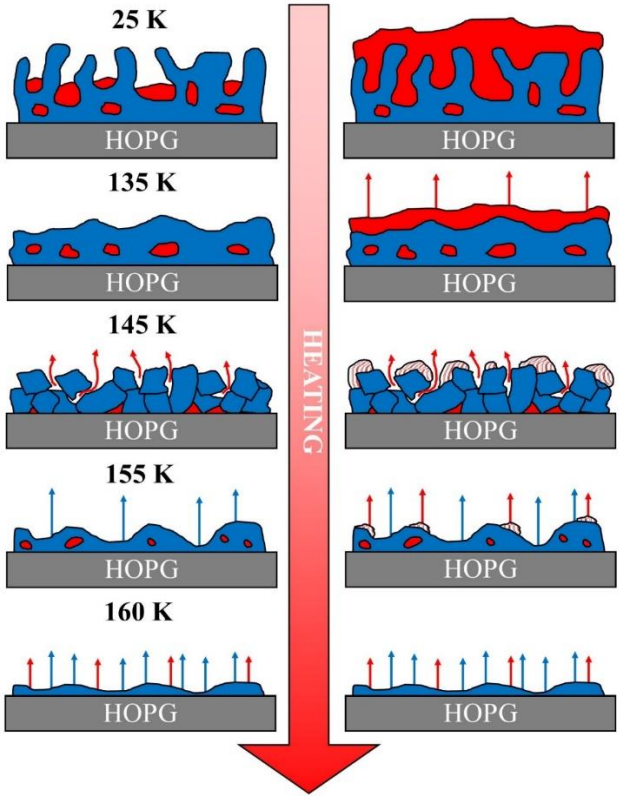

Figure 4.21 – Cartoon summarising the behaviour of formic acid (red) adsorbed on a layer of ASW (blue) under laboratory conditions (not to scale). The left-hand side depicts a thin layer of formic acid and the right-hand side depicts a layer of formic acid that has saturated the ASW. The red lined segments on the right-hand side are to indicate crystalline formic acid.

A key finding relevant to the ISM is that even if formic acid were formed on the surface of a water ice, it is likely to diffuse into the water prior to desorption. This would in turn increase its residency time on the surface of grains and put it in direct contact with multiple water molecules, thus allowing it time to react and form more complex organic species. This is fundamental to the chemical evolution of interstellar ices since formic acid shares structural similarities with several fundamental pre-biotic molecules, such as acetic acid, glycolaldehyde and glycine.

5 Examining Compaction of Amorphous Solid Water Using Temperature Programmed Desorption

5.1 Introduction

The presence of water in the interstellar medium (ISM) is well established. It is widely acknowledged that water is the most abundant species in the ices that form around dust grains[213] and that this water usually has an amorphous structure.[88,111,214] In addition to its abundance throughout the ISM, amorphous solid water (ASW) is thought to exist within the Earth's mesosphere between 81 and 92 km from the surface.[215] ASW is one of several phases of water, with the latest count being sixteen crystalline phases and two amorphous phases.[115–117] The simplicity of the molecular structure of water and its importance in several terrestrial and interstellar processes makes it a fascinating molecule to study.

There is disagreement in the literature as to the presence, identity and naming of the related structures that fall under the umbrella of ASW. A paper often cited in the literature by Jenniskens and Blake[129] refers to two polymorphs of ASW: high-density and low-density amorphous ice, HDA and LDA. They reported that deposition below 38 K results in porous HDA formation. Upon heating to between 38 and 68 K, a gradual transition to LDA occurs. When LDA is heated above ~130 K it converts to crystalline ice (CI). More recent work suggests that there are actually three distinct forms of ASW: HDA, very high-density amorphous ice (VHDA) and LDA.[115,116,216] However, recent astrochemistry literature does not discuss HDA/VHDA and LDA, rather, two morphologies of ASW: porous ASW (pASW), and compact ASW (cASW).[38,111,113,217,218] Upon heating, pASW undergoes an irreversible transition to cASW and then goes on to form CI.[38,107] Comparison of the literature indicates that HDA/VHDA are related to pASW and LDA is related to cASW.[38,41]

The ability of ASW ices to trap volatile species is well documented and has been linked to the retention of these species above their natural sublimation temperatures in the ISM.[38,219] This retention allows species the time and space to interact and potentially react, thus contributing to the chemical evolution of the ISM.[113,114,220,221] Studies show that it is the thermally induced compaction of pASW to cASW that is the mechanism by which ASW traps and retains these volatile species.[38,41] Without the large surface area offered by highly porous ASW and a mechanism to retain volatile species, it would be

unlikely that the chemical evolution of the ISM could be as elaborate as reported. In the discussions within this work porosity and surface area can be differentiated by considering the accessible surface. Porosity is a global measure of the void spaces within a material whereas surface area refers only to the area that is accessible from the vacuum, i.e. that which is on the surface.

It has been suggested that the non-detection of the O-H dangling mode of water (~3690 cm^{-1}) in interstellar vibrational spectra is an indication that ASW in the ISM is only found as cASW, and is thus non-porous.[15,109] However, recently published work by Isokoski *et al.* found that non-detection of the O-H dangling bond is not necessarily proof of full compaction, nor a total lack of porosity,[111] a conclusion also supported by Cazaux *et al.*.[112] It has also been proposed that due to the wide range of environments in the ISM, stellar events may alter already deposited ices that were originally porous.[112–114] Bombardment of ices by cosmic rays and UV radiation has been proposed to compact porous ices.[220,222,223] For example, Raut *et al.* showed that when water ices were bombarded by Ar^+ ions, used to simulate cosmic rays, they underwent compaction and a decrease in porosity.[220] Whilst the literature does not fully confirm the detection of pASW, it is certainly believed to exist at some stage of a dust cloud's life.[113,130]

Much of the literature regarding ASW focuses on methods for controlling the porosity of ices prepared in the laboratory. One of the main experimental variables examined is the angle of incidence during deposition. With regards to the ISM, the nature of accretion to surfaces is, in most cases, expected to be omnidirectional, i.e. random. However, deposition along the normal to a surface has been considered, for example when an object or particle passes through an interstellar cloud.[114]

To study the dependence of porosity and density on the angle of incidence, molecular beams are usually employed. Molecular beams allow a high degree of control over the angle at which molecules impinge on the surface. The consensus is that for angles of incidence close to the surface normal (~0°), water ices are compact and non-porous. As the angle is increased, ices adopt more porous structures. However, depending upon the nature of the study, above 70-86° the porosity drops and the ices become more compact.[130,133,224] It is reported by some that when the highest angles of incidence are used, the densities obtained are close to those obtained by background deposition.[224] Whilst the density may be comparable to background deposited ices, the micropores

formed by molecular beams are expected to be different to those formed by background deposition.[131,224] Molecular beams can also be used to control porosity by varying the collision energy of molecules. As the collision energy is increased, the porosity drops.[132] Therefore, the least dense and most porous water ices are prepared using low energy molecular beams at grazing angles or by background deposition.[40]

Although the effect of deposition method on density and porosity is generally well understood, the literature has not reached a consensus on how the structure of ASW changes with temperature. It is accepted that elevated deposition temperatures or annealing to higher temperatures will result in a decrease in porosity, a consequence of the pASW to cASW transition. However, the range and progression of this change is not agreed upon within the literature.

Mitterdorfer *et al.* recently highlighted how the different morphologies of ASW behave when subjected to increased temperatures.[217] They compared four systems: directional fast dosing, directional slow dosing, background fast dosing and background slow dosing. It was reported that even though all ices were prepared at 77 K they were pASW, rather than cASW, as some of the previous literature suggested should be the case.[41,129] Upon heating of all systems, the dominant process below 120 K was pore clustering. However, upon reaching 120 K, the background deposited ices underwent collapse of their micropores. Micropore collapse was not observed for the directionally dosed ices until the temperature reached 140 K. The background deposited ices were reported to have a considerably different structure compared to the directionally dosed ices, with the former being rather flat and the latter being composed of tower-like structures.

One of the earlier works often cited in the literature used electron diffraction to identify a transition from HDA to LDA between 38 and 68 K[129]. Below 38 K and between 68 and 120 K they observed no evolution in the structure of the ice. In contrast, Stevenson *et al.* found that, for all angles of molecular beam deposition and for background deposition, the porosity of the ice decreased immediately after the ice was heated above 22 K.[133] They reported that around 90 K all the ices studied had dropped to near-zero porosity.

A study by Collings *et al.*, using CO adsorption on ASW studied with infrared spectroscopy and TPD, found that whilst the amount of CO trapped immediately decreased at water deposition temperatures higher than 8 K, the apparent change from

HDA to LDA was complete by ~60 K.[40] They examined the fraction of CO trapped as a function of water deposition temperature. A drop from ~45 % to ~0% trapping was observed as the water deposition temperature was increased from 8 to ~60 K. They also note that above 70 K, the ice structure is still changing and one possible consequence of this is a continued loss of porosity. Each data point obtained by Collings *et al.* corresponded to an individual TPD experiment, where the water was deposited at a given temperature and then CO was deposited on top of the cooled water ice. Collings *et al.* therefore rationalised the differing progressions of the phase change reported by them and by Jenniskens and Blake to the relationship between the effective heating rates in each study and the kinetics of the phase change. Whilst Jenniskens and Blake used a laboratory scale heating rate of ~2 K min^{-1}, Collings *et al.* essentially used an infinitely slow heating rate.

Further work on the thermal evolution of ASW by Bossa *et al.* found that between 20 and 120 K there was a gradual decrease in thickness and porosity.[113] They found that for pASW (grown by background deposition) the decrease in thickness was 12%, whilst for cASW it was much less.

Isokoski *et al.*[111] noted that the previously reported decrease in thickness of 12% by Bossa *et al.*[113] was actually the upper limit and that pASW (grown by background deposition) is never fully compacted, with residual porosity being up to 17 ± 3% at 120 K. They also stated that, even though not observable by infrared spectroscopy, cavities can remain in the water ice up to desorption. As with the previous work by Bossa *et al.*,[113] Isokoski *et al.*[111] reported that the structure of the ice was continuously evolving between 20 and 120 K.

A recent study by Cazaux *et al.* used computational models and astronomically relevant time scales to study the structural evolution of pASW with increasing temperature.[112] They report that significant changes in porosity occur between 30 and 50 K. The pores do not collapse, rather they merge to make a smaller number of larger pores. The authors recognise that differences will arise between their findings and those in the experimental literature owing to the significantly different heating mechanisms used.

A number of the studies discussed above, as well as others in the literature, have made use of probe molecules, or spectator molecules.[40,130–133] These are 2nd or 3rd party species

whose presence is designed to yield information about the primary species of interest, in this case, water. The choice of the probe was made by considering the information required and the nature of the primary species. Probe molecules have also been used to study the ASW to CI phase change and to demonstrate porosity in other species. An example of which is the use of xenon atoms by Souda to probe the porosity of formic acid.[186]

A novel use of a 2nd party molecule was made by Smith *et al.*, who used CCl_4 to probe the molecular volcano that occurs as a result of the ASW to CI phase change.[42] By placing CCl_4 either on top of or below a much larger water layer, they identified the cause of the molecular volcano as being the formation of pathways throughout the water overlayer during crystallisation. CCl_4 was chosen as it would not bind to the water and would therefore not influence the phase change. Subsequent work used the selective placement of seven different molecular/atomic species to gain an insight into the propagation of crystallisation-induced cracks.[225,226]

From the discussion above, it has been shown that the thermal evolution of ASW is still not fully understood and that probe molecules can yield valuable information regarding ice structures and their evolution. Therefore, building on the work by Collings *et al.*[40] and using similar experimental methods, the work presented here will make use of two probe molecules (CO_2 and CS_2) to track the decrease in the porosity of ASW. These results will then be compared with those obtained by Collings *et al.* using a CO probe.[40] CO_2 was chosen as it cannot hydrogen bond, it is structurally similar to CO and has been shown to trap within ASW.[140] CS_2 was chosen for similar reasons: its inability to hydrogen bond, structural similarity with CO_2 (same molecular shape but larger) and its ability to trap within ASW.[140] Any apparent differences in the behaviour of the water in the presence of CO_2 and CS_2 can be used to ascertain further information regarding the pASW to cASW transition in the presence of a probe molecule.

To track the phase change, water ices were prepared at different temperatures over the range of temperatures that feature in the literature. Once the water was prepared and substrate cooled back to base temperature, the probe molecule was dosed on top of the water. This method is based on that used by Collings *et al.*,[40] and thus hopes to produce ices that are comparable to those that they studied. Once the TPD heating ramp starts, the probe molecule will become mobile and will diffuse into the water ice. The amount of

probe that can be trapped within the water ice is dependent on the level of porosity. By examining the way in which the amount of probe molecule trapped varies with water deposition temperature, the progression of the transition from pASW to cASW can be determined. By using two different probes and comparing the results with those from the CO work by Collings *et al.*, the effect of probe identity on the observed temperature range of compaction can be better understood.

Chapter 4 showed that the presence of formic acid had a direct effect on the ASW to CI phase change. Therefore, to investigate whether formic acid has a similar effect on the ASW compaction process, a small amount of formic acid will be included in the CO_2-water system. However, due to experimental complications detailed in Section 5.4.3, the results of this part of the investigation are preliminary.

5.2 Experimental

Water and formic acid were handled in the same manner as described in sections 4.2 and 3.2, respectively. A CO_2 (BOC, 99.98%) cylinder was attached to the gas line by a regulator. The gas line was filled with CO_2 and then isolated from the cylinder. CS_2 liquid (Sigma Aldrich, ≥99.9%) was attached to the gas line by a glass dosing vessel. The CS_2 was subjected to several freeze-pump-thaw cycles to remove any absorbed impurities. The surface of the liquid was briefly pumped on prior to filling the gas line to further ensure that the CS_2 was not contaminated with impurities.

The amount of adsorbate admitted to the chamber is measured in Langmuir (1 L_m = 1 × 10^{-6} mbar s). The dose amounts used here are significantly lower than those used in Chapters 3 and 4 because in the experiments described here, the ices were grown via directional dosing. Using directional dosing means that to grow an ice of a particular thickness, a smaller dose is required than if background dosing were used. By using smaller doses, experimental times are decreased and the time between bake outs is increased, both of which are highly beneficial for maximising the experimental throughput.

During dosing and TPD mass 18 was scanned for water, mass 29 for formic acid, mass 44 for CO_2 and mass 76 for CS_2. These masses were used as they are the main cracking fragments of the relevant species and therefore give the largest signals. TPD experiments were conducted using a heating rate of 0.50 ± 0.01 K s^{-1}.

Layered ices were prepared by first depositing water and then depositing the probe on top. During water deposition the highly oriented pyrolytic graphite (HOPG) substrate was held at a given temperature. After deposition, the elevated temperature was held for a further two minutes. This was done to ensure that any water that was in the chamber, but not yet adsorbed, would adsorb whilst the substrate was still at the relevant temperature. After this, the substrate was cooled to base temperature (~22 K) and the probe was then deposited onto the water. This method assumes that upon cooling the water ice it does not change structure, a valid assumption since the literature reports that the compaction process is irreversible.[38,107]

Layers were used, as opposed to mixtures, because it allows the probe to be deposited with the substrate at base temperature (~20 K), regardless of the thermal processing of the water. If mixtures were deposited in the manner detailed above, then it is likely that when the substrate was held at high temperatures, a large proportion of the probe molecules would not adsorb, due to a reduced sticking probability, and would simply be pumped away.

5.3 Calibration Experiments

A range of experiments were performed to calibrate the experimental procedure and ice system used here. These experiments were concerned with establishing the nature of the behaviour and amount of probe used, and to the thermal processing techniques that could be used.

5.3.1 CO_2 Calibration Experiments

Before a discussion of TPD experiments involving water and CO_2, the amount of water chosen should be addressed. The amount of water was chosen to ensure that thick multilayers were prepared. Thick multilayers of water are needed to make sure that there was no bare HOPG.

Figure 5.1 shows the TPD spectra recorded after depositing 1-2 L_m of water on HOPG at ~22 K. It is clear from Figure 5.1 that the traces have shared leading edges and that the peak temperature increases from 161 to 166 K as the water exposure is increased from 1 to 2 L_m. These observations indicate that water is forming multilayers on the HOPG.[44] Therefore, 1.5 L_m was chosen as this exposure of water clearly forms multilayers.

The next stage of calibrating the system was to determine the amount of CO_2 to deposit on top of the water layer. Figure 5.2 shows example TPD spectra of 0.1, 0.2 and 0.3 L_m of CO_2 deposited on 1.5 L_m of ASW, where both species were deposited with the substrate at ~22 K.

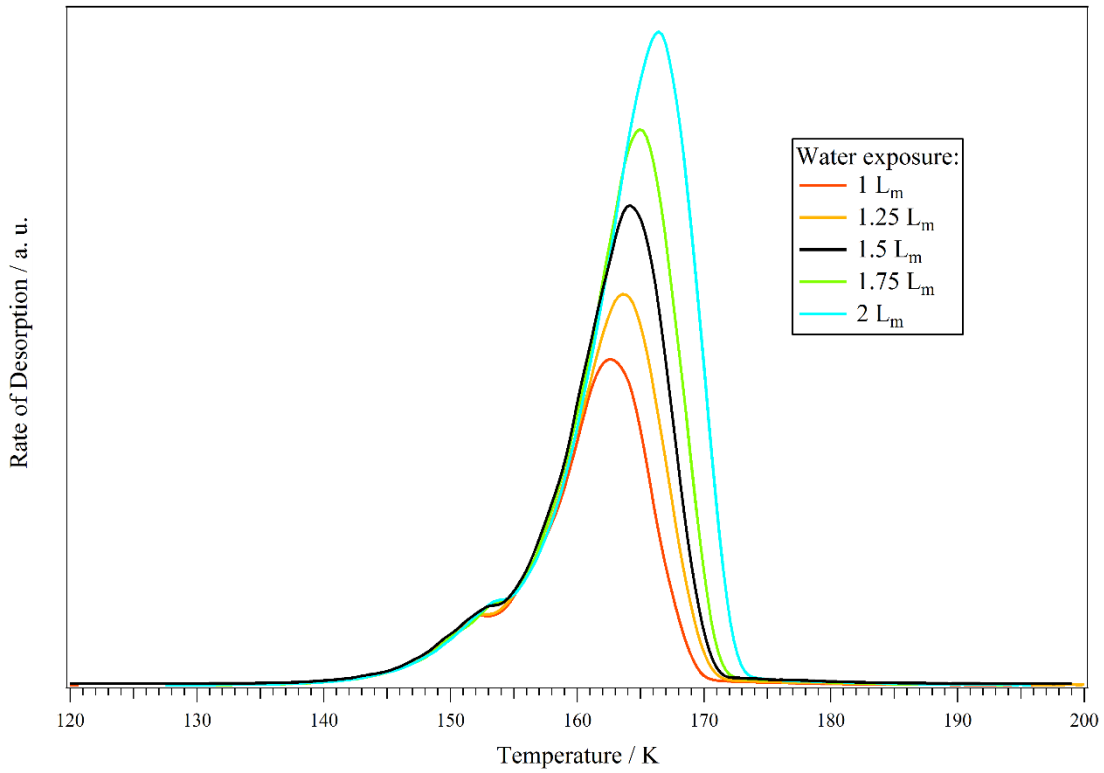

Figure 5.1 – TPD spectra of different amounts of water (1-2 L_m) deposited on HOPG at ~22 K.

Three key CO_2 features can be identified in Figure 5.2 at 84, 150 and 162 K. The broad feature at 84 K corresponds to desorption of CO_2 from the surface/near-surface of the ASW ice. The sharp peak at 150 K corresponds to trapped CO_2 that explosively desorbs through pathways created as the ASW transitions to CI. The plateau centred at 162 K, which is coincident with the main crystalline water peak, corresponds to co-desorption of CO_2 with CI. Co-desorption is present when a portion of the trapped adsorbate does not desorb during the ASW to CI phase change and remains trapped until the water around it desorbs. These observations are consistent with those seen previously for CO_2 deposited on ASW, where both species had been deposited below 30 K.[140,206]

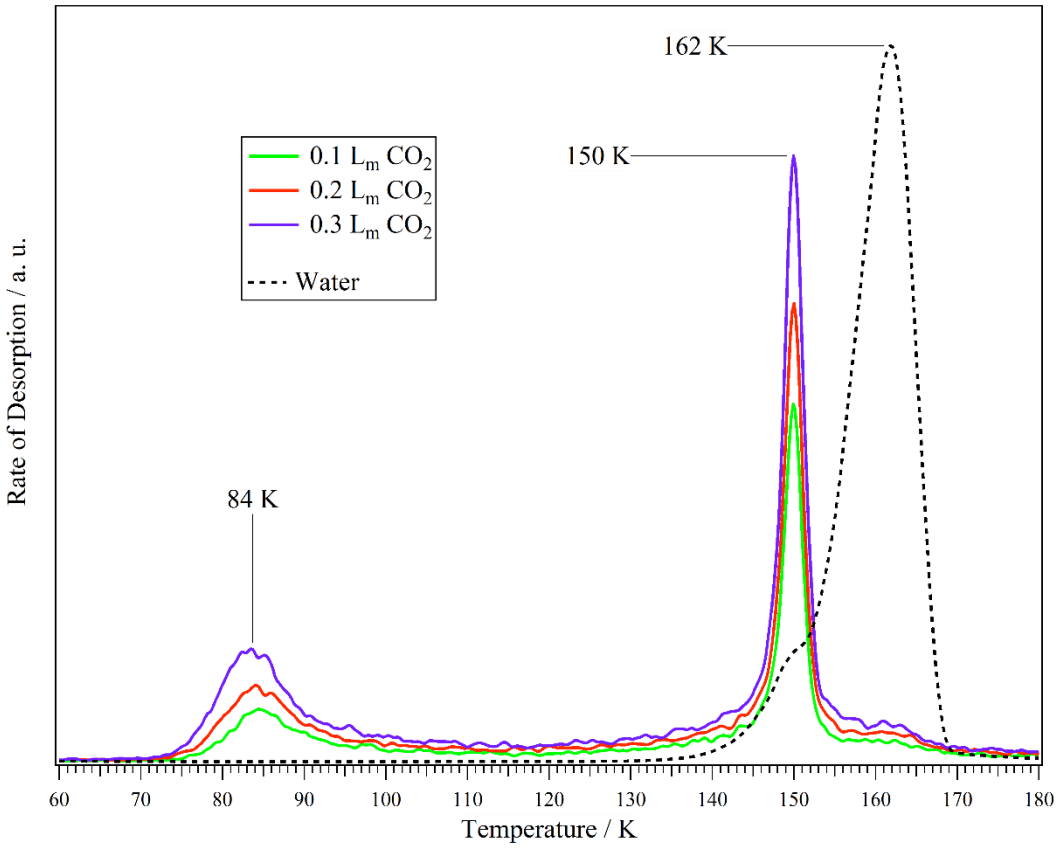

Figure 5.2 – TPD spectra obtained after 0.1, 0.2 and 0.3 L_m of CO_2 were deposited on 1.5 L_m of ASW. All deposition occurred with a substrate temperature of ~22 K.

Whilst it is not possible, using the experimental set-up used in this work, to determine the exact nature of the water structure at ~22 K, the presence of the features at 150 and 162 K in Figure 5.2 indicate that the water ice is highly porous and amorphous. The amorphous nature of the water is confirmed by the observation of the ASW to crystalline phase change TPD shoulder at 150 K.[141] The high porosity of the ASW is confirmed by the clear and distinct volcano and co-desorption peaks, at 150 and 162 K respectively.[38] If the ASW was not highly porous, these features would be significantly smaller or totally absent. Therefore, whilst the water is deposited directionally, it does not form the compact ASW that is observed for directional deposition by molecular beams. Hence, provided that the position of the surface relative to the leak valve is kept constant for all experiments, then any changes in behaviour are due to other factors, such as the substrate temperature during water deposition. Non-porous or compact ASW can also be prepared with this set-up by depositing water at an elevated substrate temperature.

The amount of probe molecule chosen was regulated to ensure that saturation of ASW did not occur when deposited at ~22 K. The experimental analysis relies upon comparing

the amount of probe molecule trapped and the amount that desorbs from the surface/near-surface as a function of water deposition temperature. This can be done by comparing the areas of the relevant TPD peaks because the area under a TPD curve is directly proportional to the coverage.[123] This method of analysis is based on the method employed by Collings *et al.*.[40] If the water ice was saturated prior to the ice being prepared at elevated temperatures, then this would artificially affect the relative amounts of probe molecule in each environment for a given water growth temperature.

In order to check for saturation of the water, a range of CO_2 doses were deposited on top of the same amount of water, with the sample in the same position and at the same temperature. The amounts chosen were 0.1, 0.2 and 0.3 L_m of CO_2 on top of 1.5 L_m of water and the resulting TPD spectra are shown in Figure 5.2. There is no significant variation between the water spectra in each case and hence only one is shown for clarity.

It is clear from Figure 5.2 that all three features - surface, volcano and co-desorption - increase with dose. The increase in the volcano and co-desorption peaks between 0.1 and 0.3 L_m suggests that the water ice has not become saturated over this range; if it had been, these features would not grow with the increased exposure. This therefore indicates that an exposure of 0.2 L_m of CO_2 on 1.5 L_m of water is suitable for use in these experiments. 0.2 L_m of CO_2 was also sufficient to ensure that the three features are clear and well defined. Desorption features that are clear and defined are crucial because the analysis method utilised in this chapter is reliant upon obtaining an accurate measure of the areas of these features (Section 5.4.1.1 gives a complete discussion of the analysis method).

5.3.2 CS_2 Calibration Experiments

When CS_2 is deposited on a layer of water adsorbed at ~22 K, the resulting TPD spectrum also displays three key features. These three features are shown in Figure 5.3 and occur at 110, 150, and 163 K. These peaks correspond to desorption of CS_2 from the surface/near-surface, volcano desorption of CS_2 and co-desorption of CS_2 with CI. All three occur at temperatures comparable to previous work conducted using the experimental set-up utilised here[140]. The temperatures of the volcano and co-desorption peaks in Figure 5.3 are the same as those seen for CO_2 in Figure 5.2, since these processes are governed by the water, rather than the probe. In contrast, the surface desorption feature for CS_2 (110 K) occurs at a much higher temperature than that for CO_2 (84 K) because CS_2 bonds more strongly to the ASW surface than CO_2.

As for CO_2, the amount of CS_2 used was chosen to ensure that saturation of the water layer did not occur. Figure 5.3 shows a selection of the saturation tests conducted using CS_2 deposited on 1.5 L_m of water.

As seen in Figure 5.3, between 0.05 and 0.2 L_m the volcano peak continues to increase with increasing CS_2 exposure. This indicates that CS_2 exposures between 0.05 and 0.2 L_m do not saturate the underlying water layer. Therefore, using 0.1 L_m of CS_2 with 1.5 L_m of water will mean that if there is any slight variation in the CS_2 dose, the water will not saturate. During the design of these experiments it was considered that the amount of probe was acceptable as long as it did not saturate the water, hence why the amount of CS_2 does not match the amount of CO_2 used.

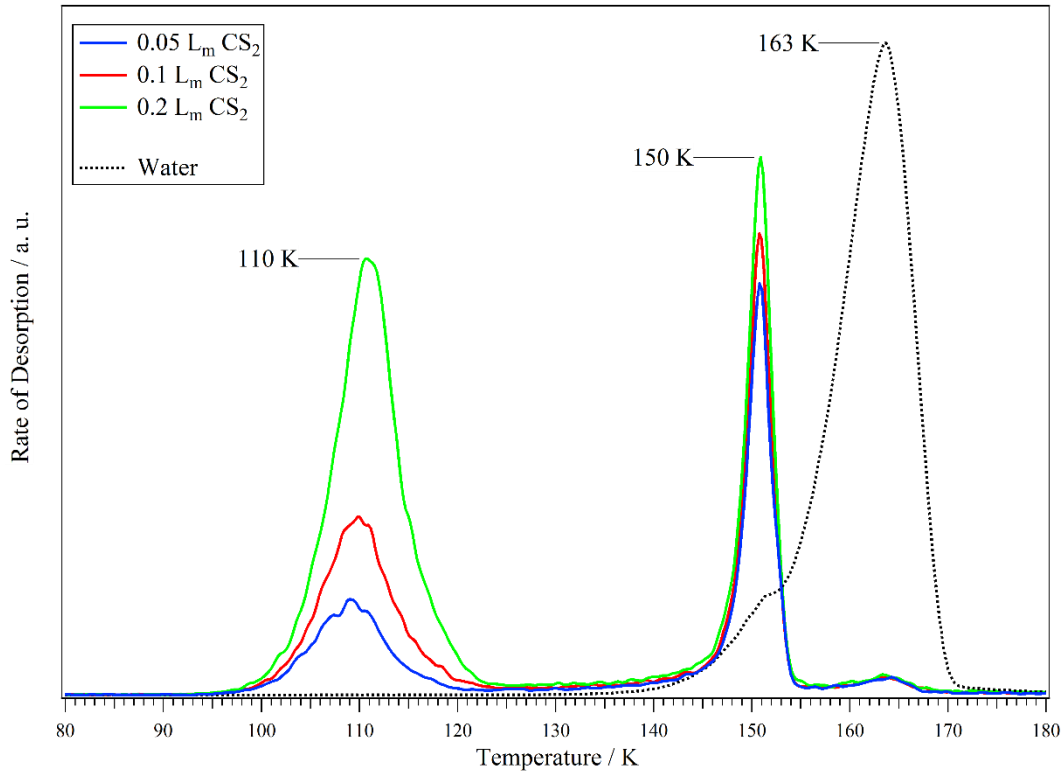

Figure 5.3 – TPD spectra of 0.05, 0.1 and 0.2 L_m of CS_2 on 1.5 L_m of water. Both species are deposited at ~22 K.

5.3.3 Water Calibration Experiments

Thermal processing of an ice can be examined in two ways: by growing the ice at base temperature and then annealing to the desired temperature, or by holding the surface at

the given temperature whilst depositing the adsorbate. The two methods differ in practical and chemical/physical senses.

If dosed at a given temperature, the ice will immediately adopt the most stable structure for that temperature. Upon annealing, the ice will rearrange to adopt the preferred structure, adding a kinetic aspect to the process. If the ice is not annealed for long enough, then the transformation will be incomplete and there will be regions within the ice with differing structures. A practical issue that arises from annealing, particularly to high temperatures, is that if the required annealing time is very long then the sample will also take a very long time to cool down, thus significantly extending the time for an experiment. This is a property of the experimental set-up, rather than a property of the water ice.

Several test experiments were conducted to examine the effect of increasing the annealing time. These tests involved dosing 1.5 L_m of water, with the substrate at ~22 K, and then annealing it to 60 K for 5, 10 and 15 minutes; annealing temperatures were reached by heating at 0.5 K s^{-1}. After the water had been annealed and the substrate was cooled back to ~22 K, 0.2 L_m of CO_2 was deposited on top and a TPD spectrum taken. The resulting TPD spectra are shown in Figure 5.4, with the inset being the percentage of CO_2 desorbing from trapped environments for each annealing time. The error bars on the inset are calculated using the standard deviation of the average ratio between the total CO_2 and water TPD areas.

Whilst there are clear differences between the annealing spectra and the spectrum that results from dosing water at 60 K, there are only subtle differences between the individual annealing spectra. As the annealing time increases the surface/near-surface desorption peak slightly increases, approaching that which is observed when water is dosed at 60 K. Any changes in the volcano and/or co-desorption features are difficult to see. The slight increase in the surface/near-surface peak with increasing annealing time indicates that more of the CO_2 is remaining on the surface of the ice, rather than being trapped. The decrease in the ability of the water to trap CO_2 suggests that the structural evolution is linked to the annealing time, as expected. It also demonstrates that annealing for less than 15 minutes will result in incomplete transformation of the ice structure.

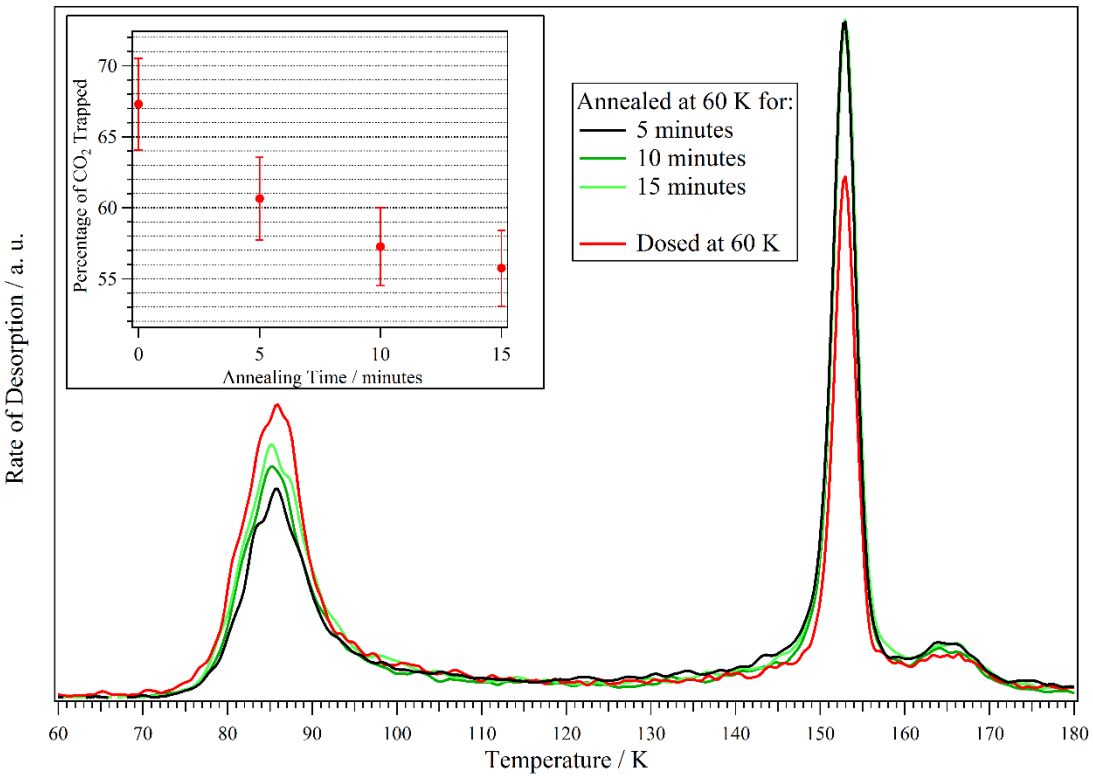

Figure 5.4 – Main figure: CO_2 TPD spectra obtained after 0.2 L_m of CO_2 was deposited on 1.5 L_m of water that had been annealed to 60 K for the indicated time. For comparison, the TPD spectrum obtained after 0.2 L_m of CO_2 was deposited on 1.5 L_m of water that had been deposited at 60 K is included. Inset: the percentage of CO_2 trapped as a function of annealing time.

As the inset of Figure 5.4 shows, the percentage of trapped CO_2 decreases from ~67% to ~56% as the annealing time is increased from 0 to 15 minutes, in comparison to ~43% when the substrate is held at 60 K during deposition. Increasing the annealing time from 0 to 15 minutes results in a non-linear decrease in the trapped CO_2, suggesting that a considerably longer annealing time would be needed to achieve an ice of comparable structure to that obtained by holding the sample at an elevated temperature during dosing. This would greatly increase experimental times since the sample takes longer to cool after being held at elevated temperatures for longer.

When depositing adsorbates at elevated temperatures, the relationship between sticking probability and surface temperature must also be considered. Whilst it can be assumed that the sticking probability of water on HOPG is unity at ~22 K, this is not necessarily the case at higher deposition temperatures. As seen in Chapter 4, when the surface was held at 140 K the sticking probability was 38% lower than when at ~22 K. As a

consequence of the lower sticking probability at 140 K, the exposure had to be increased in order to produce an ice of the same thickness as formed when the surface was at ~22 K.

Figure 5.5 shows a selection of water TPD spectra obtained after the HOPG was held at temperatures between 20 and 110 K during deposition of water. All of the spectra share leading edges and the ASW to CI phase transition occurs at the same temperature (~150 K). These observations indicate that the ASW to CI phase change and the desorption of ASW and CI are unaffected by the water deposition temperature. The only difference between some of the spectra is a very slight variance in the height of the CI desorption peak at ~162 K. This is due to the small error associated with dosing. The differences in peak height observed in Figure 5.5 are insignificant and represent only a small fraction of the total peak area. This indicates that the TPD area, and thus amount, of water is not dependent on the deposition temperature (between 20 and 110 K), hence the sticking probability remains constant. Consequently, it was decided that the water layer would be prepared by holding the surface at the relevant temperature during deposition.

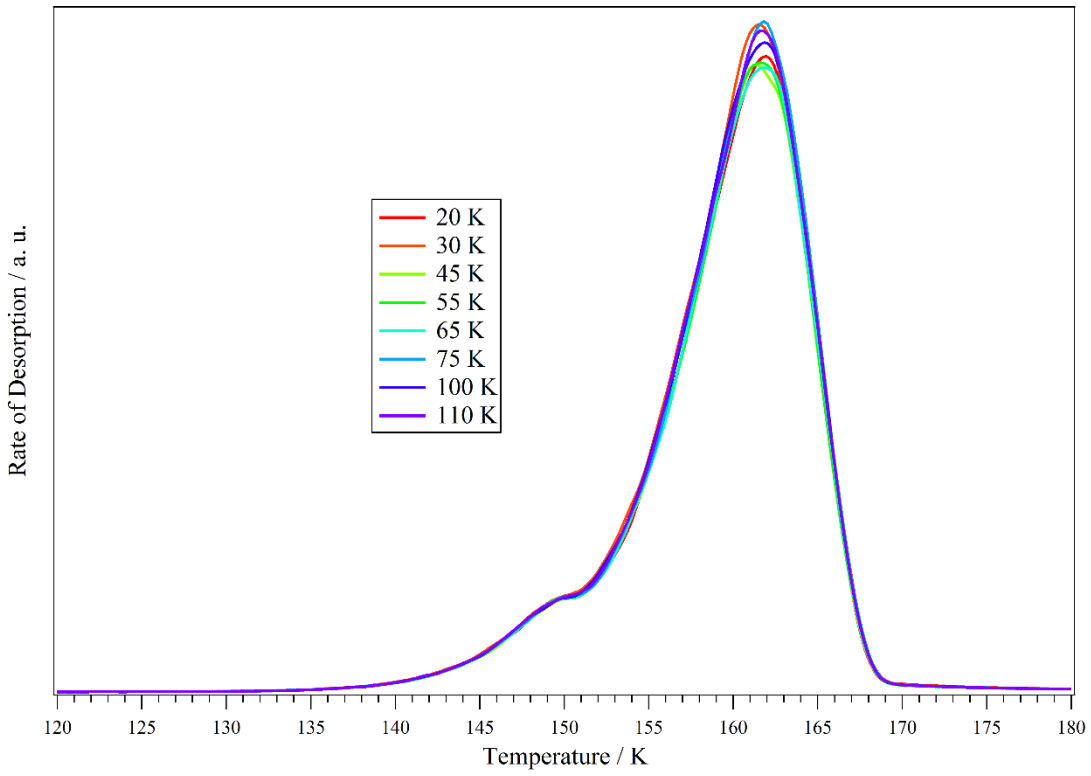

Figure 5.5 – TPD spectra of 1.5 L_m of water deposited on HOPG at the indicated temperatures. All ices were deposited with the substrate in the same position relative to the leak valve.

5.4 *Results and Discussion*

5.4.1 CO_2 Experiments

Figure 5.6 shows the TPD spectra obtained after 0.2 L_m of CO_2 has been deposited on 1.5 L_m of water adsorbed at temperature between 20 and 110 K – the water spectra have been omitted for clarity. When CO_2 is adsorbed on water deposited on HOPG at 20 K the resulting TPD spectrum displays three features relating to CO_2 desorption: surface/near-surface desorption (84 K), volcano desorption (150 K) and co-desorption (162 K).

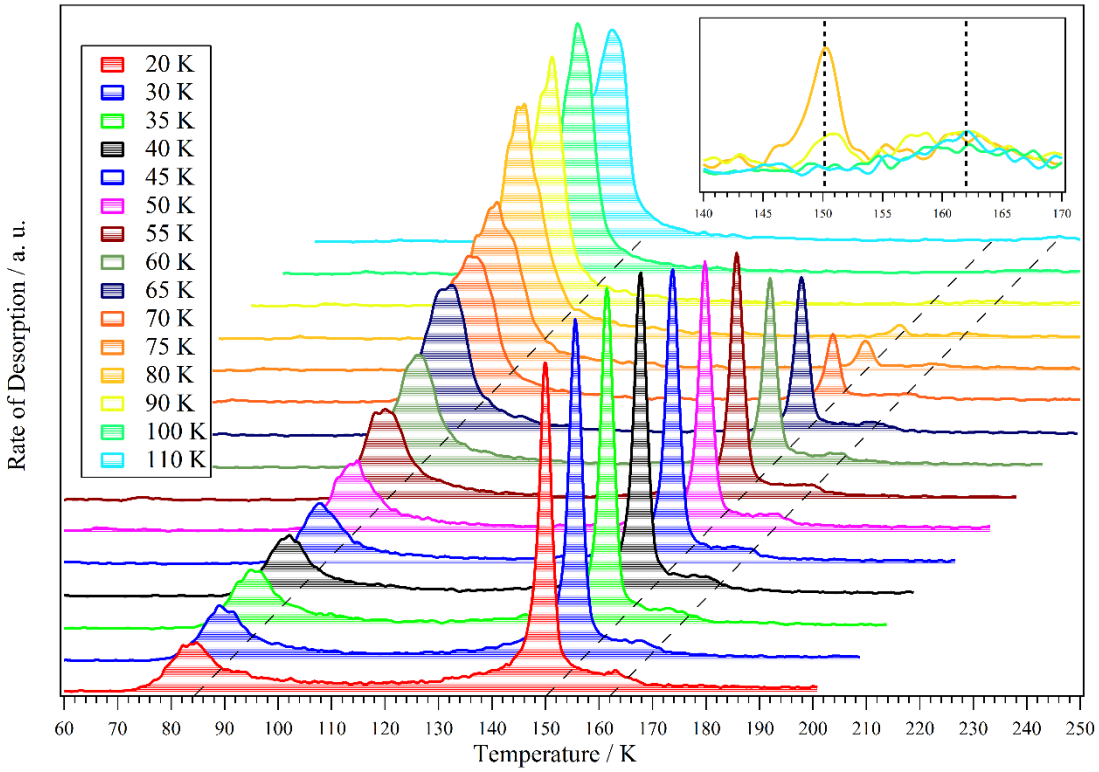

Figure 5.6 – TPD spectra of CO_2 (0.2 L_m) deposited on water (1.5 L_m) dosed at the indicated temperatures. The black dashed lines in the main figure indicate 84, 150 and 162 K. Inset: 140-170 K region of the CO_2 spectra enlarged (×25).

For water deposition temperatures below 35 K, there does not appear to be any significant evolution of the CO_2 desorption features, suggesting that the water ice has not undergone any significant structural evolution at these temperatures. Between 35 and 55 K the surface desorption peak remains centred at ~84 K but has grown in intensity and the volcano peak remains centred at 150 K but undergoes a significant reduction in intensity. This indicates that less CO_2 is being trapped as the water deposition temperature increases. As less of the CO_2 is trapped, more of it remains on, and then desorbs from,

the surface. This give rise to the increased intensity of the surface/near-surface peak at ~84 K. The co-desorption feature remains unchanged at 162 K between 35 and 55 K.

For water deposition temperature of 55 to 80 K the surface desorption feature increases in intensity and shifts to 80 K. Between 55 and 65 K the peak broadens but then between 65 and 80 K this is reversed. The volcano peak remains at 150 K but reduces in intensity. There are subtle loses in the co-desorption feature but it remains at the same temperature. Increasing it to 100 K sees the surface peak shift to ~78 K and the volcano peak disappear. Finally, increasing the water deposition temperature to 110 K results in no significant spectral changes. It is difficult to observe the co-desorption feature in Figure 5.6; however, it is present and unchanged between 80 and 110 K (as shown in the inset Figure 5.6). The observations discussed above suggests that the structural evolution of the ASW ceases between 90 and 100 K.

Figure 5.7 summarises the changes in the TPD spectra observed when water is deposited between 20 and 110 K. Only the 30, 60 and 110 K are shown for clarity.

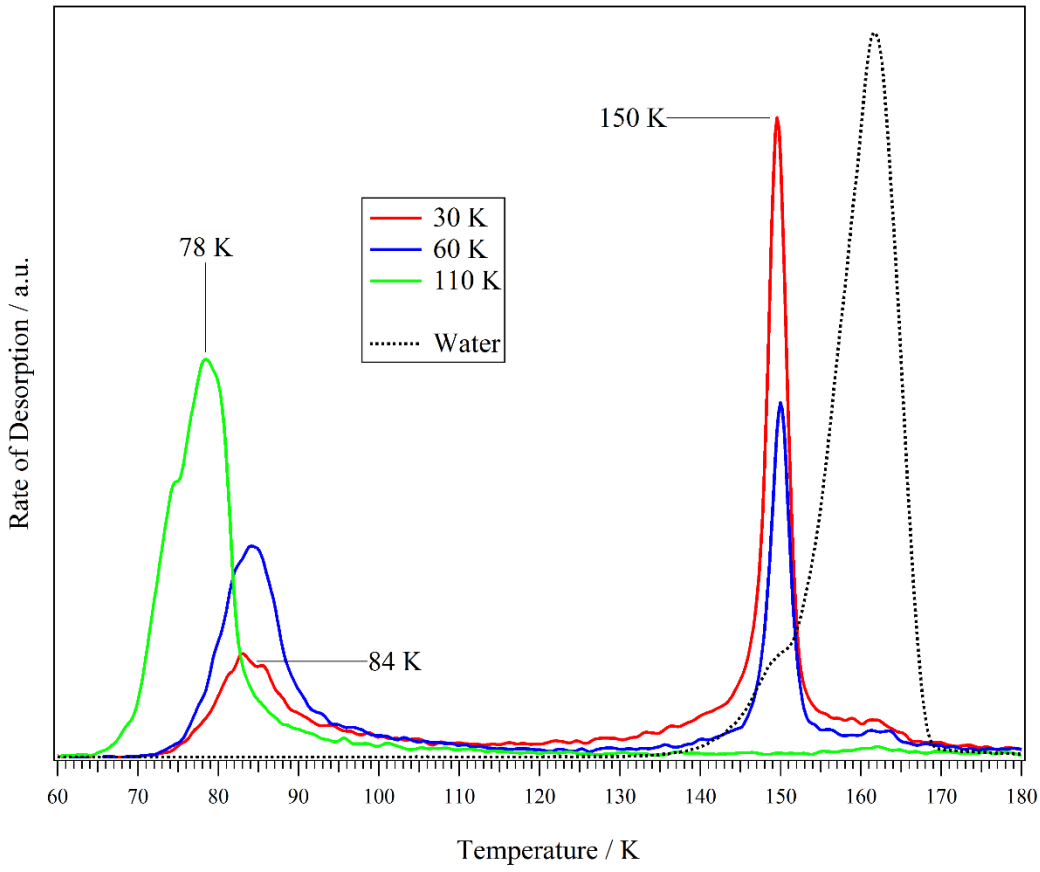

Figure 5.7 – TPD spectra of CO_2 deposited on water dosed at the indicated temperatures. Included is an example of the corresponding water TPD spectrum (black dashed line).

5.4.1.1 CO_2 Quantitative Analysis

This work is based on tracking how the ability of ASW to trap a probe molecule evolves with increasing water deposition temperature. Since the area under a TPD curve is proportional to the amount of adsorbate, the area of the TPD curve for the probe desorbing from trapped environments (volcano and co-desorption) can be divided by the total area to give the fraction of probe trapped (Equation 5.1). Calculations also confirm that the area of the volcano plus co-desorption peaks are anti-correlated, as expected.

$$Fraction\ of\ Probe\ Trapped = \frac{Trapped\ Area}{Total\ Area} \quad 5.1$$

The *Total Area* was calculated by integrating the area under the CO_2 traces between 60 and 180 K. The slight desorption above ~125 K seems to be linked to the volcano peak and so the *Trapped Area* was taken as being between 125 and 180 K. The impact of the central area on the *Fraction of Probe Trapped* was checked by ignoring the central area and calculating the fraction by summing the areas between 60 to 100 K and 135 to 180 K. There was not any significant variation between the two methods regarding the fraction trapped or the trend observed.

Figure 5.8 shows how the fraction of the CO_2 trapped varies as the water deposition temperature is increased to 110 K. The error bars were calculated using the standard deviation of the ratio between the amounts of CO_2 and water, thereby accounting for any errors in dosing. The most suitable and useful function to fit the data points in Figure 5.8 was found to be the Hill Equation (Igor Pro 6, WaveMetrics)[227,228] or 4 Parameter Logistic (4PL) function[229] (equation 5.2). This decision was based firstly on being able to make physical interpretations of the fit parameters and secondly on the quality of the fit.

$$f(x) = base + \frac{max - base}{1 + \left(\frac{x}{x_{mid}}\right)^{slope}} \quad 5.2$$

The terms in Equation 5.2 relate to the following numerical factors: *base* is the maximum asymptote, i.e. where x tends to infinity; *maximum* is the minimum asymptote, i.e. where x tends to zero; x_{mid} is the inflection point, or mid-point of the slope; *slope* is a measure of the steepness of the curve.

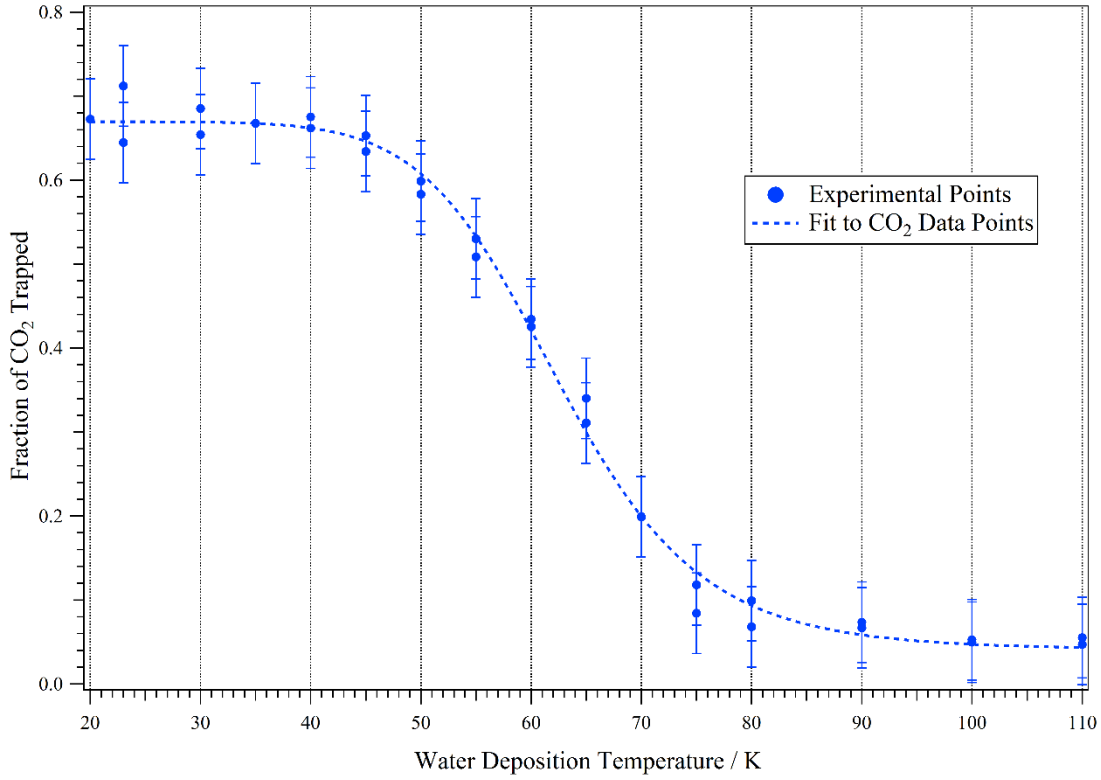

Figure 5.8 – The fraction of CO_2 trapped as a function of the water deposition temperature. Each point corresponds to an individual TPD experiment of 0.2 L_m of CO_2 deposited on top of 1.5 L_m of water. The dashed blue curve is a fit to the points made using Equation 5.2.

The parameters in Equation 5.2 can be interpreted as follows (see Equation 5.3): *maximum* refers to the fraction of probe trapped prior to structural evolution, *base* is the fraction of probe trapped after structural evolution has ceased, x_{mid} is the point at which the structural changes are greatest, and *slope* can be considered a measure of the progression of structural changes, with respect to temperature.

$$Trapping = Fraction\ trapped\ before\ structural\ evolution + \left(\frac{Fraction\ trapped\ before\ structural\ evolution - Fraction\ trapped\ after\ structural\ evolution}{1 + \left(\frac{Temperature}{Temperature_{mid}} \right)^{Progression}} \right) \quad 5.3$$

The blue dashed line in Figure 5.8 is the result of a free fit to the data points using Equation 5.2. It is clear from visual inspection that the fit is of good quality and represents the trend in the data points well. The chi-square calculated for the fit is 0.0103, highlighting the quality of the fit. The parameters used in the fit are given in Table 5.1. Both the *base* and *maximum* parameters are dimensionless since they represent the

fraction of CO_2 trapped. The x_{mid} value has units of Kelvin as it represents the curve's mid-point x coordinate, whilst *slope* is dimensionless as it is an exponent.

The parameters listed in Table 5.1 indicate that the unannealed ASW (pASW) can accommodate ~67% of the CO_2 probe above its natural sublimation point. This value drops to ~4% once the ASW has undergone compaction to cASW. The structural changes are most pronounced at ~63 K. From visual inspection, it appears that compaction begins at temperatures above 40 K and ceases between 90 and 100 K. Using the crossover of linear extensions of the curve the onset and completion temperatures can be stated as 49.7 and 75.8 K, respectively.

Table 5.1 – List of the parameters used in the 4PL/Hill Equation to fit the change in the fraction of CO_2 trapped as a function of water deposition temperature. The error quoted is one standard deviation.

Parameter	Interpreted Parameter	Value
Base	Fraction trapped after structural evolution	0.04 ± 0.01
Maximum	Fraction trapped before structural evolution	0.67 ± 0.01
x_{mid} / K	Temperature at which structural changes are the greatest / K	62.7 ± 0.4
Slope	Progression of structural changes, with respect to temperature	9.8 ± 0.6

In the introduction to this chatper the disparity in the literature between the reported onset and completion temperatures for the compaction of ASW was discussed. Jenniskens and Blake reported an onset temperature of ~38 K and a completion temperature of ~68 K.[129] The results shown in Figure 5.8 show agreement with the onset temperature but not with the temperature at which compaction is complete.[129] Collings *et al.* reported a range of 8 to ~60 K for the decrease in trapping of CO and stated that the reason their results differed to Jenniskens and Blake was due to the heating rates employed.[40] The stark differences between this work and that of Collings *et al.* is not expected to be due to preparation or analysis methods because these are similar in both cases. Collings *et al.* calculated that their HDA ices were 0.6 μm thick,[40] whereas it was calculated that the ices used in this work (when deposited at ~22 K) were ~0.02 μm, therefore, this could be the cause of the

discrepancy. This value was calculated using collision theory to estimate the number of water molecules on the surface and then using the molecular mass and water density to calculate the thickness. In addition to ice thickness, another difference between this work and that by Collings *et al.*[40] is the probe identity (CO versus CO_2). Therefore, to check the influence of the probe, CS_2 was used an alternative probe in the following section.

N_2 adsorption studies by Stevenson *et al.*[133] reported a temperature range of 22 to 90 K for the compaction of ASW. Whilst the high temperature region of their results is comparable to the results shown in Figure 5.8, they report compaction immediately upon heating above 20 K. As with Collings *et al.*[40] and the work presented here, Stevenson *et al.* deposited their ices at a given temperature and then adsorbed the probe at base temperature. Therefore, the earlier onset reported by Stevenson is due to other factors, such as the growth methods and ice thickness.

More recent work by Bossa *et al.*[113] and Isokoski *et al.*[111] using laser interferometry, reported a steady decrease in the thickness of pASW above 20 K, a process that did not appear to be complete by 120 K. This suggested to them that the progression of compaction was continuous between 20 and 120 K. These conclusions are contradictory to the results shown in Figure 5.8, where there are clear plateaus below ~30 K and above ~90-100 K. This disparity may be due to the differing methods used in their studies and the one presented here.

The fact that after annealing to 110 K the cASW can still trap ~4% of the CO_2 indicates that whilst it has lost a great deal of porosity, there are still cavities available to trap and retain some of the CO_2. This is in contrast to the findings of Stevenson *et al.*[133] and Collings *et al.*,[40] both of whom reported near-zero percent trapping at higher temperatures. The reason for the difference is not clear, although it is possibly due to a small amount of pASW remaining, even following adsorption at higher temperatures or possibly due to the different growth methods used in each study.

5.4.2 CS_2 Experiments

To test whether the probe affects the pASW to cASW transformation, the experiments were repeated using CS_2. CS_2 was chosen for several reasons, including its structural similarity to CO_2 and the nature of its interaction with water. CS_2, like CO_2, is a linear symmetrical molecule. However, owing to the size of sulphur compared to oxygen, CS_2

is much larger (C=S bond length is 1.55 Å and C=O bond length is 1.16 Å[230]). Importantly, neither molecule bonds to water and hence it is not expected that they would influence any structural changes in water.

A selection of the TPD spectra obtained over a range of water deposition temperatures are shown in Figure 5.9. The same water deposition temperatures were used for the CS_2 experiments as were used for the CO_2 experiments (~20-110 K). Only one water TPD spectrum is shown because, as for CO_2 (Figure 5.5), there was no change in the spectra as the deposition temperature was increased. Further to confirming the constant sticking probability between ~20 and 110 K, this demonstrates that the presence of a non-hydrogen bonding probe does not affect the crystallisation or desorption of water.

There are several spectral features evident in Figure 5.9, like those observed for CO_2. Both the volcano and co-desorption peaks do not shift in temperature as the water deposition temperature is increased, remaining at 150 and 163 K, respectively. With increasing water deposition temperature, the volcano and co-desorption features decrease in intensity until a point at which it is difficult to observe them, as seen for CO_2. The surface/near-surface desorption feature (108-110 K) increases with increasing water deposition temperature. This is a direct consequence of the decreasing ability of the water underlayer to accommodate the probe, as seen for CO_2. A key difference between the evolution of the CS_2 spectra shown in Figure 5.9 and those observed for CO_2 (Figure 5.6) is that there is already a notable decrease in the CS_2 volcano peak between 22 and 30 K (and subsequent increase in the surface/near-surface desorption peak), whilst there is no spectral evolution over this range for CO_2.

Further to the differences in the onset temperature of spectral evolution between CO_2 and CS_2, the profile of the CS_2 surface/near-surface peak does not change and only shifts down in temperature by 2 K, much less than observed for CO_2. The reason for this difference is probably a result of the nature of the water surface that each probe sees. The surfaces of pASW and cASW are, by definition, amorphous and thereby full of pores and other structural variations. As CO_2 is smaller than CS_2 it may be able to access more of these features than CS_2. Therefore, as the water ice compacts with increasing deposition temperatures, the CO_2 will see more of a change than the CS_2 would. Therefore, the surface/near-surface desorption temperature of CO_2 will vary more than that of CS_2.

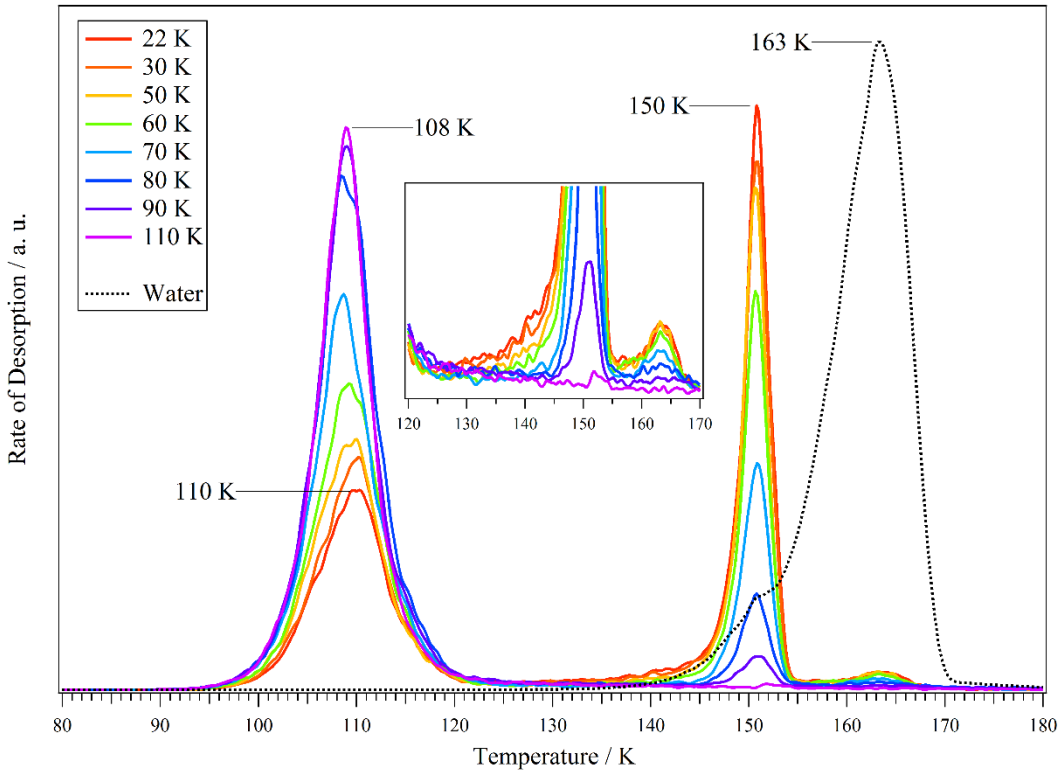

Figure 5.9 – TPD spectra of 0.1 L_m of CS_2 deposited on 1.5 L_m of water deposited at temperatures between 22 and 110 K. The black dashed trace is an example water TPD spectrum. Inset: 120-170 K region of the CS_2 spectra enlarged by a factor of 13.

5.4.1.2 CS_2 Quantitative Analysis

Quantitative analysis of the CS_2 experiments was conducted in the same manner as for the CO_2 experiments. The central region in the CS_2 spectra (Figure 5.9), between the surface/near-surface and volcano peaks (~120-140 K), does not quite reach the baseline. It appears to behave in a comparable manner to the central region of the CO_2 spectra in that the high temperature side of it decreases as the water deposition temperature increases (for example, compare the 22 K and 70 K spectra in the inset of Figure 5.9). Above ~135 K, the CS_2 desorption trace appears to lead into the volcano desorption peak. Therefore, the regions used for the analysis of the CS_2 experiments are as follows: 80-180 K for the *Total Area* and 135-180 K for the *Trapped Area*.

The fraction of CS_2 trapped as a function of water deposition temperature is shown in Figure 5.10 – the fit was produced using Equation 5.2. The fit is of good quality, with a small amount of scatter about the curve – the chi-square calculated for the fit is 0.0096, highlighting the quality of the fit. The general form of the curve is a low temperature

plateau in the fraction trapped that leads into a relatively steep decline at ~40 K. This decline appears to cease between ~100 and 110 K whereby the curve plateaus once more.

Table 5.2 lists the parameters resulting from the fit shown in Figure 5.10. Prior to increasing the water deposition temperature, approximately 50% of the CS_2 can be trapped by the water. When water is deposited at 110 K the fraction trapped falls significantly to 1.5%. The decline in trapping fraction is centred at 68.5 K.

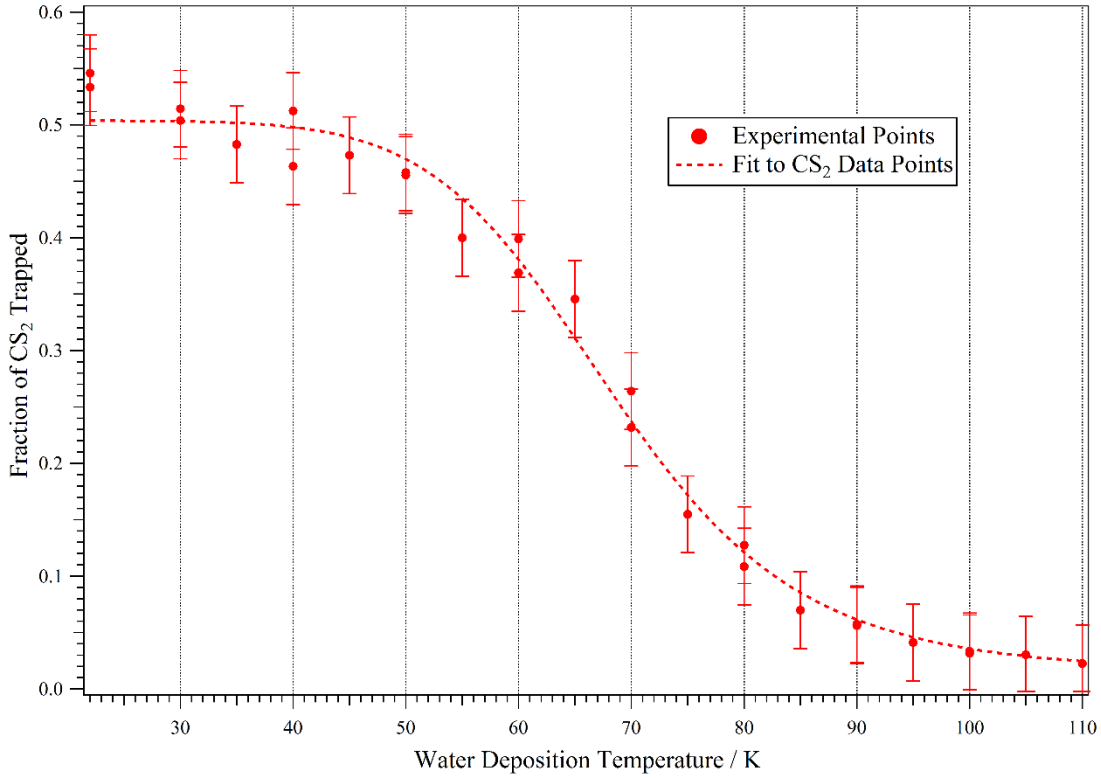

Figure 5.10 – The fraction of CS_2 trapped as a function of the water deposition temperature. Each point corresponds to an individual TPD experiment of 0.1 L_m of CS_2 deposited on top of 1.5 L_m of water. The dashed red curve is a fit to the points made using Equation 5.2.

Table 5.2 – Parameters used in the 4PL/Hill Equation to fit the change in the fraction of CS_2 trapped as a function of water deposition temperature. The error quoted is one standard deviation.

Parameter	Interpreted Parameter	Value
Base	Fraction trapped after structural evolution	0.02 ± 0.01
Maximum	Fraction trapped before structural evolution	0.50 ± 0.01
x_{mid} / K	Temperature at which structural changes are the greatest / K	68.5 ± 0.9
Slope	Progression of structural changes, with respect to temperature	8.2 ± 0.8

5.4.1.3 Comparing Probes

To compare the fraction of each probe trapped as a function of the water deposition temperature, the individual data points and their fits were plotted together in Figure 5.11. In addition to comparing the results from this work, Figure 5.11 displays the trapping fraction for CO reported by Collings *et al.*[40]. There are some striking similarities and differences between the fits for the two probes used in this work. The first key similarity is the general shape, both consist of a low temperature, high trapping fraction, plateau which undergoes a relatively steep decline above ~40 K before plateauing around ~100 K. Both fits are also centred between 60 and 70 K. Although the high temperature plateaus are at similar levels of trapping, the low temperature plateaus are considerably different. Additionally, the gradients of the declines are similar when accounting for their errors.

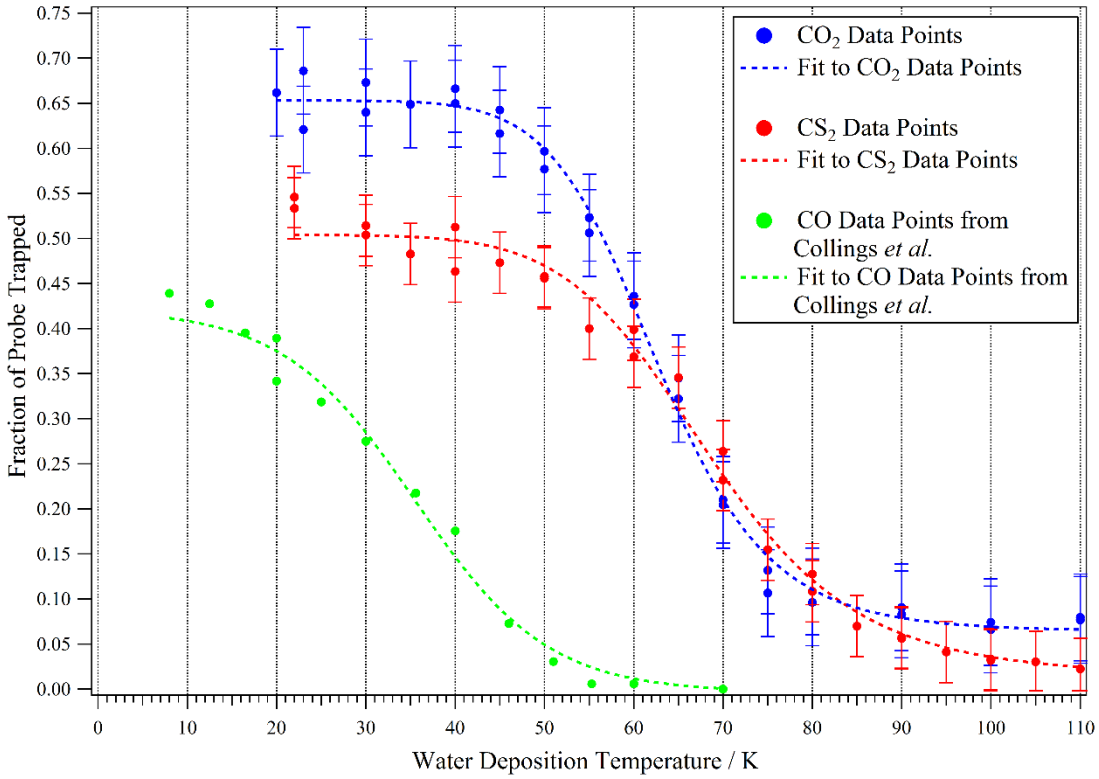

Figure 5.11 – Comparison of the fraction of CO_2 and CS_2 trapped as a function of the water deposition temperature. The CO_2 points and fit are taken from Figure 5.8 whilst the CS_2 points and fit are taken from Figure 5.10. The CO data points were obtained from Collings *et al.*.[40]

To further compare the trapping of CO_2 and CS_2, Table 5.3 lists the fit parameters for both probe molecules. Due to the considerably different shape of the CO data it was not possible to fit it with the Hill Equation and the curve included in Figure 5.11 is to guide the eye only. Both the *base* and the *maximum* values for the two probes used in this work

are considerably different, in particular the *maximum*. The amount of CS_2 trapped at base temperature is ~50%, compared to ~67% of CO_2, a ratio of ~0.75. It was calculated, using the van der Waals radii,[231] that the volume of CO_2 is ~0.72 times that of CS_2. The ratio of the volume of CO_2 and CS_2 compares well with the ratio of the amount of each probe trapped at base temperature. Therefore, it is proposed that the reason for CS_2 trapping less than CO_2 is due to the larger size of CS_2. Access to a wider range of pores is also likely to be why the CO_2 *base* value is nearly two times that of CS_2.

Table 5.3 – Comparison of the CO_2 and CS_2 4PL/Hill Equation fit parameters, shown in Figure 5.11.

Parameter	Interpreted Parameter	CO_2	CS_2
Base	Fraction trapped after structural evolution	0.04 ± 0.01	0.02 ± 0.01
Maximum	Fraction trapped before structural evolution	0.67 ± 0.01	0.50 ± 0.01
x_{mid} / K	Temperature at which structural changes are the greatest / K	62.7 ± 0.4	68.5 ± 0.9
Slope	Progression of structural changes, with respect to temperature	9.8 ± 0.6	8.2 ± 0.8

The CO_2 curve decline is slightly more rapid than the CS_2 decline and thus the CO_2 *slope* is slightly larger, as expected from inspection of Figure 5.11. This could be interpreted as meaning that when CS_2 is used as a probe, the influence of temperature on the structure of the ASW is lesser than when CO_2 is used. However, this difference might be because structural changes are more apparent to CO_2 than to CS_2. That is to say, subtle alterations in the accessibility of pores and channels will be more evident to the smaller CO_2 than the larger CS_2. Or it may simply be due to that over a comparable temperature range the CO_2 probe experiences a greater loss in trapping fraction and so the *slope* would naturally be greater than that for CS_2.

The mid-point of the CS_2 curve occurs 5.8 K higher than that of CO_2. It seems that this difference is a consequence of the high temperature ends of the curves behaving differently. As discussed above, the CO_2 curve has a larger *slope* and reaches its asymptote at a lower temperature than the CS_2. Therefore, whilst it may not be immediately obvious by visual inspection, the centre of the CS_2 curve is at a higher temperature than that of CO_2 and thus x_{mid} is higher for CS_2. The differences between

the probes in the values of *slope* and x_{mid} are likely to be a consequence of the probes' sensitivity to structural changes or the difference in the decrease of the trapping fraction (the value of *maximum-base*), rather than due to an effect of the probe on the compaction of ASW.

Whilst both probes demonstrate that the compaction of ASW is complete by 110 K, the CS_2 appears to be able to see a noticeable decrease in trapping between 100 and 110 K, whereas CO_2 has largely plateaued by this point. The cause of this discrepancy may be a consequence of the probe size and the pores or channels that the probe can access. If, by these high temperatures, the structural evolution is largely complete then slight changes will be unlikely to affect the amount of the relatively small CO_2 trapping, whereas a slight change in a pore or channel size may cut off the larger CS_2 from trapping within the water. This would therefore lead to the CS_2 seeing changes whilst CO_2 is largely unperturbed at these temperatures as the evolution is not great enough to stop the smaller CO_2 from accessing the pores and channels.

The key point to be taken from the CO_2 and CS_2 data presented in Figure 5.11 is that the onset temperature obtained from the use of the different probes is approximately the same and the overall range is comparable, with structural evolution terminating around ~100 K. This indicates that the probe identity cannot be the reason for the differences in what was reported here and what has been reported in the literature. Also, the relationship between the maximum and minimum amount of each probe trapped is as expected, the larger CS_2 will trap less in both pASW and cASW simply due to its larger size.

With regards to the Collings *et al.*[40] data shown in Figure 5.11, there are substantial differences to the data obtained in this work. At 8 K only ~44% of CO is trapped, compared to ~50% and ~67% for CS_2 and CO_2, respectively. This is unexpected as CO is much smaller than either of the other probes and so it would be anticipated that a greater proportion of it would trap. Furthermore, the minimum amount of CO trapped is ~0% compared to 1.5% and 4.1% for CS_2 and CO_2, respectively. Again, considering the size of the probes, this is unexpected. The amount of CO trapped decreases between 8 K and ~60 K, this is very different to the range obtained in this work.

Considering the similarity in the temperature ranges of compaction obtained for CO_2 and CS_2 here, it seems that the stark difference between the temperature ranges reported in

this work and that by Collings *et al.* is not due to the probe identity. Although they note that their data indicates that structural changes continue above 70 K, they do not explain the lack of trapping above 60 K. The much lower initial trapping fraction of CO would also suggest that the ice deposited by Collings *et al.* at 8 K is less porous than those grown using this set-up at ~20 K. This is because the low trapping fraction reported by Collings *et al*. is inconsistent with the relationship between the initial trapping fractions of CO_2 and CS_2.

Although the methods used to prepare the ices in this work are similar to those used by Collings *et al.*,[40] the heating methods used during TPD were different. In this work, a resistive heating circuit produces a linear heating rate of 0.5 K s^{-1} during TPD, whilst Collings *et al.* used halogen lamps to produce an average heating rate of 0.08 K s^{-1}. This could be part of the reason there is such a large difference in the temperature range obtained but it would not seem to explain the significant difference in the initial trapped percentages. The discrepancy between this work and that by Collings *et al.*,[40] could, in part, be due to thickness, with this work using thinner ices. Even if the ices are prepared in a comparable manner, the precise method of preparation evidently affects the ice structures. Further work is needed in order to properly explain the differences between this work and that by Collings *et al.*.[40]

From comparison of this work with that in the literature, in particular that of Collings *et al.*,[40] it would seem that the nature of water ice grown is highly variable between different experimental set-ups, even when comparable methods are used. Therefore, comparing studies that involve pASW and cASW needs to be done very carefully and that further work on characterising water structures is needed. However, the process of ASW compaction has been shown here to be independent of probe identity and so this factor is not responsible for the discrepancies between this work and the literature.

5.4.3 Effect of Formic Acid on the Compaction of ASW

The effect of formic acid on the pASW to cASW transition was investigated using a three-layered ice system comprised of a 1.5 L_m water layer, a 0.1 L_m formic acid layer and finally, a 0.2 L_m layer of CO_2.

5.4.3.1 CO_2 on Formic Acid

To check that formic acid was not trapping any of the CO_2, 0.2 L_m CO_2 was deposited onto 0.1 L_m of formic acid. The resulting TPD spectrum is shown in Figure 5.12. To assist in assignment of the desorption features, it was compared with the fragmentation pattern detected during formic acid deposition, Figure 5.13.

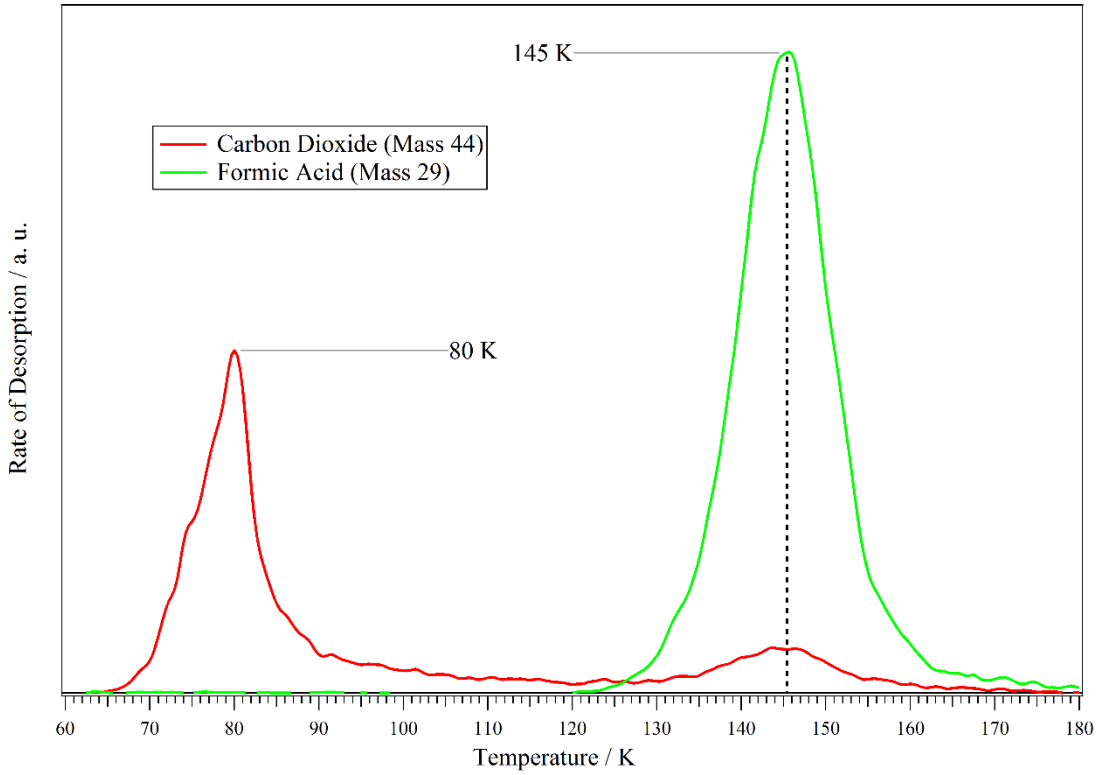

Figure 5.12 – Desorption of 0.2 L_m of carbon dioxide deposited on top of 0.1 L_m of formic acid. Both species were deposited at ~24 K.

The formic acid trace (mass 29) in Figure 5.12 shows a single feature centred at ~145 K, which compares well with the results shown in Chapter 3 for formic acid desorbing from HOPG. The mass 44 trace has a large feature at ~80 K and a smaller one at ~145 K. By comparing the ratio between the two peaks at ~145 K with those detected during dosing formic acid (see Figure 5.13), as well as those reported by the mass spectrometer manufacturers (Hiden Analytical), the mass 44 feature at ~145 K can be assigned to formic acid cracking in the mass spectrometer, rather than to trapped CO_2 desorbing with the formic acid.

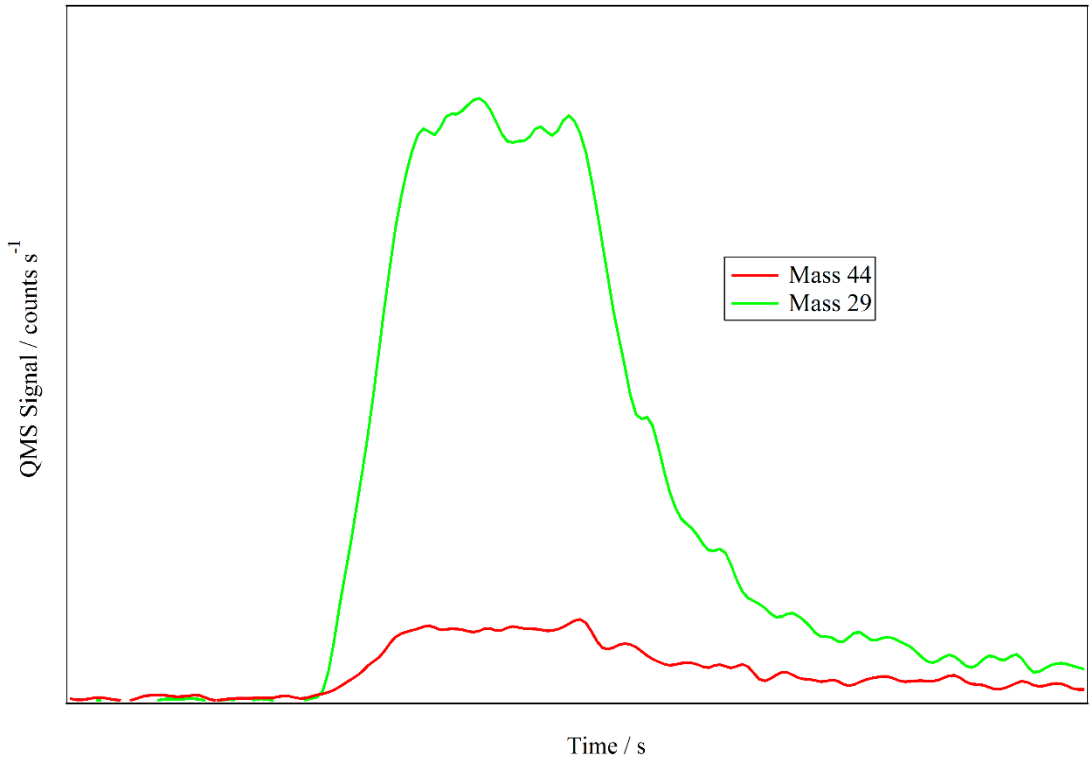

Figure 5.13 – The mass 44 and 29 quadrupole mass spectrometer signals detected during deposition of 0.1 L_m of formic acid on to HOPG at ~24 K.

5.4.3.2 Water in the CO_2/Formic Acid/Water Layered Systems

There is a significant effect of formic acid on the crystallisation of water (see Chapter 4), manifested as a changed ASW to CI shoulder but an unchanged CI desorption peak temperature. Figure 5.14 shows the water TPD spectra recorded for the three-layered systems over the full range of water deposition temperatures examined in this work (~22 to 110 K).

The only difference between the water spectra shown in Figure 5.14 is a slight difference in the peak height. This is a consequence of slight variations in dosing of the water. All of the water TPD spectra shown have the same profile and all have a peak temperature of ~162 K. A key difference between the water spectra shown in Figure 5.14 and those obtained in the absence of formic acid (Figure 5.5) is the lack of a clear shoulder at ~150 K. In the presence of formic acid, there appears to be a very slight shoulder on the water TPD spectra at ~142 K. This is in agreement with the findings discussed in Chapter 4, whereby formic acid was shown to shift the ASW to CI phase change of water to lower temperatures.

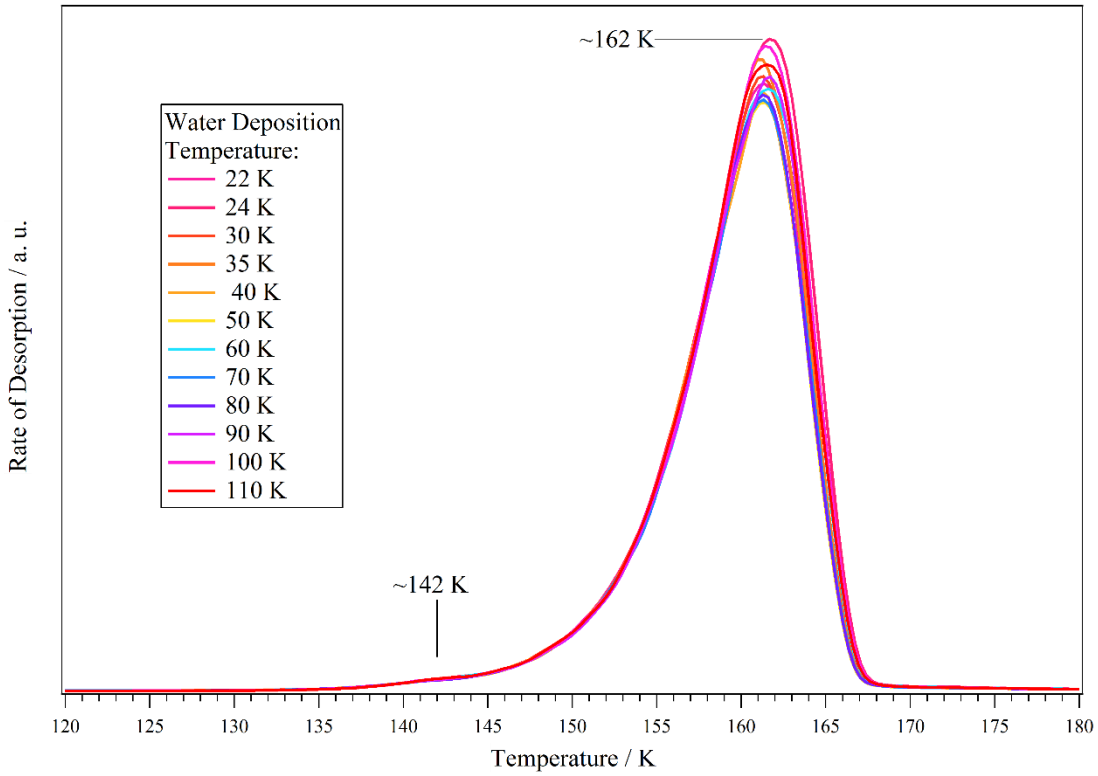

Figure 5.14 – Water TPD spectra for ices comprised of, from top to bottom, 0.2 L_m of CO_2, 0.1 L_m of formic acid and 1.5 L_m of water. The water had been deposited at the indicated temperatures. Formic acid and CO_2 and were then adsorbed with the substrate at ~24 K.

5.4.3.3 Effect of Formic Acid on the Compaction of pASW

The TPD spectrum obtained from a three-layered system (CO_2, formic acid and water) where all components had been deposited with the substrate at ~22 K is shown in Figure 5.15. The dashed grey line is to highlight the desorption temperature of water. The assignment of the desorption features in Figure 5.15 can be made by reference to Chapter 4 and earlier parts of this chapter.

The large water desorption feature at 162 K in Figure 5.15 corresponds to desorption of crystalline water. The mass 44 feature at 84 K corresponds to desorption of CO_2 from the surface/near-surface of the ice. The mass 29, formic acid, features can be assigned as corresponding to desorption promoted by the water ASW to CI phase change (~142 K), desorption of residual formic acid on the surface of the water that was able to crystallise (~156 K) and co-desorption of trapped formic acid with CI (~162 K).

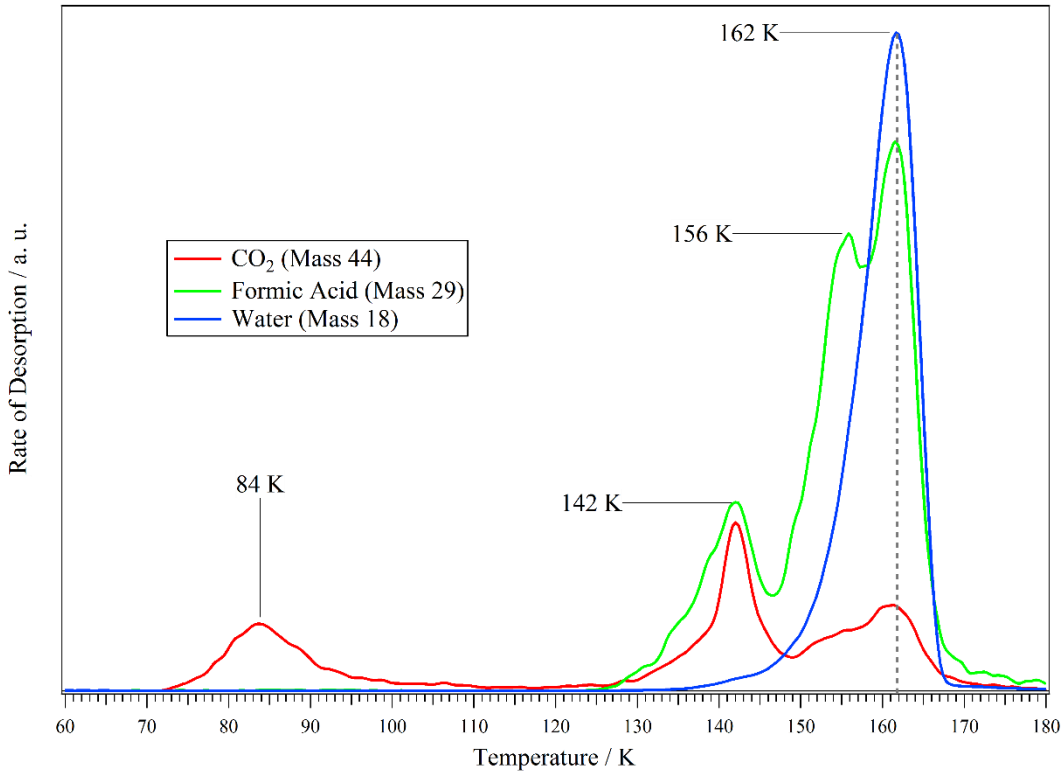

Figure 5.15 – TPD spectra of a layered system comprised of, from top to bottom, 0.2 L_m of CO_2, 0.1 L_m of formic acid, and 1.5 L_m of water, all of which had been deposited at ~22 K.

Assignment of the mass 44 features above 120 K must be made whilst considering that a fraction of formic acid cracks in the mass spectrometer to produce a mass 44 fragment. The fragmentation ratio of formic acid when it desorbs with water was calculated to be 0.12, with a standard deviation of 0.06, or 50%. This large standard deviation highlights how the fragmentation ratio of formic acid when it desorbs with water is far from constant. This contrasts with the ratio observed during formic acid deposition (Figure 5.13). This is a consequence of the strong interaction between the two species. These observations are in line with those in Chapter 4. However, they do not prevent the assignment of the features in Figure 5.15.

The sharp peak at ~142 K is approximately the same intensity as the mass 29 peak and thus is largely due to CO_2 desorbing as the ASW undergoes crystallisation. This is ~8 K lower than when formic acid is absent and thus confirms the assertion in Chapter 4 that the low temperature formic acid desorption feature is linked to the (early) crystallisation of ASW to CI. The feature at ~162 K is mainly from the formic acid cracking. However, the intensity of this peak compared to the mass 29 peak suggests that a small proportion of it can be attributed to the co-desorption of CO_2 with water and formic acid. It would

therefore seem that when a layer of formic acid is placed between CO_2 and water, the CO_2 is still trapped by the water and subsequently undergoes volcano desorption and a small amount of co-desorption.

TPD spectra (mass 44 signal) for the three-layered systems are shown in Figure 5.16. It is clear that increasing the water deposition temperature results in significant evolution of the mass 44 spectra. The general trend observed in Figure 5.16 is that upon increasing the water deposition temperature, the volcano and co-desorption peaks decrease while the low temperature surface/near-surface desorption peak simultaneously increases. At the same time, the low temperature surface/near-surface peak shifts down in temperature by ~4 K. These observations are in line with those for CO_2 on water (Figure 5.7) and CS_2 on water (Figure 5.9). Figure 5.17 shows a comparison between the TPD spectra of CO_2 dosed directly on water and dosed on top of formic acid dosed on water for a number of water deposition temperatures (24, 70 and 100 K). Small variations in CO_2 dosing cause the 100 K surface/near-surface peak to be higher than expected.

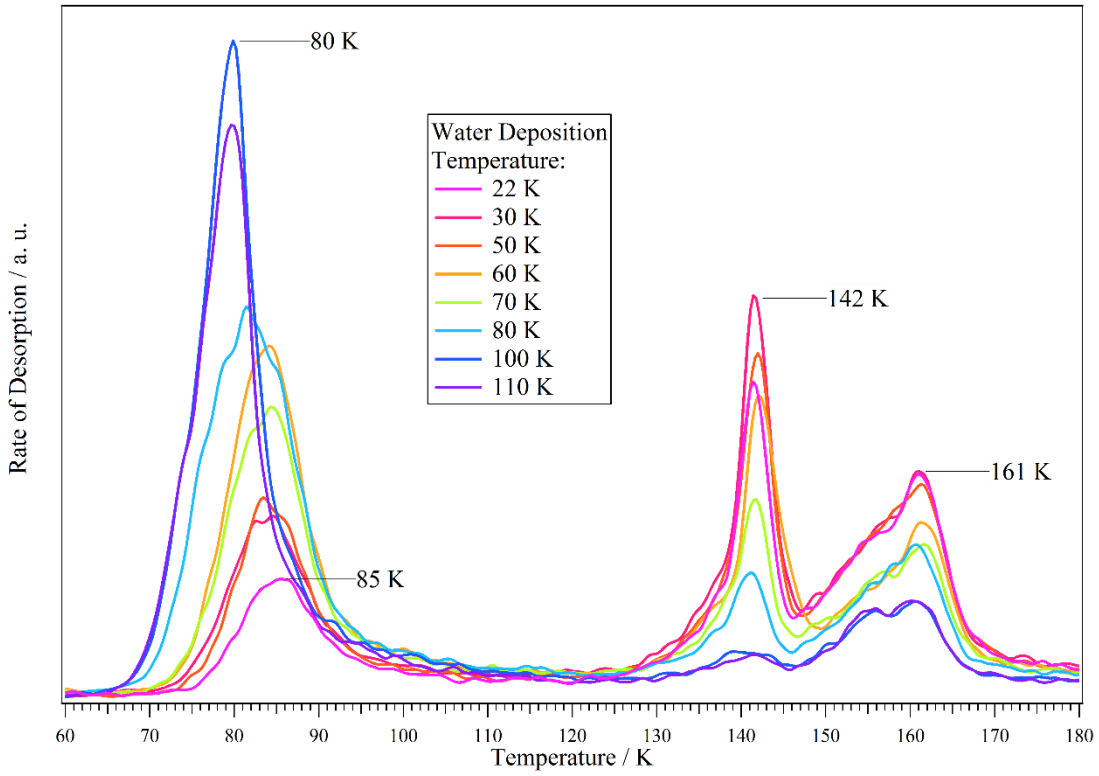

Figure 5.16 – Mass 44 traces from TPD experiments of three-layered systems of CO_2/formic acid/water, where water had been pre-adsorbed at the indicated temperature.

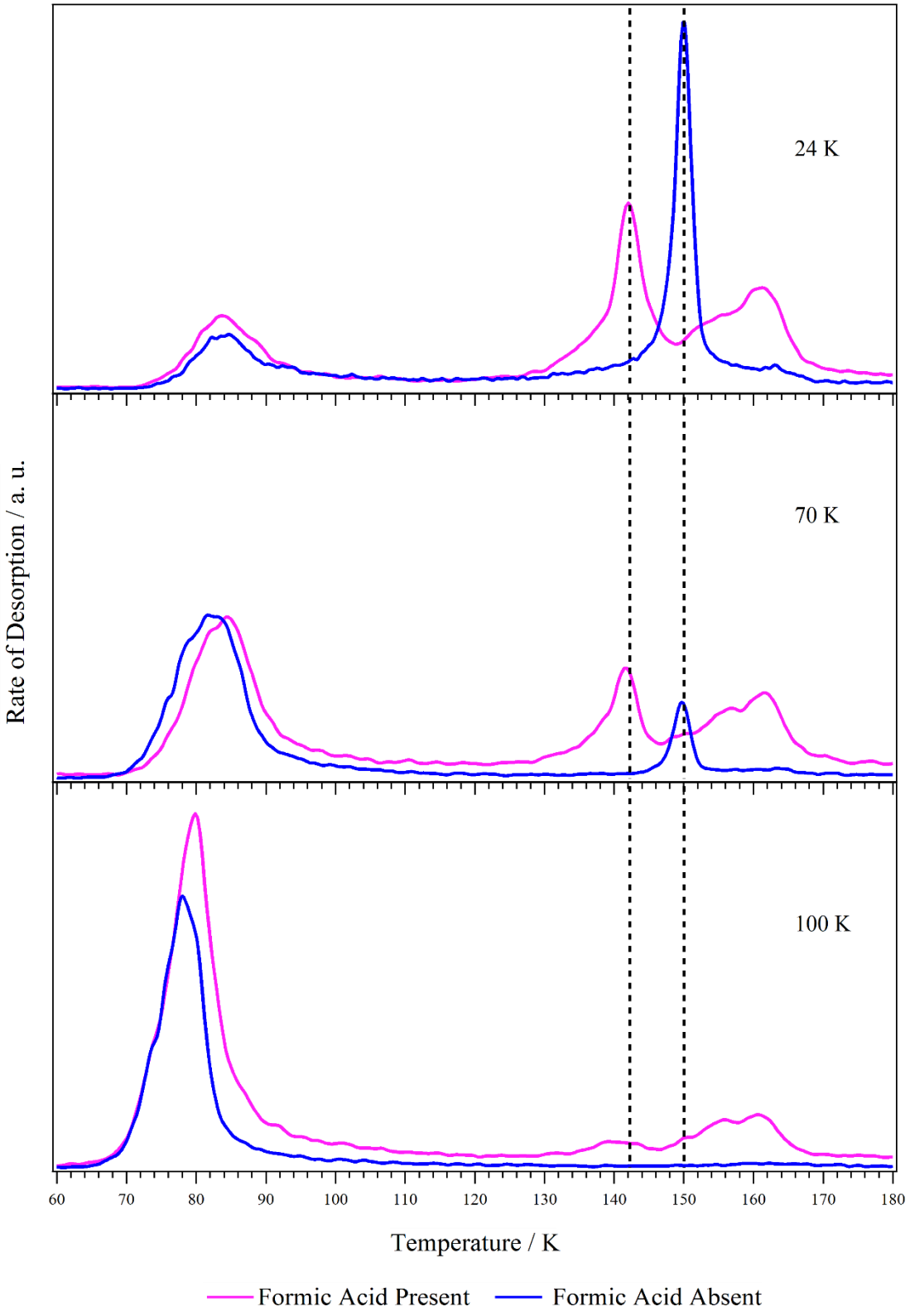

Figure 5.17 – Comparison between the CO_2 TPD spectra of two- and three-layered systems when water is deposited at different temperatures (water deposition temperature indicated on each panel). Pink traces: three-layered systems of, from top to bottom, 0.2 L_m of CO_2, 0.1 L_m of formic acid and 1.5 L_m of water. Blue traces: 0.2 L_m of CO_2 on 1.5 L_m of water.

One aspect of Figure 5.16 that should be noted is the high temperature features on the 100 and 110 K traces. Both traces overlap, indicating that between these two water deposition temperatures there is minimal or no structural evolution of the underlying water layer. This is in full agreement with data for CO_2 dosed directly on top of water where it was shown that by ~100 K, compaction of pASW to cASW had ceased. If CO_2 did not trap, the mass 44 signal above ~120 K would be entirely due to formic acid desorption. Since the profiles of these traces are comparable to the mass 29 trace in Figure 5.15, albeit with much less intensity, it is suggested that the mass 44 features above ~120 K, in the 100 and 110 K spectra, are likely to be entirely from formic acid cracking in the mass spectrometer, rather than CO_2.

Figure 5.17 highlights some important differences between the two- and three-layered systems. Firstly, the temperature of the volcano peak, and thus ASW to CI phase change, is very different in the two systems. It is clear that when formic acid is present, the volcano peaks occur at a lower temperature than when formic acid is absent. The difference in the ASW to CI phase change is due to the strong interaction between water and formic acid, resulting in an early onset of the water phase change. However, it also shows that in each system, the phase change does not change as the water deposition temperature increases. This indicates that the ASW xto CI change is independent of compaction, even when formic acid is present.

Secondly, the surface/near-surface desorption peak behaves in the same way for each system in that it grows with increasing water deposition temperature, as well as shifting and narrowing somewhat. Further to this, the shared leading edges of the surface/near-surface peaks in the 100 K spectra indicates that the nature of the surface that CO_2 is desorbing from in the two systems is comparable. This suggests that regardless of whether formic acid is present, the structural evolution of water is largely completed by 100 K.

Finally, from visual inspection of the 70 K spectra, the compaction process has progressed more in the two-layered system, as evident from the volcano peak being smaller in the three-layered system, a reversal from the relationship of the volcano peaks in the 24 K spectra. This may indicate that the presence of formic acid and the strength of its interaction with water hinders the compaction of ASW. Quantitative analysis of the three- layered systems will allow for a more detailed inspection of the compaction process when formic acid is present.

5.4.3.4 Quantitative Analysis of the Three-Layered Systems

When formic acid is in the presence of water the cracking pattern of formic acid is not constant (see Chapter 4), a consequence of the strong interaction between the two species. Hence, simply subtracting a constant formic acid contribution from the mass 44 trace to leave the CO_2 contribution was not possible. Therefore, an alternative method was developed to obtain an estimate of how the amount of CO_2 trapped varied with water deposition temperature.

Earlier, the fraction of CO_2 trapped when it was deposited on water was calculated by integrating the area of the high temperature features and dividing this by the total area. Using this analysis, it is possible to relate the area of the surface peak to the fraction of CO_2 trapped. This can be done because formic acid does not desorb at such low temperatures, meaning that the mass 44 signal will correspond to just CO_2 desorption and not any formic acid. The area of the surface peak was calculated between 60 and 120 K. The resulting plot of surface peak area against fraction of CO_2 trapped is shown in Figure 5.18. The two lines shown in Figure 5.18 are the maximum and minimum slopes of best fit. They will be used to obtain the line of best fit and give an estimate of the error in the converted surface peak area. There is a clear linear correlation between the area of the surface desorption peak and the fraction of CO_2 trapped, exactly as would be expected. The area under the mass 44 trace that corresponds to CO_2 desorption should be the same in the two- and three-layered systems and thus Figure 5.18 can be used to convert the area of the surface peaks in Figure 5.16 to the fraction of CO_2 trapped.

The midpoint between the lines of maximum and minimum slope was used to convert each of the low temperature features in Figure 5.16 to a fraction of CO_2 trapped. The resulting converted data points were then plotted against water deposition temperature in Figure 5.19. The converted data points were then fitted with a line of best fit using Equation 5.2 and shown alongside the fraction of CO_2 trapped as a function of water deposition temperature when formic acid is absent. The error bars in Figure 5.19 were calculated from the range of converted values from the maximum and minimum slopes of Figure 5.18.

There is a very large amount of scatter in the data points shown in Figure 5.19 and it is likely that the alternate method used to calculate the fraction of CO_2 trapped has

emphasised this. In the method used in the previous sections of this chapter, a ratio between the trapped area and total area was used. This was therefore not impacted by any slight variation in the amount of CO_2 present. However, the method employed here uses the area of the surface peak as a measure of trapping. Therefore, it is inherently impacted by any variation in CO_2 coverage which would have usually been negated by taking a ratio between the trapped and total areas. Variations in coverage were introduced during dosing because the high precision leak valve used to admit CO_2 to the chamber had been damaged by formic acid and this meant that the valve was difficult to accurately control. As a consequence of these dosing issues, the results presented here are only preliminary.

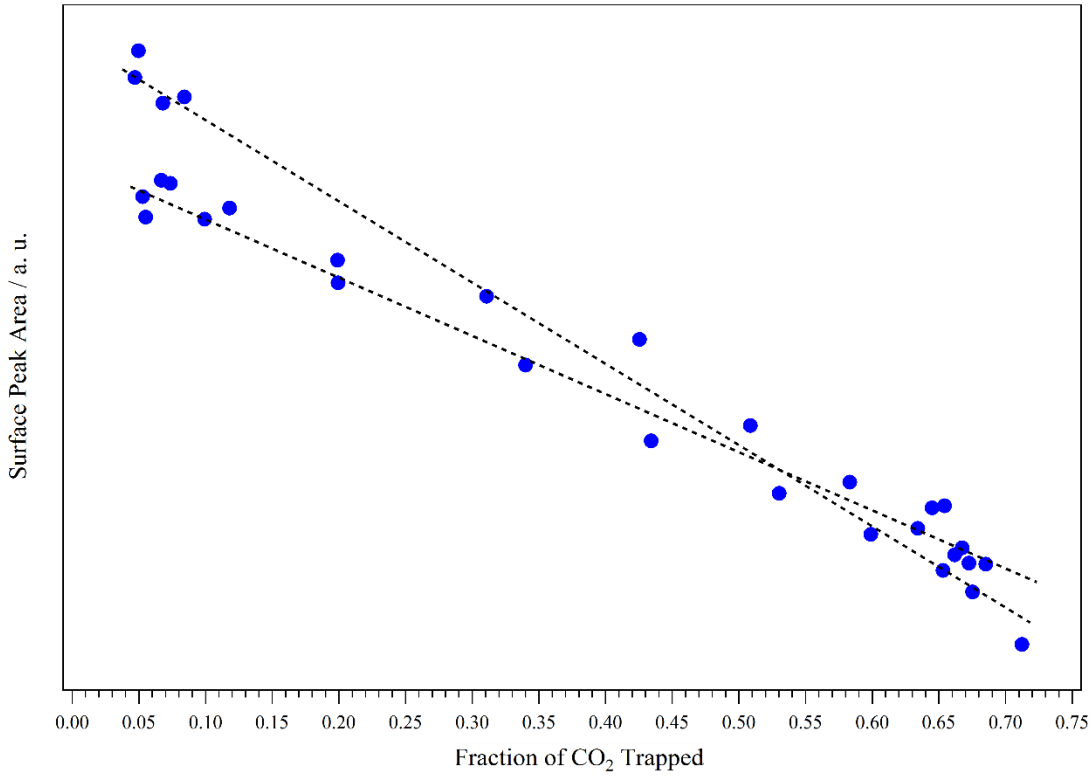

Figure 5.18 – The integrated area of the surface peak against fraction of CO_2 trapped obtained from TPD spectra of 0.2 L_m of CO_2 on 1.5 L_m of water adsorbed at a range of temperatures.

From Figure 5.19 it seems that when formic acid is present, the reduction in trapping, and thus compaction, gains pace between 50 and 60 K and is complete between 100 and 110 K. Both the start and finish of compaction appear to be much higher when formic acid is present than when it is not, and this is reflected in the x_{mid} values where it is 13.7 K higher when formic acid is present. Table 5.4 lists the Hill Equation/4PL parameters used to fit the fraction of CO_2 trapped when formic acid is present and when it was absent. However, a comparison of the parameters must be done very carefully due

to the level of scatter in the three-layered data points (reflected by the large error bars) that is a consequence of the problems during dosing discussed above. Once compaction has initiated, the slope of the curve indicates that the progression when formic acid is present is comparable to when it is not. The pre-compaction trapping fraction is lower in the three-layered system by ~0.14. The lower initial trapping when formic acid is present may be due to some of the water pores being occupied by formic acid, rather than CO_2. The observation of near-zero trapping at 10 and 110 K when formic acid is present may be due to cASW being more compact when formic acid is present or, more likely, that formic acid is occupying spaces that would have otherwise been occupied by CO_2 if formic acid had not been present.

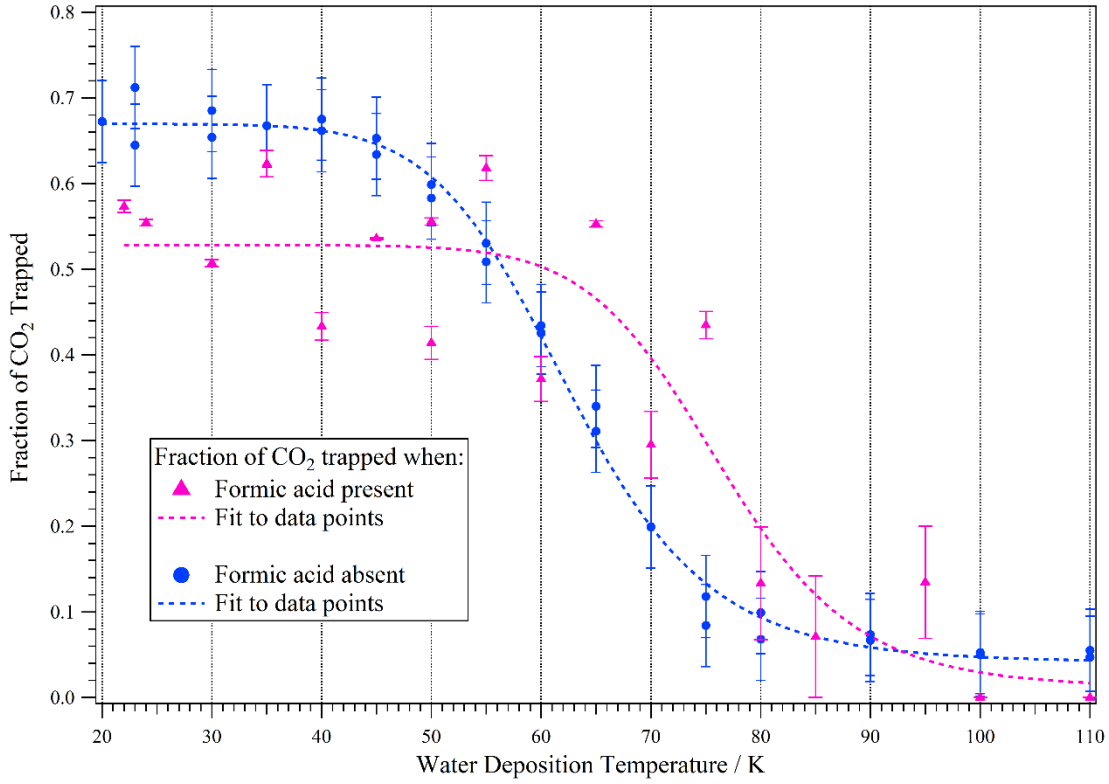

Figure 5.19 – Fraction of CO_2 trapped (calculated using Figures 5.16 and 5.18) as a function of water deposition temperature for layered systems of, from top to bottom, 0.2 L_m of CO_2, 0.1 L_m of formic acid and 1.5 L_m of water. Included are the data points and curve from Figure 5.8.

The reason for the delayed onset of compaction when formic acid is present is probably due to the strong hydrogen bonds that form between formic acid and water. These bonds can support the porous structure of pASW to higher temperatures compared with when formic acid is absent. In effect, the formic acid may be acting as a scaffold, supporting pASW against compaction.

Table 5.4 – Comparison of the 4PL/Hill Equation parameters used to fit the data points for the fraction of CO_2 trapped when formic acid is present and absent shown in Figure 5.19.

Parameter	Interpreted Parameter	Formic Acid Present	Formic Acid Absent
Base	Fraction trapped after structural evolution	0.01 ± 0.07	0.04 ± 0.01
Maximum	Fraction trapped before structural evolution	0.53 ± 0.03	0.67 ± 0.01
x_{mid} / K	Temperature at which structural changes are the greatest / K	76.4 ± 3.5	62.7 ± 0.4
Slope	Progression of structural changes, with respect to temperature	12.3 ± 6.3	9.8 ± 0.6

The preliminary results discussed above for the three-layered system show that the compaction of ASW is not immune from influence by other molecular species. The previous chapter showed how strong the formic acid-water interaction is and so it is fully expected that formic acid would affect the compaction of pASW. Once it has started, the progression of compaction when formic acid is similar to when it is absent, suggesting that the progression of the process is not influenced by the presence of formic acid. However, due to the preliminary nature of the results, this conclusion is not certain.

5.5 Summary

It has been shown using CO_2 and CS_2 as probe molecules that the structural evolution that occurs below 110 K in water ices does not affect the ASW to CI phase change. For all water deposition temperatures between ~20 and 110 K the ASW to CI phase change shoulder was evident at 150 K. When a layer of formic acid was present between the CO_2 and water layers the phase change occurred, for all water deposition temperatures, at ~142 K. This indicates that even in the presence of a hydrogen bonding species such as formic acid, the structural evolution in water ices that occurs below 110 K does not affect the ASW to CI phase change. If this structural evolution does not affect the ASW to CI phase change it will also not affect the release, via volcano and co-desorption, of molecules trapped in the water ice.

In the absence of formic acid, it was shown that above ~40 K significant structural evolution in water ices occurs. The evolution is the compaction of pASW to cASW, sometimes discussed in the literature as the transition from HDA to LDA. Compaction of

pASW is understandably accompanied by a significant loss of porosity, manifested as a decrease in the ability of ASW to accommodate the probe molecule. As less of the probe is accommodated within the ASW, less is trapped and thus more desorbs from the surface of the water at, or near, the natural sublimation temperature of the probe. The desorption of the probe (CO_2) and the compaction of ASW is summarised in the cartoons shown in Figure 5.20 – green corresponds to CO_2 and light blue to water. This would have a direct effect on the ISM since the trapping and release of molecules from water ices plays a key role in the chemical evolution of the ISM. If molecules, like CO_2, adsorb onto an already partially compacted water ice, then less of them will trap. This would result in a greater proportion of these species desorbing into the gas phase close to their natural sublimation temperatures.

Whilst both probes used, CO_2 and CS_2, showed compaction occurred to a significant degree above ~40 K, there was a difference in the temperature where this process appears to be complete. The decrease in the trapping of CO_2 seems to be largely complete by 90-100 K. However, when using CS_2, the loss of trapping does not seem to be complete until between 100 and 110 K. It is proposed that this difference is unlikely to result from an effect of the probe on the compaction of ASW; rather, it is a consequence of the pores and channels that the two different probes can access. These results compared with those obtained by Collings *et al.*[40] suggest that the discrepancy between the temperature ranges is not due to probe effects. The cause of the significant disagreement with Collings *et al.* is uncertain, particularly due to the similarity between the experimental methods used by them and those used in this work. However, the different heating methods may be part of the cause of the difference. The thickness of the water ices used may also play a part in the observed discrepancies. An initial onset temperature of between ~35 and ~40 K for both CO_2 and CS_2, in agreement with a key previous study by Jenniskens and Blake.[129] A compaction range of ~35-100 K reported here is comfortably included within the range reported by Bossa *et al.*[113] and Isokoski *et al.*,[111] however, the steady decrease they report over this range is not in agreement with the work presented here.

The differences in the values of x_{mid} and *slope* values for the two probes is proposed to be due to the probes' sensitivity to structural changes or the overall change of trapping of each probe. It is not suggested that the differences in these parameters are indicative of the different probes affecting the compaction process of water.

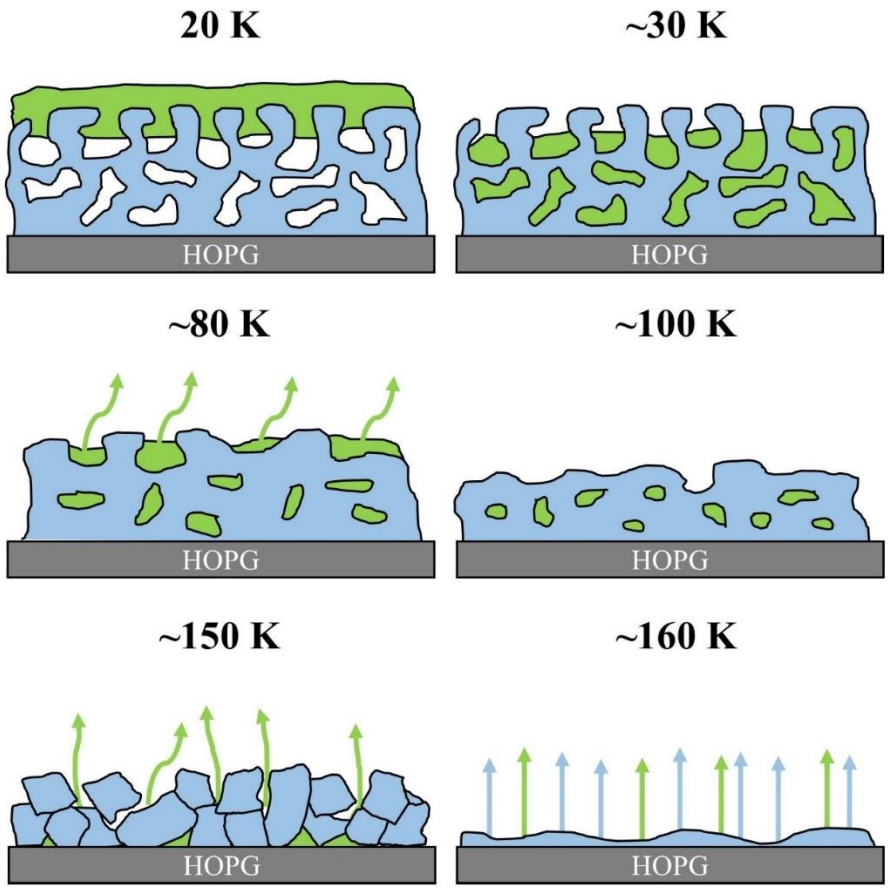

Figure 5.20 – Cartoon summarising the compaction of pASW, the crystallisation of cASW to CI and the desorption of CI. Shown in green is a probe (CO_2) deposited on top of a layer of pASW. The coloured arrows indicate the desorption of the corresponding species.

An alternative explanation for the differing behaviour at low temperatures is that the initial part of the trapping curves is artificial. This could be the case if the probes were not probing all the ASW due to a sub-saturation coverage. It is possible that if the probe had not *just* saturated the pASW then any changes in its structure would go unnoticed until the compaction had reached a point at which the pASW had become saturated. After this point, the probe would begin to show a reduction in trapping. However, two factors suggest that the initial part of the trapping curves are not artificial. Firstly, the ratio between the maximum amount of the two probes correlates with the ratio of their van der Waals radii. And secondly, the temperature range for which compaction is observed agrees with several pieces of literature, the low temperature part of the curves cannot be conclusively assigned.[111,113,129]

Layered systems of, from top to bottom, CO_2, formic acid and ASW were also studied to examine the effect of a hydrogen bonding species on the compaction of ASW. Assertions made in Chapter 4 as to the nature of formic acid TPD peaks when it is deposited on water

were further validated, in particular the low temperature feature corresponding to accelerated desorption during the ASW to CI phase change, termed volcano desorption. Furthermore, it was confirmed that the ASW to CI phase change occurs at a lower temperature when formic acid is present.

Regarding compaction of ASW when formic acid is present, it is clear from Figure 5.16 that the general trends observed in layered systems of CO_2 (or CS_2) on water are apparent in this system. The evolution of the surface/near-surface peak clearly follows the same trend, as does the volcano peak. However, the co-desorption feature is more complex owing to the overlapping of the CO_2 peak and the mass 44 cracking fragment of formic acid. Preliminary analysis showed a trend in decreasing probe trapping with increasing water deposition temperature, similar to what was seen when formic acid was not present. The onset and completion of compaction occurred at higher temperatures when formic acid was present. It is suggested that formic acid may be acting as a scaffold, supporting the pASW against compaction.

The work here has shown that using a non-hydrogen bonding molecule, it is possible to non-invasively probe a structural change in an underlying ice in a similar manner as that used by Collings *et al.*.[40] The high temperature region of the trapping fraction curve was shown to subtly vary between CO_2 and CS_2, but was not significant enough to explain the major differences reported in the literature. It is believed that these subtle differences are not the probe affecting the compaction process; rather, one probe is more sensitive to structural changes in the host water. The slight variations between the two probes used here do not account for the stark differences between this work and that of Collings *et al.* and indicates that further work understanding the compaction of pASW is needed. It also shows that comparisons between studies involving, or using, ASW deposited below 110 K must be done very carefully, even when comparable experimental methods are employed.

This work also demonstrates the need for astronomical models to intricately model the thermal history and evolution of ASW. Collings *et al.* previously modelled the compaction process using an autocatalytic reaction scheme and obtained a good fit to their experimental data.[40] However, the reaction scheme Collings *et al.* used was not temperature dependent. A similar reaction scheme could possibly be used to fit the data presented here but it would be required to be temperature dependent. This is because,

unlike the results of Collings *et al.*,[40] the results presented here show that the onset of pASW compaction is not immediate and only occurs once a certain temperature is reached. Furthermore, models must account for the influence of hydrogen bonding species on the structural evolution of water ices that occurs prior to crystallisation. It is important to consider the implications of ASW compaction in the ISM, as it is possible that this process is key to the retention of molecules above their desorption temperatures. This may allow these species to contribute to the chemical evolution of ices that surround interstellar dust grains and could ultimately lead to the formation of more complex molecules.

It was not possible to carry out complimentary RAIRS experiments for the experiments discussed in this work due to experimental constraints. The purge system could not provide sufficiently stable levels of CO_2, meaning that the key CO_2 absorption feature could not be used for analysis purposes. Financial constraints meant that it was not possible to use isotopically labelled CO_2 to overcome this problem. It was not possible to use CO in TPD experiments because CO was detected desorbing from surfaces other than the substrate, such as the cold finger, and consequently the TPD spectra were distorted.

6 Examining Compaction of Amorphous Solid Water Using Reflection Absorption Infrared Spectroscopy

6.1 Introduction

Amorphous solid water (ASW) is prevalent in both the interstellar medium (ISM)[88,111,213,214] and the Earth's atmosphere.[215] There is disagreement within the literature regarding the nature and evolution of structures that fall under the umbrella term ASW.[41,107,111,113,115,116,216–218] In Chapter 5, temperature programmed desorption (TPD) was used, in conjunction with probe molecules (CO_2 and CS_2), to investigate the thermally induced compaction of porous ASW (pASW) to compact ASW (cASW). Compaction of ASW is accompanied by a reduction in the porosity of the water ice. The present work uses reflection absorption infrared spectroscopy (RAIRS) to study the same compaction process, using CO as a probe. This allows for comparison with the work of Collings *et al.*,[40] whose RAIRS investigations also used CO. It was possible to use CO here because RAIRS does not sample any surfaces in the chamber other than the substrate.

One of the reasons that CO was chosen as a probe is that the RAIR spectrum of physisorbed CO is well-documented in the literature and has previously been studied using the experimental set-up used here.[40,41,140,156,232] With this set-up, CO was deposited at 26 K on a highly oriented pyrolytic graphite (HOPG) sample.[140] The RAIR spectra collected after the lowest CO exposures showed a single feature at 2143 cm^{-1}, corresponding to the CO fundamental stretch.[233] For higher CO exposures, a second peak appeared at 2137 cm^{-1}. These two features were assigned to the longitudinal optical (LO) and transverse optical (TO) modes of the CO stretch in multilayer CO.[140] Work by Palumbo and Strazzulla[233] demonstrated that CO adsorbed on a Si(111) surface produced a single feature centred between 2139 and 2140 cm^{-1}. They also showed that CO desorbed from the Si(111) substrate at ~30 K.[233] Collings *et al.* reported that a sub-monolayer coverage of CO deposited onto a silica substrate has a single peak at 2137 cm^{-1}, that did not change until desorption started at 26 K.[118]

CO can also be used to probe the water in a CO and water containing ice. In the presence of water, the CO absorption band is usually reported as having two components: a dominant feature at ~2138 cm^{-1} and a shoulder at ~2152 cm^{-1}. The dual feature is due to the different binding sites of CO on water.[41,102,118,233–236] These assignments have been

the subject of debate in the literature, as has the way in which they evolve with heating. The relationship between these two CO absorption features has previously been studied and will be used here to examine the compaction of pASW to cASW.[40,234,236–238] However, the CO-water interaction must be understood prior to using CO to probe the compaction of ASW.

Work by Sandford *et al.*[235] on CO-water mixtures assigned the two components of the CO absorption band by comparing their relative positions to the gas phase fundamental mode. The main feature at 2136.7 cm^{-1} was attributed to CO substituting a H_2O molecule in the larger matrix. The shoulder at 2152 cm^{-1} was assigned to an interstitial CO within the pores of the ASW. Sandford *et al.* observed that when CO-water mixtures were annealed above 40 K the ratio between the two CO infrared features underwent significant change.[235] At the lowest temperatures the ratio of the main feature to the shoulder was ~4:1 and upon annealing to 100 K it was ~20:1. This change in the ratio was assigned to a loss of interstitial binding sites.

Furthering the work by Sandford *et al.*,[235] Devlin used innovative experiments, involving the contaminants ethylene oxide and CF_4, to better understand the two-component CO infrared band observed when CO is in the presence of water (D_2O).[239] By exploiting the hydrophobicity/hydrophilicity of the contaminants, Devlin assigned the 2152 cm^{-1} component to CO binding to dangling OD (or OH) bonds. Dangling OD (or OH) bonds are found on the surface of water (internal pore surface or external surface) and are not bound to other water molecules within the structure[237]. Water molecules with dangling OH bonds can be 2 or 3 coordinate, with the former having a non-hydrogen bonded oxygen lone pair.[214,240] The two types of dangling OH bonds are denoted together as dOH. The focus of the work by Devlin was the 2152 cm^{-1} component, but they tentatively assigned the 2136 cm^{-1} component to CO interacting with the oxygen of water molecules on the pore surfaces. Subsequent work by Palumbo,[109] where CO-water mixtures and CO-irradiated water systems were studied, agreed with the assignments of Devlin,[239] rather than Sandford *et al.*.[235]

Palumbo and Strazzulla recorded a number of observations regarding the two components of the CO absorption band when CO is in the presence of water. Between 47 and 67 K the 2152 cm^{-1} shoulder was lost, and the 2138 cm^{-1} main feature redshifted to ~2135 cm^{-1}

between 17 and 150 K. Observation of the main feature up to 150 K indicated to Palumbo and Strazzulla that CO can remain trapped in water ices up to 150 K.[233]

The nature of CO binding sites on the surface of water was studied by Al-Halabi *et al.* using computational methods.[102] With reference to earlier computational work by Collings *et al.*,[40] they calculated the possible binding configurations of CO and water that could be responsible for the two CO infrared absorption features. Collings *et al.* used *ab initio* calculations to compare two different CO-water complexes, shown in Figure 6.1. These complexes were an extended complex, where CO binds almost linearly to a dangling OH bond on the pore surface, and a compact complex, where CO binds almost parallel to the OH.[40] From the energy difference between the two complexes, they assigned the compact complex to the 2139 cm^{-1} feature in their RAIR spectra.

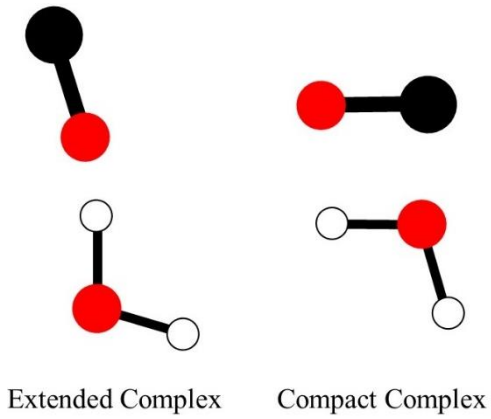

Figure 6.1 – Cartoon depicting the CO-water bonding geometries as reported by Collings *et al.*.[40] Red circles are oxygen, black circles are carbon and white circles are hydrogen.

Al-Halabi[102] built on Collings *et al.* simple *ab initio* calculations and assigned the 2139 cm^{-1} feature as CO binding to several bonded-OH simultaneously, in a parallel or near parallel geometry. A recent publication by Collings *et al.* takes their earlier *ab initio* calculations further and compares them with experimental data for CO interacting with water and other species.[234] They concluded, in agreement with Al-Halabi,[102] that the 2139 cm^{-1} band originated from CO interacting with water in a parallel or near parallel geometry. The water molecules at the surface which bind to CO – the interaction responsible for the 2139 cm^{-1} feature – have one of two possible geometries.[214,234,240] These water geometries are either 3 coordinate (with an unbound and exposed oxygen lone pair at the surface, denoted dO), or 4 coordinate (with no unbound OH bonds, or

oxygen lone pairs, denoted s4). The s4 and dO geometries are depicted in . The s4 geometry has been described in the literature as a modified tetrahedron.[214]

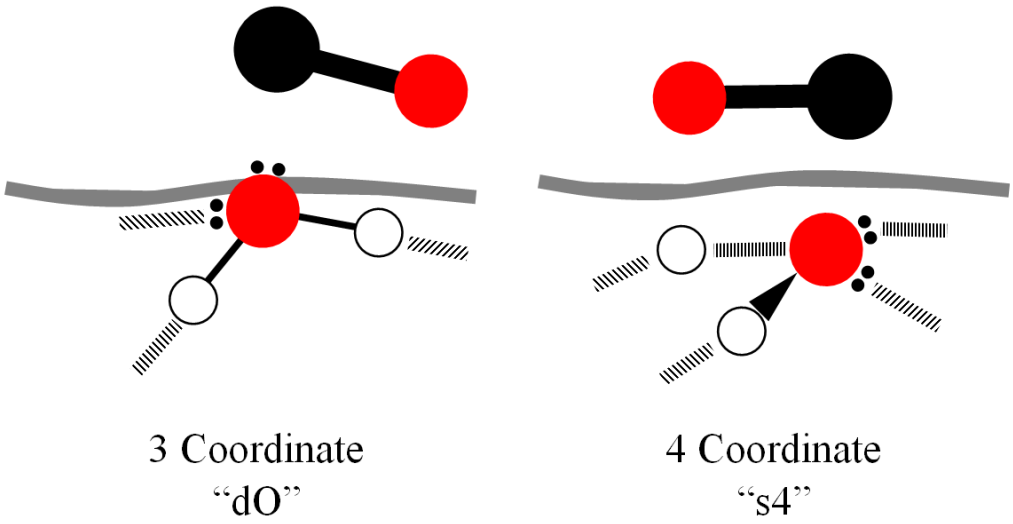

Figure 6.2 – Cartoon depicting the water dO and s4 geometries, adapted from Noble *et al.*.[214] Red circles are oxygen, black circles are carbon and white circles are hydrogen.

More recent work published by Karssemeijer *et al.* studied the CO-water interaction using computational and experimental methods.[236] In this work, they refer to the two different CO features observed for CO-water systems as the polar and non-polar components. Bouwman *et al.*,[110] referenced by Karssemeijer *et al.*,[236] defined polar and non-polar ices as CO in the proximity of molecules that could hydrogen bond and those that could only bind via van der Waals interactions, respectively. These assignments by Bouwman *et al.*[110] are in line with those of Collings *et al.*[234] and Al-Halabi,[102] who stated that the 2139 cm^{-1} feature originates from CO binding parallel, or nearly parallel, to the water surface. However, the experimental results reported by Karssemeijer *et al.* suggest something slightly different.[236] They imply that CO in direct contact with the water (i.e. with the walls of the pore/channels) is polar (2152 cm^{-1} component), whilst CO between these polar areas is non-polar (2139 cm^{-1} component). The assignments of Karssemeijer *et al.* are in contrast to those of Collings *et al.*[234] and Al-Halabi[102] who concluded that the different features in the CO absorption band were a consequence of *how* CO binds, rather than to what.

When a CO-water system is heated, it is consistently reported that the main 2139 cm^{-1} feature remains due to CO trapping within the water, and remaining so up to temperatures as high as 120 to 150 K. However, the 2152 cm^{-1} feature will be lost at much lower

temperatures than the main feature.[233,235,241] This behaviour changes when the nature/thermal history of the water is varied and is why CO is used to probe the water compaction process.[40,41,237,238]

In the work by Sandford *et al.*, it was shown that the 2152 cm^{-1} feature for a CO-water mixture gradually loses intensity when warmed above 10 K and is most likely lost by 80 K.[235] Regarding the main feature, they report that between 10 and 150 K it shifts from 2136.7 to 2134.4 cm^{-1} and that there does not seem to be any appreciable intensity loss. However, they calculate that the ratio of the high to low wavenumber components decreases significantly upon annealing to 80 K. They do not refer to any changes in the water that may be causing the shift in the components, rather they discuss it as a competition between migration and desorption of CO.

Palumbo and Strazzulla[233] reported that the CO band behaved in a similar way to that reported by Sandford *et al.*.[235] They observed that when heating above 17 K, the main features loses intensity. They credited the loss of the 2152 cm^{-1} feature by ~67 K to desorption of CO from interstitial sites. Although they reported that CO remains trapped up to 150 K, they did not discuss, or show, the spectral profile in any detail above 117 K.

Two key pieces of work by Collings *et al.*, discussed above, addressed the evolution of the CO fundamental band with regards to the high density amorphous (HDA) ice to low density amorphous (LDA) ice transition.[40,41] HDA and LDA are used in some of the literature to denote pASW and cASW, respectively. When examining the effect of annealing on the CO band for layered and mixed systems that had been deposited at 8 K, they noticed several changes. Between 30 and 70 K, the 2153 cm^{-1} feature decreased in intensity, whilst the 2139 cm^{-1} feature redshifted to 2138 cm^{-1} and increased in intensity. The decrease in the 2153 cm^{-1} feature is related to a loss of OH dangling bonds, a consequence of the compaction of HDA to LDA that occurs between 30 and 70 K. They suggested that the small redshift in the 2139 cm^{-1} feature indicated that the environment responsible for this component of the CO band remained relatively unchanged. The increase in intensity of the 2139 cm^{-1} component and the decrease in the 2153 cm^{-1} component is credited to some of the CO bound to dangling OH bonds migrating, rather than the loss in the 2153 cm^{-1} feature being solely due to desorption. Upon further heating, they observed that some of the CO is lost as LDA crystallises to crystalline water (CI) and finally, any remaining CO desorbs during the desorption of CI. They also discussed

the annealing of layered ices, prepared by depositing water at 80 K (forming LDA) and then depositing CO on top at 8 K. Both the 2153 and 2139 cm^{-1} features were observed at 25 K, however, upon annealing to 50 K, both features were lost. They noted that the 2139 cm^{-1} band is not retained up to higher temperatures because, unlike the ices deposited at 8 K, there is no mechanism to trap CO.

Later work by Fraser *et al.*[238] described a third key feature at 2136 cm^{-1}, which appears above 80 K. They linked this third feature with the 2139 cm^{-1} feature and assigned it to CO trapped in collapsed pores.[40,41,160,242] They also reported that when CO was deposited on CI the overall CO band, prior to annealing, was comparable to that observed when CO was deposited on compact ASW (referred to as LDA in the Collings publications). When the CO on CI system was heated, total desorption occurred between 25 and 30 K, as expected since CI can be considered a smooth, flat surface.[238]

A later publication by Collings *et al.* examined in more detail the differences in the CO spectra obtained when it was deposited on different types of ASW.[237] They reported that when CO is deposited at 8 K, adsorption is ballistic. When the water was deposited at temperatures of 70 K and below, the high wavenumber CO infrared feature was broad, whilst for water deposition temperatures of 120 and 130 K it was sharper. This sharpness in the CO absorption feature is due to the water surface being more well-ordered. CO was then deposited onto pre-adsorbed water layers at 30 K in order to prevent the growth of CO multilayers, this allowed them to examine CO monolayer and sub-monolayer behaviour.[237] They observed that for all water deposition temperatures the ratio of the intensities of the low and high wavenumber CO absorption features remained relatively constant. However, when water was deposited at 80 K, the high wavenumber feature was reduced.[237] For mixed ices they reported an increased absorption intensity between 20 and 30 K, suggesting that there had been an increase in the absorption cross-section of CO and, as such, quantitative analysis of the spectra may be limited. However, since they did not observe a similar effect in layered systems they cautioned against this conclusion.[237]

The structural changes that occur in water between ~10 to ~160 K have been studied by examining the infrared signature of the OH dangling bond itself.[88,113,131,132,214,220,243] With certain experimental set-ups it is possible to detect the difference between dangling OH bonds from two or three coordinated water molecules and use any changes in these

infrared bands as a measure of compaction.[132] However, in the experimental set-up used in the present work, the OH dangling bond absorption band is non-detectable, a problem also experienced by Collings *et al.*.[237] Whilst it may not be possible to directly detect the OH dangling bond, work such as that by Collings *et al.*[237] demonstrates that use of a probe molecule still allows for detailed and useful conclusions regarding ASW to be made from RAIRS experiments.

Considering the discrepancies between the conclusions reached in Chapter 5 and some of the literature, this work aims to use RAIRS studies of CO and water systems to investigate the compaction of ASW and determine the temperature range over which compaction occurs. By examining the compaction process using a different probe molecule and technique from Chapter 5, the probe identity and experimental technique can be discounted as reasons for the conclusions in Chapter 5 differing from those in some of the literature, in particular the work by Collings *et al.*.[40,41]

To achieve the goals described above, water ices will be deposited with the substrate at a given temperature, cooled and then exposed to a controlled amount of CO. These ices will then be subjected to repeated annealing cycles with RAIR spectra taken throughout. The difference between the initial state and thermal evolution of these systems will be used to assess the nature of the water. Initial experiments will focus on characterising the behaviour of CO in the system used here and then developing the ice system that will be used to examine the compaction of pASW.

6.2 Experimental

The water used throughout this chapter was handled as described in Chapter 4. A CO lecture bottle (CK Gas, 99% purity) was attached to the gas line via a regulator. The gas line was filled with CO and then isolated from the lecture bottle prior to dosing.

Due to the experimental requirement that the sample must remain in the RAIRS position throughout the entirety of an experiment, it was necessary to dose with the high precision leak valves directed behind the sample mount. As a consequence of using background dosing, the dose amounts in this chapter will seem large in comparison to those used in Chapter 5. The amounts of water and CO used in the present work will be addressed in the following section.

Water ices were prepared by holding the HOPG at the temperature of interest whilst admitting water into the chamber. The elevated substrate temperature was held for 3 minutes after deposition had ceased, to ensure that any water that adsorbed as the chamber pressure was brought down did so at the appropriate temperature. Ices were annealed by raising the temperature at a rate of 0.5 K s^{-1} and then holding the desired temperature for 3 minutes. The substrate was then cooled and the RAIR spectrum recorded. RAIR spectra were obtained in the same manner as detailed in Section 3.2, by the co-addition of 256 scans using a resolution of 4 cm^{-1}.

6.3 Results and Discussion

6.3.1 CO on HOPG

Figure 6.3 displays the 2200 to 2080 cm^{-1} region for CO adsorbed on HOPG at ~22 K. For all exposures of CO between 1 and 50 L_m, there is a single absorption band at 2141 cm^{-1}, which compares well with CO spectra obtained previously on HOPG[140] and other surfaces.[118,233,235] As there is minimal difference between the gas phase CO fundamental band (at 2143.3 cm^{-1})[244] and the band observed in Figure 6.3, it can be assumed that CO physisorbs on HOPG at ~22 K.

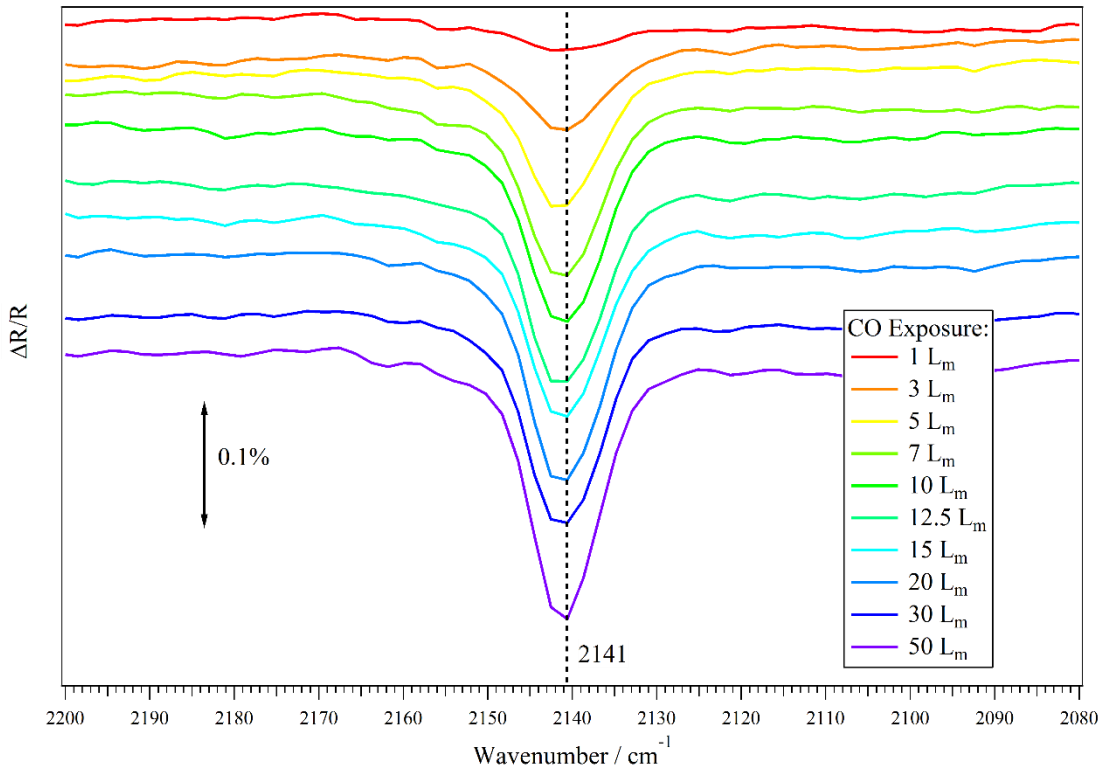

Figure 6.3 – RAIR spectra obtained after exposing HOPG to CO at a substrate temperature of ~22 K.

Figure 6.3 shows that the band may be saturating at higher coverages, suggesting the absence of multilayers. The previous work using this experimental set-up observed LO and TO splitting when CO multilayers were prepared on HOPG. Therefore, the absence of LO and TO splitting further suggests that multilayer growth is being prevented.[140] Saturation of the absorption band can be probed further by integrating the band area and plotting as a function of CO exposure. This is possible because, assuming there are no orientation effects, the area of an infrared absorption band is proportional to the quantity of absorber. The resulting plot of CO infrared band area as a function of total CO exposure is shown in Figure 6.4. It is clear from this figure that between exposures of 10 and 20 L_m the CO absorption band is saturating. The error bars in Figure 6.4 were calculated using the standard deviation of the dose curve areas for each of the CO exposures.

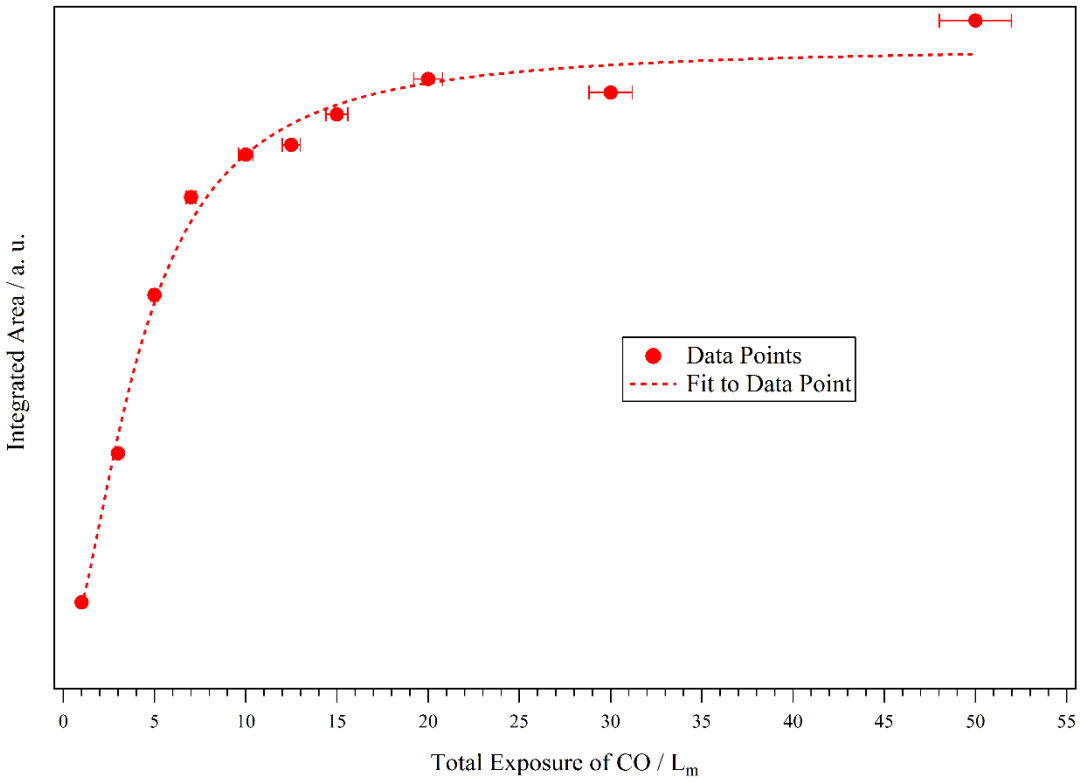

Figure 6.4 – Integrated area of the CO infrared absorption band (shown in Figure 6.3) as a function of total CO exposure.

Figure 6.5 shows the spectra obtained after depositing 10 L_m of CO on HOPG at ~22 K and then annealing to temperatures between 24 and 44 K in a stepwise manner. 10 L_m of CO was chosen as it is the exposure that will be used in latter parts of this chapter (where the rationale for this choice will also be given), and also because it was shown in Figure 6.3 that it produces a clear and defined absorption band.

It is clear from Figure 6.5 that the CO band remains centred at 2141 cm^{-1}, and that immediately after annealing to 24 K there is significant intensity loss, indicating that desorption has commenced. An onset of desorption between 22 and 24 K is somewhat lower than observed for CO physisorbed on other substrates (23-26 K, depending upon the substrate).[38,118,245,246] Considering that the CO infrared band saturates, indicating that multilayer growth is absent, and the seemingly low desorption onset temperature, it appears that the actual temperature of the substrate was slightly higher than that recorded by the thermocouple. Based on the CO desorption onset temperatures in the literature, it is estimated that the temperature recorded by the thermocouple could be ~2 K lower than the actual temperature.

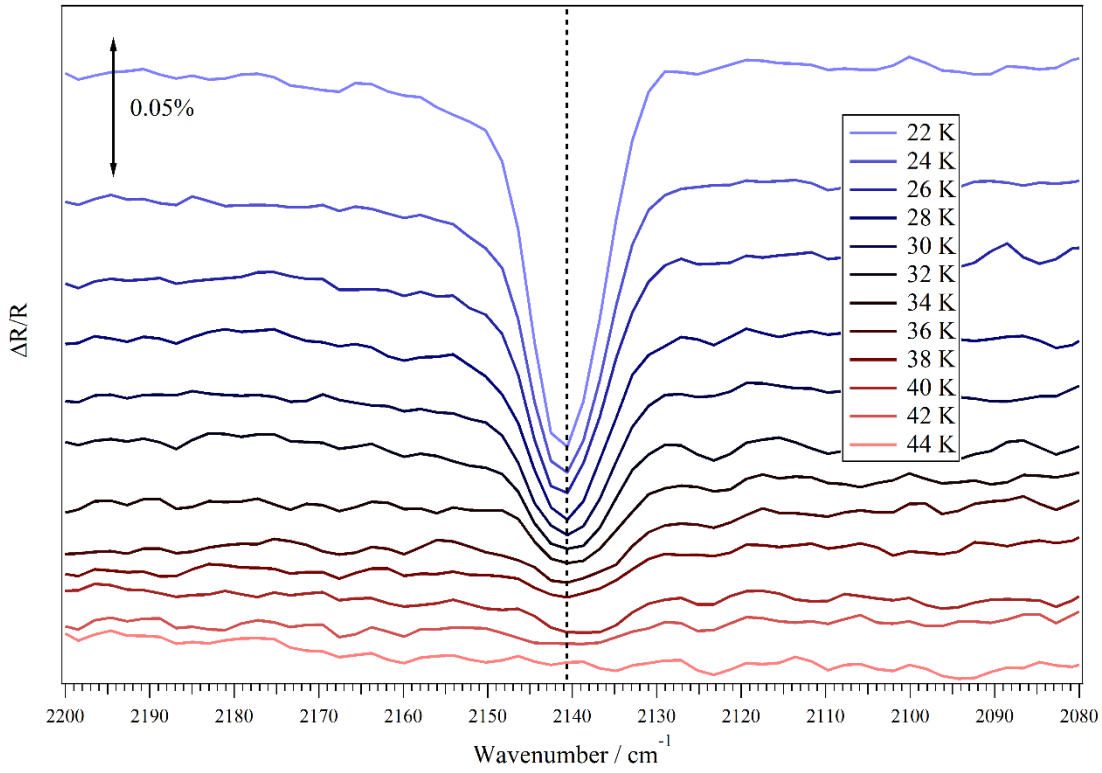

Figure 6.5 – RAIR spectra obtained after depositing 10 L_m of CO on HOPG at ~22 K and then annealing to the indicated temperatures. The dashed line indicates ~2141 cm^{-1}.

From visual inspection of Figure 6.5 it appears that desorption of CO from HOPG is complete at about 42 K. To track the desorption process, the area of the peaks in Figure 6.5 were calculated, normalised with respect to the 22 K spectrum and then plotted as a function of annealing temperature, as shown in Figure 6.6. The error bars in Figure 6.6 represent the ~2 K proposed error in the thermocouple reading.

From Figure 6.6 it seems that there is a small amount of CO remaining at 42 K and that desorption completes between 42 and 44 K. Accounting for the apparent error in the temperature recorded by the thermocouple, desorption is thus complete between 44 and 46 K. The temperature at which desorption is complete in RAIRS annealing experiments is difficult to compare directly with TPD experiments, which form the majority of desorption studies, due to the very different heating mechanisms (linear heating ramp compared to repeated annealing cycles). However, Collings *et al.* reported that a monolayer of CO on a gold substrate produced a desorption peak centred at ~31 K in TPD experiments.[40] This compares well with the results presented here, where, by ~31 K, ~60% of the CO on the HOPG surface had desorbed.

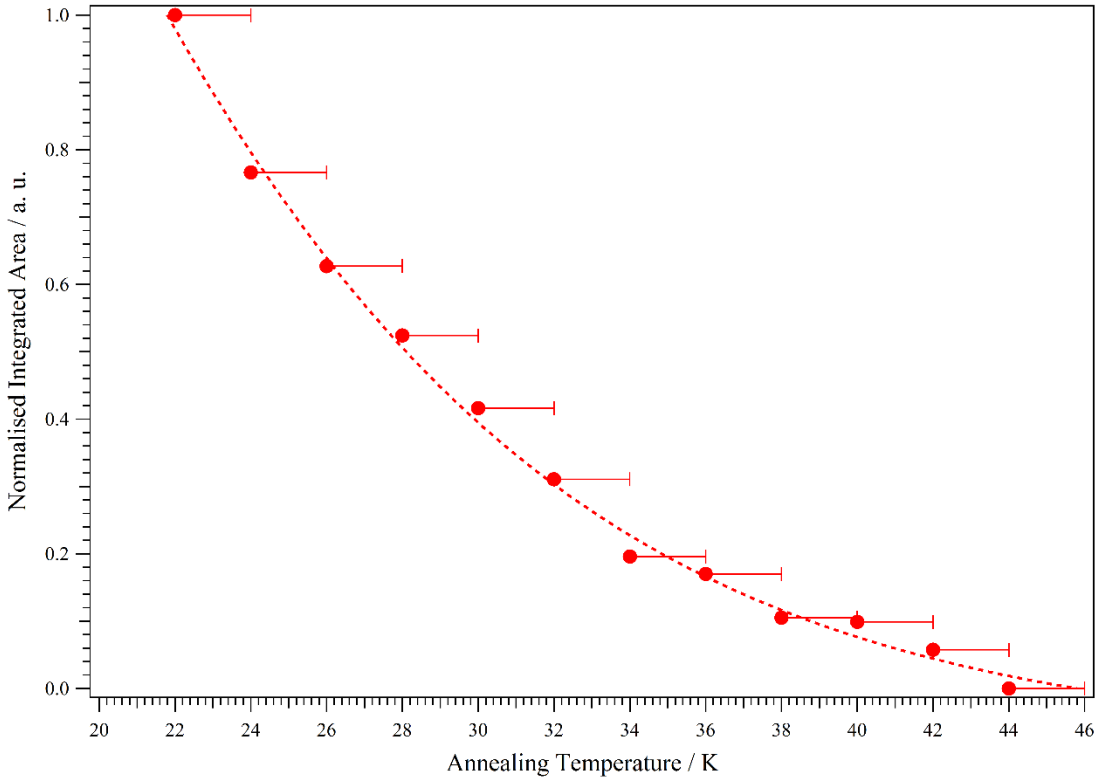

Figure 6.6 – Integrated areas of the peaks shown in Figure 6.5 plotted as a function of annealing temperature. The dashed curve is to guide the eye.

6.3.2 Characterising the CO-Water System

The CO-water system was prepared in three steps: depositing 100 L_m of water onto HOPG held at a given temperature, cooling the HOPG back down to base temperature, and then depositing CO on top of the water. Sufficiently thick multilayers of water were needed to ensure that there was no bare HOPG for the CO to interact with and previous work using

this set-up had shown that 100 L_m was an adequate exposure to achieve this.[140,141] Although the water ice thickness used here is not the same as that used in Chapter 5, the key condition that must be met, as discussed below, is that the amount of CO used does not saturate the water layer. This is in addition to the requirement that water multilayer ices are used.

The O-H stretching region (~3700-3100 cm^{-1}) of the water infrared spectra is commonly used as an indicator of the phase of the water ice. Figure 6.7 shows the O-H stretching region of the RAIR spectrum collected after 100 L_m of water was deposited on HOPG at ~22 K. The broad feature centred at ~3415 cm^{-1} is indicative of an amorphous water ice.[141,207]

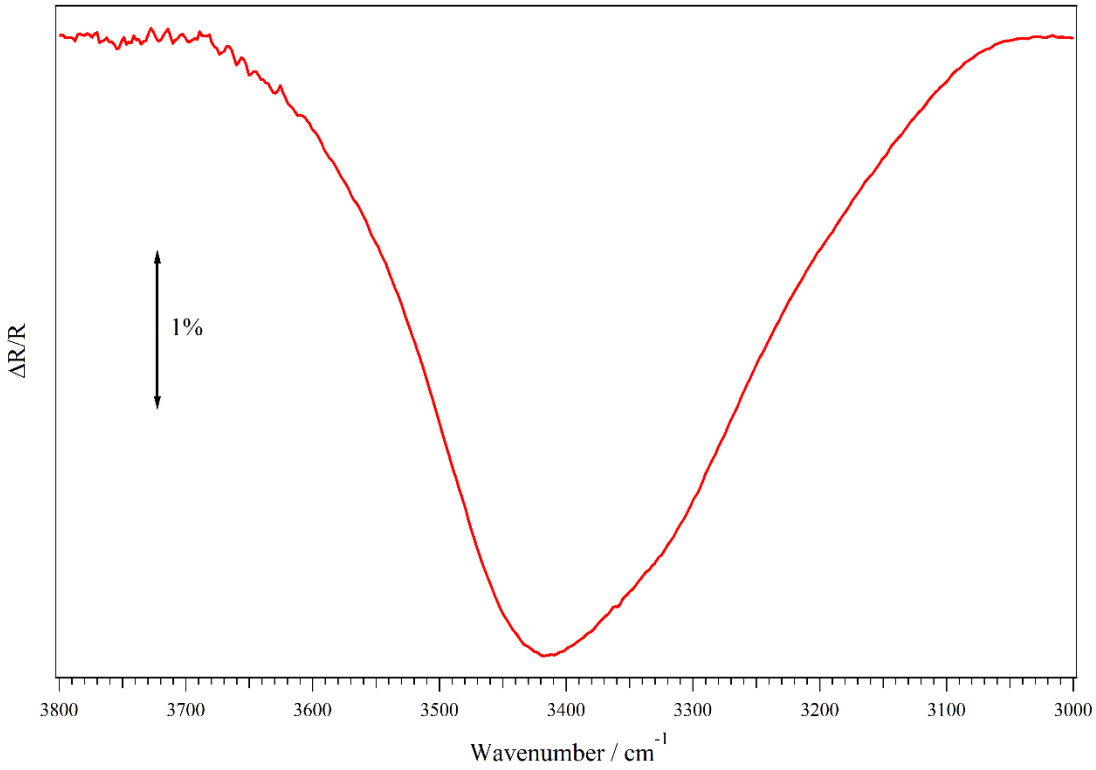

Figure 6.7 – O-H stretching region of the RAIR spectrum collected after 100 L_m of water was deposited on HOPG at ~22 K.

To characterise the CO-water system, different amounts of CO were deposited onto 100 L_m of water. The amount of CO used should not saturate the water ice because significant amounts of CO could then remain on the surface of the water and the pure CO vibrational band would dominate the spectrum. If this occurred, the spectral features of CO bonding to the different water sites would not be observable. Furthermore, any

individual binding sites on the water surface should not be saturated at base temperature since this study aims to use changes in the binding of CO to the water surface to track the compaction of ASW. If saturation occurred at base temperature, then it would not allow for proper analysis by comparison of the spectral components that relate to CO binding to water.

Figure 6.8 displays the RAIR spectra obtained after a 100 L_m water ice was exposed to 1-30 L_m of CO, with both species being deposited at ~22 K. Below 15 K, CO is unable to diffuse across a CO or water surface and so adsorption is ballistic.[237,239] However, above 15 K, CO is able to diffuse across a CO surface and above 28 K, it is reported that CO can diffuse across a water surface.[40,41,238] Therefore, a deposition temperature of ~22 K, even when a thermocouple error adjustment of ~2 K is factored in, means that CO will be mobile across any CO already on the surface and that it will bind to the first water site it encounters.

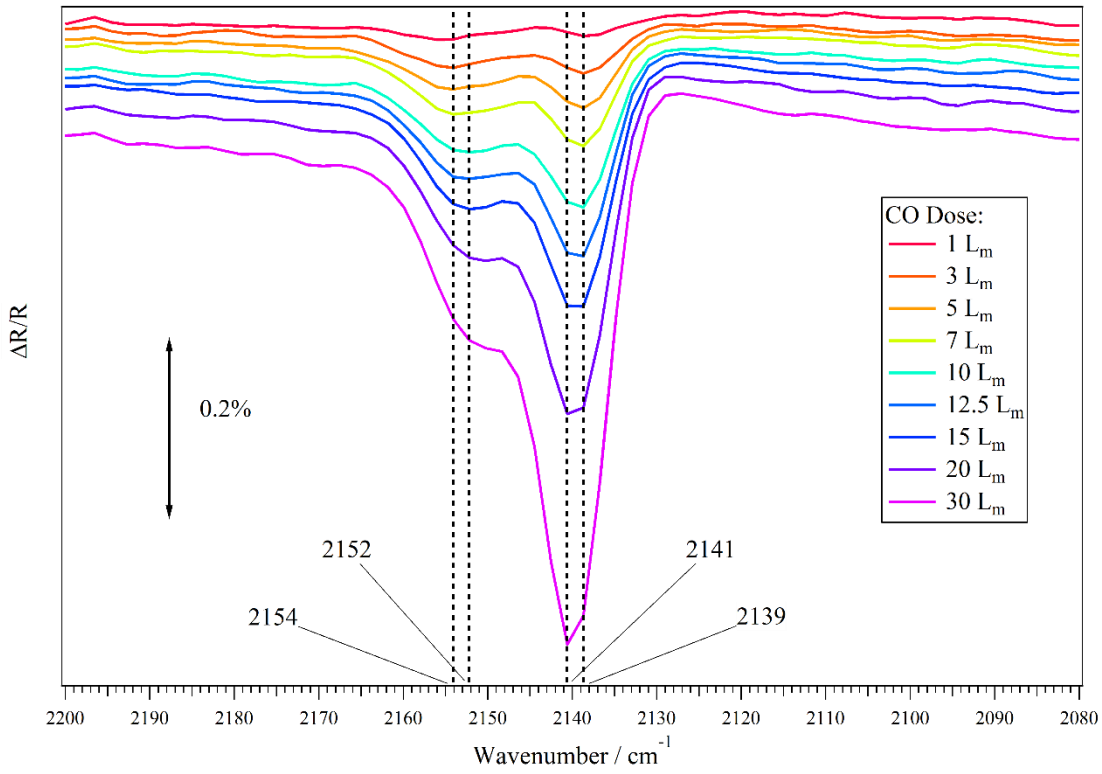

Figure 6.8 – RAIR spectra obtained after depositing 1-30 L_m of CO on top of 100 L_m of water. Both species were deposited at ~ 22 K.

There are two key features visible in all the spectra shown in Figure 6.8. The low wavenumber feature, that is at 2139 cm^{-1} in the 1 L_m spectrum, blueshifts to 2141 cm^{-1}

between exposures of 12.5 and 20 L_m. This is assigned, with reference to the literature, as CO bound almost parallel to water molecules in dO and s4 geometries at the surface. Therefore, this feature is denoted as $CO_{dO\text{-}s4}$. A shoulder on the $CO_{dO\text{-}s4}$ feature is initially centred at ~2154 cm^{-1} in the 1 L_m spectrum, but between exposures of 10 and 12.5 L_m it redshifts to ~2152 cm^{-1}. The position of the shoulder, between 2152 and 2154 cm^{-1}, is entirely in line with the literature and is indicative of CO bound to dangling OH bonds on the surface of water. Therefore, this band is denoted as CO_{dOH}[234]. The redshift of the CO_{dOH} feature as coverage increases is suggested by Collings *et al.* to be due to crowding of CO molecules bound to the dangling OH bonds of the water.[237] The blueshift of the $CO_{dO\text{-}s4}$ feature occurs as it becomes increasingly dominant over the less intense CO_{dOH} feature, signifying a link between the two processes. This suggests that the blueshift of the $CO_{dO\text{-}s4}$ feature is caused by contributions to the infrared band from CO binding to a different site – or in a different state – than the one responsible for the 2139 cm^{-1} feature.

Figure 6.9 shows the RAIR spectra obtained for CO exposures of 30-150 L_m on 100 L_m of water, where both species had been deposited at ~22 K. Unlike in Figure 6.8, neither of the features shift. However, it is clear that the whole CO infrared absorption band has saturated between 50 and 100 L_m. Saturation of the CO infrared absorption band indicates the absence of multilayers.[237] This is in line with the observations of pure CO ices on HOPG where it was seen that multilayer CO ices were prevented from forming. Therefore, the absence of CO multilayers on water indicates that the temperature reported by the thermocouple is, as suggested earlier, lower than the actual substrate temperature by ~2 K.

An interpretation of the blueshift in the $CO_{dO\text{-}s4}$ feature can be made by considering work by Collings *et al.*,[237] who suggested that the blueshift is a coverage effect. They deposited CO on ASW at 30 K – the temperature was chosen in order to prevent the growth of CO multilayers. The absence of multilayers was confirmed by the CO absorption band saturating with a sufficiently large CO exposure. For low CO exposures they reported that the adsorption sites in/on ASW for CO were occupied simultaneously, whilst for higher exposures, the relative intensity of the $CO_{dO\text{-}s4}$ feature had increased and blueshifted. This suggested to them that a more weakly bound CO state contributed to the $CO_{dO\text{-}s4}$ feature at high coverages.

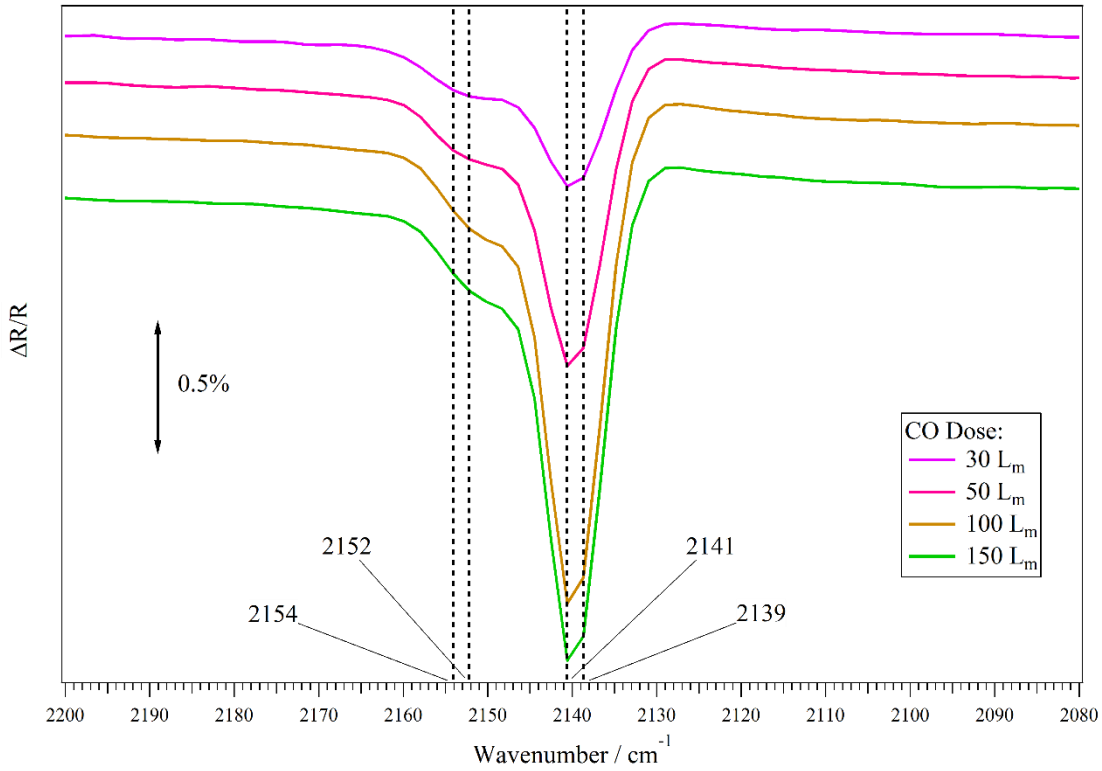

Figure 6.9 – RAIR spectra obtained after depositing 30-150 L_m of CO on 100 L_m of water. Both species were deposited at ~ 22 K. The dashed lines are to guide the eye.

To better understand the evolution of the CO absorption features as the CO coverage increases, the individual areas were calculated and plotted as a function of CO coverage. This analysis was possible, since – providing there are no orientation effects – the area of an infrared band is proportional to the amount of absorber. To calculate the individual areas, the overall CO absorption was fitted with two Gaussian curves. Gaussian curves were chosen, rather than another function, due to the quality of the fit, as judged by visual inspection.

Figure 6.10 shows an example of fitting the overall CO absorption band with two Gaussian curves and it demonstrates the good quality fit possible. The example shown is the RAIR spectrum obtained for 10 L_m of CO on 100 L_m of water, where both species had been deposited at ~ 22 K. By knowing the areas of the individual features it was possible to check for saturation of the bands, and thus water binding sites, allowing for proper characterisation of the CO-water system.

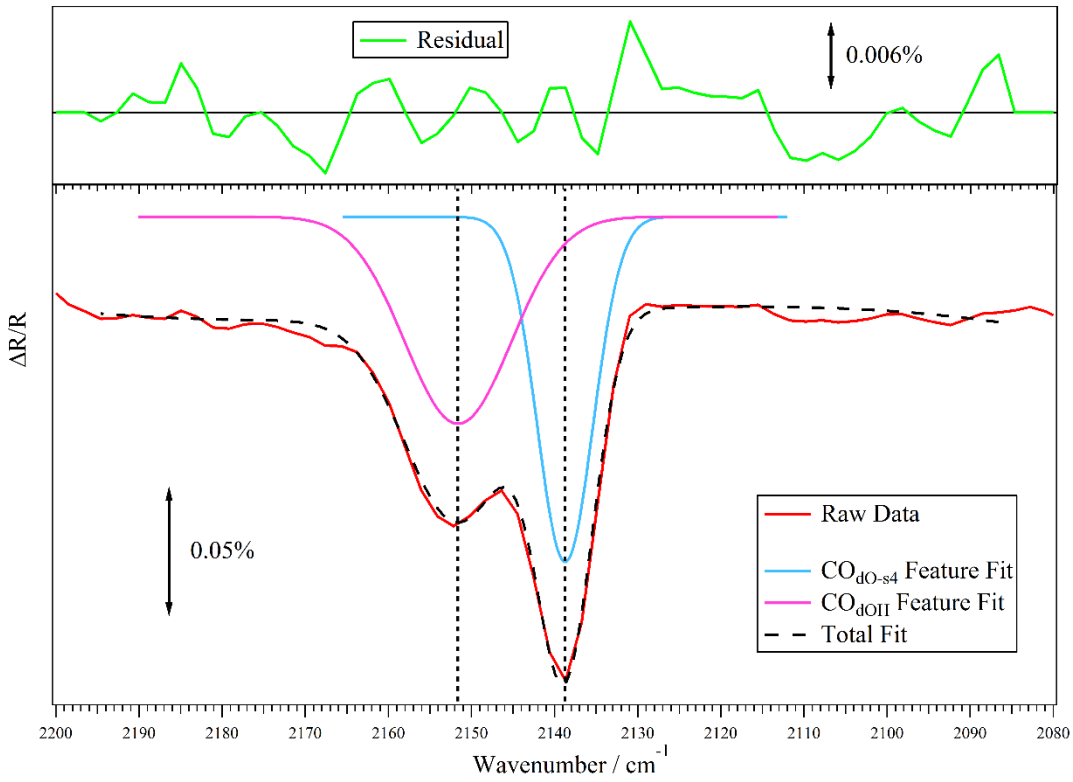

Figure 6.10 – An example of how multicomponent RAIRS features can be fitted using a composition of Gaussian curves. The raw data corresponds to 10 L_m of CO deposited on 100 L_m of water, with both species deposited at ~22 K.

Figure 6.11 shows the areas of the $CO_{dO\text{-}s4}$ and the CO_{dOH} features, alongside the total area, plotted as a function of the CO exposure. The data points for 100 and 150 L_m are not included as they make it difficult to observe how the areas of the features change for the lowest CO exposures. However, they do confirm saturation of the CO absorption band, as seen in Figure 6.9. The error bars were calculated using the standard deviation of the dose curve areas for each of the CO exposures. Up to 12.5 L_m the two components increase with CO exposure concurrently, with the CO_{dOH} feature dominating slightly. At 15 L_m the difference between the two areas is minimal and at 20 L_m the $CO_{dO\text{-}s4}$ feature becomes dominant. As the $CO_{dO\text{-}s4}$ feature becomes dominant, the CO_{dOH} feature begins to saturate. The lines (curves) are lines of best of fit and the curvature at low temperatures is a result of the change which feature is dominant. These observations are in line with the findings of Collings *et al.*[237] and also support the suggestion that CO binds to the first water molecule it encounters at the surface because this is, by definition, random.

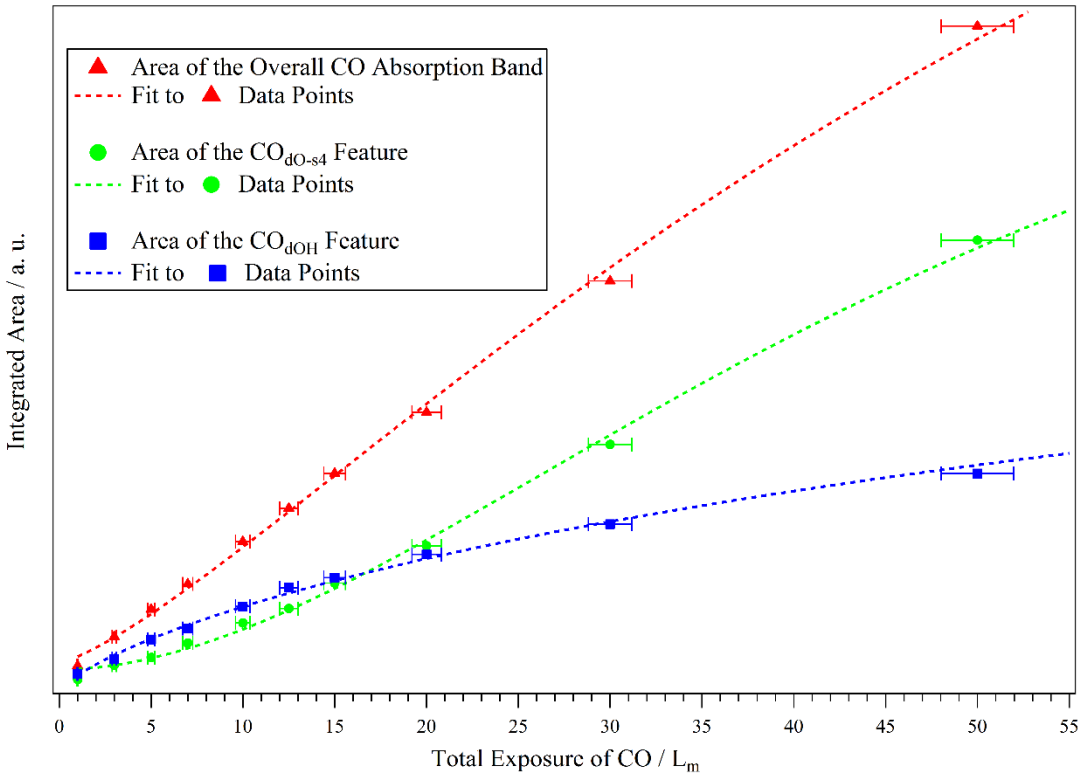

Figure 6.11 – Plot of the integrated areas of the Gaussian curves used to fit the CO_{dO-s4} feature (green circles) and the CO_{dOH} feature (blue squares) of the spectra shown in Figure 6.8 as a function of the CO exposure. Also included is the area of the two features summed together (red triangles).

Saturation of the CO_{dOH} feature above ~15-20 L_m indicates that there are no remaining dangling OH bonds for CO to bind to or that they are no longer accessible to the CO molecules. From Figure 6.8 it can be seen that after a CO exposure of 15 L_m, the CO_{dO-s4} feature is centred between 2139 and 2141 cm^{-1}, and from Figure 6.11, it is clear that this coincides with the point at which the CO_{dO-s4} feature becomes dominant. This indicates that the saturation of the OH dangling bond is linked with the blueshift in the CO_{dO-s4} feature, which itself is a consequence of CO occupying a more weakly bound state.

From inspection of Figures 6.8 and 6.1it was decided that a CO exposure of 10 L_m would be used throughout this study. This decision was made because it is clear that a CO exposure of 10 L_m precedes saturation of the CO_{dOH} feature and that it also results in a CO_{dO-s4} feature that has little, or no, contribution from the more weakly bound state that becomes occupied after higher CO exposures. Further to this, a CO exposure of 10 L_m produces an absorption band that is clear and defined above the baseline.

6.3.3 Thermal Evolution of CO on pASW

Ices comprised of CO deposited on ASW were prepared with the substrate at ~22 K and then annealed in order to understand the way in which CO behaves as the ice is heated. The observed changes in the CO spectrum are caused by two competing factors: the loss of CO by desorption and the changing nature of the water matrix under/around it. An example of the spectra obtained after annealing 10 L_m of CO on 100 L_m of water, with both species deposited at ~22 K, is shown in Figure 6.12.

It is evident from Figure 6.12 that between 22 and 36 K the changes in the spectra, and thus in the ice, are minimal. Since CO desorption from HOPG is well underway by 36 K, it is clear that the strength of the CO-water interaction is greater than that between CO and HOPG. Annealing to 40 K results in a decrease in the intensity of both features of the CO absorption band, indicating that desorption has commenced. The $CO_{dO\text{-}s4}$ feature also appears to lose some of its sharpness after annealing to 40 K, a possible indication that it is beginning to redshift.

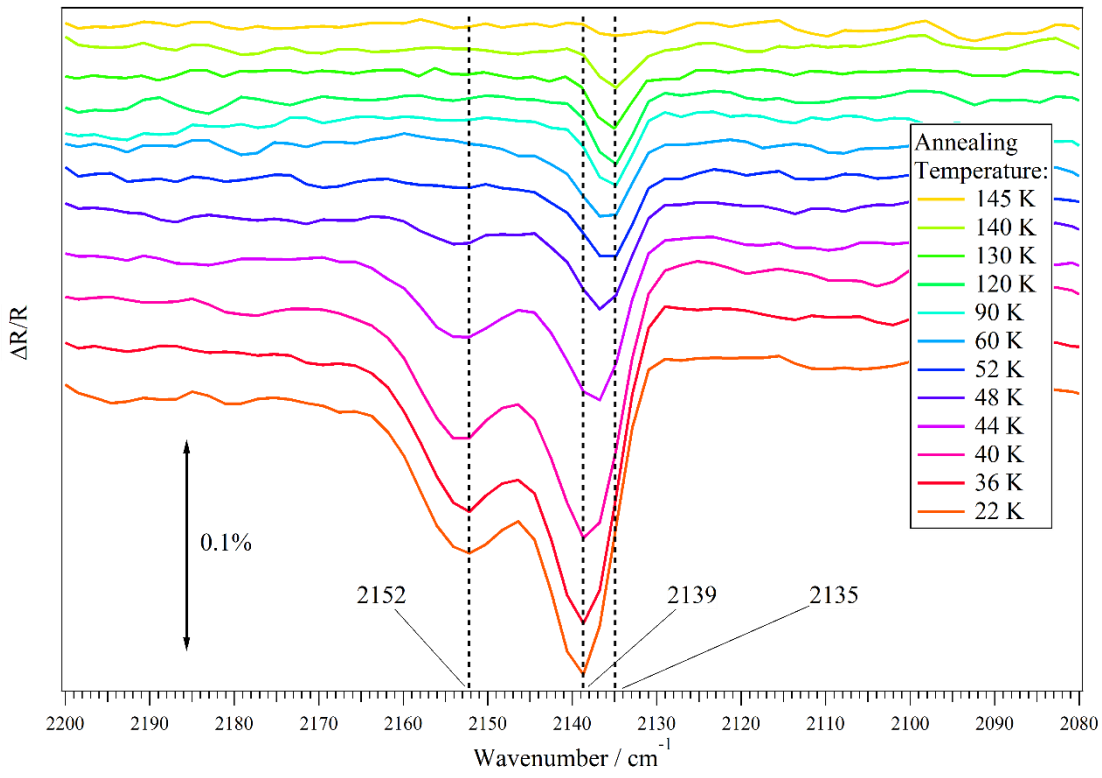

Figure 6.12 – RAIR spectra obtained after depositing 10 L_m of CO on top of 100 L_m of water and then annealing to the indicated temperatures. Both species were deposited at ~22 K.

Annealing to 44 K results in a significant decrease in both features and, furthermore, the $CO_{dO\text{-}s4}$ feature has clearly begun to redshift. By 48 K the CO_{dOH} feature has lost

definition, whilst the $CO_{dO\text{-}s4}$ feature has become dominant. After annealing to 52 K, the $CO_{dO\text{-}s4}$ feature has redshifted further and the CO_{dOH} feature has all but disappeared. Between 52 and 60 K there are minimal changes in the spectra. However, there appears to be a broad high wavenumber leading edge on the $CO_{dO\text{-}s4}$ feature by 60 K.

Annealing to 90 K results in the $CO_{dO\text{-}s4}$ feature narrowing slightly. After annealing to 120 K, the $CO_{dO\text{-}s4}$ feature gets smaller and becomes more well defined at 2135 cm^{-1}. There do not appear to be any changes in the spectra after annealing to 130 and 140 K. Annealing to 145 K results in total loss of the CO absorption band, indicating that CO has fully desorbed. The loss of CO after annealing to 145 K coincides with the crystallisation of ASW to CI, and is called volcano desorption.[42] This type of desorption occurs due to the formation of cracks and channels as the ASW reorganises during the phase change to CI.[108] Figure 6.13 shows the OH stretching mode of water after annealing to 145 K. The sharp peak at 3238 cm^{-1}, with a defined shoulders at ~3354 and ~3486 cm^{-1}, confirms that ASW has crystallised to form CI at 145 K.[103,141,247]

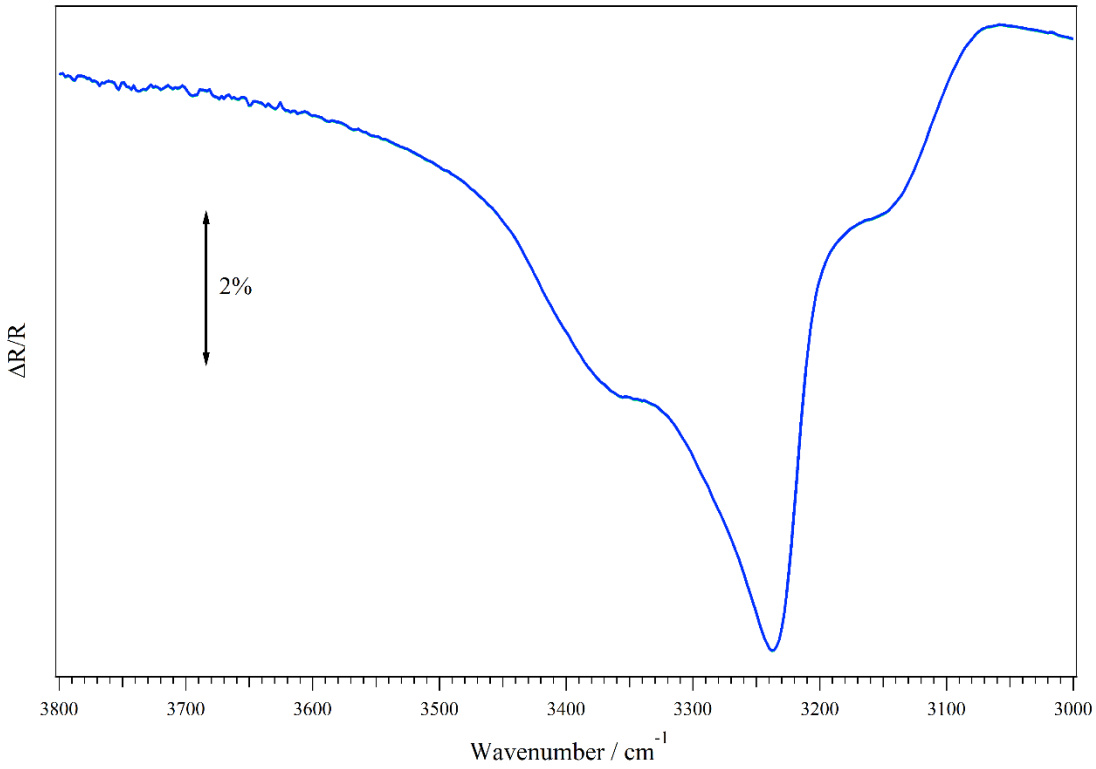

Figure 6.13 – RAIR spectrum of the O-H stretching region for 100 L_m of water deposited on HOPG at ~22 K and then annealed to 145 K.

Retention of CO in the water ice up to 145 K indicates that some of the CO has been trapped during the compaction of pASW to cASW. Therefore, the feature that remains up to 145 K (2135 cm^{-1}) can be assigned to CO trapped within collapsed pores, denoted as $CO_{trapped}$. The assignment of $CO_{trapped}$ is in line with the literature.[41,238] From Figure 6.12 it is difficult to ascertain whether or not the apparent shift in the $CO_{dO\text{-}s4}$ feature, which starts between 40 and 44 K, is due to the growth of the $CO_{trapped}$ feature or whether it is just being obscured less and less as the $CO_{do\text{-}s4}$ feature reduces due to desorption. If it is due to the $CO_{trapped}$ feature growing in, this would agree with the previous chapter whereby compaction was shown to be underway by 40 K.

Figure 6.14 displays the integrated areas of the CO_{dOH} and $CO_{dO\text{-}s4}$ features as a function of annealing temperature. The error bars shown represent the proposed error in the thermocouple reading.

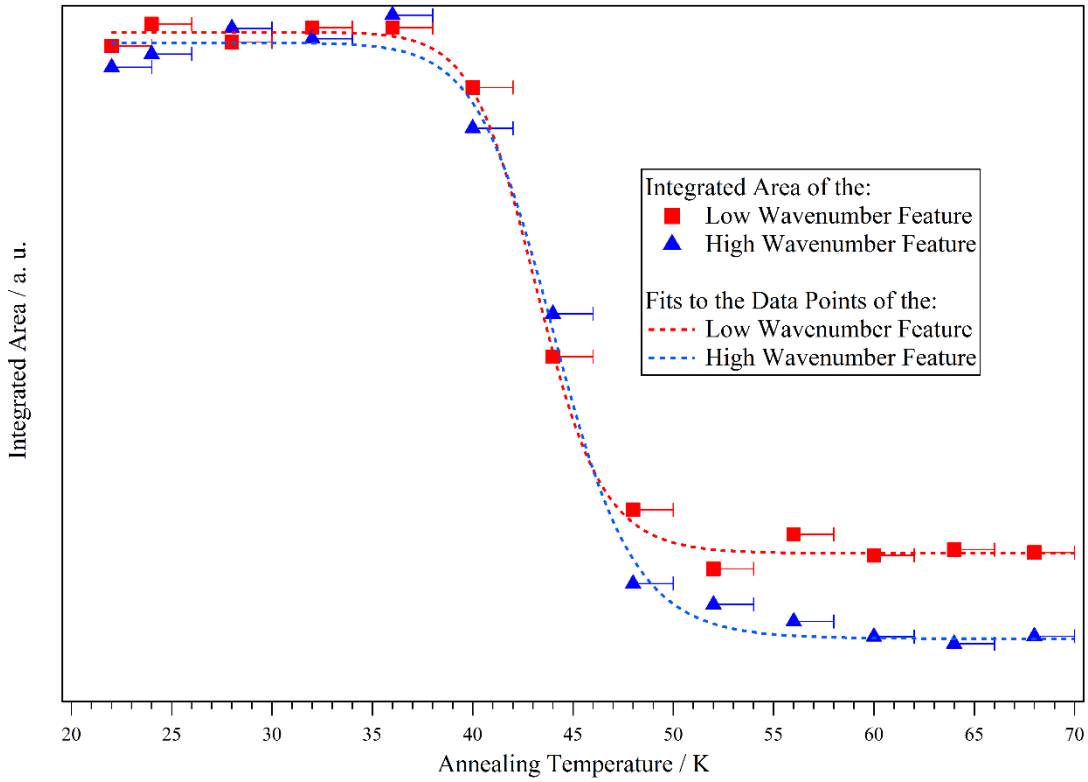

Figure 6.14 – Integrated areas of the $CO_{dO\text{-}s4}$ and CO_{dOH} features observed in RAIR spectra of 10 L_m of CO on 100 L_m of ASW annealed sequentially to the indicated temperatures. Both species deposited at ~22 K.

It is difficult to ascertain when the $CO_{trapped}$ feature appears and so the $CO_{dO\text{-}s4}$ and $CO_{trapped}$ features were fitted together. The figure only displays the integrated areas for the 22 to 60 K annealing cycles because above 60 K it is not possible to reliably identify

and integrate the area of the CO_{dOH} feature. This suggests that by this temperature, the OH dangling bonds have disappeared, or are no longer able to interact with CO.

It is clear from Figure 6.14 that below 36 K the overall absorption band is made up of approximately equal contributions from the two features. Desorption of CO begins above 36 K, with both features decreasing in area simultaneously. The concurrent loss of both features suggests that the strength of the CO-water interactions responsible for each feature are comparable. Desorption slows considerably around 48 to 52 K, with the CO_{dOH} feature having reduced to a much greater extent than the $CO_{dO\text{-}s4}$ feature. Between 52 and 60 K there are minimal changes in either feature. Above 60 K, the CO_{dOH} cannot be reliably detected or integrated. There are minimal changes in the integrated area of the $CO_{dO\text{-}s4}$ feature above 60 K, however, there is a slight decrease between 80 and 90 K. The remaining $CO_{dO\text{-}s4}$ feature is totally lost during volcano desorption as water crystallises at 145 K. Behaviour of this nature is in line with that reported in the literature for comparable CO-water system.[40,41,238]

Figure 6.14 can be used to aid the comparison of this work with that of Collings *et al.*[40,41] and Fraser *et al.*.[238] From examination of Figure 6.14 the loss of the CO_{dOH} appears to start at ~36 K and is complete by 60 K. However, Collings *et al.*[40,41] and Fraser *et al.*[238] report that the loss of both features starts at 25-30 K, and is complete by 70-80 K. Even if the apparent error in the thermocouple reading were factored in, there is a clear difference between the range reported here and that reported by Collings *et al.*[40,41] and Fraser *et al.*.[238] Whilst the CO_{dOH} feature is easy to observe, identifying when the $CO_{dO\text{-}s4}$ feature is completely lost is difficult due to it overlapping with the $CO_{trapped}$ feature. Fraser *et al.*[238] suggested that between ~25 and 80 K desorption of CO from dOH, dO and s4 water sites competes with trapping as pASW compacts. However, it is difficult to conclusively link the reduction in the CO_{dOH} feature (as the ice is annealed) with the compaction process. This difficulty arises because there are two processes that could be responsible for the reduction in CO binding to dangling OH bonds: desorption of CO from the dangling OH bonds or loss of the dangling OH bonds. Although not shown, it is clear that total desorption of CO occurs during volcano desorption after annealing to 145 K, whereas Collings *et al.*[41] report that some CO remains after crystallisation and desorbs only when the surrounding CI does so (called co-desorption). The amount of CO that remains after volcano desorption does not appear to be relevant to this investigation

into compaction and is possibly due to different annealing methods and/or ice thicknesses, or that the water ice was not saturated with CO.

6.3.4 Effect of ASW Compaction on Base Temperature CO Spectra

Unlike the TPD experiments reported in Chapter 5, it is possible to use RAIRS to take snapshots of the system without altering or destroying it. To do this, 100 L_m of water was deposited onto HOPG at a given temperature, the substrate was then cooled to base temperature and 10 L_m of CO was then deposited on top of the water. The range of water deposition temperatures was chosen with reference to the findings of Chapter 5. In earlier sections of this chapter it was shown that, using the experimental set-up used here, CO multilayer growth is prevented. Furthermore, it is expected that CO will bind to the first water molecule it encounters. Thus, CO should randomly sample the available water binding sites. Therefore, the RAIR spectra obtained after CO deposition (at base temperature) should, by comparison with the 22 K trace in Figure 6.12, provide an insight into the progression of compaction.

Figure 6.15 displays RAIR spectra obtained after CO was deposited on ASW that had been adsorbed at a range of temperatures. It also includes the same amount of CO deposited on CI for comparison.

For all water deposition temperatures, the CO absorption band consists of two features: the main $CO_{dO\text{-}s4}$ feature (2139-2141 cm^{-1}) and the smaller CO_{dOH} feature (2152-2154 cm^{-1}). At low water deposition temperatures, the $CO_{dO\text{-}s4}$ is centred at 2139 cm^{-1} and as the water deposition temperature increases, it gradually blueshifts to 2141 cm^{-1}. The CO_{dOH} feature is centred at ~2152 cm^{-1} and is relatively broad for the lowest water deposition temperatures. As the water deposition temperature increases from 24 to 65 K, the CO_{dOH} feature loses definition but remains centred at ~2152 cm^{-1}. For water deposition temperatures of 75 K and higher, the CO_{dOH} feature is increasingly well-defined and has blueshifted to 2154 cm^{-1}. It is clear from Figure 6.15 that the underlying ASW is evolving between 24 and 95 K, and also that there is some evolution between ASW deposited at 95 K and CI. This suggests that structural changes occur in the water underlayer over the whole temperature range, in line with the findings of Chapter 5.

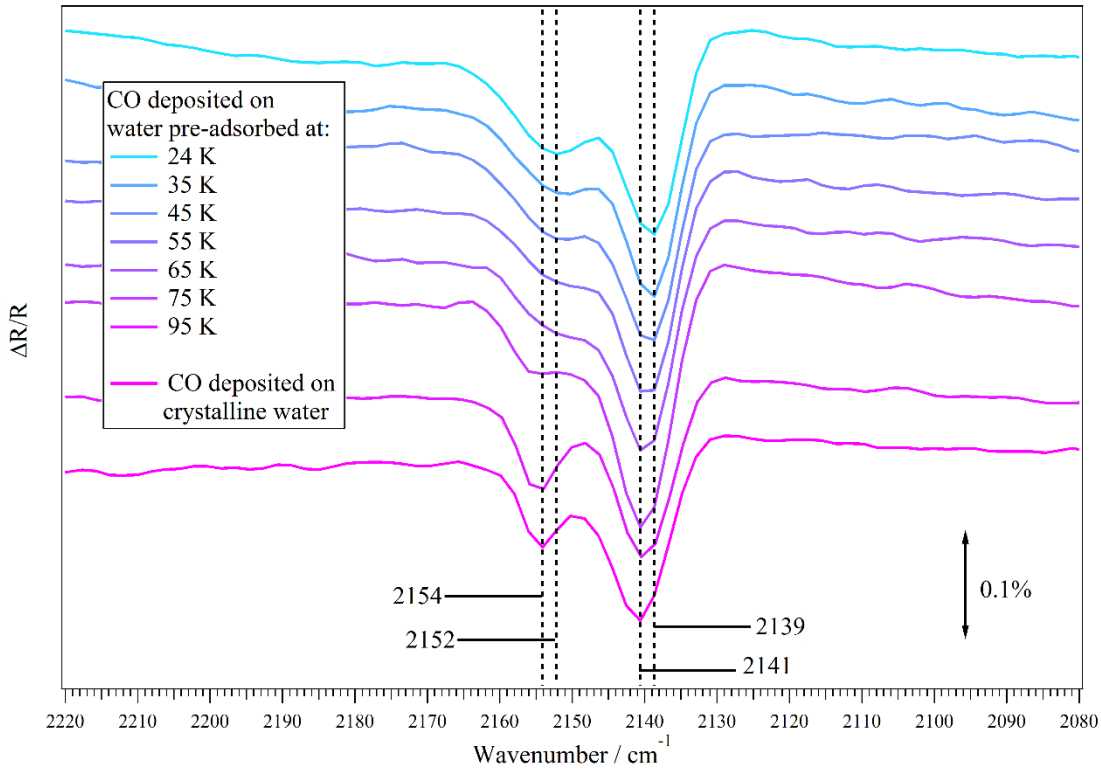

Figure 6.15 – RAIR spectra obtained after depositing 10 L_m of CO on to 100 L_m of water that had been deposited at the indicated temperature. For CI the water was deposited at 140 K.

The changing nature of the CO_{dOH} feature across the full range of water deposition temperatures is entirely as expected. Chapter 5 showed that when water is deposited at temperatures between 35 and 95 K, there are substantial changes in the porosity and structure of the water. Any changes in porosity as a result of compaction will inevitably affect the availability and nature of dangling OH bonds, which in turn will affect the CO_{dOH} feature, as shown clearly in Figure 6.15.

The particular sharpness of the CO_{dOH} feature observed when CO is deposited on CI is likely to be due to the character of the CI surface. Since CI has a crystalline structure, the surface will consist of much more ordered and regularly spaced surface groups, including some dangling OH bonds.[237]. As these dangling OH bonds will be far more regularly orientated than in pASW, any CO bound to them will also be more highly ordered and thus generate a sharper absorption band. Whilst cASW is still amorphous, it has been suggested that as a result of compaction, the ice will be more highly orientated than pASW.[237] Therefore, this could be the cause for the increased sharpness in the shoulders of the CO on ASW deposited at 95 and 75 K spectra.

Figure 6.8 showed that when increasing amounts of CO were deposited on pASW, the $CO_{dO\text{-}s4}$ feature shifted from 2139 to 2141 cm^{-1} due to the population of a more weakly bound CO state. This shift was a direct consequence of the increased amount of CO. As ASW compacts, the surface area will decrease and the relative surface concentration of CO will increase as compaction progresses. This will lead to greater occupation of the more weakly bound CO state as compaction increases, i.e. as the water deposition temperature increases there will be an increase in the 2141 cm^{-1} contribution. Furthermore, as compaction proceeds, the amount of dangling OH bonds available will decrease[214], and thus, the amount of CO bound to dangling OH bonds will also decrease. This decrease in the amount of CO bound to dangling OH bonds will have to be compensated by an increase in CO bound to the sites that are responsible for the 2139-2141 cm^{-1} component of the CO infrared band. From Figure 6.15 it can be seen that between 35 and 45 K the $CO_{dO\text{-}s4}$ feature has begun to blueshift and at 65 K there is a considerable contribution from the more weakly bound CO state (2141 cm^{-1} component). Water deposition temperatures of 75 and 95 K see further sharpening of the $CO_{dO\text{-}s4}$ feature at 2141 cm^{-1}, indicating substantial contributions from the 2141 cm^{-1} component. This indicates that, in line with the behaviour observed in the CO_{dOH} feature, compaction of ASW is occurring between 24 and 95 K.

To observe the changing nature of the $CO_{dO\text{-}s4}$ and CO_{dOH} features as the water deposition temperature varies, the absorption bands shown in Figure 6.15 were fitted with Gaussian curves (in the same manner as earlier in this chapter). The ratio of the $CO_{dO\text{-}s4}$ feature to the CO_{dOH} feature was then calculated as a function of water deposition temperature, the result is shown in Figure 6.16. The error bars shown represent the proposed error in the thermocouple reading.

At low water deposition temperatures, when the ASW is highly porous, there is little variation in the ratio of binding sites occupied by CO. As the water deposition temperature increases above ~40 K, the ratio begins to noticeably change, indicating a reduction in CO binding to dangling OH bonds. This indicates the onset of compaction and reduction in the availability of dangling OH bonds. Between 75 and 95 K the increase in the ratio, as suggested by Figure 6.15, indicates that compaction is continuing to a significant extent. These findings disagree with Collings *et al.* who state that depositing water at 80 K will produce cASW.[237]. Whilst it is clear that depositing water at 80 K will produce

a substantially compacted ASW, Figure 6.16 suggests that it will not be fully compacted. Since the method used to prepare the water ice in the present work is based on that used by Collings *et al.*,[237] it is expected that the structures of the water ices will be comparable. However, the different water ice thicknesses used may be part of the reason for the discrepancy between the present work and that of Collings *et al.*.[237] There is a further increase in the ratio between cASW deposited at 95 K and CI, which is to be expected as the surface will evolve when cASW crystallises to form CI. Whilst cASW will have a considerably reduced surface area compared to pASW, it is still amorphous, whereas CI will have a much more regularly ordered surface with a different arrangement of binding sites.

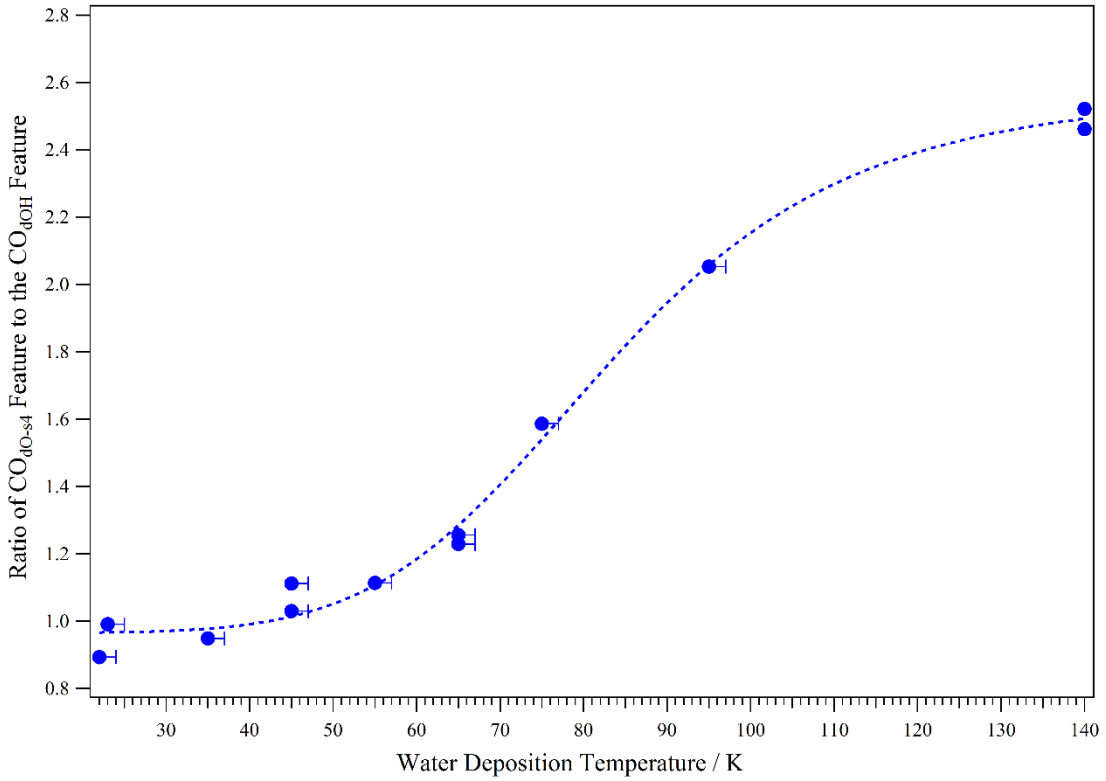

Figure 6.16 – Ratio of the CO_{dO-s4} feature to the CO_{dOH} feature plotted against the water deposition temperature. The dashed line is to guide the eye.

The ratio of the CO_{dO-s4} feature to the CO_{dOH} feature obtained when CO was deposited on CI could be artificially low due to surface ordering effects that may enhance the CO_{dOH} feature. It is proposed in the literature that CI will show significant orientation to the substrate.[237] Theoretical work has suggested that CO bound to dangling OH bonds will largely be perpendicular to the water surface.[40,102] Therefore, it follows that if CI is oriented with the substrate, CO bound to dangling OH bonds on the surface of the CI will

also be oriented with the substrate. As a consequence of the metal surface selection rule, the CO_{dOH} infrared absorption band will be enhanced because a greater component of the CO bond vibration is perpendicular to the surface. If this occurs, then it will not change the conclusions discussed above. If the CO_{dOH} enhancement was accounted for when calculating the ratio of the two features, then the ratio would be even higher than the value reported in Figure 6.16.

6.3.5 Effect of Compaction on the Desorption of CO on ASW

In the previous section, the effects of ASW compaction were discussed by considering how the CO absorption band varied when the ASW deposition temperature was increased. The reduced accessible surface area leads to a lesser proportion of the CO binding to OH dangling bonds, and an increase in CO adsorbing in a weakly bound state. So, it is expected that each of the ice systems shown in Figure 6.15 will show different spectral evolution as they are annealed.

It is evident from Figure 6.6 that by 45 K, CO has completely desorbed from HOPG, and from Figure 6.12, it is clear that after annealing to 45 K there is a marked change in the CO on ASW deposited at ~22 K system. Therefore, in order to highlight how the ice systems with different water deposition temperatures evolve with increasing temperature, Figure 6.17 displays the spectra recorded for a selection of the systems after they had been annealed to 45 K.

The traces corresponding to CO on HOPG, CI and ASW deposited at 65 K are identical and show that CO has totally desorbed following annealing to 45 K. Due to the ordered and non-porous nature of the surface, the similarity in the desorption of CO from HOPG and CI is not unexpected. For CO deposited on water adsorbed at 65 K, the absence of CO indicates that desorption preceded any process within the water that could trap CO.

Both the ASW deposited at 24 K and the ASW deposited at 45 K traces in Figure 6.15 show that CO remains on the surface after annealing to 45 K. Both traces consist of two features, one centred at ~2152 cm^{-1}, CO_{dOH}, and one at 2137 cm^{-1}. As seen in Section 6.3.3, the main peak centred at 2137 cm^{-1} is between the literature reported values for CO binding to water dO and s4 sites and CO trapped in cASW. This would therefore suggest that the CO responsible for this feature is in a partially collapsed pore, exactly as expected since compaction is underway, but not complete, by 45 K.

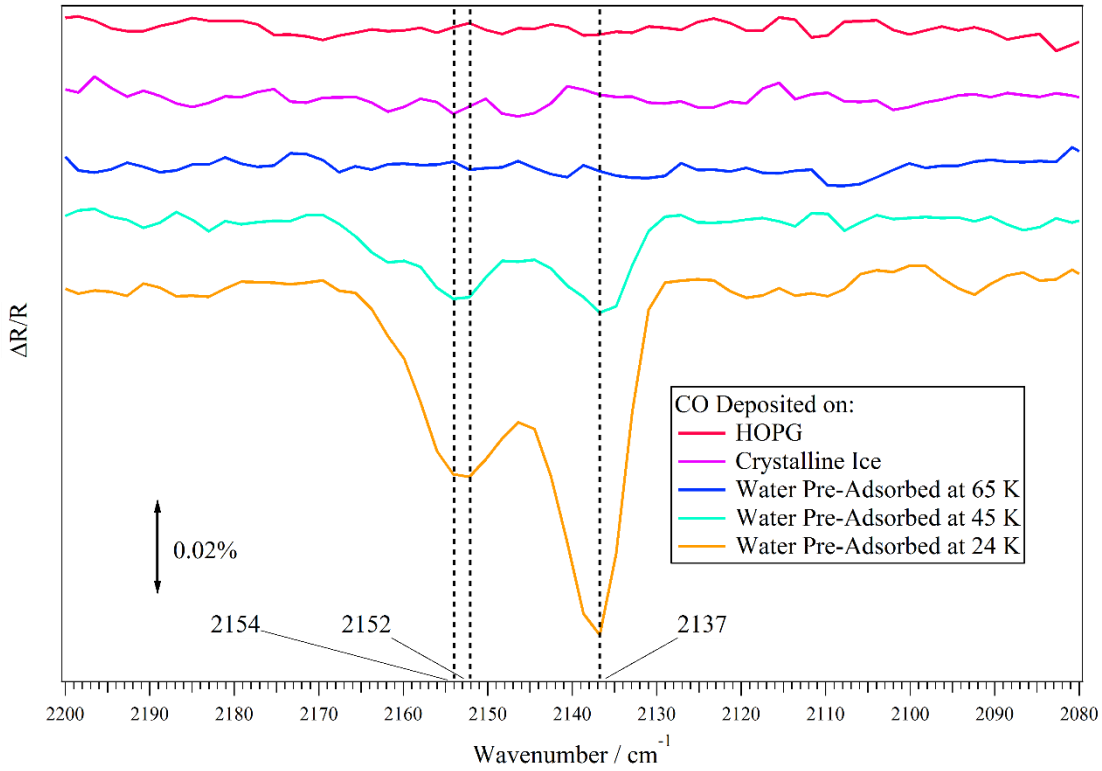

Figure 6.17 – RAIR spectra obtained after ices consisting of CO deposited on the indicated substrate were annealed to 45 K and then cooled.

Two key differences between the traces that correspond to ASW deposited at 24 K and 45 K are the profile of the overall band and the intensities of the individual features. These can be explained by considering how advanced the compaction of ASW is. There will be a larger proportion of CO in the weakly bound state when water is deposited at 45 K than when it is deposited at 24 K. As such, the system with water deposited at 45 K will lose CO more readily when annealed than the system with water deposited at 24 K. Additionally, when the water is deposited at 24 K it will undergo compaction, as it is annealed up to 45 K. Thus, some of the CO will be retained in the partially collapsed ASW. However, if ASW is deposited at 45 K, there should be no structural changes in the ASW ice after it has been annealed to 45 K. Without structural evolution of the ASW, CO will not trap and it will thus desorb more readily as it is annealed to higher temperatures. However, it is proposed that in addition to CO being trapped during ASW compaction, there may be another process responsible for retaining CO on the ice surface. This process involves CO desorbing from an internal pore but not being able to reach the ice-vacuum interface prior to the annealing cycle stopping. If this occurred, then as the ice was re-cooled, CO that had not reached the ice-vacuum interface could just reabsorb

when it collides with the water surface. To confirm whether this process occurs, an additional series of experiments and/or theoretical studies would be needed.

Figure 6.18 shows the normalised integrated area of the CO absorption band (integrated as a single unit) for each water deposition temperature as a function of CO-water ice annealing temperature. The error bars shown represent the proposed error in the thermocouple reading. Regardless of CO migration between the different water binding sites, each curve is a CO loss profile that corresponds to the relevant CO-water system.

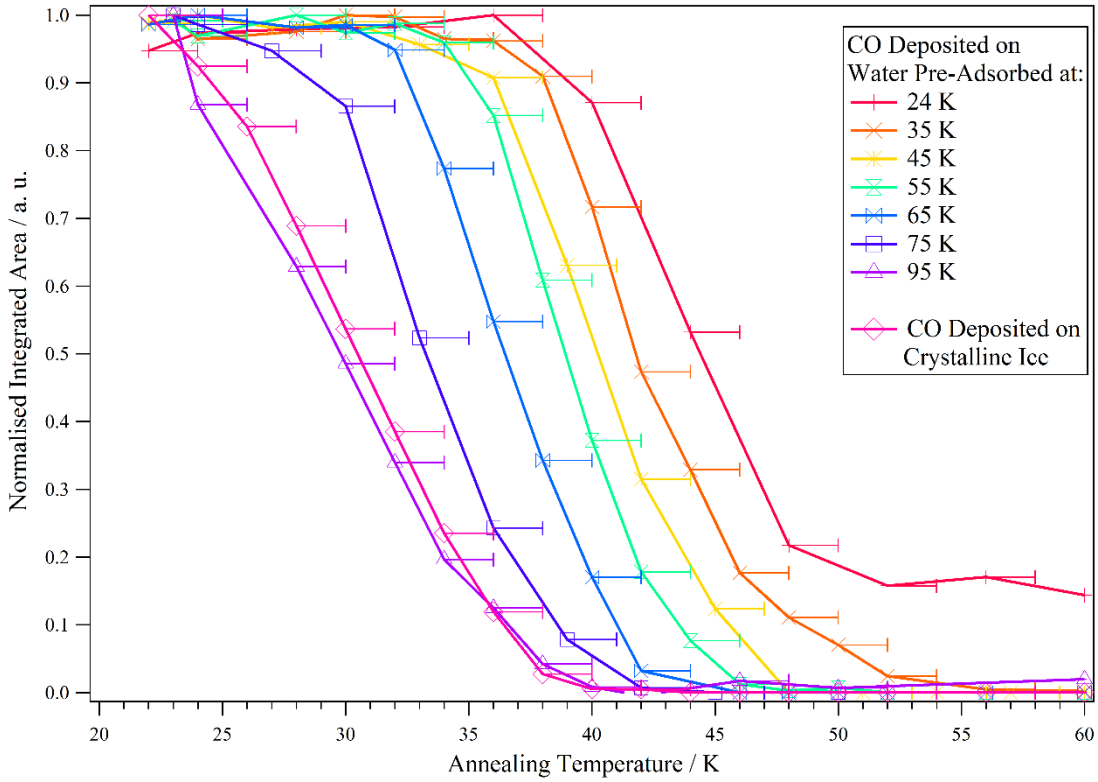

Figure 6.18 – Normalised integrated areas of the CO absorption band after 10 L_m of CO is deposited on 100 L_m of pre-adsorbed water, which had been deposited at the indicated temperature, and then annealed. The lines between each data point are to guide the eye.

The loss profile for water deposited at 24 K is in perfect agreement with the trend seen in Figure 6.14, where the areas of the individual components were plotted as a function of annealing temperature. When comparing the 24 K loss profile with the others, it is clear that it is the only system whereby CO is retained above 50-55 K. All the loss profiles have comparable gradients, with the key distinction between each profile being the point at which the integrated area begins to decline. The 95 K and CI loss profiles almost overlap, showing essentially the same evolution as the annealing temperature is increased.

It is not known why CO is observed above 55 K only when water is deposited at 24 K, and not any higher. However, two possibilities for this observation can be proposed. The first is that the process responsible for retaining CO above 55 K is complete by 35 K. The second possibility is that the CO that is trapped is particularly deep, and so if by 35 K compaction has occurred to some extent, then the deep level pores responsible for trapping are already closed off. Additional experimental and/or theoretical work is required to ascertain exactly why CO is observed above 55 K only when water has been deposited at 24 K.

From Figure 6.18 it is evident that the onset of desorption is dependent on the water deposition temperature, and thus, the compaction or porosity of the ASW. As the water deposition increases from 24 K, the ASW that forms will be increasingly compact. Therefore, the amount of CO binding on external surfaces will increase as the water deposition temperature increases, and this may encourage an earlier onset of desorption. Furthermore, Figure 6.18 shows that the level of compaction influences the desorption of CO, regardless of whether it is subsequently trapped above 50 K. This could have important ramifications for astrochemistry because CO is proposed to partake in the chemical evolution of ISM.[65,134] The clear differences between the loss profiles for water deposition temperatures of 24 to 95 K indicates, in agreement with Chapter 5, that compaction of pASW to cASW occurs over this temperature range. These findings disagree with some of the literature, where both narrower and wider temperature ranges have been reported.[40,41,111,113,238]

6.3.6 Comparison with TPD Experiments in Chapter 5

The method used in this chapter to prepare the water ices was similar to that used in Chapter 5. In the previous chapter, water was admitted to the chamber with the HOPG directed towards the high precision leak valve, whereas in this chapter, the HOPG was facing away from the valve. Much of the literature reports that directional dosing will produce cASW, even below 24 K,[130,133,224] however, these studies have typically used molecular beams. The diffusive nature of dosing in this set-up means that even when directional dosing was used, a highly porous ASW ice was grown. As such, the ices studied in this chapter and the previous one should have comparable structures, even if the thicknesses are not identical.

Chapter 5 showed that, regardless of the probe used, when water was deposited above ~40 K there was a dramatic reduction in the ability of ASW to trap the adsorbates above their natural sublimation temperatures. This was a consequence of the increasingly compact structure adopted by ASW as the water deposition temperature was increased. Compaction of ASW appeared to continue up to ~100 K and had no bearing on the crystallisation process that occurred at higher temperatures.

The ratio of the two features observed in the base temperature spectra, obtained after depositing CO onto water that had been adsorbed at different temperatures (shown in Figure 6.16), suggests that there are differences in the surfaces above ~35 K. These differences are indicative of the compaction of ASW. Figure 6.16 also showed that between deposition temperatures of 95 and 140 K, the water ice continued to evolve. The onset temperature obtained from RAIRS is in broad agreement with the TPD experiments. However, the upper temperature limit requires careful consideration. The data shown in Figure 6.16 was a non-invasive snapshot of the ice system, whereas TPD experiments are destructive. Furthermore, TPD experiments are unable to observe any changes once trapping ceases because it is the relative amount of probe trapped used to trace compaction. However, RAIRS experiments can observe changes in the surface, even once trapping has stopped. The results presented in this chapter do not indicate that ASW compaction continues up to crystallisation; rather, that the cASW surface is noticeably different to the surface of CI, as would be expected. The loss profiles shown in Figure 6.18 show that desorption of CO from ASW deposited at 95 K is essentially the same as from CI. This suggests that whilst the snapshots taken at base temperature show continued evolution in the absorption band between 95 and 140 K (CI), the compaction and loss of porosity is largely complete by 95 K, in line with the TPD findings in Chapter 5.

6.4 Summary

Compaction of ASW has been monitored using RAIRS experiments that examined evolution of the CO absorption band as the water deposition temperature was varied. It was shown that when CO is deposited on compacted ASW, a lesser proportion of it binds to dangling OH bonds than when it is deposited on highly porous ASW. This is due to the process of compaction reducing the accessible surface area of ASW and, in turn, reducing the number of available dangling OH bonds.

In Chapter 5, using TPD and two different probe molecules, it was shown that pASW is formed below ~40 K and cASW above ~100 K. Between these temperatures, ASW will be partially porous. The work in this chapter used a different probe and experimental technique to those used in Chapter 5. However, it was observed that compaction occurred over a comparable temperature range. The temperatures discussed in this chapter must be taken with care due to the likelihood that the thermocouple was recording a slightly lower temperature than the surface actually was. It is not possible to explicitly state the level of error, but from the observations presented here it is unlikely to be more than ~2 K. The thermocouple error may have been caused by the position of the thermocouple behind the sample shifting during the continued heating and cooling of the sample.

In addition to confirming the conclusions of the previous chapter, this work has also shown that the onset of CO desorption from pASW and semi-porous ASW is dependent on the water deposition temperature and, thus, the porosity of water. As the water is deposited at higher temperatures, the onset of CO desorption moves to lower and lower temperatures until it occurs at the same temperature as CO on CI and CO on HOPG. The compaction range reported above is further reinforced by the onset of CO desorption varying between water deposition temperatures of 24 and 95 K.

Chapters 5 and 6 indicate that compaction of ASW occurs up to ~100 K; this is higher than some values reported in the literature.[40,129,133] Since comparable temperature ranges for ASW compaction were reported when using different probe molecules and different experimental techniques, these two factors can be discounted from the possible causes of the discrepancies seen in the literature. One possibility is that although ices may be similarly porous, they may be structurally different due to different growth methods. However, from the work here it is not clear what causes the differences between this work and the literature, and further work is needed to explain them. Nevertheless, it has been shown that the degree of compaction of ASW has a strong impact on the nature of the CO-water interaction and the onset of desorption of CO from ASW. This could have an impact on the chemical evolution of the ISM because CO is proposed to be involved in the formation of more complex species and so the nature of its interaction with water, the most abundant solid phase species in the ISM, is profoundly important.[213]

7 Concluding Remarks

This thesis has aimed to answer the following question:

> *How do ices that contain formic acid and/or water evolve with increasing temperatures?*

Both molecules of interest are important in the interstellar medium (ISM). Formic acid is significant because it is found in numerous interstellar environments and is believed to partake in the chemical evolution of the ISM. Water is considered important because it is the most abundant species in the solid phase on interstellar dust grains.[28,74] Furthermore, water can trap volatile molecules above their natural sublimation points and is thus influential in the chemical composition of the ISM. It is believed that the compaction of amorphous solid water (ASW) is involved in this process.[38,41]

To answer the question above, two key techniques were employed: reflection absorption infrared spectroscopy (RAIRS) and temperature programmed desorption (TPD). In answering the question above, three key conclusions were found.

7.1 Key Conclusion 1 – Formic Acid Desorption from Astronomically Relevant Surfaces

The first key conclusion regards the desorption of formic acid. A basic understanding of formic acid desorption from, and its thermal evolution on, highly oriented pyrolytic graphite (HOPG) was examined in Chapter 3. With the findings of Chapter 3, Chapter 4 examined formic acid desorption from more astronomically relevant water-dominated ices. From these two chapters it was concluded that the desorption of formic acid from water-dominated ices is heavily dependent on the structural evolution and desorption of water.

Since water is the most abundant species in interstellar ices, the interaction between formic acid and water is crucial to fully understanding how formic acid desorbs from icy mantles that surround interstellar dust grains. The desorption of formic acid on water ices was shown to be complex, a consequence of the strong hydrogen bonds that can form between formic acid and water. It was observed that formic acid desorbed during the ASW to crystalline ice (CI) phase change (volcano desorption), and during the desorption of CI (co-desorption) for all formic acid coverages studied.[38] This indicates that formic

acid traps within ASW. For the highest formic acid coverages studied, the water saturated and some of the formic acid remained on, and then desorbed from, the surface of the water. RAIRS supported the assignments of the TPD spectra and further highlighted the complexity of the formic acid-water interaction.

Formic acid is observed to constitute 1-5%, with respect to water, of icy mantles.[75] Therefore, the findings of Chapter 4 suggest that formic acid will desorb from water-dominated interstellar ices via volcano and co-desorption. As such, the release of formic acid in the ISM will be dependent on the thermal evolution of water.

The desorption and evolution of formic acid being linked to thermal evolution of water has important ramifications when protoplanetary snow lines are considered. A snow line is the radius at which the temperature of a protoplanetary disk becomes cold enough to allow molecules to freeze out onto dust grains. The bulk composition of a planet formed in a protoplanetary disk is proposed to be dependent on where it forms in relation to different molecules' snow lines.[248–250] Therefore, the presence of formic acid adsorbed within ASW, and thus beyond the water snow line, means formic acid will be involved in determining the composition of planets formed beyond the water snow line.

7.1.1 Formic Acid Desorption Under Astronomical Conditions

Both desorption processes (volcano and co-desorption) were shown to be highly dependent on the formic acid coverage. Therefore, modelling formic acid desorption from water-dominated ices under astronomical conditions would be highly complex and require a better understanding of the water phase change dependence on the quantity of formic acid present. However, it is possible, using the kinetic parameters calculated in Chapter 3, to model formic acid desorption from HOPG under astronomical conditions. This will also yield an astronomically relevant desorption temperature for formic acid from a model carbonaceous dust grain surface.

Desorption temperatures under astronomical conditions are considerably different to those observed in the laboratory because desorption temperatures are dependent on the ice thickness and, crucially, the heating rate.[44] The heating rate of an icy mantle in a dust cloud surrounding a young star, which is typically regarded as being ~1 K millennium^{-1} to ~1 K century^{-1}.[40,44,153] Using heating rates this low would not be practical in the laboratory, hence the need to model the desorption. To show how the desorption

temperature is affected by the heating rate, TPD spectra for monolayer formic acid on HOPG were simulated using a range of heating rates. The simulations were performed using the stochastic integration package used in Chapter 3 (CKS). The resulting TPD spectra, for heating rates of 0.5 K s^{-1} to 1 K $millennium^{-1}$, are shown in Figure 7.1. The kinetic parameters used were calculated in Chapter 3 and are as follows: an order of desorption (n) of 1.35, an energy of desorption (E_{des}) of 49.5 kJ mol^{-1} and a pre-exponential factor (ν_n) of 7.6×10^{10} (molecules m^{-2})$^{-0.35}$ s^{-1}. The coverage used had been calculated in Chapter 3 and relates to a formic acid exposure of 10 L_m, equating to a surface concentration of 2.24×10^{19} molecules m^{-2}. The pumping rate for the 0.5 K s^{-1} spectrum was 0.25 s^{-1} and was scaled in line with heating rates.

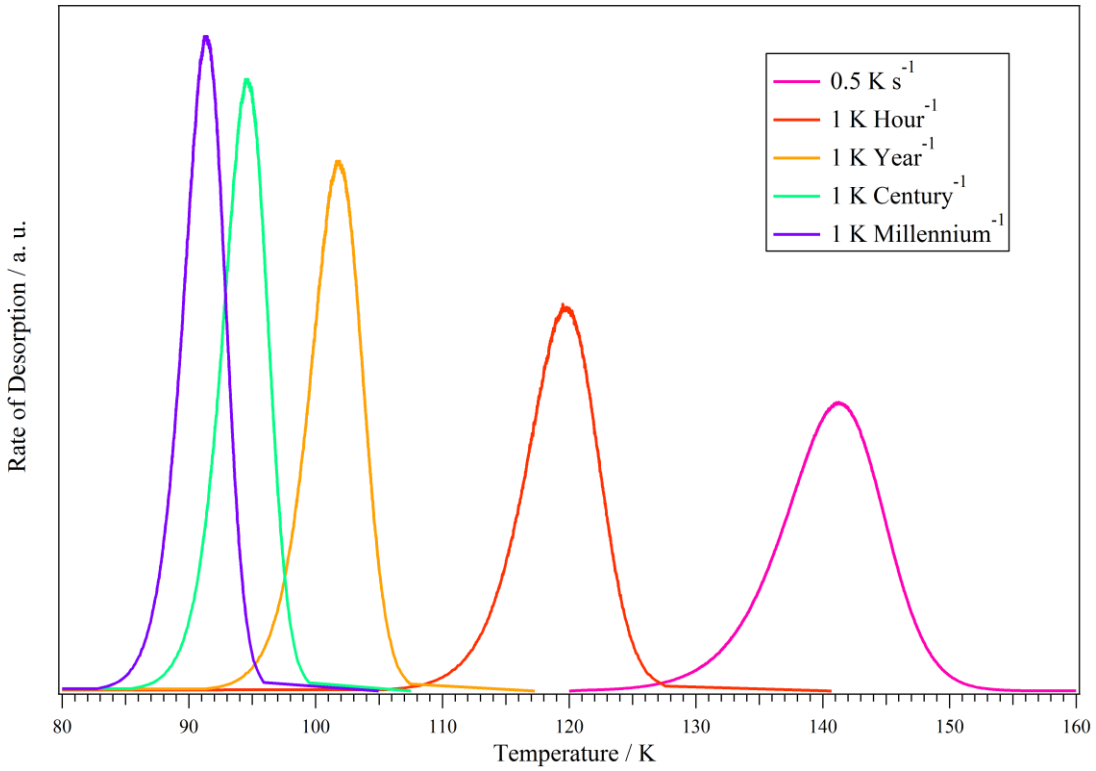

Figure 7.1 – Simulated TPD spectra for the desorption of monolayer formic acid from HOPG, using a range of heating rates.

It is clear from Figure 7.1 that the formic acid monolayer desorption temperature is highly dependent on the heating rate. Reducing the heating rate from 0.5 K s^{-1} to 1 K $millennium^{-1}$ results in the desorption temperature dropping by ~50 K. Therefore, if formic acid was adsorbed directly on a carbonaceous grain surface in the ISM, it would be expected to desorb between 91 and 94 K, depending on the precise heating rate. Chapter 4 also showed that if the water layer were saturated, formic acid would begin to

desorb at temperatures comparable to those when it was adsorbed directly on HOPG. Consequently, if formic acid formed or adsorbed on the surface of a saturated water ice in the ISM, the results in Chapter 4 would suggest that it would also desorb between ~91 and ~94 K.

7.2 Key Conclusion 2 – Thermal Evolution of Water and the Trapping of Volatile Species

The second key conclusion found in answering the main question relates to the thermally induced compaction of ASW between ~20 and 110 K. Chapters 5 and 6 examined this process using probe molecules – the former using TPD and the latter using RAIRS. This process is believed to be involved in trapping and retaining molecules above their natural sublimation points, which can then be released during volcano and co-desorption.[38,41] The main finding to come from these two chapters was that there exists a mechanism in water ices to trap volatile species up to between 100 and 110 K.

A mechanism to trap volatiles in water ices up to 110 K could mean that if any molecules in the gas phase adsorb onto an ASW in the ISM below this temperature then they may trap within the water ice – this also applies to molecules formed on the water ice surface. These molecules could then remain trapped until either the ASW to CI phase change, or CI desorbs. This means that these species will be available within the solid phase to help drive forward the formation of more complex species, as discussed in Chapter 1. Since the chemical composition of planets formed in protoplanetary disks is influenced by the abundances of species in the solid and gas phases, the compaction of ASW has an impact on the chemical make-up planets formed in protoplanetary disks.

Further to the main points made above, Chapter 5 – which built on the work of Collings *et al.*[40] – showed that the discrepancies in the literature regarding ASW compaction could not be attributed to probe effects. The results of experiments using two different probes (CO_2 and CS_2) yielded comparable temperature ranges for the compaction of pASW to cASW. The subtle differences at high temperatures are proposed to be due to the size of the probes and each probe's sensitivity to changes in the porosity. Chapter 6, which used CO and RAIRS, concurred with those of Chapter 5. The results obtained in this work differed considerably from those reported by Collings *et al.*,[40] even though the water was prepared in a comparable manner.[40] This indicates that even where methods are similar,

the comparison between studies involving ASW deposited below 110 K must be done very carefully. This is particularly pertinent where the studies involve the trapping of a second molecular species within ASW.

Chapter 6 produced an additional conclusion, linked to the second key conclusion discussed above. It was found that as compaction progresses, the retention of CO by ASW decreases. These results indicate that if CO adsorbs onto ASW that has undergone a small degree of compaction, it will not be retained in the water ice above ~55 K. It has been reported in the literature that in addition to elevated temperatures, compaction of ASW in the ISM can be caused by cosmic rays and UV irradiation.[220,222,223] Therefore, if CO adsorbs on an ASW ice that has undergone some degree of compaction, then it is quite possible that CO will totally desorb below ~55 K. This will mean that CO will not be retained in the water ice and thus will not be available for reaction within the solid phase. This would thus impact the gas phase concentration of CO. Since the CO surface reaction network is understood to be the origin of many of the complex organic molecules in the ISM, the abundance of CO on the surface of dust grains in the ISM will have important ramifications on the chemical make-up of the ISM.[236,251]

A specific example of the impact of a reduction in CO retention by ASW on the chemical make-up of the ISM relates to the formation of comets. Comets are known to have a high abundance of CO.[252–254] However, due to conditions in in the comet-forming region of protoplanetary disks, CO must be trapped in water ices for it to be available during comet formation.[252] The results presented here indicate that if ASW has undergone a small amount of compaction, CO retention above its natural sublimation point will be reduced when compared with an ASW ice that has not undergone any compaction. Therefore, the amount of CO available for comet formation will need to be readdressed as it is possible that it is less than previously predicted.[252]

Linking the first two results chapters of this thesis with the latter two, preliminary experiments were conducted on the effect of formic acid on the compaction of ASW. Initial results indicate that in the presence of formic acid, the onset and completion of the compaction process occurred at noticeably higher temperatures than when formic acid was absent. It is proposed that these results are due to the strong hydrogen bonding between formic acid and water, with formic acid acting as a scaffold against ASW compaction. As such, it is also proposed that the compaction of ASW will be affected by

the presence of other hydrogen bonding species. These findings thus indicate that the presence of hydrogen bonding species in water ices will affect the mechanism by which volatile species are trapped and will in turn affect, among other things, comet formation and the chemical make-up of new planets.

It is clear from the comparison of the present work and the literature that much more work needs to be done to fully understand the ASW compaction process, both when hydrogen bonding species are and are not present. Without a full and comprehensive understanding of the compaction process, the trapping mechanism that accompanies ASW compaction cannot be properly incorporated into chemical models of interstellar dust clouds.

7.3 Key Conclusion 3 – Influence of Formic Acid on the Crystallisation of ASW

The third key conclusion regards the impact of formic acid on the ASW to CI phase change. It was seen for all formic acid coverages, the water phase change occurred at a lower temperature than when formic acid was absent. Furthermore, the temperature at which the water phase change occurred was dependent on the formic acid coverage.

Comparison of these results with those for methanol[188] suggested that it was the hydrogen bonding capability of formic acid that was responsible for effect on the ASW to CI phase change. Consequently, if formic acid were present in or on water-dominated ices in the ISM, the release of molecules trapped in the water ice would occur at lower temperatures than if formic acid were absent. However, the extent of the temperature difference would be dependent on the amount of formic acid present. In addition to this, the combined effect on the water phase change of formic acid and a second hydrogen bonding species is not yet known – complicating the matter even further.

Once the experiments detailed in the following section are completed, this key conclusion – regarding the effect of formic acid on the crystallisation of water – suggests that astrochemistry models need to be modified to account for the modified ASW to CI phase change.[188] Once the effect of multiple hydrogen bonding species is understood, these models will be able to better reflect the complicated nature of ISM ice desorption. As the discussions above have highlighted, the composition of ISM ices has significant ramifications on the formation of planets and comets and so the proper modelling of the ASW to CI phase change is crucial to understanding these processes.

7.4 Future Work

Further work is needed in order to properly understand the effect that formic acid has on the ASW to CI phase change. This work should involve investigations into the formic acid coverage dependence and whether the location of formic acid within, or on, the water affects the level of change. Additional theoretical studies focussing on the molecular interaction between the two species may help in understanding the larger scale effect of formic acid on water. This work could then be compared with other species that exhibit a similar effect on water crystallisation, such as methanol, and those that have structural similarities. With an understanding of the change to water crystallisation in the presence of a single hydrogen bonding species, more astronomically relevant systems that contain multiple hydrogen bonding species can be considered.

Future work regarding the compaction process in ASW could take several directions, but one that is clear from this work is trying to understand the different results obtained by Collings *et al.*[40] and those reported here. This could involve a comprehensive survey of the effect of varying experimental variables typically present in UHV systems. Examples of these variables include: proximity of the dose tube to the surface; the ratio between time and pressure for a given dose/exposure; the heating rate during TPD experiments; and thickness of the water layer. By knowing how each of the variables affects the amount of probe trapped, the causes of the disagreement within the literature could be clarified.

To properly understand the differences in the CO_2 and CS_2 trapping curves, another structurally related molecule could be used to repeat the experiments in Chapter 5. This would mean that the causes of differences between the trapping curves could be confirmed. For example, confirming that the differences in the initial trapping amounts is due to the space occupied by the probe molecules. Another possibility is the use of an isotopically labelled CO_2 probe in order to avoid mass overlap when formic acid is present. However, if these experiments proceeded then any damage to the high-precision leak valves would need to be avoided. A comprehensive investigation into the effect of other hydrogen bonding species on the compaction process would also be interesting. This would involve repeating the experiments in the latter part of Chapter 5, where a three-layered system of (from top to bottom) a probe, a hydrogen bonding molecule and ASW were studied. These studies could include a comparison between molecules that

have a single hydrogen bonding site (for example, methanol) and those that have multiple hydrogen bonding sites (for example, carboxylic acids).

It was not possible to use CO as a probe in the experiments described in Chapter 5 due to undesired sources of desorption during TPD, for example, from the cold finger. Therefore, modifying the set up or developing a method that prevents these sources interfering with TPD experiments would allow direct comparison with the work by Collings *et al.*.[40] One such modification could be a shield around the mass spectrometer that would limit the detection area to the line of sight. If this were possible, then the experiments proposed above could be conducted with CO and the results would then be directly comparable to Collings *et al.*, hopefully allowing the cause of the differences between the present work and that by Collings *et al.* to be revealed.

8 References

1 J. Mullaney, *The Herschel Objects and How to Observe Them*, Springer Science & Business Media, Berlin, 2007.

2 D. A. Williams and E. Herbst, *Surf. Sci.*, 2002, **500**, 823–837.

3 J. M. Greenberg and C. Shen, *Astrophys. Space Sci.*, 1999, **269**–**270**, 33–55.

4 J. F. Alves, C. J. Lada and E. A. Lada, *Nature*, 2001, **409**, 159–161.

5 H. Cottin, M. C. Gazeau and F. Raulin, *Planet. Space Sci.*, 1999, **47**, 1141–1162.

6 E. Herbst, *J. Phys. Chem. A*, 2005, **109**, 4017–4029.

7 K. M. Ferrière, *Rev. Mod. Phys.*, 2001, **73**, 1031–1066.

8 M. E. van Steenberg and J. M. Shull, *Astrophys. J.*, 1988, **330**, 942–963.

9 B. D. Savage and K. R. Sembach, *Annu. Rev. Astron. Astrophys.*, 1996, **34**, 279–329.

10 J. C. Howk and B. D. Savage, *Astrophys. J.*, 1999, **517**, 746–766.

11 A. G. G. M. Tielens, *The Physics and Chemistry of the Interstellar Medium*, Cambridge University Press, Cambridge, 2005.

12 C. F. McKee and J. P. Ostriker, *Astrophys. J.*, 1977, **218**, 148–169.

13 G. B. Field, D. W. Goldsmith and H. J. Habing, *Astrophys. J.*, 1969, **155**, L149–L154.

14 R. McCray and T. P. Snow, *Annu. Rev. Astron. Astrophys.*, 1979, **17**, 213–240.

15 E. F. van Dishoeck, E. Herbst and D. A. Neufeld, *Chem. Rev.*, 2013, **113**, 9043–9085.

16 F. Le Petit, E. Roueff and E. Herbst, *Astron. Astrophys.*, 2004, **417**, 993–1002.

17 D. Prialnik, *An Introduction to the Theory of Stellar Structure and Evolution*, Cambridge University Press, Cambridge, 2000.

18 J. P. Williams, L. Blitz and A. A. Stark, *Astrophys. J.*, 1995, **451**, 252–274.

19 A. Jones, *EAS Publ. Ser.*, 2009, **34**, 107–118.

20 B. T. Draine, *Annu. Rev. Astron. Astrophys.*, 2003, **41**, 241–289.

21 A. Li and B. T. Draine, *Astrophys. J.*, 2002, **564**, 803–812.

22 D. A. Williams, *Astron. Geophys.*, 2000, **41**, 3.8-3.16.

23 E. L. Fitzpatrick, *Publ. Astron. Soc. Pacific*, 1999, **111**, 63–75.

24 E. L. Gibb, D. C. B. Whittet, W. A. Schutte, A. C. A. Boogert, J. E. Chiar, P. Ehrenfreund, P. A. Gerakines, J. V. Keane, A. G. G. M. Tielens, E. F. van Dishoeck and O. Kerkhof, *Astrophys. J.*, 2000, **536**, 347–356.

25 T. P. Snow and A. N. Witt, *Astrophys. J.*, 1996, **468**, L65–L68.

26 J. Spitzer, Lyman and E. L. Fitzpatrick, *Astrophys. J.*, 1993, **409**, 299–318.

27 U. J. Sofia and D. M. Meyer, *Astrophys. J.*, 2001, **554**, L221–L224.

28 L. J. Allamandola, M. P. Bernstein, S. A. Sandford and R. L. Walker, *Space Sci.*

Rev., 1999, **90**, 219–232.

29 D. A. Adriaens, T. P. M. Goumans, C. R. A. Catlow and W. A. Brown, *J. Phys. Chem. C*, 2010, **114**, 1892–1900.

30 D. Ward-Thompson and A. P. Whitworth, *An Introduction to Star Formation*, Cambridge University Press, Cambridge, 2011.

31 G. Vidali, *Chem. Rev.*, 2013, **113**, 8762–8782.

32 R. J. Gould and E. E. Salpeter, *Astrophys. J.*, 1963, **138**, 393–407.

33 D. Hollenbach, *J. Chem. Phys.*, 1970, **53**, 79–86.

34 S. S. Prasad and S. P. Tarafdar, *Astrophys. J.*, 1983, **267**, 603–609.

35 J. M. Greenberg, *Astrophys. Space Sci.*, 1976, **39**, 9–18.

36 M. P. Bernstein, S. A. Sandford, L. J. Allamandola, S. Chang and M. A. Scharberg, *Astrophys. J.*, 1995, **454**, 327–344.

37 M. H. Moore, B. Donn, R. Khanna and M. F. A'Hearn, *Icarus*, 1983, **54**, 388–405.

38 M. P. Collings, M. A. Anderson, R. Chen, J. W. Dever, S. Viti, D. A. Williams and M. R. S. McCoustra, *Mon. Not. R. Astron. Soc.*, 2004, **354**, 1133–1140.

39 S. Viti and D. A. Williams, *Mon. Not. R. Astron. Soc.*, 1999, **305**, 755–762.

40 M. P. Collings, J. W. Dever, H. J. Fraser and M. R. S. McCoustra, *Astrophys. Space Sci.*, 2003, **285**, 633–659.

41 M. P. Collings, J. W. Dever, H. J. Fraser, M. R. S. McCoustra and D. A. Williams, *Astrophys. J.*, 2003, **583**, 1058–1062.

42 R. S. Smith, C. Huang, E. K. L. Wong and B. D. Kay, *Phys. Rev. Lett.*, 1997, **79**, 909–912.

43 P. Ayotte, R. S. Smith, K. P. Stevenson, Z. Dohnálek, G. A. Kimmel and B. D. Kay, *J. Geophys. Res.*, 2001, **106**, 33387–33392.

44 D. J. Burke and W. A. Brown, *Phys. Chem. Chem. Phys.*, 2010, **12**, 5947–5969.

45 S. Liu, D. M. Mehringer and L. E. Snyder, *Astrophys. J.*, 2001, **552**, 654–663.

46 C. J. Bennett and R. I. Kaiser, *Astrophys. J.*, 2007, **661**, 899–909.

47 R. T. Garrod, S. L. W. Weaver and E. Herbst, *Astrophys. J.*, 2008, **682**, 283–302.

48 Y. Miao, D. M. Mehringer, Y.-J. Kuan and L. E. Snyder, *Astrophys. J.*, 1995, **445**, L59–L62.

49 D. M. Mehringer and L. E. Snyder, *Astrophys. J.*, 1996, **471**, 897–902.

50 P. F. Goldsmith, D. C. Lis, R. Hills and J. Lasenby, *Astrophys. J.*, 1990, **350**, 186–194.

51 D. C. Lis and P. F. Goldsmith, *Astrophys. J.*, 1989, **337**, 704–711.

52 N. Z. Scoville, P. M. Solomon and A. A. Penzias, *Astrophys. J.*, 1975, **201**, 352–365.

53 J. M. Hollis, S. N. Vogel, L. E. Snyder, P. R. Jewell and F. J. Lovas, *Astrophys. J.*, 2001, **554**, L81–L85.

54 L. E. Snyder, *Proc. Natl. Acad. Sci. U. S. A.*, 2006, **103**, 12243–12248.

55 E. C. Sutton, P. A. Jaminet, W. C. Danchi and G. A. Blake, *Astrophys. J. Suppl. Ser.*, 1991, **77**, 255–285.

56 B. Zuckerman, J. A. Ball and C. A. Gottlieb, *Astrophys. J.*, 1971, **163**, L41–L45.

57 G. Winnewisser and E. Churchwell, *Astrophys. J.*, 1975, **200**, L33–L36.

58 R. D. Brown, J. G. Crofts, P. D. Godfrey, F. F. Gardner, B. J. Robinson and J. B. Whiteoak, *Astrophys. J.*, 1975, **197**, L29–L31.

59 L. E. Snyder, F. J. Lovas, D. M. Mehringer, N. Y. Miao, Y. Kuan, J. M. Hollis and P. R. Jewell, *Astrophys. J.*, 2002, **578**, 245–255.

60 J. M. Hollis, F. J. Lovas, P. R. Jewell and L. H. Coudert, *Astrophys. J.*, 2002, **571**, L59–L62.

61 D. M. Mehringer, L. E. Snyder, Y. Miao and F. J. Lovas, *Astrophys. J.*, 1997, **480**, L71–L74.

62 J. M. Hollis, F. J. Lovas and P. R. Jewell, *Astrophys. J.*, 2000, **540**, L107–L110.

63 J. M. Hollis, P. R. Jewell, F. J. Lovas and A. Remijan, *Astrophys. J.*, 2004, **613**, L45–L48.

64 D. T. Halfen, A. J. Apponi, N. Woolf, R. Polt and L. M. Ziurys, *Astrophys. J.*, 2006, **639**, 237–245.

65 C. J. Bennett, T. Hama, Y. S. Kim, M. Kawasaki and R. I. Kaiser, *Astrophys. J.*, 2011, **727**, 27–41.

66 P. Redondo, A. Largo and C. Barrientos, *Astron. Astrophys.*, 2015, **579**, A125.

67 S. E. Bisschop, J. K. Jørgensen, E. F. van Dishoeck and E. B. M. de Wachter, *Astron. Astrophys.*, 2007, **465**, 913–929.

68 S. Liu, J. M. Girart, A. Remijan and L. E. Snyder, *Astrophys. J.*, 2002, **576**, 255–263.

69 S. Bottinelli, C. Ceccarelli, J. P. Williams and B. Lefloch, *Astron. Astrophys.*, 2007, **463**, 601–610.

70 M. A. Requena-Torres, J. Martín-Pintado, A. Rodríguez-Franco, S. Martín, N. J. Rodríguez-Fernández and P. de Vicente, *Astron. Astrophys.*, 2006, **455**, 971–985.

71 W. Irvine, P. Friberg, N. Kaifu, H. Matthews, Y. Minh, M. Ohishi, Ish and S. Ikawa, *Astron. Astrophys.*, 1990, **229**, L9–L12.

72 B. E. Turner, R. Terzieva and E. Herbst, *Astrophys. J.*, 1999, **518**, 699–732.

73 W. A. Schutte, A. C. A. Boogert, A. G. G. M. Tielens, D. C. B. Whittet, P. A. Gerakines, J. E. Chiar, P. Ehrenfreund, J. M. Greenberg, E. F. van Dishoeck and T. de Graauw, *Astron. Astrophys.*, 1999, **343**, 966–976.

74 E. L. Gibb, D. C. B. Whittet, A. C. A. Boogert and A. G. G. M. Tielens, *Astrophys. J. Suppl. Ser.*, 2004, **151**, 35–73.

75 S. E. Bisschop, G. W. Fuchs, A. C. A. Boogert, E. F. van Dishoeck and H. Linnartz, *Astron. Astrophys.*, 2007, **470**, 749–759.

76 Z. Peeters, S. D. Rodgers, S. B. Charnley, L. Schriver-Mazzuoli, A. Schriver, J. V. Keane and P. Ehrenfreund, *Astron. Astrophys.*, 2006, **445**, 197–204.

77 A. I. Vasyunin and E. Herbst, *Astrophys. J.*, 2013, **769**, 34–42.

78 C. J. Bennett and R. I. Kaiser, *Astrophys. J.*, 2007, **660**, 1289–1295.

79 C. J. Bennett, S. Chen, B. Sun, A. H. H. Chang and R. I. Kaiser, *Astrophys. J.*, 2007, **660**, 1588–1608.

80 A. F. Jalbout, *Orig. Life Evol. Biosph.*, 2008, **38**, 489–497.

81 C. Walsh, T. J. Millar, H. Nomura, E. Herbst, S. W. Weaver, Y. Aikawa, J. C. Laas and A. I. Vasyunin, *Astron. Astrophys.*, 2014, **563**, A33.

82 R. T. Garrod and E. Herbst, *Astron. Astrophys.*, 2006, **457**, 927–936.

83 E. C. Sutton, R. Peng, W. C. Danchi, P. A. Jaminet, G. Sandell and A. P. G. Russell, *Astrophys. J. Suppl. Ser.*, 1995, **97**, 455–496.

84 S. Cazaux, A. G. G. M. Tielens, C. Ceccarelli, A. Castets, V. Wakelam, E. Caux, B. Parise and D. Teyssier, *Astrophys. J.*, 2003, **593**, L51–L55.

85 S. Bottinelli, C. Ceccarelli, B. Lefloch, J. P. Williams, A. Castets, E. Caux, S. Cazaux, S. Maret, B. Parise and A. G. G. M. Tielens, *Astrophys. J.*, 2004, **615**, 354–358.

86 F. L. Schöier, J. K. Jörgensen, E. F. van Dishoeck and G. A. Blake, *Astron. Astrophys.*, 2002, **390**, 1001–1021.

87 S. Maret, C. Ceccarelli, E. Caux, A. G. G. M. Tielens, J. K. Jörgensen, E. F. van Dishoeck, A. Bacmann, A. Castets, B. Lefloch, L. Loinard, B. Parise and F. L. Schöier, *Astron. Astrophys.*, 2004, **416**, 577–594.

88 J. A. Noble, C. Martin, H. J. Fraser, P. Roubin and S. Coussan, *J. Phys. Chem. Lett.*, 2014, **5**, 826–829.

89 S. Hellebust, B. O'Riordan and J. Sodeau, *J. Chem. Phys.*, 2007, **126**, 84702.

90 P. Jenniskens and D. F. Blake, *Astrophys. J.*, 1996, **473**, 1104–1113.

91 A. C. Cheung, D. M. Rank, C. H. Townes, D. D. Thornton and W. J. Welch, *Nature*, 1969, **221**, 626–628.

92 V. G. Anicich, *An Index of the Literature for Bimolecular Gas Phase Cation-Molecule Reaction Kinetics*, Jet Propulsion Laboratory, National Aeronautics and Space Administration, Pasadena, 2003.

93 G. B. Field and G. Steigman, *Astrophys. J.*, 1971, **166**, 59–64.

94 P. B. Rimmer, E. Herbst, O. Morata and E. Roueff, *Astron. Astrophys.*, 2011, **537**, A7.

95 E. F. van Dishoeck, *Faraday Discuss.*, 2014, **168**, 9–47.

96 A. G. G. M. Tielens and W. Hagen, *Astron. Astrophys.*, 1982, **114**, 245–260.

97 Y. Oba, N. Watanabe, T. Hama, K. Kuwahata, H. Hidaka and A. Kouchi, *Astrophys. J.*, 2012, **749**, 67–79.

98 F. Dulieu, L. Amiaud, E. Congiu, J.-H. Fillion, E. Matar, A. Momeni, V. Pirronello and J. L. Lemaire, *Astron. Astrophys.*, 2010, **512**, A30.

99 H. M. Cuppen and E. Herbst, *Astrophys. J.*, 2007, **668**, 294–309.

100 F. Du, B. Parise and P. Bergman, *Astron. Astrophys.*, 2012, **538**, A91.

101 S. Ioppolo, H. M. Cuppen, C. Romanzin, E. F. van Dishoeck and H. Linnartz,

Astrophys. J., 2008, **686**, 1474–1479.

102 A. Al-Halabi, H. J. Fraser, G. J. Kroes and E. F. van Dishoeck, *Astron. Astrophys.*, 2004, **422**, 777–791.

103 W. Hagen, A. G. G. M. Tielens and J. M. Greenberg, *Chem. Phys.*, 1981, **56**, 367–379.

104 H. J. Fraser, M. P. Collings, M. R. S. McCoustra and D. A. Williams, *Mon. Not. R. Astron. Soc.*, 2001, **327**, 1165–1172.

105 D. K. Aitken, P. F. Roche, C. H. Smith, S. D. James and J. H. Hough, *Mon. Not. R. Astron. Soc.*, 1988, **230**, 629–638.

106 A. A. Schegerer and S. Wolf, *Astron. Astrophys.*, 2010, **517**, A87.

107 L. Hornekaer, A. Baurichter, V. V Petrunin, A. C. Luntz, B. D. Kay and A. Al-Halabi, *J. Chem. Phys.*, 2005, **122**, 124701.

108 R. A. May, R. S. Smith and B. D. Kay, *J. Phys. Chem. Lett.*, 2012, **3**, 327–331.

109 M. E. Palumbo, *J. Phys. Chem. A*, 1997, **101**, 4298–4301.

110 J. Bouwman, W. Ludwig, Z. Awad, K. I. Öberg, G. W. Fuchs, E. F. van Dishoeck and H. Linnartz, *Astron. Astrophys.*, 2007, **476**, 995–1003.

111 K. Isokoski, J.-B. Bossa, T. Triemstra and H. Linnartz, *Phys. Chem. Chem. Phys.*, 2014, **16**, 3456–3465.

112 S. Cazaux, J.-B. Bossa, H. Linnartz and A. G. G. M. Tielens, *Astron. Astrophys.*, 2015, **573**, A16.

113 J.-B. Bossa, K. Isokoski, M. S. de Valois and H. Linnartz, *Astron. Astrophys.*, 2012, **545**, A82.

114 J.-B. Bossa, K. Isokoski, D. M. Paardekooper, M. Bonnin, E. P. van der Linden, T. Triemstra, S. Cazaux, A. G. G. M. Tielens and H. Linnartz, *Astron. Astrophys.*, 2014, **561**, A136.

115 T. Loerting, K. Winkel, M. Seidl, M. Bauer, C. Mitterdorfer, P. H. Handle, C. G. Salzmann, E. Mayer, J. L. Finney and D. T. Bowron, *Phys. Chem. Chem. Phys.*, 2011, **13**, 8783–8794.

116 A. Parmentier, J. J. Shephard, G. Romanelli, R. Senesi, C. G. Salzmann and C. Andreani, *J. Phys. Chem. Lett.*, 2015, **6**, 2038–2042.

117 C. G. Salzmann, P. G. Radaelli, B. Slater and J. L. Finney, *Phys. Chem. Chem. Phys.*, 2011, **13**, 18468–18480.

118 M. P. Collings, V. L. Frankland, J. Lasne, D. Marchione, a. Rosu-Finsen and M. R. S. McCoustra, *Mon. Not. R. Astron. Soc.*, 2015, **449**, 1826–1833.

119 V. Pirronello, O. Biham, C. Liu, L. Shen and G. Vidali, *Astrophys. J.*, 1997, **483**, L131–L134.

120 C. Yuan, R. S. Smith and B. D. Kay, *Surf. Sci.*, 2016, **652**, 350–354.

121 D. J. Burke, F. Puletti, P. M. Woods, S. Viti, B. Slater and W. A. Brown, *J. Phys. Chem. A*, 2015, **119**, 6837–6849.

122 W. A. Brown and A. S. Bolina, *Mon. Not. R. Astron. Soc.*, 2007, **374**, 1006–1014.

123 A. S. Bolina, A. J. Wolff and W. A. Brown, *J. Chem. Phys.*, 2005, **122**, 44713.

124 H. Ulbricht, R. Zacharia, N. Cindir and T. Hertel, *Carbon N. Y.*, 2006, **44**, 2931–2942.

125 S. Ioppolo, H. M. Cuppen, C. Romanzin, E. F. van Dishoeck and H. Linnartz, *Phys. Chem. Chem. Phys.*, 2010, **12**, 12065–12076.

126 J. Cyriac and T. Pradeep, *Chem. Phys. Lett.*, 2005, **402**, 116–120.

127 A. Bergantini, S. Pilling, H. Rothard, P. Boduch and D. P. P. Andrade, *Mon. Not. R. Astron. Soc.*, 2013, **437**, 2720–2727.

128 P. Jenniskens, D. F. Blake, M. A. Wilson and A. Pohorille, *Astrophys. J.*, 1995, **455**, 389–401.

129 P. Jenniskens and D. Blake, *Science (80-.).*, 1994, **265**, 753–756.

130 G. A. Kimmel, K. P. Stevenson, Z. Dohnálek, R. S. Smith and B. D. Kay, *J. Chem. Phys.*, 2001, **114**, 5284–5294.

131 U. Raut, M. Famá, B. D. Teolis and R. A. Baragiola, *J. Chem. Phys.*, 2007, **127**, 204713–204718.

132 R. S. Smith, T. Zubkov, Z. Dohnálek and B. D. Kay, *J. Phys. Chem. B*, 2009, **113**, 4000–4007.

133 K. P. Stevenson, *Science (80-.).*, 1999, **283**, 1505–1507.

134 R. L. Hudson and M. H. Moore, *Icarus*, 1999, **140**, 451–461.

135 K. I. Öberg, R. T. Garrod, E. F. van Dishoeck and H. Linnartz, *Astron. Astrophys.*, 2009, **504**, 891–913.

136 B. E. Hayden, K. Prince, D. P. Woodruff and A. M. Bradshaw, *Surf. Sci.*, 1983, **133**, 589–604.

137 N. Watanabe, K. Iwatsu, A. Yamakata, T. Ohtani, J. Kubota, J. N. Kondo, A. Wada, K. Domen and C. Hirose, *Surf. Sci.*, 1996, **357**–**358**, 651–655.

138 H. Yamamoto, N. Watanabe, A. Wada, K. Domen and C. Hirose, *J. Chem. Phys.*, 1997, **106**, 4734–4744.

139 T. Tomaru, T. Suzuki, T. Uchiyama, A. Yamamoto, T. Shintomi, C. . Taylor, K. Yamamoto, S. Miyoki, M. Ohashi and K. Kuroda, *Phys. Lett. A*, 2002, **301**, 215–219.

140 J. L. Edridge, PhD Thesis, University College London, 2010.

141 A. S. Bolina, A. J. Wolff and W. A. Brown, *J. Phys. Chem. B*, 2005, **109**, 16836–16845.

142 T. Carstens, R. Gustus, O. Höfft, N. Borisenko, F. Endres, H. Li, R. J. Wood, A. J. Page and R. Atkin, *J. Phys. Chem. C*, 2014, **118**, 10833–10843.

143 B. Chilukuri, U. Mazur and K. W. Hipps, *Phys. Chem. Chem. Phys.*, 2014, **16**, 14096–14107.

144 Y. Li, C. Liu, Y. Xie, X. Li, X. Li, X. Fan, K. Deng, Q. Zeng and C. Wang, *Phys. Chem. Chem. Phys.*, 2013, **15**, 125–128.

145 C. D. Zeinalipour-Yazdi and D. P. Pullman, *Chem. Phys.*, 2008, **348**, 233–236.

146 H. G. Drickamer, *Science*, 1967, **156**, 1183–1189.

147 C. Chen, Q.-H. Yang, Y. Yang, W. Lv, Y. Wen, P.-X. Hou, M. Wang and H.-M. Cheng, *Adv. Mater.*, 2009, **21**, 3007–3011.

148 K. S. Novoselov, A. K. Geim, S. V Morozov, D. Jiang, Y. Zhang, S. V Dubonos, I. V Grigorieva and A. A. Firsov, *Science*, 2004, **306**, 666–669.

149 S. Kwon, R. Vidic and E. Borguet, *Surf. Sci.*, 2003, **522**, 17–26.

150 D. A. King, *Surf. Sci.*, 1975, **47**, 384–402.

151 M. C. Wu, C. M. Truong and D. W. Goodman, *J. Phys. Chem.*, 1993, **97**, 4182–4186.

152 A. M. de Jong and J. W. Niemantsverdriet, *Surf. Sci.*, 1990, **233**, 355–365.

153 S. D. Green, A. S. Bolina, R. Chen, M. P. Collings, W. A. Brown and M. R. S. McCoustra, *Mon. Not. R. Astron. Soc.*, 2009, **398**, 357–367.

154 S. Viti, M. P. Collings, J. W. Dever, M. R. S. McCoustra and D. A. Williams, *Mon. Not. R. Astron. Soc.*, 2004, **354**, 1141–1145.

155 T. Leitner, J. Kattner and H. Hoffmann, *Appl. Spectrosc.*, 2003, **57**, 1502–1509.

156 J. Heidberg, M. Warskulat and M. Folman, *J. Electron Spectros. Relat. Phenomena*, 1990, **54**–**55**, 961–970.

157 R. G. Greenler, *J. Chem. Phys.*, 1966, **44**, 310–315.

158 Y. J. Chabal, *Surf. Sci. Rep.*, 1988, **8**, 211–357.

159 R. G. Greenler, *J. Vac. Sci. Technol.*, 1975, **12**, 1410–1418.

160 M. P. Collings, J. W. Dever, H. J. Fraser and M. R. S. McCoustra, in *NASA Laboratory Astrophysics Workshop*, 2002, vol. 1, p. 192.

161 A. S. Bolina, PhD Thesis, University College London, 2005.

162 J. E. Prue and A. J. Read, *Trans. Faraday Soc.*, 1966, **62**, 1271–1274.

163 Y. Qi, R. Zhu and D. Zhang, *J. Mol. Model.*, 2014, **20**, 2264.

164 P. A. Dilara and J. M. Vohs, *J. Phys. Chem.*, 1993, **97**, 12919–12923.

165 M. A. Shoaib and C. H. Choi, *J. Phys. Chem. C*, 2013, **117**, 4181–4188.

166 C. Iuga, C. I. Sainz-Díaz and A. Vivier-Bunge, *J. Phys. Chem. C*, 2012, **116**, 2904–2914.

167 P. Ehrenfreund, L. D'Hendecourt, S. Charnley and R. Ruiterkamp, *J. Geophys. Res.*, 2001, **106**, 33291–33301.

168 D. Bockelee-Morvan, D. Lis, J. Wink, D. Despois, J. Crovisier, R. Bachiller, D. Benford, N. Biver, P. Colom, J. Davies, E. Gerard, B. Germain, M. Houde, D. Mehringer, R. Moreno, G. Paubert, T. Phillips and H. Rauer, *Astron. Astrophys.*, 2000, **353**, 1101–1114.

169 T. J. Millar, P. R. A. Farquhar and K. Willacy, *Astron. Astrophys. Suppl. Ser.*, 1997, **121**, 139–185.

170 M. D. Boamah, K. K. Sullivan, K. E. Shulenberger, C. M. Soe, L. M. Jacob, F. C. Yhee, K. E. Atkinson, M. C. Boyer, D. R. Haines and C. R. Arumainayagam, *Faraday Discuss.*, 2014, **168**, 249–266.

171 R. C. Millikan and K. S. Pitzer, *J. Am. Chem. Soc.*, 1958, **80**, 3515–3521.

172 Y. Mikawa, *J. Chem. Phys.*, 1966, **45**, 4750–4751.

173 Y. Mikawa, J. W. Brasch and R. J. Jakobsen, *J. Mol. Spectrosc.*, 1967, **24**, 314–329.

174 W. S. Sim, P. Gardner and D. A. King, *J. Phys. Chem.*, 1996, **100**, 12509–12516.

175 M. Gantenberg, M. Halupka and W. Sander, *Chemistry*, 2000, **6**, 1865–1869.

176 C. Xu and D. W. Goodman, *J. Phys. Chem.*, 1996, **100**, 245–252.

177 J. L. Davis and M. A. Barteau, *Surf. Sci.*, 1991, 256, 50–66.

178 S. W. Jorgensen and R. J. Madix, *J. Am. Chem. Soc.*, 1988, **110**, 397–400.

179 M. A. Henderson, *J. Phys. Chem. B*, 1997, **101**, 221–229.

180 M. R. Columbia, A. M. Crabtree and P. A. Thiel, *J. Am. Chem. Soc.*, 1992, **114**, 1231–1237.

181 T. Ohtani, J. Kubota, A. Wada, J. N. Kondo, K. Domen and C. Hirose, *Surf. Sci.*, 1996, **368**, 270–274.

182 A. Borodin, O. Höfft, S. Bahr, V. Kempter and A. Allouche, in *Nuclear Instruments and Methods in Physics Research, Section B: Beam Interactions with Materials and Atoms*, Ise-Shima, Japan, 2005, vol. 232, pp. 79–87.

183 S. Bahr, A. Borodin, O. Höfft, V. Kempter and A. Allouche, *J. Chem. Phys.*, 2005, **122**, 234704.

184 M. D. Weisel, J. G. Chen, F. M. Hoffmann, Y.-K. Sun and W. H. Weinberg, *J. Chem. Phys.*, 1992, **97**, 9396–9411.

185 C. Houtman and M. A. Barteau, *Surf. Sci.*, 1991, **248**, 57–76.

186 R. Souda, *Surf. Sci.*, 2006, **600**, 3135–3140.

187 M. Kazempoor and G. Pirug, *Appl. Phys. A*, 2007, **87**, 435–441.

188 D. J. Burke and W. A. Brown, *Mon. Not. R. Astron. Soc.*, 2015, **448**, 1807–1815.

189 R. S. Smith and B. D. Kay, *Nature*, 1999, **398**, 788–791.

190 S. Y. Nishimura, R. F. Gibbons and N. J. Tro, *J. Phys. Chem. B*, 1998, **102**, 6831–6834.

191 R. S. Smith, J. Matthiesen and B. D. Kay, *J. Phys. Chem. A*, 2014, **118**, 8242–8250.

192 S. A. Sandford and L. J. Allamandola, *Astrophys. J.*, 1993, **417**, 815–825.

193 F. Puletti, PhD Thesis, University College London, 2014.

194 J. D. Thrower, M. P. Collings, F. J. M. Rutten and M. R. S. McCoustra, *Mon. Not. R. Astron. Soc.*, 2009, **394**, 1510–1518.

195 D. J. Burke, A. J. Wolff, J. L. Edridge and W. A. Brown, *J. Chem. Phys.*, 2008, **128**, 104702.

196 R. Raval and S. Munro, *J. Electron Spectros. Relat. Phenomena*, 1993, **64**–**65**, 461–468.

197 S. Ioppolo, H. M. Cuppen, E. F. van Dishoeck and H. Linnartz, *Mon. Not. R. Astron. Soc.*, 2011, **410**, 1089–1095.

198 S. Ioppolo, B. A. McGuire, M. A. Allodi and G. A. Blake, *Faraday Discuss.*, 2014, **168**, 461–484.

199 P. Jedlovszky, G. Hantal, K. Neuróhr, S. Picaud, P. N. M. Hoang, P. von Hessberg and J. N. Crowley, *J. Phys. Chem. C*, 2008, **112**, 8976–8987.

200 J. Cyriac and T. Pradeep, *J. Phys. Chem. C*, 2008, **112**, 1604–1611.

201 L. George and W. Sander, *Spectrochim. Acta. A. Mol. Biomol. Spectrosc.*, 2004, **60**, 3225–3232.

202 R. Souda, *J. Chem. Phys.*, 2003, **119**, 2774–2779.

203 R. Souda, *Phys. Rev. B*, 2004, **70**, 165412.

204 A. Allouche, *J. Chem. Phys.*, 2005, **122**, 234703.

205 J. Park and D. E. Woon, *Astrophys. J.*, 2006, **648**, 1285–1290.

206 J. L. Edridge, K. Freimann, D. J. Burke and W. A. Brown, *Philos. Trans. R. Soc. A*, 2013, **371**, 20110578–20110578.

207 R. S. Smith, J. Matthiesen, J. Knox and B. D. Kay, *J. Phys. Chem. A*, 2011, **115**, 5908–5917.

208 R. S. Smith, C. Huang and B. D. Kay, *J. Phys. Chem. B*, 1997, **101**, 6123–6126.

209 D. J. Burke, F. Puletti, P. M. Woods, S. Viti, B. Slater and W. A. Brown, *J. Chem. Phys.*, 2015, **143**, 164704.

210 A. J. Wolff, C. Carlstedt and W. A. Brown, *J. Phys. Chem. C*, 2007, **111**, 5990–5999.

211 P. A. Thiel and T. E. Madey, *Surf. Sci. Rep.*, 1987, **7**, 211–385.

212 D. Chakarov, L. Österlund and B. Kasemo, *Vacuum*, 1995, **46**, 1109–1112.

213 L. J. Allamandola, M. P. Bernstein, S. A. Sandford and R. L. Walker, *Space Sci. Rev.*, 1999, **90**, 219–232.

214 J. A. Noble, C. Martin, H. J. Fraser, P. Roubin and S. Coussan, *J. Phys. Chem. C*, 2014, **118**, 20488–20495.

215 B. J. Murray and E. J. Jensen, *J. Atmos. Solar-Terrestrial Phys.*, 2010, **72**, 51–61.

216 T. Loerting, V. Fuentes-Landete, P. H. Handle, M. Seidl, K. Amann-Winkel, C. Gainaru and R. Böhmer, *J. Non. Cryst. Solids*, 2015, **407**, 423–430.

217 C. Mitterdorfer, M. Bauer, T. G. A. Youngs, D. T. Bowron, C. R. Hill, H. J. Fraser, J. L. Finney and T. Loerting, *Phys. Chem. Chem. Phys.*, 2014, **16**, 16013–16020.

218 F. Mispelaer, P. Theulé, H. Aouididi, J. Noble, F. Duvernay, G. Danger, P. Roubin, O. Morata, T. Hasegawa and T. Chiavassa, *Astron. Astrophys.*, 2013, **555**, A13.

219 S. Malyk, G. Kumi, H. Reisler and C. Wittig, *J. Phys. Chem. A*, 2007, **111**, 13365–13370.

220 U. Raut, B. D. Teolis, M. J. Loeffler, R. A. Vidal, M. Famá and R. A. Baragiola, *J. Chem. Phys.*, 2007, **126**, 244511–244515.

221 A. Fresneau, G. Danger, A. Rimola, P. Theule, F. Duvernay and T. Chiavassa, *Mon. Not. R. Astron. Soc.*, 2014, **443**, 2991–3000.

222 M. E. Palumbo, G. A. Baratta, G. Leto and G. Strazzulla, *J. Mol. Struct.*, 2010,

972, 64–67.

223 M. E. Palumbo, *Astron. Astrophys.*, 2006, **453**, 903–909.

224 Z. Dohnálek, G. A. Kimmel, P. Ayotte, R. S. Smith and B. D. Kay, *J. Chem. Phys.*, 2003, **118**, 364–372.

225 R. A. May, R. S. Smith and B. D. Kay, *J. Chem. Phys.*, 2013, **138**, 104501.

226 R. A. May, R. S. Smith and B. D. Kay, *J. Chem. Phys.*, 2013, **138**, 104502.

227 A. V. Hill, *J. Physiol.*, 1910, **40**, i–vii.

228 S. R. Gadagkar and G. B. Call, *J. Pharmacol. Toxicol. Methods*, 2015, **71**, 68–76.

229 P. G. Gottschalk and J. R. Dunn, *Anal. Biochem.*, 2005, **343**, 54–65.

230 G. Herzberg, *Molecular Spectra and Molecular Structure. Volume II: Infrared and Raman Spectra of Polyatomic Molecules*, Van Nostrand Reinhold, New York, 1945.

231 A. Bondi, *J. Phys. Chem.*, 1964, **68**, 441–451.

232 M. E. Palumbo, G. A. Baratta, M. P. Collings and M. R. S. McCoustra, *Phys. Chem. Chem. Phys.*, 2006, **8**, 279–284.

233 M. Palumbo and G. Strazzulla, *Astron. Astrophys.*, 1993, **269**, 568–580.

234 M. P. Collings, J. W. Dever and M. R. S. McCoustra, *Phys. Chem. Chem. Phys.*, 2014, **16**, 3479–3492.

235 S. A. Sandford, L. J. Allamandola, A. G. G. M. Tielens and G. J. Valero, *Astrophys. J.*, 1988, **329**, 498–510.

236 L. J. Karssemeijer, S. Ioppolo, M. C. van Hemert, A. van der Avoird, M. A. Allodi, G. A. Blake and H. M. Cuppen, *Astrophys. J.*, 2014, **781**, 16–30.

237 M. P. Collings, J. W. Dever and M. R. S. McCoustra, *Chem. Phys. Lett.*, 2005, **415**, 40–45.

238 H. J. Fraser, M. P. Collings, J. W. Dever and M. R. S. McCoustra, *Mon. Not. R. Astron. Soc.*, 2004, **353**, 59–68.

239 J. P. Devlin, *J. Phys. Chem.*, 1992, **96**, 6185–6188.

240 C. Manca, C. Martin, A. Allouche and P. Roubin, *J. Phys. Chem. B*, 2001, **105**, 12861–12869.

241 B. Schmitt, J. M. Greenberg and R. J. A. Grim, *Astrophys. J.*, 1989, **340**, L33–L36.

242 A. Al-Halabi, A. W. Kleyn, E. F. van Dishoeck, M. C. van Hemert and G. J. Kroes, *J. Phys. Chem. A*, 2003, **107**, 10615–10624.

243 B. Maté, Y. Rodríguez-Lazcano and V. J. Herrero, *Phys. Chem. Chem. Phys.*, 2012, 14, 10595–10602.

244 G. E. Ewing and G. C. Pimentel, *J. Chem. Phys.*, 1961, **35**, 925–930.

245 S. E. Bisschop, H. J. Fraser, K. I. Öberg, E. F. van Dishoeck and S. Schlemmer, *Astron. Astrophys.*, 2006, **449**, 1297–1309.

246 J. A. Noble, E. Congiu, F. Dulieu and H. J. Fraser, *Mon. Not. R. Astron. Soc.*, 2012, **421**, 768–779.

247 E. Backus, M. Grecea, A. Kleyn and M. Bonn, *Phys. Rev. Lett.*, 2004, **92**, 236101.

248 M. L. R. van 't Hoff, C. Walsh, M. Kama, S. Facchini and E. F. van Dishoeck, *Astron. Astrophys.*, 2017, **599**, A101.

249 K. I. Öberg, R. Murray-Clay and E. A. Bergin, *Astrophys. J.*, 2011, **743**, L16.

250 N. Madhusudhan, M. A. Amin and G. M. Kennedy, *Astrophys. J.*, 2014, **794**, L12.

251 H. M. Cuppen, G. W. Fuchs, S. Ioppolo, S. E. Bisschop, K. I. Öberg, E. F. van Dishoeck and H. Linnartz, *Proc. Int. Astron. Union*, 2008, **4**, 377–382.

252 R. Visser, E. F. van Dishoeck, S. D. Doty and C. P. Dullemond, *Astron. Astrophys.*, 2009, **495**, 881–897.

253 D. Bockelée-Morvan, N. Biver, P. Colom, J. Crovisier, F. Henry, A. Lecacheux, J. K. Davies, W. R. F. Dent and H. A. Weaver, *Icarus*, 2004, **167**, 113–128.

254 H. Kobayashi, H. Kawakita, M. J. Mumma, B. P. Bonev, J. Watanabe and T. Fuse, *Astrophys. J.*, 2007, **668**, L75–L78.